Magnetic Soft Continuum Robots
for Telerobotic Stroke Intervention

by

Yoonho Kim

B.S., Seoul National University (2013)
S.M., Massachusetts Institute of Technology (2018)

Submitted to the Department of Mechanical Engineering
in partial fulfillment of the requirements for the degree of

Doctor of Philosophy in Mechanical Engineering

at the

MASSACHUSETTS INSTITUTE OF TECHNOLOGY

May 2022

Author . . . .
Department of Mechanical Engineering
April 29, 2022

Certified by. . . . .
Xuanhe Zhao
Professor of Mechanical Engineering
Thesis Supervisor

Accepted by . . . .
Nicolas Hadjiconstantinou
Chairman, Department Committee on Graduate Theses

Magnetic Soft Continuum Robots

for Telerobotic Stroke Intervention

by

Yoonho Kim

Submitted to the Department of Mechanical Engineering
on April 29, 2022, in partial fulfillment of the
requirements for the degree of
Doctor of Philosophy in Mechanical Engineering

Abstract

Robotic technologies have been adopted in various subspecialties of both open and minimally invasive surgery, offering benefits such as enhanced surgical precision and accuracy with reduced effort and fatigue of the surgeon. However, robotic applications to endovascular neurosurgery for treating stroke or brain aneurysms have remained largely unexplored. The brain's blood vessels are considerably challenging to navigate with a manually controlled passive guidewire, and improper or redundant guidewire manipulation can lead to devastating complications. Existing vascular robotic systems are designed to manipulate conventional guidewires with limited steering capabilities and remain unsuited for neurovascular intervention. In this thesis, we propose a telerobotic neurointerventional platform based on a magnetically controlled soft continuum robot. Composed of soft polymers containing tiny magnetic particles as distributed actuation sources, our magnetic soft continuum robot is thin and flexible enough to navigate the narrow and winding pathways of the brain's blood vessels. Our magnetic manipulation system consists of a robot arm with an actuating magnet and motorized linear drives to remotely steer and advance the continuum robot under the real-time teleoperation of the system. We evaluate our system's performance both in vitro with realistic anatomical models and in vivo with a porcine model and demonstrate telerobotically assisted therapeutic procedures for endovascular treatments of stroke and aneurysms. When compared with manually controlled passive guidewires, our telerobotic neurointerventional system based on magnetic manipulation helps to achieve safer and quicker access to hard-to-reach areas in the complex cerebral vasculature. Our system also allows an operator to work remotely from the radiation source to minimize x-ray exposure during the intervention. Furthermore, it may open the possibility of remote procedural services for telerobotic stroke intervention to address the logistical challenge in current stroke systems of care.

Thesis Supervisor: Xuanhe Zhao
Title: Professor of Mechanical Engineering

Thank you, Lord, my father in heaven, for establishing every step of my journey over the years. You always led me into the right path even when I felt disoriented and lost, and You supplied wisdom and strength every time I was going through tough times.

In their hearts humans plan their course, but the Lord establishes their steps.

– Proverbs 16:9 –

Acknowledgments

I am indebted to many mentors, colleagues, and friends that I met during my graduate studies. First, I would like to thank my advisor, Prof. Xuanhe Zhao, for always encouraging me to pursue creative and bold ideas while being intellectually engaged so that I could grow as an independent researcher. I am also thankful to Prof. Rohan Abeyaratne, Prof. Ellen Roche, and Prof. Alberto Rodriguez for their insightful comments and valuable inputs on my dissertation and presentation. My sincere gratitude also goes to Prof. Lallit Anand, from whom I learned solid mechanics and continuum mechanics, which laid the foundation for the theoretical modeling part of my thesis.

This thesis would not have been possible without the help and support of many collaborators. First of all, I feel extremely grateful to Dr. Aman Patel and Dr. Pablo Harker at Massachusetts General Hospital (MGH) and Dr. Marcin Balicki at Philips Research North America for their significant help and guidance on the preclinical validation of the developed telerobotic neurointerventional platform. I am thankful to my teammates, Emily Genevriere and Jaehun Choe, for their tremendous help in developing the user interface of our telerobotic neurointerventional system. I would also like to thank the co-authors of my papers, Ruike Zhao, Liu Wang, and Shengduo Liu, for their help in the simulation of magnetic soft materials based on the developed theoretical models, and German Parada for his help in the characterization of the hydrogel skin for lubrication of the magnetic soft continuum robots.

MIT was by far the greatest place that I could ever possibly belong, and I was extremely privileged to be part of this intelligent community. I thank all my friends here at MIT for being together with me during this exciting journey. I acknowledge financial support through a scholarship from ILJU Academy and Culture Foundation and MIT School of Engineering MathWorks Fellowship, which I truly appreciate.

Last but not least, I would like to thank my family, especially my parents and grandmother, and my fiancé, Yeongeun, for their unconditional love and continuous support. They have been the greatest source of strength during my graduate studies at MIT, and I am so thankful to them because they made me who I am today.

Prior publications

Some of the findings presented in this thesis were published in the following journal articles [1, 2, 3, 4, 5, 6], conference proceedings [7], and patent applications [8, 9]:

$^{\#}$*Co-first-authors*   *Corresponding author(s)*

1. **Y. Kim**$^{\#}$, H. Yuk$^{\#}$, R. Zhao$^{\#}$, S. A. Chester, and X. Zhao*, "Printing ferromagnetic domains for untethered fast-transforming soft materials," *Nature*, vol. 558, no. 7709, pp. 274-279, 2018.

2. R. Zhao$^{\#}$, **Y. Kim**$^{\#}$, S. A. Chester, P. Sharma, and X. Zhao*, "Mechanics of hard-magnetic soft materials," *Journal of the Mechanics and Physics of Solids*, vol. 124, pp. 244-263, 2019.

3. **Y. Kim**, G. A. Parada, S. Liu, and X. Zhao*, "Ferromagnetic soft continuum robots," *Science Robotics*, vol. 4, no. 33, p. eaax7329, 2019.

4. L. Wang$^{\#}$, **Y. Kim**$^{\#}$, C. F. Guo, and X. Zhao*, "Hard-magnetic elastica," *Journal of the Mechanics and Physics of Solids*, vol. 142, p. 104045, 2020.

5. **Y. Kim*** and X. Zhao*, "Magnetic soft materials and robots," *Chemical Reviews*, vol. 122, no. 5, pp. 5317-5364, 2022.

6. **Y. Kim**, E. Genevriere, P. Harker, J. Choe, M. Balicki, R. W. Regenhardt, J. E. Vranic, A. A. Dmytriw, A. B. Patel, and X. Zhao*, "Telerobotic neurovascular interventions with magnetic manipulation," *Science Robotics*, vol. 7, p. eabg9907, 2022.

7. **Y. Kim***, E. Genevriere, P. Harker, J. Choe, M. Balicki, A. B. Patel, and X. Zhao, "Telerobotically controlled magnetic soft continuum robots for neurovascular interventions," in *2022 IEEE International Conference on Robotics and Automation (ICRA)*, 2022.

8. **Y. Kim**, H. Yuk, and X. Zhao, "Programmable soft materials containing ferromagnetic domains and methods of making," US Patent Application, Publication number: US 2020/0223099 A1 (pending).

9. **Y. Kim** and X. Zhao, "Magnetically steerable continuum robotic guidewires for neurovascular applications," 2021, US Patent 11,103,324 (granted).

Contents

List of Acronyms and Abbreviations

ACA	anterior cerebral artery
ACoA	anterior communicating artery
AP	anteroposterior
AVF	arteriovenous fistula
AVM	arteriovenous malformation
CAD	computer-aided design
CAU	caudal
CMOS	complementary metal-oxide semiconductor
CRA	cranial
DOF	degree of freedom
DSA	digital subtraction angiography
FDA	Food and Drug Administration
IACUC	Institutional Animal Care and Use Committee
ICA	internal carotid artery
ISO	International Organization for Standardization
LAO	left anterior oblique
LAT	lateral
MCA	middle cerebral artery
NdFeB	neodymium-iron-boron
PCI	percutaneous coronary intervention
PCoA	posterior communicating artery
PDMAA	polydimethylacrylamide

PDMS   polydimethysiloxane

PMA   premarket approval

PVI   peripheral vascular intervention

RAO   right anterior oblique

TEM   transmission electron microscope

TEOS   tetraethylorthosilicate

TMOS   tetramethylorthosilicate

TPU   thermoplastic polyurethane

VSM   vibrating sample magnetometer

List of Mathematical Symbols

$\mathbf{m}$	magnetic moment $[\mathrm{A\cdot m^2}]$
M, $\mathbf{M}$	magnetization (magnetic moment density per volume) $[\mathrm{A\cdot m^{-1}}]$
V	volume of magnetic media $[\mathrm{m^3}]$
M_s, $\mathbf{M}_\mathrm{s}$	saturation magnetization $[\mathrm{A\cdot m^{-1}}]$
M_r, $\mathbf{M}_\mathrm{r}$	remanence in the current deformed configuration $[\mathrm{A\cdot m^{-1}}]$
$\tilde{M}_\mathrm{r}$, $\tilde{\mathbf{M}}_\mathrm{r}$	remanence in the undeformed reference configuration $[\mathrm{A\cdot m^{-1}}]$
B, $\mathbf{B}$	magnetic flux density $[\mathrm{T}] = [\mathrm{N\cdot A^{-1}\cdot m^{-1}}]$
H, $\mathbf{H}$	magnetic field $[\mathrm{A\cdot m^{-1}}]$
H_c, $\mathbf{H}_\mathrm{c}$	coercivity $[\mathrm{A\cdot m^{-1}}]$
H^sat, $\mathbf{H}^\mathrm{sat}$	saturating magnetic field $[\mathrm{A\cdot m^{-1}}]$
$\mathbf{H}_\mathrm{a}$	applied magnetic field $[\mathrm{A\cdot m^{-1}}]$
$\mathbf{H}_\mathrm{m}$	magnetostatic field $[\mathrm{A\cdot m^{-1}}]$
χ_m	magnetic susceptibility $[\cdot]$
μ_0	magnetic permeability $[\mathrm{N\cdot A^{-2}}]$
u_m	magnetic potential energy $[\mathrm{J}]$
U_m	magnetic potential energy density $[\mathrm{J\cdot m^{-3}}]$
$\mathcal{U}_\mathrm{m}$	magnetostatic energy density $[\mathrm{J\cdot m^{-3}}]$
$\bar{\mathbf{f}}$, $\bar{\boldsymbol{\tau}}$	body force density $[\mathrm{N\cdot m^{-3}}]$ and body torque density $[\mathrm{N\cdot m^{-2}}]$
f_m, $\mathbf{f}_\mathrm{m}$	magnetic body force $[\mathrm{N}]$
$\bar{f}_\mathrm{m}$, $\bar{\mathbf{f}}_\mathrm{m}$	magnetic body force density $[\mathrm{N\cdot m^{-3}}]$
τ_m, $\boldsymbol{\tau}_\mathrm{m}$	magnetic body torque $[\mathrm{N\cdot m}]$
$\bar{\tau}_\mathrm{m}$, $\bar{\boldsymbol{\tau}}_\mathrm{m}$	magnetic body torque density $[\mathrm{N\cdot m^{-2}}]$

$\mathbf{J}$	current density $[\text{A·m}^{-2}]$
$\mathbf{J}_\text{f}$	free current density $[\text{A·m}^{-2}]$
$\mathbf{J}_\text{m}$	magnetization current density $[\text{A·m}^{-2}]$
$\mathbf{K}$	surface current density $[\text{A·m}^{-1}]$
$\mathbf{K}_\text{f}$	free surface current density $[\text{A·m}^{-1}]$
$\mathbf{K}_\text{m}$	surface magnetization current density $[\text{A·m}^{-1}]$
ρ_m	magnetic charge density $[\text{N·A}^{-1}\text{·m}^{-2}]$
ρ_ms	magnetic surface charge density $[\text{N·A}^{-1}\text{·m}^{-1}]$
Φ	magnetic scalar potential $[\text{A}]$
$\mathcal{N}$	demagnetizing tensor $[\cdot]$
Ψ	total Helmholtz free energy $[\text{J}]$
ψ	Helmholtz free energy per unit current volume $[\text{J·m}^{-3}]$
ψ_R	Helmholtz free energy per unit reference volume $[\text{J·m}^{-3}]$
$\mathcal{D}_\text{int}$	internal energy dissipation rate per unit reference volume $[\text{J·m}^{-3}\text{·s}^{-1}]$
$\mathcal{W}$	energy (mechanical work) density $[\text{J·m}^{-3}]$
$\mathbf{F}$	deformation gradient tensor $[\cdot]$
$\dot{\mathbf{F}}$	time derivative of $\mathbf{F}$ $[\text{s}^{-1}]$
J	volumetric Jacobian $[\cdot]$
$\boldsymbol{\sigma}$	Cauchy stress tensor $[\text{Pa}] = [\text{N·m}^{-2}]$
$\mathbf{P}$	Piola stress tensor $[\text{Pa}] = [\text{N·m}^{-2}]$
$\boldsymbol{\mathcal{E}}$	third-order permutation tensor $[\cdot]$
ε_{ijk}	Levi–Civita symbol $[\cdot]$
$\otimes$	dyadic (tensor) product
$\mathbf{C}$	right Cauchy–Green tensor $[\cdot]$
I_1	first invariant of the right Cauchy–Green tensor $[\cdot]$
$\mathbf{R}$	rotation tensor $[\cdot]$
$\mathbf{U}$	right stretch tensor $[\cdot]$
$\mathbf{1}$	identity tensor $[\cdot]$
E	Young's modulus $[\text{Pa}] = [\text{N·m}^{-2}]$

G	shear modulus $[\mathrm{Pa}] = [\mathrm{N\cdot m^{-2}}]$
K	bulk modulus $[\mathrm{Pa}] = [\mathrm{N\cdot m^{-2}}]$
G', G''	storage and loss moduli $[\mathrm{Pa}] = [\mathrm{N\cdot m^{-2}}]$
s	arc length of a beam $[\mathrm{m}]$
κ	curvature of the centerline of a beam $[\mathrm{rad\cdot m^{-1}}]$
θ	deflection angle of a beam $[\mathrm{rad}]$
θ_L	maximum deflection angle at the free end $[\mathrm{rad}]$
I	area moment of inertia of a beam $[\mathrm{m^4}]$
A	cross-sectional area of a beam $[\mathrm{m^2}]$
L, W, T	length, width, and thickness of a rectangular beam $[\mathrm{m}]$
L_1, L_2	length of stiff and soft segments $[\mathrm{m}]$
D	diameter of a circular beam $[\mathrm{m}]$
d	diameter of an incorporated functional core $[\mathrm{m}]$
$F_{\mathrm{eq}}, \mathbf{F}_{\mathrm{eq}}$	equivalent point load at the free end of a beam $[\mathrm{N}]$
φ	actuating field angle relative to a beam $[\mathrm{rad}]$
δ_x, δ_y	x and y coordinates of the free end $[\mathrm{m}]$
$\mathbf{e}_1, \mathbf{e}_2, \mathbf{e}_3$	Cartesian basis vectors $[\cdot]$
p	hydrostatic pressure $[\mathrm{Pa}] = [\mathrm{N\cdot m^{-2}}]$
$\mathcal{M}, \boldsymbol{\mathcal{M}}$	internal bending moment $[\mathrm{N\cdot m}]$
λ	stretch $[\cdot]$
$\lambda_1, \lambda_2, \lambda_3$	principal stretches $[\cdot]$
ϕ	magnetic particle volume fraction $[\cdot]$
M_{p}	remanence of magnetized particles $[\mathrm{A\cdot m^{-1}}]$
$\mathbf{q}$	joint-space vector $[\mathrm{rad}]$
$\mathbf{x}$	task-space vector $[\mathrm{m}]$
$\mathbf{J}(\mathbf{q}), \mathbf{J}^{\dagger}(\mathbf{q})$	Jacobian and pseudo-inverse of the Jacobian $[\mathrm{m\cdot rad^{-1}}]$
R	radius of an actuating magnet $[\mathrm{m}]$
B_{re}	remanence of an actuating magnet $[\mathrm{T}] = [\mathrm{N\cdot A^{-1}\cdot m^{-1}}]$
α	rotation angle of an actuating magnet $[\mathrm{rad}]$

$$\nabla \mathbf{A} = \operatorname{grad} \mathbf{A} \qquad \text{gradient of a vector field } \mathbf{A}$$

$$\nabla f = \operatorname{grad} f \qquad \text{gradient of a scalar field } f$$

$$\nabla^2 f \qquad \text{Laplacian of a scalar field } f$$

$$\nabla \cdot \mathbf{A} = \operatorname{div} \mathbf{A} \qquad \text{divergence of a vector field } \mathbf{A}$$

$$\nabla \times \mathbf{A} = \operatorname{curl} \mathbf{A} \qquad \text{curl of a vector field } \mathbf{A}$$

Chapter 1

Introduction

1.1 Motivation

Stroke is one of today's major health problems worldwide. Globally, stroke remains the leading cause of serious long-term disability [10, 11] and the second-leading cause of death [12]. According to the statistics, every 40 seconds one person suffers a stroke in the United States, and it claims a life every 4 minutes [11]. In the United States alone, stroke kills about 140,000 people and costs around $46 billion each year [11]. Stroke occurs either when blood flow to the brain is blocked by blood clots or plaques (ischemic) or when a weakened blood vessel ruptures to cause bleeding (hemorrhagic) into the brain (**Figure 1-1A**). Both ischemic and hemorrhagic strokes can lead to permanent brain damage, and hence early intervention is critical to better protect the brain. However, current stroke systems of care require physically transporting patients to tertiary care centers (large university hospitals) for interventions (**Figure 1-1B**). For patients in rural areas, where acute-care services are often unavailable, stroke is particularly more challenging to treat in a timely fashion, and patients can become no longer eligible for therapies when their brains are irreparably damaged. One potential solution to this logistical challenge is to use teleoperated robotic systems for remote surgery [13]. Such telerobotic platforms could enable skilled interventionalists at large institutions to perform surgical tasks remotely on patients at their local hospitals, obviating transport of patients at the expense of time [14].
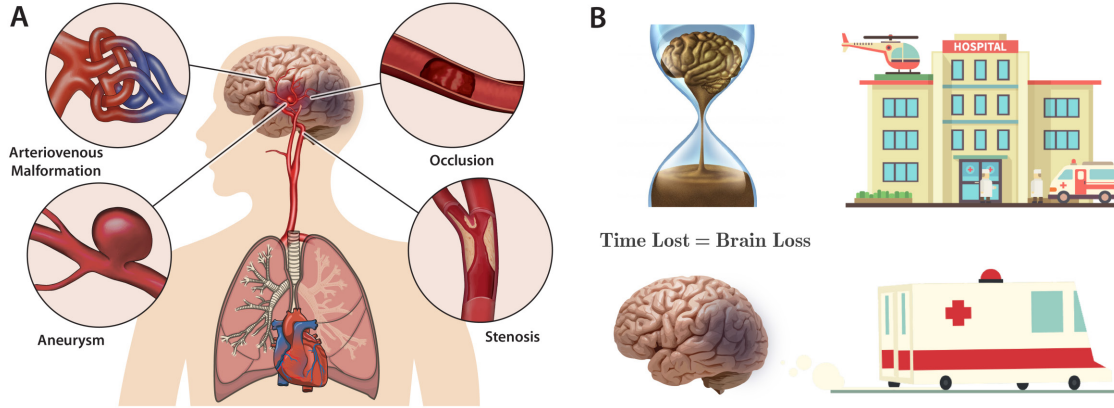
Figure 1-1: (**A**) Neurovascular diseases that can lead to hemorrhagic or ischemic stroke. Hemorrhagic stroke occurs when a weakened blood vessel in diseased states such as arteriovenous malformations/fistulas (AVMs/AVFs) or intracranial aneurysms ruptures to cause bleeding. Ischemic stroke occurs when blood flow to the brain is blocked by blood clots or plaques. (**B**) Logistical challenge in current stroke systems of care pertaining to the patient transport to tertiary care centers at the expense of time. The human nervous tissues can be rapidly and irretrievably lost as stroke progresses, and the phrase "*time is brain*" [15] emphasizes the critical importance of early stroke intervention for protection of the brain.

In the broader context of endovascular neurosurgery, there are several challenges in the operating room as well. In neuroendovascular interventions, microguidewires are primarily used for intravascular access to target lesions and to facilitate the placement of other interventional or therapeutic devices such as microcatheters, coils, and stents. For steering purposes, typical vascular guidewires have pre-shaped or shapeable distal tips which can be oriented toward a desired direction by manually rotating the wires from their proximal ends (**Figure 1-2A**). However, this twist-based maneuver for such conventional passive guidewires often becomes ineffective and rather unpredictable due to the jerky motion of the pre-bent tip caused by friction, also known as "*whipping* [16]," particularly when navigating in narrow and winding pathways of the brain's blood vessels (**Figure 1-2A**). This unpredictable guidewire behavior makes it difficult to reach distal branches of cerebral arteries and in some circumstances renders distal target access infeasible. The predefined shape of the tip might also deform within the vessel, especially during complicated and lengthy guiding maneuvers [17]. Moreover, interventionalists often need to continuously turn the guidewire while inserting it to prevent the pre-bent tip from latching onto any small ostium or opening

along the path; the distal tip could otherwise become stuck and potentially cause vascular injury or perforation upon further pushing. To avoid such complications, physicians always need to keep verifying the distal tip movement under fluoroscopy while manually manipulating guidewires, which exposes them to continuous x-rays during the interventional procedures (**Figure 1-2B**). For interventionalists, this repetitive radiation exposure is being recognized as a greater risk than previously appreciated [18, 19]. Telerobotic interventional systems, which allow for remote control of robotic guidewires with active steering and navigational capabilities, could potentially help to resolve these clinical and technical challenges as well.
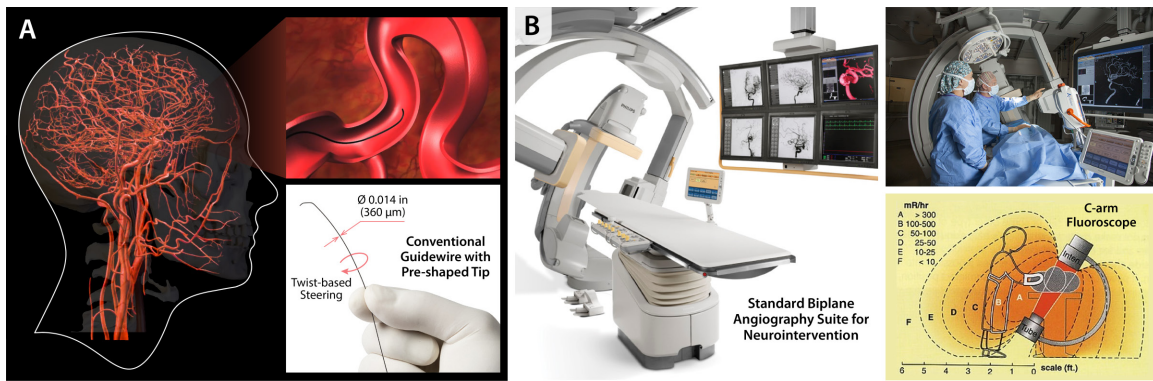
Figure 1-2: Technical challenges in endovascular neurosurgery. (**A**) The human brain's blood vessels are considerably challenging to navigate because of their complex and tortuous vascular anatomy. Conventional intravascular guidewires have pre-shaped or shapeable distal tips for steering purposes so that they can be manually manipulated through twist-based steering. (**B**) Complex neurodendovascular procedures require standard biplane fluoroscopy to better identify the complex angulation of the intracranial arteries. During the image-guided endovascular procedures, physicians are exposed to continuous x-ray, which is required for real-time state observation of the manually controlled guidewire in the patient's blood vessels. This repetitive radiation exposure is being recognized as a greater concern than previously appreciated, due to the increased risk of cancer and cataract formation.

However, robotic applications to endovascular neurosurgery have remained largely underexplored due to the lack of appropriate technologies. The biggest hurdle thus far has been the miniaturization of robotic devices so that they are thin and flexible enough to navigate in the narrow and complex neurovasculature. Existing steerable robotic catheters or endoscopes are often limited to relatively large scales (i.e., a few millimeters in diameter), due to the miniaturization challenges inherent in their

conventional actuation mechanisms [3], and are therefore unsuitable for neuroendovascular applications [20]. Instead of directly tackling the miniaturization challenges of realizing robotically steerable guidewires and catheters at submillimeter scale, industry has developed vascular robotic platforms that can accommodate and manipulate conventional guidewires and catheters under remote control. For example, the Magellan™ Robotic System of Hansen Medical (acquired by Auris Health, part of Johnson & Johnson) features an articulating sheath with linear and rotary drives to enable insertion, rotation, and retraction of conventional guidewires (**Figure 1-3A**) [20, 21].
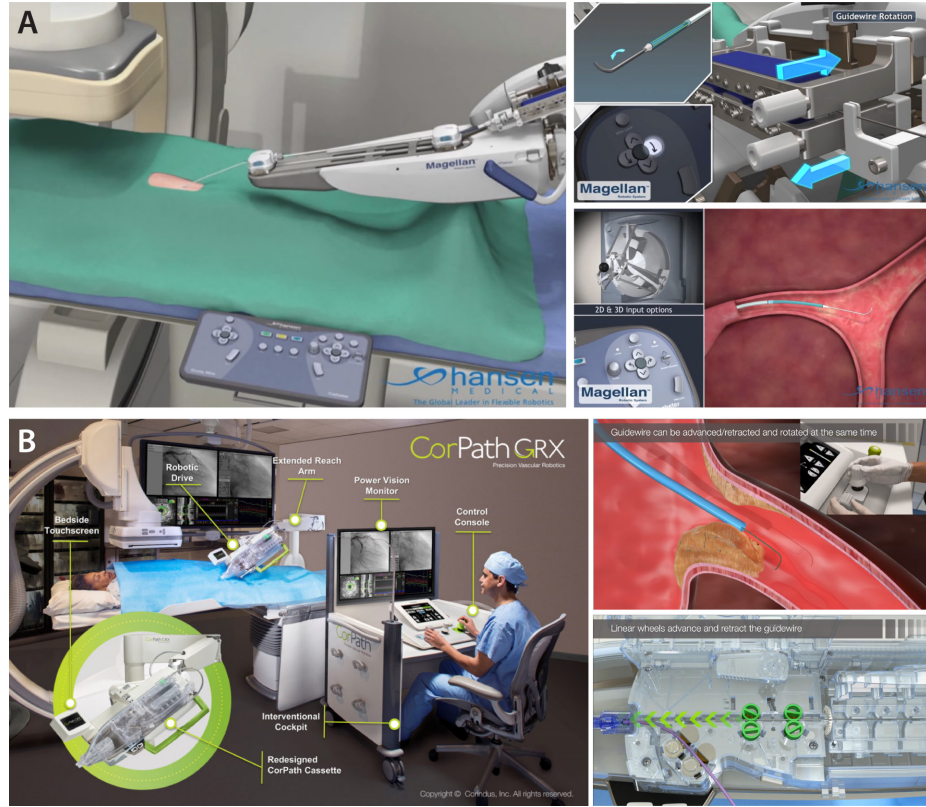
Figure 1-3: Existing vascular robotic systems. The existing platforms are designed to manipulate conventional passive guidewires with pre-shaped distal tips for either percutaneous coronary intervention (PCI) or peripheral vascular intervention (PVI): (**A**) Magellan™ Robotic System of Hansen Medical and (**B**) CorPath® GRX of Corindus Vascular Robotics.

Other examples include the CorPath® GRX of Corindus Vascular Robotics (acquired by Siemens Healthineers) and R-One™ of Robocath, both of which can similarly advance or retract and rotate commercially available guidewires and catheters using

linear and rotary drives under remote control [22] (**Figure 1-3B**). The R-One™ system has recently been approved for percutaneous coronary intervention (PCI) only in the European Union [23], and the CorPath® GRX system is currently approved for peripheral vascular intervention (PVI) as well as PCI in the United States, European Union, and other countries [24]. Although the CorPath® GRX system was originally designed to manipulate larger-gauge devices for PCI and PVI, the system is cleared for neurovascular intervention in the European Union, Australia, and New Zealand [24]. However, it has not yet been approved for neurovascular intervention in other countries including the United States [25], possibly because of its current technical limitations for intracranial applications as discussed in a recent case report [26].
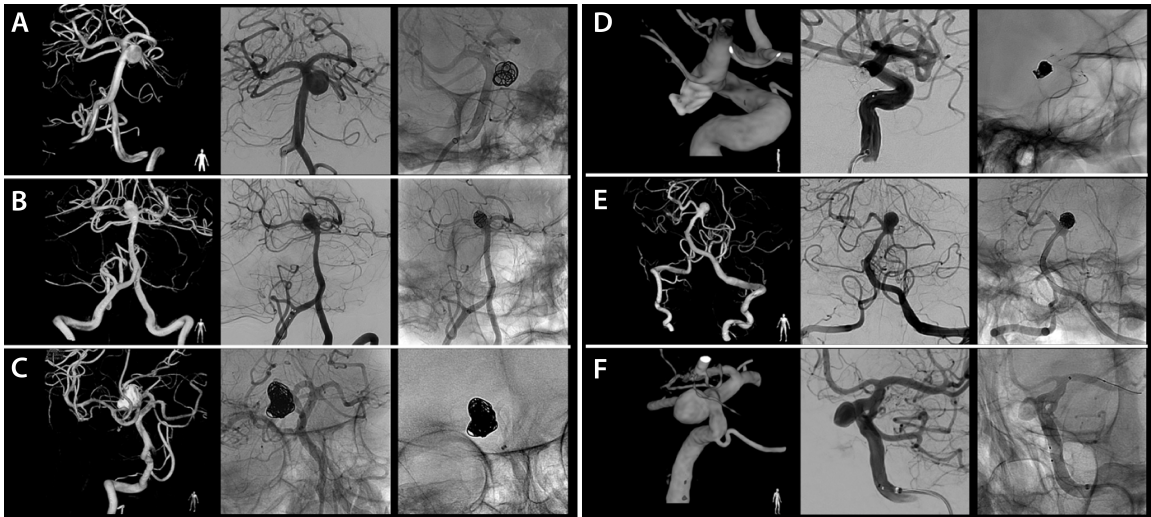
Figure 1-4: Reported clinical cases of robotically assisted intracranial aneurysm treatments. The CorPath® GRX system of Corindus Vascular Robotics was used for the reported clinical cases. The treated aneurysm locations include (**A**) the basilar sidewall; (**B**, **E**) the basilar tips; (**C**, **D**) the posterior communicating artery (PCoA); and (**F**) the supraclinoid segment of the intracranial carotid artery (ICA). Images are adapted from Pereira *et al.*, 2021 [27].

After some technical modifications of the CorPath® GRX system to facilitate the use of smaller guidewires and microcatheters for intracranial access and intervention, recent publications reported its first-in-human, off-label use for endovascular coiling of aneurysms in the basilar artery—a relatively large and linear blood vessel at the base of the skull—and other proximal intracranial arteries that are relatively easy to

access (**Figure 1-4**) [24, 27]. To date, however, no vascular robotic systems have been reported to accomplish robotically assisted endovascular treatment of cerebral aneurysms or infarctions (stroke), which commonly occur in more distal (hence more difficult-to-reach) areas such as the middle or anterior cerebral arteries (MCA or ACA). More importantly, those existing vascular robotic systems are designed to manipulate conventional passive guidewires with pre-shape tips, and therefore they would retain the functional limitations inherent in the twist-based steering of such passive guidewires as discussed earlier (**Figure 1-2A**). Currently, there is no FDA-approved robotic system for neurovascular intervention in the market.

1.2   Objectives and System Overview

This thesis is aimed at tackling the aforementioned technical challenges in current stroke systems of care and endovascular neurosurgery, where the application of robotics can be central to their solution. For example, actively steerable soft continuum robots can help to improve the quality and safety of endovascular procedures by reducing the unpredictable behavior and potentially risky maneuvers of conventional passive guidewires under manual manipulation. In addition, the ability to control such continuum robots remotely from the x-ray source can help to minimize or eliminate the radiation exposure to interventionalists during the endovascular procedures. In this thesis, we present a telerobotic neurointerventional platform based on magnetic manipulation to enable robotic applications to endovascular neurosurgery for treating stroke or brain aneurysms, which have remained largely unattainable with existing continuum or vascular robotic systems.

Our developed telerobotic neurointerventional system allows for precise robotic control of a magnetically steerable soft-robotic guidewire, which can navigate through the narrow and winding pathways of the brain's blood vessels under magnetic manipulation (**Figure 1-5**, **A** and **B**). **Figure 1-5C** provides an overview of our system deployed in realistic clinical settings for image-guided neurovascular intervention for endovascular treatments of stroke or aneurysms. Our telerobotic neurointerventional

24

system consists of a seven-degree-of-freedom (7-DOF) serial robot arm manipulator with an actuating magnet attached to its end-effector, which can be remotely controlled by an operator from the control console to apply the magnetic fields required for actuation and steering of the magnetic soft continuum guidewire. In addition, a set of motorized linear drives is used to advance or retract the magnetic soft continuum guidewire along with a microcatheter—a thin hollow tube that travels over the guidewire along the navigated path—under real-time teleoperation of the system.
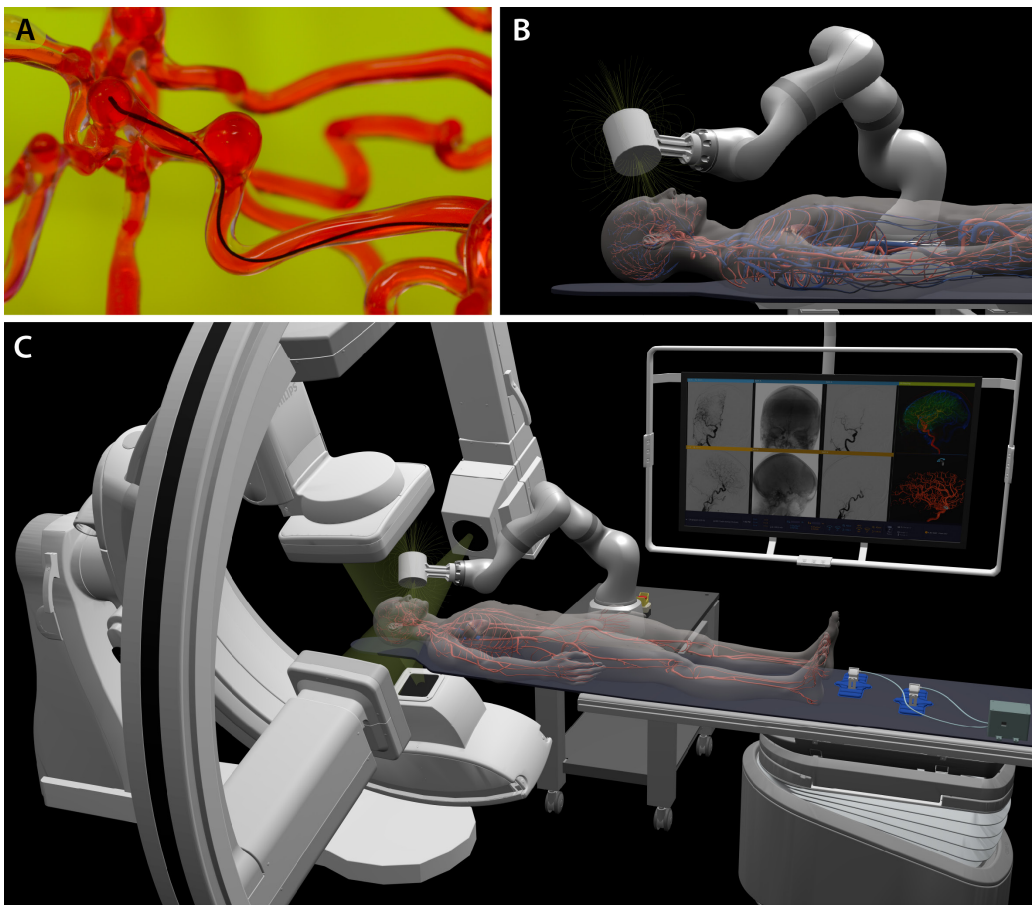
Figure 1-5: Overview of the proposed telerobotic neurointerventional platform based on magnetic manipulation. (**A-B**) Submillimeter-scale magnetic soft continuum robot as an actively steerable soft-robotic guidewire navigating in the complex and tortuous vasculature of the brain through its omnidirectional steering under magnetic manipulation. (**C**) Telerobotic magnetic manipulation platform for the magnetic soft continuum robot based on a robot arm with an actuating magnet to remotely steer the magnetic soft continuum guidewire and a guidewire/microcatheter advancing unit deployed in clinical settings for image-guided neurovascular intervention for endovascular treatments of stroke or aneurysms under real-time x-ray fluoroscopy based on the standard biplane angiography suite.

1.3   Outline of the Thesis

In **Chapter 2: Mechanics of Magnetic Soft Materials**, we discuss different types of magnetic soft materials and their key characteristics to elucidate their actuation mechanisms under externally applied magnetic fields. After reviewing the fundamental equations in magnetostatics, we formulate a continuum mechanical framework for hard-magnetic soft materials to model their behavior as soft bending actuators driven by magnetic torques and forces through finite element simulation. Applying geometric constraints specific to slender beams, we also formulate the theory of hard-magnetic elastica to model the behavior of magnetic soft continuum robots under magnetic fields. We then validate the developed models by comparing the experimental results with the model-based simulation and analytical solutions for two representative cases.

In **Chapter 3: Magnetic Soft Continuum Robots**, we describe our invention of magnetic soft continuum robots, which are developed to tackle the miniaturization challenges in continuum robots and to enable robotic applications to endovascular neurosurgery. On the basis of our theoretical analyses in **Chapter 2**, we provide a set of design guidelines for optimization of the actuation performance of the magnetic soft continuum robot based on hard-magnetic soft composites. We then discuss the materials and fabrication techniques for magnetic soft continuum robots with considerations of design requirements specific to their endovascular applications. To validate the proposed concept of magnetically steerable soft continuum robots at submillimeter scales, we provide a set of experimental demonstrations with proof-of-concept prototypes to illustrate their steering and navigational capabilities in highly nonlinear and complex environments as well as additional functionalities enabled by incorporated functional cores.

In **Chapter 4: Telerobotic Magnetic Neurointerventional Platform**, we discuss different types of existing magnetic actuation and manipulation platforms based on permanent or electromagnets and identify their inherent limitations for applications to telerobotic stroke intervention in terms of their compatibility with the standard imaging modality based on x-ray fluoroscopy. We then introduce our pro-

posed telerobotic neurointerventional platform based on a compact and lightweight robot arm with a single actuating magnet at its end-effector. We define a set of steering control principles that can provide guidance on how to manipulate the actuating magnet with minimal motion of the robot arm to achieve the desired configuration of the magnetic soft continuum guidewire in the target vasculature. We discuss the working distance, shape, and size of the actuating magnet considering the workspace constraints due to the patient geometry as well as the steering principle for the magnetic soft continuum guidewire.

In **Chapter 5: Telerobotically Assisted Neurovascular Interventions**, we showcase the performance of our developed telerobotic neurointerventional platform in realistic clinical settings for neurovascular intervention. As part of the benchtop verification of our system, we demonstrate the steering and navigational capabilities of the magnetic soft continuum guidewire to selectively reach different branches of cerebral arteries under real-time teleoperation of our system, using realistic anatomical models that include all relevant pathway attributes to represent the human neurovascular anatomy. We validate the safety and effectiveness of magnetic steering and navigation under realistic in vivo conditions using an animal model simulating the tortuosity of the intracranial arteries. We also quantitatively assess the learning curve for our developed system for a group of neurointerventionalists and evaluate the steering and navigational performance of the telerobotically controlled magnetic guidewire in comparison with the conventional approach based on manually controlled passive guidewires using the anatomical models. We further demonstrate our system's capability to assist therapeutic procedures that are commonly performed in endovascular neurosurgery such as coil embolization for treating cerebral aneurysms and clot retrieval thrombectomy for treating ischemic stroke due to cerebral infarctions.

In **Chapter 6: Conclusions and Future Work**, we summarize the findings and contributions of this thesis and provide considerations for clinical translation of our telerobotic neurointerventional platform in terms of the biocompatibility of the magnetic soft continuum robot. We also discuss more considerations for future developments of our system in the context of robotic telesurgery for stroke intervention,

implementation of tactile and haptic feedback, and automation of the magnetic steering and navigational tasks through pre-procedural planning based on pre-operative imaging data.

Chapter 2

Mechanics of Magnetic Soft Materials

2.1 Magnetic Soft Materials

2.1.1 Introduction

Historically, magnetically responsive soft materials in the form of elastically deformable solids have been referred to by a variety of terms such as magnetorheological [28, 29, 30, 31, 32], magnetoactive [33, 34] or magnetosensitive [35, 36, 37] elastomers or gels or, simply ferrogels [38, 39, 40, 41], depending on their applications or the type of materials used. For simplicity, we refer to such elastic solids with mechanical softness or compliance as well as magnetic properties as magnetic soft materials. In our definition, and throughout this review, the term "magnetic" generally implies "strongly magnetic". Accordingly, we will use the term "magnetic materials" to generically refer to "ferromagnetic" or "ferrimagnetic" materials that are strongly attracted to a magnet due to spontaneous magnetization (i.e., magnetic moments present in the material even in the absence of an external magnetic field). Magnetic soft materials in general have at least two constituent materials to form a composite, in which magnets of varying sizes (from nanometers to millimeters) are attached to or integrated into deformable bodies made of soft materials or flexible structures [42].

Depending on their composite structure, magnetic soft materials can be classified into either discrete or continuous systems. Discrete systems have one or a few finite-sized magnets or some patches of magnetic composite attached to or embedded in the

deformable body [43, 44, 45, 46, 47] and hence feature highly concentrated and localized magnetic moments (**Figure 2-1A**). Continuous systems have dispersed magnetic materials in the form of micro- or nanoscale particles, which give rise to diluted and distributed magnetic moments throughout the composite matrices (**Figure 2-1B**). Continuous magnetic soft materials can be further divided into either isotropic or anisotropic composites, depending on the distribution and orientation of the embedded magnetic particles in the composite matrix. In isotropic composites, the magnetic particles are uniformly dispersed and randomly oriented (**Figure 2-1C**), regardless of whether the particles themselves are isotropic or anisotropic in shape. In anisotropic composites, however, the embedded magnetic particles are either connected to form microscopic chains that are aligned in the same direction or all oriented toward the same direction (**Figure 2-1D**), both of which can result from an external field applied during the solidification of the polymer matrix to immobilize the aligned particles.
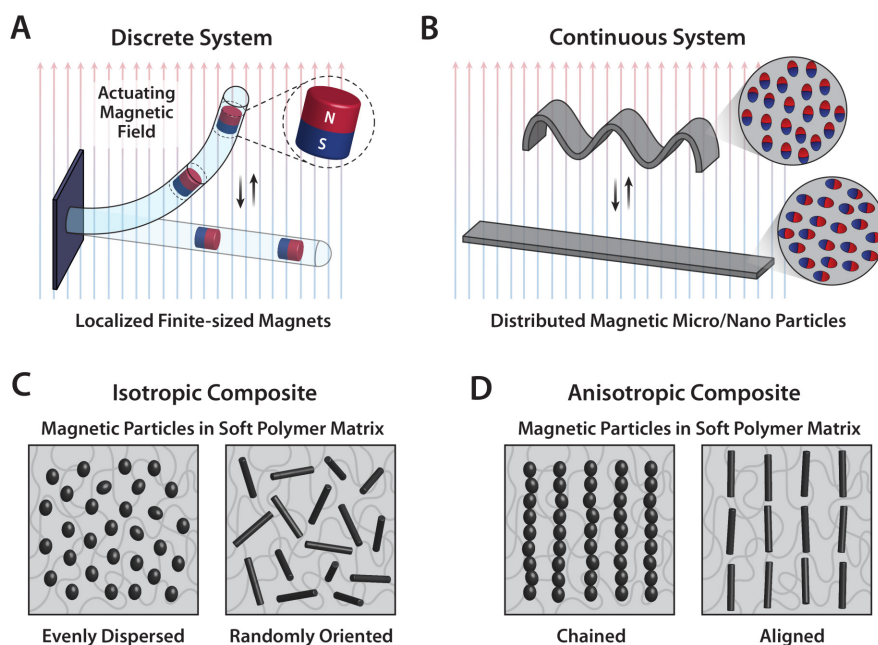
Figure 2-1: Classification and composition of magnetic soft materials. Magnetic soft materials can be classified into either (**A**) discrete or (**B**) continuous systems depending on whether the magnetic components are in the form of finite-sized magnets embedded in the flexible structure or micro- or nanoparticles dispersed in the soft polymer matrix. Continuous magnetic soft materials can be further categorized into either (**C**) mechanically isotropic or (**D**) anisotropic composites depending on the microscopic structure or arrangement of the magnetic filler particles in the host polymer matrix.

2.1.2 Classification of Magnetic Materials

Among the different classes of magnetic materials, the focus here is primarily on ferromagnetic or ferrimagnetic substances, which are generally considered "magnetic" due to their strong response to an externally applied magnetic field. Depending on the magnetization characteristics, these strongly magnetic materials can be classified into three categories: soft-magnetic, hard-magnetic, and superparamagnetic. The key difference among these types of magnetic materials can be described by the qualitatively different features of their magnetization curves (**Figure 2-2**).
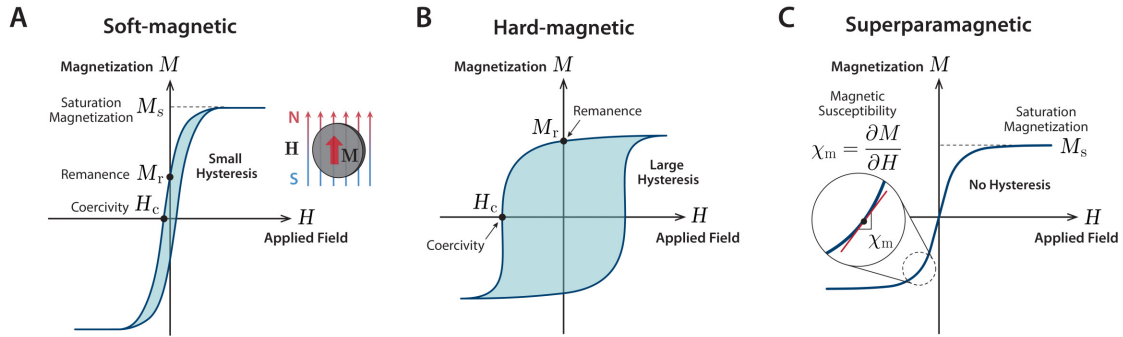
Figure 2-2: Classification of magnetic materials and their characteristics. Magnetic materials can be divided into three categories: (**A**) soft-magnetic, (**B**) hard-magnetic, and (**C**) superparamagnetic, depending on their magnetization characteristics. In general, soft-magnetic materials are characterized by their high saturation magnetization (M_s), low coercivity (H_c), and low remanence (M_r) with narrow hysteresis curves, whereas hard-magnetic materials are characterized by large hysteresis due to their high coercivity and remanence. Superparamagnetic materials exhibit no hysteresis and become quickly saturated under relatively low fields.

In doing so, two quantities of particular importance are the remanence (or remanent magnetization), M_r, and the coercivity (or coercive field), H_c. The remanence denotes the magnetization that remains in the material even in the absence of external actions once the material is magnetized by a large magnetic field. The coercivity represents the resistance to being demagnetized and measures the magnetic field strength required to reverse the remanent magnetization in the material. Other important parameters are the magnetic susceptibility χ_m, and the saturation magnetization M_s. The magnetic susceptibility indicates how much of the material of interest will be

magnetized in a given applied magnetic field and corresponds to the slope of the magnetization curve ($\chi_{\mathrm{m}} = \partial M / \partial H$, M: induced magnetization, H: applied magnetic field) in a differential sense for magnetically isotropic materials. As the field strength H increases, the material becomes further magnetized and eventually saturated when all moments are aligned substantially with the applied magnetic field, with the induced magnetization $M(H)$ approaching the saturation magnetization M_{s}.

2.1.3   Soft-magnetic Soft Materials

Soft-magnetic materials such as iron and nickel- or silicon-based alloys of iron are characterized by high magnetic susceptibility and saturation magnetization but relatively low remanence and coercivity (**Figure 2-2A**). Owing to these properties, soft-magnetic materials are strongly attracted to a magnet and easy to magnetize, but at the same time, they are easily demagnetized as well by a relatively weak magnetic field. Conventional magnetic soft composites based on magnetorheological elastomers and ferrogels mostly use carbonyl iron or iron oxide particles embedded in soft polymer matrices. This type of composite exhibits soft-magnetic characteristics (i.e., low remanence and low coercivity) while being mechanically soft (i.e., low Young's modulus), and we therefore refer to this type as *soft-magnetic soft materials*. In general, the response of magnetic soft materials to externally applied magnetic fields is complex and largely dependent on the microstructure of the composite as well as the concentration and configuration of the embedded magnetic particles [48, 49, 50].

In the context of soft robotic applications, traditional soft-magnetic soft materials in the form of magnetostrictive or magnetorheological elastomers and gels have somewhat limited utility in terms of creating useful functions to perform a set of different tasks. For instance, it is challenging to reproduce walking gaits or grasping tasks, which typically utilize bending motions or complex shape changes, using the simple deformation based on uniaxial elongation of isotropic composites. Magnetic torques can help to increase the level of complexity in terms of available actuation modes and achievable shapes by introducing additional degrees of freedom associated with the rotation of body parts. However, when the embedded soft-magnetic particles have

spherical shapes, the individual particles cannot produce magnetic torques. This is because the induced magnetic moment in each particle is always aligned with the applied magnetic field, meaning zero torque, as a consequence of the spherical particles being magnetically isotropic to have no preferred magnetization direction. For this reason, typical soft-magnetic soft materials have utilized force-driven magnetic actuation to create material deformation (shortening [51], elongation [38], or bending [52]) (**Figure 2-3B**) based on the attractive force acting on the magnetized particles under spatially nonuniform actuating fields (**Figure 2-3A**). Another force-driven actuation mode for isotropic soft-magnetic soft materials in the shape of a cylindrical rod utilizes buckling and coiling instability in the presence of confinement under a strong magnetic field [53, 54, 55], which leads to the contraction of the rod in its axial direction to function as an artificial muscle (**Figure 2-3B**).
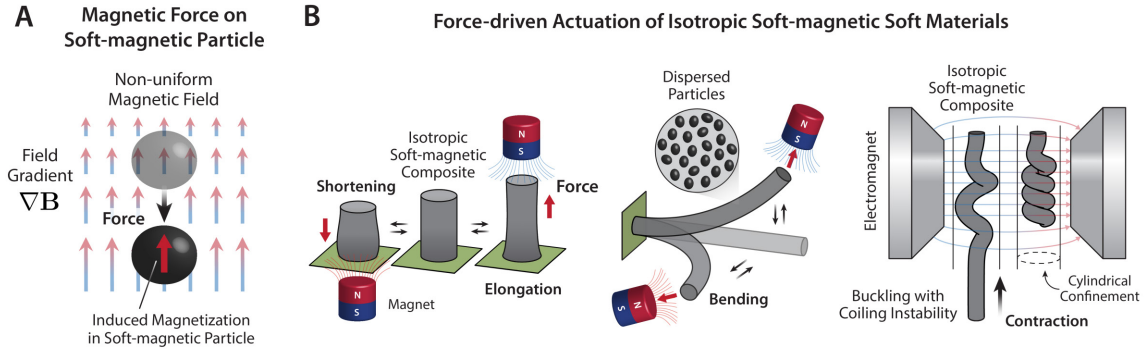
Figure 2-3: Different actuation modes of soft-magnetic soft materials. (**A**) Magnetic force acting on a single soft-magnetic particle under spatially nonuniform magnetic fields. (**B**) Force-driven actuation modes for isotropic soft-magnetic soft composites under spatially nonuniform actuating fields: shortening, elongation, bending, and contraction based on buckling and coiling instability.

2.1.4 Hard-magnetic Soft Materials

The most distinctive feature of hard-magnetic materials is that they can become a stable and permanent source of magnetic field after being magnetized, due to their large magnetic hysteresis characterized by the high coercivity and high remanence (**Figure 2-2B**). For example, the coercivities of alnico (iron alloys consisting of aluminum, nickel, cobalt, and copper) range from 30 to 150 kA/m, which is orders of

magnitude greater than that of soft-magnetic materials. In hexagonal ferrites, such as barium hexaferrite ($BaFe_{12}O_{19}$) [30, 47, 56] or strontium hexaferrite ($SrFe_{12}O_{19}$), the coercivity can be around 300 kA/m. It can even exceed 1000 kA/m in rare-earth magnets such as samarium-cobalt ($SmCo_5$ or Sm_2Co_{17}) or neodymium-iron-boron ($Nd_2Fe_{14}B$). The high coercivity allows them to be relatively insensitive to external conditions (e.g., temperature and magnetic fields) and have much greater resistance to being demagnetized when compared with soft-magnetic materials. In other words, hard-magnetic materials can retain their high remanent magnetization even when exposed to external magnetic fields (below the coercive field at which the magnetization reversal occurs) or elevated temperature (below the Curie point at which the material begins to lose its remanence). When hard-magnetic particles are incorporated into a soft polymer matrix, the resulting composite can exhibit hard-magnetic characteristics (i.e., high remanence and high coercivity) while being mechanically soft, acting as a flexible and deformable permanent magnet. We refer to this type of magnetic soft composite as *hard-magnetic soft materials.*

One of the unique advantages of using hard-magnetic materials is that magnetic torques can be readily exploited from individual magnetic dipole moments, which act as distributed actuation sources under spatially uniform magnetic fields (**Figure 2-4A**). Once the embedded hard-magnetic particles are magnetized to saturation, their remanent magnetization can be considered independent of the external actuating field below the coercivity. The implication of this stable remanence is that the magnetic torque acting on the material linearly increases with the applied field within the actuation range below the coercivity. As a representative example of hard-magnetic soft actuators, we consider a simple rectangular beam composed of a hard-magnetic soft material that is uniformly magnetized to have its remanent magnetization formed along the length direction (**Figure 2-4B**). Under a spatially uniform actuating field that is applied perpendicularly to the beam, the embedded hard-magnetic particles tend to align their remanent magnetization with the actuating field due to the magnetic torques, creating bending actuation of the beam toward the applied field direction (**Figure 2-4B**). Under spatially nonuniform magnetic fields, magnetic forces as

well as the magnetic torques act on the particles such that they are attracted toward the direction in which the field strength increases (**Figure 2-4C**), which helps to further increase the deflection of the beam (**Figure 2-4D**).
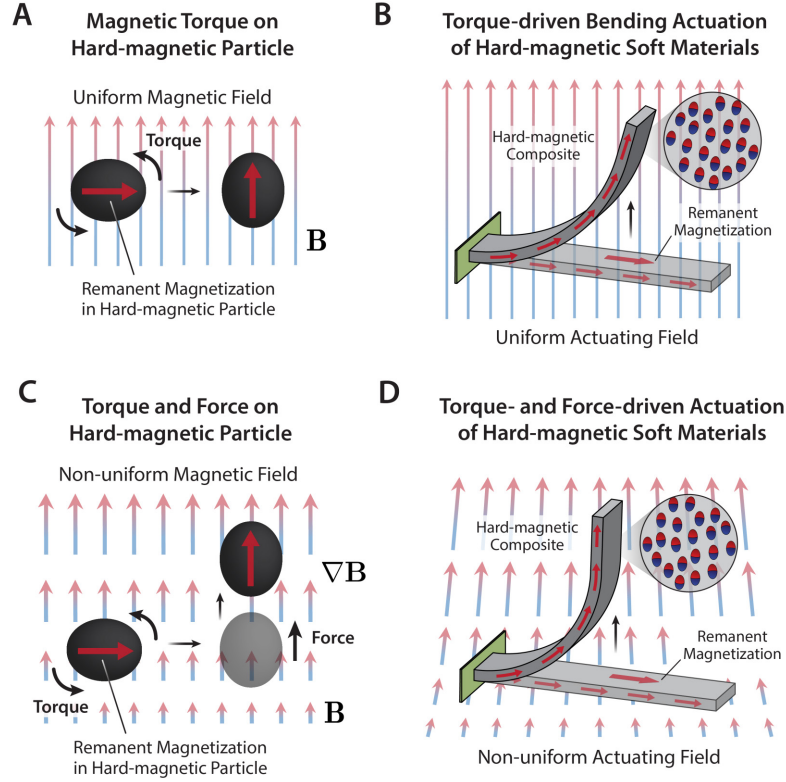
Figure 2-4: Hard-magnetic soft materials as soft bending actuators. (**A**) Magnetic torque acting on a magnetized hard-magnetic particle under a spatially uniform field. (**B**) Uniformly magnetized rectangular beam of a hard-magnetic soft composite and its torque-driven bending actuation under a uniform field. (**C**) Magnetic torque and force acting on a magnetized hard-magnetic particle under a spatially nonuniform field, in which the particle rotates due to the magnetic torque and moves toward the direction of the increasing field due to the attractive magnetic force. (**D**) Bending actuation under nonuniform actuating fields is initially driven by the magnetic torque and further supported by the increasing magnetic force as the body deforms to align its magnetization with the applied field.

2.2 Preliminaries for Mathematical Modeling

2.2.1 Magnetic Force and Torque

The actuation of magnetic soft materials relies on forces and torques acting on the embedded magnetic components under externally applied magnetic fields. When a magnetic dipole (i.e., point-like source) with the magnetic moment **m** is located at

the position $\mathbf{x}$ in free space under an externally applied magnetic field $\mathbf{B}$, it possesses the magnetic potential energy u_m (also known as Zeeman energy) defined as the dot product of the two vector quantities as

$$u_\mathrm{m} = -\mathbf{m} \cdot \mathbf{B}. \tag{2.1}$$

A small variation in the position and orientation of the magnetic moment, with the constraint of fixed magnitude $|\mathbf{m}|$, causes the change in the potential energy, which can be expressed as

$$-\delta u_\mathrm{m} = \mathbf{m} \cdot \delta \mathbf{B} + \delta \mathbf{m} \cdot \mathbf{B}. \tag{2.2}$$

For irrotational (i.e., curl-free) magnetic fields with no free electric currents (see Equation (2.10) below), Equation (2.2) can be transformed using relevant vector and tensor identities into an equivalent form (see **Appendix A** for its derivation) as

$$-\delta u_\mathrm{m} = \delta \mathbf{x} \cdot (\mathrm{grad}\,\mathbf{B})\mathbf{m} + \delta \boldsymbol{\theta} \cdot (\mathbf{m} \times \mathbf{B}), \tag{2.3}$$

where $\delta \mathbf{x}$ is the change in the magnetic moment position, and $\delta \boldsymbol{\theta}$ is a vector that points along the axis of rotation with its magnitude corresponding to the angle of rotation of the magnetic moment $\mathbf{m}$. In Equation (2.3), $\mathrm{grad}\,\mathbf{B}$ represents the spatial gradient of the applied magnetic field with respect to the point $\mathbf{x}$. It is worth noting that the infinitesimal rotation of the magnetic moment $\delta \mathbf{m}$ is related to $\delta \boldsymbol{\theta}$ by the following cross-product relation: $\delta \mathbf{m} = \delta \boldsymbol{\theta} \times \mathbf{m}$. From Equation (2.3), the magnetic force, $\mathbf{f}_\mathrm{m}$, acting on the magnetic moment is given by

$$\mathbf{f}_\mathrm{m} = -\frac{\partial u_\mathrm{m}}{\partial \mathbf{x}} = (\mathrm{grad}\,\mathbf{B})\mathbf{m}, \tag{2.4}$$

while the magnetic torque, $\boldsymbol{\tau}_\mathrm{m}$, acting on the magnetic moment is given by

$$\boldsymbol{\tau}_\mathrm{m} = -\frac{\partial u_\mathrm{m}}{\partial \boldsymbol{\theta}} = \mathbf{m} \times \mathbf{B}. \tag{2.5}$$

It is worth noting that Equation (2.4) can be expressed equivalently as

$$\mathbf{f}_\mathrm{m} = (\mathbf{m} \cdot \nabla)\mathbf{B}, \tag{2.6}$$

using a more common expression in the literature based on the vector operator $\nabla = (\partial/\partial x_i)\,\mathbf{e}_i$, where $\mathbf{e}_i$ represents the three Cartesian basis vectors ($i = 1, 2, 3$).

From Equation (2.5) we know that the magnetic torque vanishes when the magnetic moment $\mathbf{m}$ is aligned (either parallel or antiparallel) with the actuating field $\mathbf{B}$. We also know from Equation (2.4) (or equivalently from Equation (2.6)) that the magnetic force $\mathbf{f}_{\mathrm{m}}$ exists only in the presence of magnetic field gradients. This implies that the actuation based on spatially uniform magnetic fields is driven solely by the magnetic torque $\boldsymbol{\tau}_{\mathrm{m}}$. Under spatially nonuniform actuating fields, magnetic forces as well as torques can contribute to the actuation of magnetic soft materials. In Equation (2.6), $(\mathbf{m} \cdot \nabla)$ denotes the directional derivative in the direction of $\mathbf{m}$ multiplied by its magnitude. Physically, this implies that the magnetic force can be produced when there is a variation in the applied field in the direction of the magnetic moment. In general, it is the magnetic torque that drives the actuation by rotating the magnetic object to align its remanent or induced magnetic moment with the applied field, while the magnetic force attracts the aligned object in the direction of increasing field strength (**Figure 2-4C**), usually toward the external source of actuating fields.

2.2.2   Fundamental Equations in Magnetostatics

In the presence of homogeneous magnetizable media, it is often more convenient to introduce an additional field, the $\mathbf{H}$ field, which shares with $\mathbf{B}$ the name and the status of magnetic field (for differentiation, $\mathbf{B}$ is usually termed the magnetic induction or flux density, while $\mathbf{H}$ is called the magnetic field) [57]. $\mathbf{B}$ and $\mathbf{H}$ fields are related by

$$\mathbf{B} = \mu_0 (\mathbf{M} + \mathbf{H}), \tag{2.7}$$

where μ_0 is the magnetic permeability of free space (vacuum) and $\mathbf{M}$ is the magnetization that measures the average magnetic moment density in the magnetic media (per unit volume). The magnetization vector at a material point $\mathbf{x}$ can be defined such that

$$\mathbf{m} = \int_V \mathbf{M}(\mathbf{x}) \, \mathrm{d}V \quad \text{or} \quad \mathbf{M} = \frac{\mathrm{d}\mathbf{m}}{\mathrm{d}V}, \tag{2.8}$$

where $\mathbf{m}$ is the total magnetic moment and V is the volume of the magnetic media. When the material is uniformly magnetized, Equation (2.8) becomes $\mathbf{m} = V\mathbf{M}$. It is worth noting that $\mathbf{B}$ and $\mathbf{H}$ fields are simply related by $\mathbf{B} = \mu_0 \mathbf{H}$ in the absence

of magnetizable media, under which Equations (2.1) to (2.6) can also be written in terms of $\mathbf{H}$ fields.

For magnetostatic systems with no time variation of the pertinent electromagnetic quantities, the Maxwell's equations in differential forms can be stated as

$$\text{div}\,\mathbf{B} = \nabla \cdot \mathbf{B} = 0, \tag{2.9}$$

$$\text{curl}\,\mathbf{B} = \nabla \times \mathbf{B} = \mu_0 \mathbf{J}, \tag{2.10}$$

where $\text{div}\,\mathbf{B}$ denotes the spatial divergence of $\mathbf{B}$ fields, $\text{curl}\,\mathbf{B}$ denotes the spatial curl of $\mathbf{B}$ fields, and $\mathbf{J}$ is the electric current density. Then, the boundary conditions corresponding to Equations (2.9) and (2.10) are given by

$$\mathbf{n} \cdot [\![\mathbf{B}]\!] = 0, \tag{2.11}$$

$$\mathbf{n} \times [\![\mathbf{B}]\!] = \mu_0 \mathbf{K}, \tag{2.12}$$

where $\mathbf{n}$ is the outward unit normal to the boundary, $[\![\ ]\!]$ denotes the jump of the field at the interface (i.e., $[\![\mathbf{B}]\!] = \mathbf{B}^{\text{out}} - \mathbf{B}^{\text{in}}$), and $\mathbf{K}$ denotes the surface current density. Equation (2.9) is also known as Gauss's law for magnetism and states that no magnetic monopoles exist and suggests that $\mathbf{B}$ fields be solenoidal (i.e., divergence-free).

Substituting Equation (2.7) into Equation (2.9) leads to the definition of magnetic charge density, ρ_{m}, in the material (per unit volume) which is given by

$$\nabla \cdot \mu_0 \mathbf{H} = -\nabla \cdot \mu_0 \mathbf{M} = \rho_{\text{m}}, \tag{2.13}$$

from the analogy to the description of the electric charge density in electrostatics, except for the absence of magnetic monopoles, which are analogous to unpaired electric charges. Although they have no physical existence, the concept of magnetic charges often provides a useful abstraction when understanding the behavior of a magnetized body (**Figure 2-5**) [57]. Equation (2.10) is usually referred to as Ampere's law and can also be expressed by using Equation (2.7) as

$$\text{curl}\,\mathbf{H} = \nabla \times \mathbf{H} = \mathbf{J}_{\text{f}}, \tag{2.14}$$

where $\mathbf{J}_{\text{f}}$ denotes the free electric current density, along with the definition of the magnetization current density $\mathbf{J}_{\text{m}}$ given by

$$\operatorname{curl}\mathbf{M} = \nabla \times \mathbf{M} = \mathbf{J}_{\mathrm{m}}, \tag{2.15}$$

with the total current density given by the sum of two: $\mathbf{J} = \mathbf{J}_{\mathrm{f}} + \mathbf{J}_{\mathrm{m}}$. Equation (2.14) requires $\mathbf{H}$ fields to be irrotational (i.e., curl-free) when there is no free current (i.e., $\mathbf{J}_{\mathrm{f}} = \mathbf{0}$), while Equation (2.15) allows the magnetization to be treated as a current.
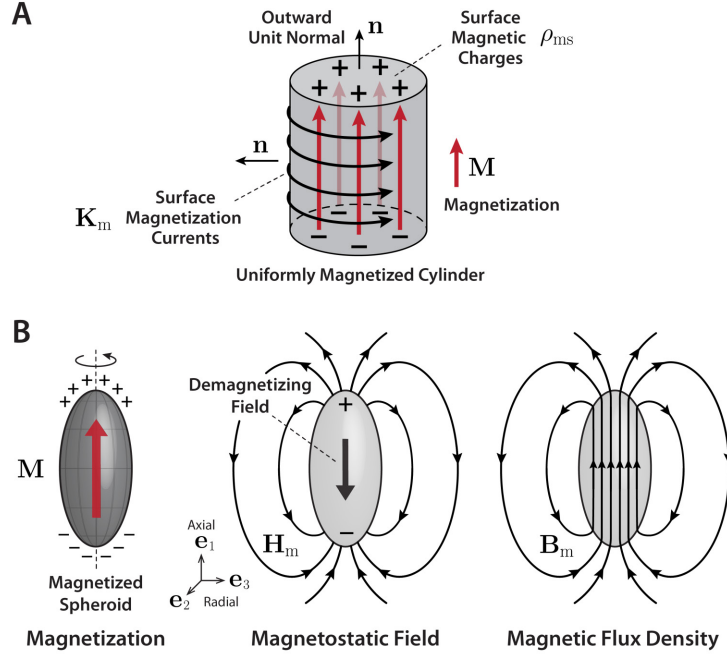
Figure 2-5: Graphical representation of a uniformly magnetized body. (**A**) Uniformly magnetized cylinder with graphical representations of the surface magnetic charges (ρ_{ms}) and the magnetization currents ($\mathbf{K}_{\mathrm{m}}$). (**B**) Magnetization ($\mathbf{M}$), magnetostatic field ($\mathbf{H}_{\mathrm{m}}$), and magnetic flux density ($\mathbf{B}_{\mathrm{m}}$) of a uniformly magnetized spheroid, which represent the effect of a demagnetizing field inside the magnetized body.

At the material surface, the magnetic surface charge density (per unit area), denoted by ρ_{ms}, can be defined from Equation (2.13) as

$$\mathbf{n} \cdot [\![\mu_0 \mathbf{H}]\!] = -\mathbf{n} \cdot [\![\mu_0 \mathbf{M}]\!] = \rho_{\mathrm{ms}}, \tag{2.16}$$

while the boundary conditions for Equations (2.14) and (2.15) are given by

$$\mathbf{n} \times [\![\mathbf{H}]\!] = \mathbf{K}_{\mathrm{f}}, \tag{2.17}$$

$$\mathbf{n} \times [\![\mathbf{M}]\!] = \mathbf{K}_{\mathrm{m}}, \tag{2.18}$$

where $\mathbf{K}_{\mathrm{f}}$ denotes the free surface current density and $\mathbf{K}_{\mathrm{m}}$ is the surface magnetization

current density. Since the magnetization is zero outside the body (**Figure 2-5A**), which yields $[\![\mathbf{M}]\!] = -\mathbf{M}$, the boundary conditions for a magnetized body given in Equations (2.16) and (2.18) can be simplified as $\rho_{\mathrm{ms}} = \mu_0 \mathbf{M} \cdot \mathbf{n}$ and $\mathbf{K}_{\mathrm{m}} = \mathbf{M} \times \mathbf{n}$.

The $\mathbf{H}$ fields being irrotational in the absence of free electric currents from Equation (2.14) implies that the magnetic scalar potential, denoted by Φ, can be defined such that

$$\mathbf{H} = -\mathrm{grad}\,\Phi = -\nabla\Phi, \tag{2.19}$$

from the vector identity, $\mathrm{curl}\,(\mathrm{grad}\,f) = \nabla \times (\nabla f) \equiv 0$, which holds for any scalar field $f(\mathbf{x})$. Then, from Equations (2.13) and (2.19), it follows that the magnetic scalar potential Φ obeys Poisson's equation:

$$\nabla^2 \Phi = -\frac{\rho_{\mathrm{m}}}{\mu_0}, \tag{2.20}$$

which reduces to $\nabla^2 \Phi = 0$ for uniformly magnetized materials with no divergence (i.e., $\nabla \cdot \mathbf{M} = 0$).

2.2.3   Magnetostatic and Demagnetizing Fields

In the absence of magnetizable media (i.e., $\mathbf{M} = \mathbf{0}$), the externally applied magnetic field in empty space can be expressed as $\mathbf{B}_{\mathrm{a}} = \mu_0 \mathbf{H}_{\mathrm{a}}$ from Equation (2.7), with the subscript a used to denote the applied fields. When a magnetizable body is introduced into the space, it becomes magnetized by the externally applied field $\mathbf{H}_{\mathrm{a}}$ to have the induced magnetization $\mathbf{M}$ inside the body. Then, it follows from Equation (2.16) that positive and negative magnetic surface charges are induced on its top and bottom surfaces, respectively (**Figure 2-5B**). The surface charges induce another magnetic field, often termed the *magnetostatic field* and denoted by $\mathbf{H}_{\mathrm{m}}$, originating from the positive charge at the top and terminating on the negative charge at the bottom. Then, the total magnetic field $\mathbf{H}$ can be expressed as

$$\mathbf{H} = \mathbf{H}_{\mathrm{a}} + \mathbf{H}_{\mathrm{m}}, \tag{2.21}$$

and from Equation (2.7), the corresponding $\mathbf{B}$ field (magnetic flux density) becomes

$$\mathbf{B} = \mathbf{B}_{\mathrm{a}} + \mathbf{B}_{\mathrm{m}} = \mu_0(\mathbf{M} + \mathbf{H}_{\mathrm{a}} + \mathbf{H}_{\mathrm{m}}), \tag{2.22}$$

with $\mathbf{B}_\mathrm{m} = \mu_0(\mathbf{M} + \mathbf{H}_\mathrm{m})$ inside the body and $\mathbf{B}_\mathrm{m} = \mu_0\mathbf{H}_\mathrm{m}$ outside the body and with $\mathbf{B}_\mathrm{a} = \mu_0\mathbf{H}_\mathrm{a}$ everywhere. It is worth noting that, since $\nabla \cdot \mathbf{B}_\mathrm{a} = \nabla \cdot \mu_0\mathbf{H}_\mathrm{a} = 0$ from Equation (2.9), Equations (2.13) and (2.16) can be expressed in terms of the magnetostatic field $\mathbf{H}_\mathrm{m}$ by simply replacing $\mathbf{H}$ with $\mathbf{H}_\mathrm{m}$.

In a uniformly magnetized body, the magnetostatic field $\mathbf{H}_\mathrm{m}$ acts to oppose the magnetization $\mathbf{M}$ and hence reduces the overall magnetization (**Figure 2-5B**). For this reason, the magnetostatic field $\mathbf{H}_\mathrm{m}$ inside the body is often termed the *demagnetizing field* and is given by

$$\mathbf{H}_\mathrm{m} = -\boldsymbol{\mathcal{N}}\mathbf{M}, \tag{2.23}$$

where $\boldsymbol{\mathcal{N}}$ denotes the demagnetizing tensor. When the coordinate frame is chosen such that the Cartesian axes are aligned with the principal axes of the magnetized body, the demagnetizing tensor becomes diagonal in the following matrix form:

$$[\boldsymbol{\mathcal{N}}] = \mathrm{diag}\,(N_1, N_2, N_3) = \begin{bmatrix} N_1 & 0 & 0 \\ 0 & N_2 & 0 \\ 0 & 0 & N_3 \end{bmatrix}, \tag{2.24}$$

where N_i $(i = 1, 2, 3)$ represents the three eigenvalues that correspond to the demagnetizing factors associated with each of the principal axes. These factors obey the general constraint $N_1 + N_2 + N_3 = 1$, which suggests that $N_1 = N_2 = N_3 = 1/3$ when the body is of spherical shape due to symmetry. For an ellipsoidal body with axial symmetry (i.e., the spheroid in **Figure 2-5B**), the demagnetizing factors are further constrained by $N_2 = N_3 = (1 - N_1)/2$, with N_1 denoting the demagnetizing factor along the axis of symmetry and $N_2 = N_3$ denoting the factors along the radial directions perpendicular to the symmetry axis.

In an idealized sense, a magnetic body can be considered an assembly of magnetic moments that are subject to magnetostatic interactions with each other. Then, the mechanical work spent in building the body by assembling the elementary magnetic moments can be represented by the magnetostatic energy, which is determined by the spatial distribution of the magnetization and by the geometric shape of the magnetic body. The magnetostatic energy density (per unit volume) is defined by

$$\mathcal{U}_{\mathrm{m}} = -\frac{\mu_0}{2}\mathbf{H}_{\mathrm{m}} \cdot \mathbf{M}, \qquad (2.25)$$

which is calculated as $\mathcal{U}_{\mathrm{m}} = \mu_0(N_1 M_1^2 + N_2 M_2^2 + N_3 M_3^2)/2$ when the coordinate frame is aligned with the principal axes of the body. For isotropic (spherical) particles, the magnetostatic energy density can be expressed as $\mathcal{U}_{\mathrm{m}} = \mu_0 M^2/2$, with M denoting the magnitude of the magnetization vector.

2.2.4 Idealized Magnetic Constitutive Laws

The constitutive law of a magnetic medium describes the material's response to the magnetic field acting on it and can be stated in the form of either $\mathbf{M}(\mathbf{H})$ or $\mathbf{B}(\mathbf{H})$, with $\mathbf{H}$ denoting the field experienced by the material. In general, the constitutive laws for ferromagnetic materials can be quite complex when the magnetization process exhibits anisotropic, nonlinear, and hysteretic behavior. Therefore, to simplify the analysis without loss of generality, it is often practically more advantageous to idealize the constitutive laws for typical magnetic materials.

In soft-magnetic materials, the induced magnetization is largely dependent on the applied field and hence the magnetization process should be taken into account when modeling their behavior. In the presence of magnetic anisotropy, the induced magnetization is dependent on the particle orientation and can occur in directions other than that of the applied magnetic field. Ideal soft-magnetic materials are assumed to have no hysteresis (i.e., zero remanence and zero coercivity) as superparamagnetic particles (**Figure 2-1C**). In addition, at low fields below the saturating field, $\mathbf{H}^{\mathrm{sat}}$, the induced magnetization $\mathbf{M}$ in ideal soft-magnetic materials is assumed to increase linearly with the magnetic field $\mathbf{H}$ experienced by the material (**Figure 2-6A**), until it reaches the saturation magnitude (denoted M_{s} in **Figure 2-6A**). The constitutive law for such linearly magnetic materials can be stated as

$$\mathbf{M}(\mathbf{H}) = \begin{cases} \chi_{\mathrm{m}}\mathbf{H} & \text{for } |\mathbf{H}| < |\mathbf{H}^{\mathrm{sat}}| \\ \mathbf{M}_{\mathrm{s}} & \text{for } |\mathbf{H}| \geq |\mathbf{H}^{\mathrm{sat}}|, \end{cases} \qquad (2.26)$$

where χ_{m} denotes the magnetic susceptibility of the soft-magnetic particle under the applied field and $\mathbf{M}_{\mathrm{s}}$ represents the saturation magnetization of the particle.
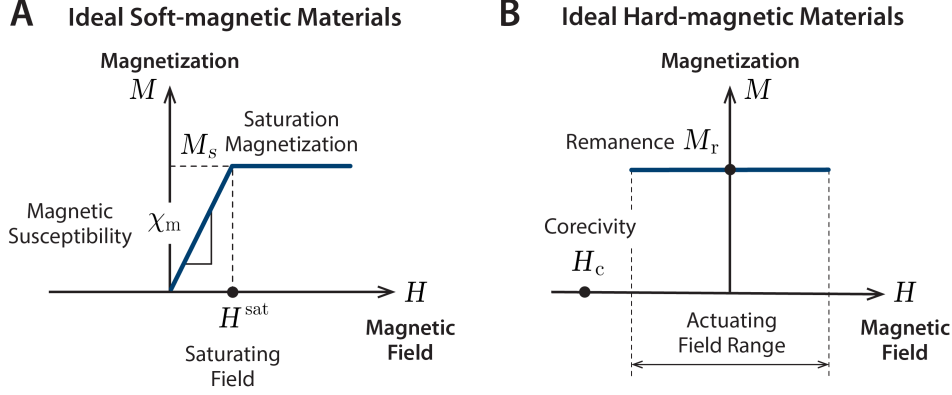
Figure 2-6: Idealized magnetic constitutive laws for soft-magnetic and hard-magnetic materials. (**A**) Ideal soft-magnetic materials are characterized by the linear relationship between the induced magnetization and the magnetic field with constant magnetic susceptibility before saturation and constant magnetization after saturation without magnetic hysteresis (zero remanence and coercivity). (**B**) Ideal hard-magnetic soft materials are characterized by large magnetic hysteresis (high remanence and coercivity) to maintain the remanence under an actuating field below the coercivity.

It is worth noting that χ_m is a dimensionless constant on the order of 10^3 to 10^6 for typical soft-magnetic materials. It is also worth noting that the graphical representation of the constitutive law for ideal soft-magnetic materials in **Figure 2-6A** shows the representative magnetization curve where both the induced magnetization $\mathbf{M}$ and the applied magnetic field $\mathbf{B}$ point along the same direction.

In contrast to soft-magnetic materials, ideal hard-magnetic materials are considered to have strong hysteresis (i.e., high remanence and high coercivity). When hard-magnetic particles are magnetized to saturation, they can be regarded as small permanent magnets whose magnetic moments are independent of the actuating field below coercivity, $\mathbf{H}_\mathrm{c}$ (**Figure 2-6B**). Thus, in the context of magnetic actuation, the constitutive law for ideal hard-magnetic materials can be expressed as

$$\mathbf{M}(\mathbf{H}) = \mathbf{M}_\mathrm{r} \ \text{ for } \ |\mathbf{H}| < |\mathbf{H}_\mathrm{c}|, \tag{2.27}$$

where $\mathbf{M}_\mathrm{r}$ is the remanent magnetization of the hard-magnetic particle after magnetization. This constitutive law in Equation (2.27) implies that there is no energy transformation related to the magnetization process taking place during actuation.

2.3 Continuum Mechanical Framework

2.3.1 Introduction

Nonlinear Constitutive Theory based on Finite Hyperelasticity

For magnetic soft materials with one or a few rigid, finite-sized magnets attached to or incorporated in a deformable body (**Figure 2-1A**), the force and torque generated by the attached magnet can be considered a point load acting on the center of the magnet. For such discrete systems with simple geometry, theoretical models can be derived by considering the global force and moment balance of the structure to find its deformed configuration in static equilibrium [58]. For continuous systems with dispersed magnetic particles in the polymer matrices (**Figure 2-1B** and **Figure 2-4**, **B** and **D**), the composite matrix can be treated as a homogeneous continuum that exhibits both elastic and magnetic characteristics simultaneously (**Figure 2-7A**). Modeling of such continuous systems can be formulated in a continuum mechanical framework by considering the local force and moment balance that holds at every point of the material. In this section, we will develop a continuum mechanical model for idealized hard-magnetic soft materials, based on a set of practical and reasonable assumptions, using a nonlinear constitutive theory based on finite hyperelasticity.
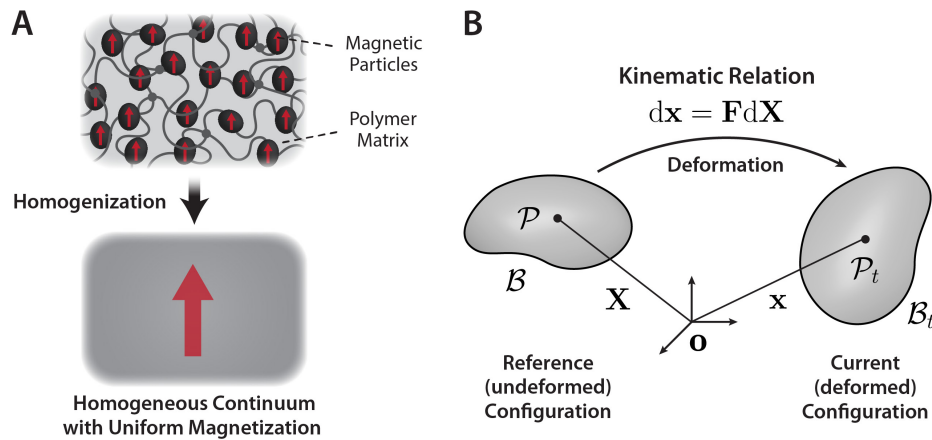
Figure 2-7: Continuum mechanical framework for magnetic soft materials. (A) Treatment of magnetic soft composites based on polymer matrices with filler particles as a homogeneous continuum with uniform magnetization for continuum mechanical approaches. (**B**) Kinematic relation for deformable solids in the continuum mechanical framework.

Underlying assumptions: Before we begin to formulate the theory, we consider the following three underlying assumptions to hold for ideal hard-magnetic soft materials:

1. *Homogeneous continua*: Deformable, elastic solids with hard-magnetic characteristics (i.e., flexible permanent magnets).

2. *Magnetically saturated*: Remanent magnetization ($\mathbf{M}_r$) is independent of external magnetic fields ($\mathbf{H}$) below coercivity ($\mathbf{H}_c$).

3. *Isothermal conditions*: Work done by an externally applied magnetic field ($\mathbf{B}$) is stored in the material as Helmholtz free energy (ψ).

2.3.2   Kinematics and Equations of Motion

Kinematic relations: When a continuum (denoted by $\mathcal{B}$) deforms (**Figure 2-7B**), a material point $\mathbf{X}$ (denoted by $\mathcal{P}$) on the body in its reference (undeformed) configuration is mapped to a spatial point $\mathbf{x}$ (denoted by $\mathcal{P}_t$) on the deformed body (denoted by $\mathcal{B}_t$) in the current configuration. The deformation of the body can be measured by the deformation gradient tensor $\mathbf{F}$ which is defined by

$$\mathbf{F} = \frac{\mathrm{d}\mathbf{x}}{\mathrm{d}\mathbf{X}}. \tag{2.28}$$

The deformation gradient is a linear transformation that maps the infinitesimal line elements $\mathrm{d}\mathbf{X}$ and $\mathrm{d}\mathbf{x}$ between the reference and current configurations, and hence it can serve as a primary measure of deformation. The determinant of the deformation gradient tensor, $\det \mathbf{F}$, characterizes the change in volume during the deformation as

$$J = \det \mathbf{F} = \frac{\mathrm{d}v}{\mathrm{d}V} > 0, \tag{2.29}$$

which is termed the volumetric Jacobian that relates the infinitesimal volume elements $\mathrm{d}V$ and $\mathrm{d}v$ in the reference and current configurations, respectively [59, 60].

Equations of motion: For quasi-static equilibrium, the principle of linear momentum balance reduces to the force balance equation that holds for each point $\mathbf{x}$:

$$\mathrm{div}\,\boldsymbol{\sigma} + \bar{\mathbf{f}} = \mathbf{0}, \tag{2.30}$$

which is also known as Cauchy's equilibrium equation, where $\boldsymbol{\sigma}$ is the Cauchy stress, with denoting its spatial divergence with respect to the point $\mathbf{x}$, and $\bar{\mathbf{f}}$ is the body force density (per unit current volume of the continuum) exerted by the environment on $\mathbf{x}$ (including the gravitational body force), with the bar symbol used to denote the force density per unit volume. For a polar continuum with distributed body torque density $\bar{\boldsymbol{\tau}}$ (per unit volume of the continuum), with the bar symbol used to denote the torque density per unit volume, the balance of angular momentum reduces to the following moment balance [61]:

$$\boldsymbol{\mathcal{E}} : \boldsymbol{\sigma}^{\mathsf{T}} + \bar{\boldsymbol{\tau}} = \mathbf{0}, \tag{2.31}$$

where $\boldsymbol{\mathcal{E}} = \varepsilon_{ijk}\, \mathbf{e}_i \otimes \mathbf{e}_j \otimes \mathbf{e}_k$ is the third-order permutation tensor with ε_{ijk} being the permutation (also known as Levi–Civita) symbol and the operator $\otimes$ denoting the tensor (dyadic) product that takes two vectors to produce a second-order tensor, and $\boldsymbol{\sigma}^{\mathsf{T}}$ is the transpose of the Cauchy stress tensor. When there is no body torque (i.e., $\bar{\boldsymbol{\tau}} = \mathbf{0}$), Equation (2.31) requires the Cauchy stress to be symmetric (i.e., $\boldsymbol{\sigma} = \boldsymbol{\sigma}^{\mathsf{T}}$). In the presence of body torques, however, the Cauchy stress may no longer be symmetric.

2.3.3 Hyperelastic Constitutive Equations

Free energy imbalance: The second law of thermodynamics requires the following equation, also referred to as *free energy imbalance* in a referential local form, to hold in every material point under isothermal conditions [61, 62, 63]:

$$\mathcal{D}_{\mathrm{int}} = \mathbf{P} : \dot{\mathbf{F}} - \dot{\psi}_{\mathrm{R}} \geq 0, \tag{2.32}$$

where $\mathcal{D}_{\mathrm{int}}$ indicates the internal dissipation rate, $\mathbf{P}$ is the first Piola–Kirchhoff stress tensor (or simply Piola stress), which forms a work conjugate pair with the time derivative of the deformation gradient $\dot{\mathbf{F}}$, and $\dot{\psi}_{\mathrm{R}}$ is the rate of change in the Helmholtz free energy density per unit reference (undeformed) volume, with the subscript R used to denote that the Helmholtz free energy density is expressed in the referential form. The term $\mathbf{P} : \dot{\mathbf{F}}$ denotes the rate of internal mechanical work (i.e., stress power), with the operator " : " denoting the double contraction of the two tensors.

Piola and Cauchy stresses: The dissipation inequality in Equation (2.32) implies

that the rate of change in the Helmholtz free energy stored in the body is less than, or at most equal to, the power expended on the body. By applying the chain rule, Equation (2.32) can be expanded as

$$\mathcal{D}_{\text{int}} = \mathbf{P} : \dot{\mathbf{F}} - \frac{\partial \psi_{\text{R}}}{\partial \mathbf{F}} : \dot{\mathbf{F}} = \left(\mathbf{P} - \frac{\partial \psi_{\text{R}}}{\partial \mathbf{F}} \right) : \dot{\mathbf{F}} \geq 0, \tag{2.33}$$

from which we know that the Piola stress can be obtained, for hyperelastic materials (see **Appendix D**), as the derivative of the free energy function with respect to $\mathbf{F}$:

$$\mathbf{P} = \frac{\partial \psi_{\text{R}}}{\partial \mathbf{F}}, \tag{2.34}$$

which measures the force acting on the deformed material per unit reference (undeformed) area. By definition, the Piola stress is related to the Cauchy stress $\boldsymbol{\sigma}$ (force per unit current area) by $\mathbf{P} = J\boldsymbol{\sigma}\mathbf{F}^{-\mathsf{T}}$, which leads to

$$\boldsymbol{\sigma} = \frac{1}{J} \frac{\partial \psi_{\text{R}}}{\partial \mathbf{F}} \mathbf{F}^{\mathsf{T}}, \tag{2.35}$$

where $\mathbf{F}^{\mathsf{T}}$ denotes the transpose of the deformation gradient tensor.

2.3.4 Helmholtz Free Energy Functions

Elastic part of the free energy: For ideal hard-magnetic soft materials, we consider that the material's Helmholtz free energy can be divided into two components:

$$\psi_{\text{R}} = \psi_{\text{R}}^{\text{elastic}} + \psi_{\text{R}}^{\text{magnetic}}, \tag{2.36}$$

with $\psi_{\text{R}}^{\text{elastic}}$ denoting the elastic part and $\psi_{\text{R}}^{\text{magnetic}}$ denoting the magnetic part of the Helmholtz free energy, both expressed per unit reference volume. The mechanical behavior of the magnetic soft composite can be described by relevant constitutive models for hyperelastic solids. There are several hyperelastic material models such as neo-Hookean, Mooney-Rivlin, Gent, Ogden, and Arruda-Boyce models, to name a few [64, 65]. These material models define the elastic part of the Helmholtz free energy per unit reference volume (also known as *strain energy density*), denoted by $\psi_{\text{R}}^{\text{elastic}}(\mathbf{F})$, as a function of the deformation gradient tensor $\mathbf{F}$ with the subscript e denoting the free energy due to 'elastic' deformation. Among these constitutive models, we choose the

simplest neo-Hookean model (see **Appendix D**) in the following generalized form:

$$\psi_{\mathrm{R}}^{\mathrm{elastic}}(\mathbf{F}) = \frac{G}{2}\left(J^{-2/3}I_1 - 3\right) + \frac{K}{2}(J-1)^2, \tag{2.37}$$

where G is the shear modulus, K is the bulk modulus, and $I_1 = \mathrm{tr}(\mathbf{F}^{\mathsf{T}}\mathbf{F})$ is the first invariant of the right Cauchy–Green tensor $\mathbf{C} = \mathbf{F}^{\mathsf{T}}\mathbf{F}$.

Magnetic part of the free energy: Under the assumption that the interaction between the magnetized particles is negligible, the magnetic Helmholtz free energy is given simply by the magnetic potential (Zeeman) energy discussed in Equation (2.1) above. Since there is no magnetization process taking place during actuation, we can neglect the magnetostatic energy. Then, from Equations (2.1) and (2.8), the magnetic potential energy can be expressed per unit current volume as

$$U_{\mathrm{m}} = \psi^{\mathrm{magnetic}} = -\mathbf{M}_{\mathrm{r}} \cdot \mathbf{B}. \tag{2.38}$$

It should be noted that the remanent magnetization of the hard-magnetic soft composite changes from its reference configuration as the material deforms. With $\tilde{\mathbf{M}}_{\mathrm{r}}$ denoting the remanent magnetization of the composite in its reference configuration (i.e., magnetic moment density per unit reference volume), the transformation rule for the remanent magnetization vector between the reference and current configurations can be stated as

$$\mathbf{M}_{\mathrm{r}} = J^{-1}\mathbf{F}\tilde{\mathbf{M}}_{\mathrm{r}}, \tag{2.39}$$

which can be obtained from the conservation of the flux integral of the magnetization vectors in the two configurations (see **Appendix B** for its derivation). This is conceptually equivalent to the conservation of the magnetic charge introduced earlier in Equation (2.13). Then, the magnetic Helmholtz free energy per unit reference volume, denoted by $\psi_{\mathrm{R}}^{\mathrm{magnetic}}$, can be obtained by multiplying the volumetric Jacobian:

$$\psi_{\mathrm{R}}^{\mathrm{magnetic}}(\mathbf{F}) = J\psi^{\mathrm{magnetic}} = -\mathbf{F}\tilde{\mathbf{M}}_{\mathrm{r}} \cdot \mathbf{B}. \tag{2.40}$$

2.3.5 Elastic and Magnetic Cauchy Stresses

Now that we have both the elastic and magnetic parts of the Helmholtz free energy, each as a function of the deformation gradient $\mathbf{F}$ in Equations (2.35) and (2.38),

respectively, we can calculate the elastic and magnetic parts of the Cauchy stress. From Equations (2.34), (2.35), and (2.37), the elastic Piola and Cauchy stresses are given by (see **Appendix C** for derivation)

$$\mathbf{P}^{\text{elastic}} = GJ^{-2/3}\left(\mathbf{F} - \frac{I_1}{3}\mathbf{F}^{-\mathsf{T}}\right) + KJ(J-1)\mathbf{F}^{-\mathsf{T}}, \tag{2.41}$$

$$\boldsymbol{\sigma}^{\text{elastic}} = GJ^{-5/3}\left(\mathbf{F}\mathbf{F}^{\mathsf{T}} - \frac{I_1}{3}\mathbf{1}\right) + K(J-1)\mathbf{1}, \tag{2.42}$$

respectively, with $\mathbf{1}$ denoting the identity tensor. Similarly, from Equations (2.34), (2.35), and (2.40), the magnetic Piola and Cauchy stresses are given by

$$\mathbf{P}^{\text{magnetic}} = -\mathbf{B} \otimes \tilde{\mathbf{M}}_{\text{r}}, \tag{2.43}$$

$$\boldsymbol{\sigma}^{\text{magnetic}} = -J^{-1}\mathbf{B} \otimes \mathbf{F}\tilde{\mathbf{M}}_{\text{r}} = -\mathbf{B} \otimes \mathbf{M}_{\text{r}}, \tag{2.44}$$

where the transformation rule for magnetization discussed in Equation (2.39) was used (see **Appendix C** for derivation). The total Cauchy stress is then given by the sum of the two components in Equations (2.42) and (2.44):

$$\boldsymbol{\sigma} = \boldsymbol{\sigma}^{\text{elastic}} + \boldsymbol{\sigma}^{\text{magnetic}}. \tag{2.45}$$

Substituting this into the equilibrium equation in Equation (2.30) and solving it for the deformation gradient $\mathbf{F}$, typically through the finite element method with relevant boundary conditions taken into account, the deformed configuration of the material in equilibrium can be found. The magnetic Cauchy stress in Equation (2.44) allows us to treat the magnetic forces and torques as stresses in a homogeneous continuum. This continuum-mechanical approach based on the magnetic Cauchy stress is particularly useful in finite element environments when the given geometry is complicated, because the constitutive equations can be readily implemented in commercial finite element software packages such as Abaqus [1, 2].

2.3.6 Magnetic Force and Torque Densities

Ideal hard-magnetic soft materials are characterized by their remanent magnetization $\mathbf{M}_{\text{r}}$, which remains constant and independent of the applied field below the coercivity

(**Figure 2-6B**), as described in the constitutive law in Equation (2.27). This implies that there is no energy transformation related to the magnetization process taking place during magnetic actuation under an externally applied field. In other words, the magnetostatic energy in Equation (2.25) plays no role in generating magnetic forces and torques for hard-magnetic soft materials within the actuating field range below the coercivity. Therefore, the magnetic force and torque acting on a hard-magnetic soft composite (**Figure 2-4**, **A** and **C**) per unit volume can be expressed simply as

$$\bar{\mathbf{f}}_{\mathrm{m}} = (\mathrm{grad}\,\mathbf{B})\mathbf{M}_{\mathrm{r}} = (\mathbf{M}_{\mathrm{r}} \cdot \nabla)\mathbf{B} \tag{2.46}$$

$$\bar{\boldsymbol{\tau}}_{\mathrm{m}} = \mathbf{M}_{\mathrm{r}} \times \mathbf{B}, \tag{2.47}$$

by replacing $\mathbf{m}$ with $\mathbf{M} = \mathbf{M}_{\mathrm{r}}$, in Equations (2.4) and (2.5), respectively, with the bar symbol used to denote the force and torque densities per unit volume. Equations (2.46) and (2.47) can also be written in terms of $\mathbf{H}_{\mathrm{a}}$ as

$$\bar{\mathbf{f}}_{\mathrm{m}} = \mu_0(\mathrm{grad}\,\mathbf{H}_{\mathrm{a}})\mathbf{M}_{\mathrm{r}} = \mu_0(\mathbf{M}_{\mathrm{r}} \cdot \nabla)\mathbf{H}_{\mathrm{a}} \tag{2.48}$$

$$\bar{\boldsymbol{\tau}}_{\mathrm{m}} = \mu_0(\mathbf{M}_{\mathrm{r}} \times \mathbf{H}_{\mathrm{a}}), \tag{2.49}$$

by replacing $\mathbf{B}$ with $\mathbf{B}_{\mathrm{a}} = \mu_0\mathbf{H}_{\mathrm{a}}$. It is worth emphasizing that the remanent magnetization $\mathbf{M}_{\mathrm{r}}$ being independent of the applied field $\mathbf{H}_{\mathrm{a}}$ greatly simplifies the calculation of the magnetic force and torque for hard-magnetic soft materials.

When the magnetic Cauchy stress is employed in the analysis of hard-magnetic soft materials, the magnetic body torque and force are automatically taken into account via suitable mechanical balance laws. For uniformly magnetized hard-magnetic soft composites, the magnetic body force density (per unit current volume) can be expressed in terms of the magnetic Cauchy stress as

$$\bar{\mathbf{f}}_{\mathrm{m}} = -\mathrm{div}\,\boldsymbol{\sigma}^{\mathrm{magnetic}} = \mathrm{div}\,(\mathbf{B} \otimes \mathbf{M}_{\mathrm{r}}) = (\mathrm{grad}\,\mathbf{B})\mathbf{M}_{\mathrm{r}}, \tag{2.50}$$

from the linear momentum balance in Equation (2.30) (see **Appendix E** for derivation). Likewise, the magnetic body torque density (per unit current volume) can be expressed in terms of the magnetic Cauchy stress as

$$\bar{\boldsymbol{\tau}}_{\mathrm{m}} = -\boldsymbol{\mathcal{E}} : \left(\boldsymbol{\sigma}^{\mathrm{magnetic}}\right)^{\mathsf{T}} = \mathbf{M}_{\mathrm{r}} \times \mathbf{B}, \tag{2.51}$$

from the angular momentum balance in Equation (2.31) (see **Appendix E** for derivation). The magnetic body force density in Equation (2.50) can be equivalently obtained from the negative gradient of the magnetic potential energy density as

$$\bar{\mathbf{f}}_{\mathrm{m}} = -\mathrm{grad}\,\psi^{\mathrm{magnetic}} = (\mathrm{grad}\,\mathbf{B})^{\mathsf{T}}\,\mathbf{M}_{\mathrm{r}}. \tag{2.52}$$

It should be noted that, for irrotational (curl-free) magnetic fields with no free current, the spatial gradient of $\mathbf{B}$ field is symmetric (i.e., $\mathrm{grad}\,\mathbf{B} = (\mathrm{grad}\,\mathbf{B})^{\mathsf{T}}$), which makes the two expressions in Equations (2.50) and (2.52) identical.

It is worth noting that the magnetic body torques generated by the embedded magnetized particles under external magnetic fields cause the magnetic Cauchy Stress in Equation (2.44) to be asymmetric. Correspondingly, in the presence of magnetic body torques, the total Cauchy stress in Equation (2.45) can also be asymmetric. It should also be noted that for conventional isotropic magnetorheological elastomers with soft-magnetic inclusions, where no body torque or couple stress exists, the Cauchy stress should remain symmetric to satisfy the angular momentum balance in equilibrium, as discussed in a large volume of literature [36, 66, 67, 68, 69, 70].

2.4 Hard-magnetic Elastica Theory

2.4.1 Introduction

We now focus our attention on a thin elastic rod with hard-magnetic properties—termed the *hard-magnetic elastica*, which produces large deflections under externally applied magnetic fields owing to the presence of intrinsic dipoles (**Figure 2-8A**). Although we still confine ourselves to quasi-static problems under isothermal conditions, the transition from the general continuum mechanical framework for hard-magnetic soft materials to the analysis of hard-magnetic elastica requires a set of restrictions specific to the slender geometry and planar motion of the elastica. While more generalized rod theories (e.g., Kirchhoff's, Cosserat's, and Green and Naghi's) can analyze stretching, twisting, and transverse shearing as well as bending of rods [71, 72, 73, 74], the twisting motion has low practical implications for magnetically steerable soft continuum robots and hence can be ruled out. In addition, for a slender body with a

diameter much smaller than its length, we can further assume that the cross-section remains perpendicular to the centerline of the body during deformation (i.e., no transverse shearing). Furthermore, we can assume that the centerline length of the elastica remains unchanged during deformation (i.e., centerline inextensibility). Lastly, given that most polymeric materials can sustain finite strains without noticeable volume changes, we will also assume the incompressibility of constituent materials ($J = 1$), which, along with the assumption of inextensibility, implies that the cross-sectional area does not vary during the magnetically induced deflection of the elastica.
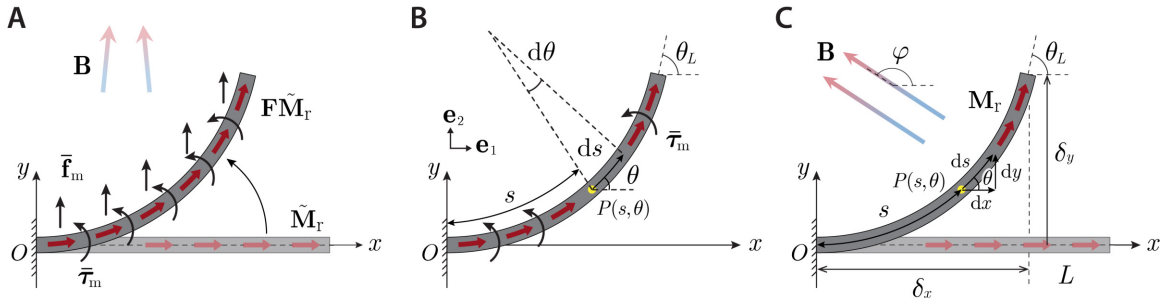
Figure 2-8: Hard-magnetic elastica. (A) Uniformly magnetized hard-magnetic elastica deforming under the applied magnetic field **B**. Magnetization vector $\tilde{\mathbf{M}}_r$ in the undeformed reference state changes to $\mathbf{M}_r = \mathbf{F}\tilde{\mathbf{M}}_r$ in the deformed state, where $\mathbf{F}$ is the deformation gradient with $J = \det \mathbf{F} = 1$ assumed due to the incompressibility of the material. Symbols $\bar{\mathbf{f}}_m$ and $\bar{\boldsymbol{\tau}}_m$ denote the magnetic body force and torque densities, respectively. **(B)** The geometry of the deformed beam is referred to as *elastica* and characterized by a parameterized spatial curve, $\theta = \theta(s)$, in which s and θ represent the arc length and tangential angle at the spatial point, $P(s, \theta)$, respectively. The rotation angle at the free-tip is denoted as θ_L. **(C)** Hard-magnetic elastica under a uniform magnetic field **B** applied at an angle of φ relative to the beam. The position of the distal tip is characterized by a Cartesian coordinate $(\delta_x, \delta y)$.

2.4.2 Kinematics and Governing Equations

With these underlying assumptions specific to the slender geometry and planar motion of the hard-magnetic elastica, the curvature of the centerline (i.e., a spatial curve in the current configuration) can be expressed as

$$\kappa(s) = \frac{d\theta(s)}{ds} = \theta'(s), \tag{2.53}$$

where s denotes the arc length from the origin to the spatial point of interest (denoted by P in **Figure 2-8B**) and $\theta(s)$ denotes the angle between the tangent to the curve at point P and the reference direction (i.e., x-axis or $\mathbf{e}_1$-direction in **Figure 2-8B**).

For our bendable, yet inextensible, twist-free hard-magnetic elastica, the strain energy density (or the elastic Helmholtz free energy per unit current volume) includes only the bending energy, but no stretching or torsional energy. The bending energy then can be expressed as a function of the curvature: $\psi^{\text{elastic}}(\theta')$. Commonly, for a slender rod, the bending energy (per unit volume) takes the following quadratic form proposed by Euler for the inextensible elastica [75]:

$$\psi^{\text{elastic}}(\theta') = \frac{EI}{2A}\theta'^2, \tag{2.54}$$

where E denotes Young's modulus, I is the area moment of inertia, and A is the cross-sectional area of the hard-magnetic elastica. It is worth noting that the constitutive relation for the bending energy in Equation (2.54) implies the following moment-curvature relation, also known as the Euler–Bernoulli relation [76, 77]:

$$\mathcal{M}(s) = EI\kappa(s), \tag{2.55}$$

where $\mathcal{M}(s)$ denotes the internal bending moment. This linear relation holds only for beams or rods made of linear elastic materials for which stress and strain are linearly related by Young's modulus. Even though the hard-magnetic elastica overall exhibits large scale deflections, the local maximum strain developed on an infinitesimal segment due to local compression or stretching during bending is small. Within this limited range, the constitutive relations for the constituent hyperelastic materials can be linearized, which yields the linear moment-curvature relation in Equation (2.55) and the quadratic form for the bending energy in Equation (2.54).

The deformation gradient, which can be decomposed into $\mathbf{F} = \mathbf{R}\mathbf{U}$ where $\mathbf{R}$ and $\mathbf{U}$ denote the rotation and right stretch tensors, respectively, now becomes identical to pure rotation ($\mathbf{F} = \mathbf{R}$) because of the underlying assumption of inextensibility ($\mathbf{U} = \mathbf{1}$). Furthermore, because the motion of the elastica is planar, the rotation $\mathbf{R}$ takes the following matrix form for the rotation around the z-axis (i.e., $\mathbf{e}_3$-direction):

$$[\mathbf{R}] = \begin{bmatrix} \cos\theta & -\sin\theta & 0 \\ \sin\theta & \cos\theta & 0 \\ 0 & 0 & 1 \end{bmatrix}. \tag{2.56}$$

Then, from Equations (2.38) and (2.39) with $J = 1$, the magnetic potential energy per unit current volume can be expressed as

$$\psi^{\mathrm{magnetic}}(\theta, s) = -\mathbf{R}\tilde{\mathbf{M}}_{\mathrm{r}} \cdot \mathbf{B}, \tag{2.57}$$

which leads to the total Helmholtz free energy density as a function of three variables (θ, θ', s): $\psi(\theta, \theta', s) = \psi^{\mathrm{elastic}}(\theta') + \psi^{\mathrm{magnetic}}(\theta, s)$. Then the total Helmholtz free energy of the elastica, denoted by Ψ, can be expressed as the following functional:

$$\Psi = A \int_0^L \psi(\theta, \theta', s) \, \mathrm{d}s, \tag{2.58}$$

where L denotes the total length of the beam. The equilibrium state in the deformed configuration can be found from the principle of stationary potential energy $\delta\Psi = 0$, which yields the following equation also known as the Euler–Lagrange equation:

$$\frac{\mathrm{d}}{\mathrm{d}s}\left(\frac{\partial\psi}{\partial\theta'}\right) = \frac{\partial\psi}{\partial\theta}, \tag{2.59}$$

from which we obtain the following governing equation for the hard-magnetic elastica:

$$\frac{\mathrm{d}}{\mathrm{d}s}\left(\frac{\partial\psi^{\mathrm{elastic}}}{\partial\theta'}\right) = \frac{\partial\psi^{\mathrm{magnetic}}}{\partial\theta}. \tag{2.60}$$

Substituting the elastic and magnetic Helmholtz free energy densities in Equations (2.54) and (2.57) into Equation (2.60), we obtain

$$\frac{EI}{A}\frac{\mathrm{d}^2\theta}{\mathrm{d}s^2} = -\frac{\partial}{\partial\theta}\left(\mathbf{R}\tilde{\mathbf{M}}_{\mathrm{r}} \cdot \mathbf{B}\right), \tag{2.61}$$

where the right-hand side can be expanded by applying chain rule into

$$-\frac{\partial}{\partial\theta}\left(\mathbf{R}\tilde{\mathbf{M}}_{\mathrm{r}} \cdot \mathbf{B}\right) = -\frac{\partial\mathbf{R}}{\partial\theta}\tilde{\mathbf{M}}_{\mathrm{r}} \cdot \mathbf{B} - \mathbf{R}\tilde{\mathbf{M}}_{\mathrm{r}} \cdot \left(\mathrm{grad}\,\mathbf{B}\,\frac{\partial\mathbf{x}}{\partial\theta}\right). \tag{2.62}$$

Here, as mentioned earlier, the remanent magnetization is assumed to be spatially uniform. Given that the derivative of a rotation tensor can be expressed in terms of a skew-symmetric tensor and its axial vector (see **Appendix F**), the first term on the right-hand side of Equation (2.62) can be written as

$$\frac{\partial\mathbf{R}}{\partial\theta}\tilde{\mathbf{M}}_{\mathrm{r}} \cdot \mathbf{B} = \mathbf{e}_3 \cdot \left(\mathbf{R}\tilde{\mathbf{M}}_{\mathrm{r}} \times \mathbf{B}\right) = \left[\mathbf{R}\tilde{\mathbf{M}}_{\mathrm{r}} \times \mathbf{B}\right]_3, \tag{2.63}$$

while the second term can be rearranged as

$$\mathbf{R}\tilde{\mathbf{M}}_{\mathrm{r}} \cdot \left(\operatorname{grad} \mathbf{B}\, \frac{\partial \mathbf{x}}{\partial \theta} \right) = \left((\operatorname{grad} \mathbf{B})^{\mathsf{T}} \mathbf{R}\tilde{\mathbf{M}}_{\mathrm{r}} \right) \cdot \frac{\partial \mathbf{x}}{\partial \theta}. \tag{2.64}$$

Then, the governing equation in Equation (2.60) can be expressed as

$$\frac{EI}{A} \frac{\mathrm{d}^2\theta}{\mathrm{d}s^2} + \left[\mathbf{R}\tilde{\mathbf{M}}_{\mathrm{r}} \times \mathbf{B} \right]_3 + \left((\operatorname{grad} \mathbf{B})^{\mathsf{T}} \mathbf{R}\tilde{\mathbf{M}}_{\mathrm{r}} \right) \cdot \frac{\partial \mathbf{x}}{\partial \theta} = 0, \tag{2.65}$$

which can be equivalently expressed in terms of the magnetic body torque and force from Equations (2.51) and (2.52) as

$$\frac{EI}{A} \frac{\mathrm{d}^2\theta}{\mathrm{d}s^2} + \mathbf{e}_3 \cdot \bar{\boldsymbol{\tau}}_{\mathrm{m}} + \frac{\partial \mathbf{x}}{\partial \theta} \cdot \bar{\mathbf{f}}_{\mathrm{m}} = 0. \tag{2.66}$$

Physically, the first term in Equation (2.66) can be interpreted as the variation in strain energy, while the second and third terms can be interpreted as work done by the magnetic body torque and force, respectively, per unit volume of an infinitesimal element at point P in the deformed configuration during a small variation in angle θ. Equation (2.66) can also be written in terms of the scalar components as

$$\frac{EI}{A} \frac{\mathrm{d}^2\theta}{\mathrm{d}s^2} + \bar{\tau}_{\mathrm{m},3} - \bar{f}_{\mathrm{m},1} \int_0^s \sin\theta(\eta)\, \mathrm{d}\eta + \bar{f}_{\mathrm{m},2} \int_0^s \cos\theta(\eta)\, \mathrm{d}\eta = 0, \tag{2.67}$$

in which the following kinematic relations are employed for a clamped-free elastica:

$$\mathbf{x} = \int_0^s \cos\theta(\eta)\, \mathrm{d}\eta\, \mathbf{e}_1 + \int_0^s \sin\theta(\eta)\, \mathrm{d}\eta\, \mathbf{e}_2, \tag{2.68}$$

$$\frac{\partial \mathbf{x}}{\partial \theta} = -\int_0^s \sin\theta(\eta)\, \mathrm{d}\eta\, \mathbf{e}_1 + \int_0^s \cos\theta(\eta)\, \mathrm{d}\eta\, \mathbf{e}_2, \tag{2.69}$$

where η is used as a dummy variable for integration. It is worth noting that Equation (2.67) can also be derived by considering the force and moment balance [78].

2.4.3 Analytical Solutions for Uniform Fields

When the actuating magnetic field is spatially uniform, (i.e., $\operatorname{grad} \mathbf{B} = \mathbf{0}$), the magnetic body force terms vanish, significantly simplifying the governing equation in Equation (2.66). In general, the bending actuation of ferromagnetic soft continuum

robots is driven by the magnetic body torque and further supported by the magnetic body force as the body deforms [3]. Therefore, studying the response of the hard-magnetic elastica under uniform magnetic fields is of primary importance.

Consider a beam of hard-magnetic elastica lying on the x-axis with a uniform magnetization density along the body in the reference configuration, which is represented as $\tilde{\mathbf{M}}_r = \tilde{M}_r\,\mathbf{e}_1$ where $\tilde{M}_r$ denotes the magnitude. When a uniform field is applied at an angle φ with respect to the reference configuration (i.e., $\mathbf{B} = B\cos\varphi\,\mathbf{e}_1 + B\sin\varphi\,\mathbf{e}_2$), as depicted in **Figure 2-8C**, the governing equation in Equation (2.66) reduces to

$$\frac{EI}{A}\frac{\mathrm{d}^2\theta}{\mathrm{d}s^2} + \tilde{M}_r B \sin\left(\varphi - \theta\right) = 0. \tag{2.70}$$

With the help of chain rule, Equation (2.70) can be expressed in an integral form:

$$\int \frac{\mathrm{d}^2\theta}{\mathrm{d}s^2}\frac{\mathrm{d}\theta}{\mathrm{d}s}\,\mathrm{d}s = -\int \frac{\tilde{M}_r BA}{EI}\sin\left(\varphi - \theta\right)\mathrm{d}\theta, \tag{2.71}$$

which upon integration yields

$$\frac{1}{2}\left(\frac{\mathrm{d}\theta}{\mathrm{d}s}\right)^2 = -\frac{\tilde{M}_r BA}{EI}\cos\left(\varphi - \theta\right) + C. \tag{2.72}$$

The constant of integration C can be determined from the boundary condition that there is no internal bending moment at the free end (i.e., $\theta'(L) = 0$ from Equations (2.53) and (2.55)), which leads to

$$C = \frac{\tilde{M}_r BA}{EI}\cos\left(\varphi - \theta_L\right), \tag{2.73}$$

where θ_L denotes the angular displacement at the free end in the deformed configuration. Then, Equation (2.72), along with Equation (2.73), can be rearranged as

$$\mathrm{d}s = \sqrt{\frac{EI}{2\tilde{M}_r BA}}\frac{\mathrm{d}\theta}{\sqrt{\cos\left(\varphi - \theta_L\right) - \cos\left(\varphi - \theta\right)}}. \tag{2.74}$$

Integration of Equation (2.74) leads to the expression for the length of the elastica:

$$L = \sqrt{\frac{EI}{2\tilde{M}_r BA}}\int_0^{\theta_L}\left(\cos\left(\varphi - \theta_L\right) - \cos\left(\varphi - \theta\right)\right)^{-1/2}\mathrm{d}\theta = \sqrt{\frac{EI}{2\tilde{M}_r BA}}\,\xi(\varphi, \theta_L), \tag{2.75}$$

where the non-dimensional function $\xi(\varphi, \theta_L)$ is defined as

$$\xi(\varphi, \theta_L) = \int_0^{\theta_L} \left(\cos(\varphi - \theta_L) - \cos(\varphi - \theta) \right)^{-1/2} d\theta, \tag{2.76}$$

With this, Equation (2.75) can be expressed in a dimensionless form as

$$\frac{\tilde{M}_r B A L^2}{EI} = \frac{1}{2} \xi^2(\varphi, \theta_L), \tag{2.77}$$

which relates the dimensionless parameter $\tilde{M}_r B A L^2 / EI$ with the angular displacement at the free end θ_L. Physically, this parameter $\tilde{M}_r B A L^2 / EI$ means the actuating field strength B normalized by the material properties (remanent magnetization $\tilde{M}_r$ and Young's modulus E) and the geometrical factors (cross-sectional area A, length L, and area moment of inertia I).

The kinematic relation in Equation (2.68) in a differential form can be written as

$$\frac{d\mathbf{x}}{ds} = \cos\theta\, \mathbf{e}_1 + \sin\theta\, \mathbf{e}_2, \tag{2.78}$$

which, along with Equation (2.74), can also be expressed component-wise as

$$\begin{aligned}
dx = ds\cos\theta = \sqrt{\frac{EI}{2\tilde{M}_r BA}} \frac{\cos\theta\, d\theta}{\sqrt{\cos(\varphi - \theta_L) - \cos(\varphi - \theta)}}, \\
dy = ds\sin\theta = \sqrt{\frac{EI}{2\tilde{M}_r BA}} \frac{\sin\theta\, d\theta}{\sqrt{\cos(\varphi - \theta_L) - \cos(\varphi - \theta)}}.
\end{aligned} \tag{2.79}$$

Then, the Cartesian coordinates of the free end in the current configuration can be expressed as

$$\delta_x = \sqrt{\frac{EI}{2\tilde{M}_r BA}}\, X(\varphi, \theta_L) \quad \text{and} \quad \delta_y = \sqrt{\frac{EI}{2\tilde{M}_r BA}}\, Y(\varphi, \theta_L), \tag{2.80}$$

where the functions $X(\varphi, \theta_L)$ and $Y(\varphi, \theta_L)$ are defined as

$$\begin{aligned}
X(\varphi, \theta_L) = \int_0^{\theta_L} \cos\theta \Big(\cos(\varphi - \theta_L) - \cos(\varphi - \theta) \Big)^{-1/2} d\theta, \\
Y(\varphi, \theta_L) = \int_0^{\theta_L} \sin\theta \Big(\cos(\varphi - \theta_L) - \cos(\varphi - \theta) \Big)^{-1/2} d\theta.
\end{aligned} \tag{2.81}$$

When normalized by L, the free-end coordinates in Equation (2.81) can be given by

57

$$\frac{\delta_x}{L} = \frac{X(\varphi, \theta_L)}{\xi(\varphi, \theta_L)} \quad \text{and} \quad \frac{\delta_y}{L} = \frac{Y(\varphi, \theta_L)}{\xi(\varphi, \theta_L)}. \tag{2.82}$$

We can solve Equation (2.77) for the free-end angular displacement θ_L, with given material properties $(\tilde{M}_r, E)$ and geometry (A, L, I) under the prescribed field strength and direction (B, φ), which is presented in **Figure 2-9A**. The deflection angle θ_L increases monotonically as the field strength increases and eventually approaches φ as the elastica becomes more aligned with the applied actuating field direction. From Equations (2.81) and (2.82), we can also obtain the free-end location of the deflected beam (normalized by the length L) with respect to its fixed end, as plotted in **Figure 2-9B** against the normalized magnetic field $\tilde{M}_r B A L^2 / EI$ applied at different angles φ relative to the reference configuration of the hard-magnetic elastica. When $\varphi \leq 90°$, the normalized free-end deflection δ_y / L increases monotonically and then becomes saturated. When $\varphi > 90°$, however, the normalized deflection δ_y / L initially increases and then drops after reaching its peak as the elastica further deflects with the free-end angle θ_L being greater than 90°. It is worth noting that the discontinuous behavior predicted for $\varphi = 180°$ (**Figure 2-9**) is valid, only in an idealized sense, when the applied field is perfectly antiparallel to a perfectly straight beam. In reality, any small misalignment between $\mathbf{B}$ and $\tilde{\mathbf{M}}_r$ would exist to prevent such discontinuous behavior.
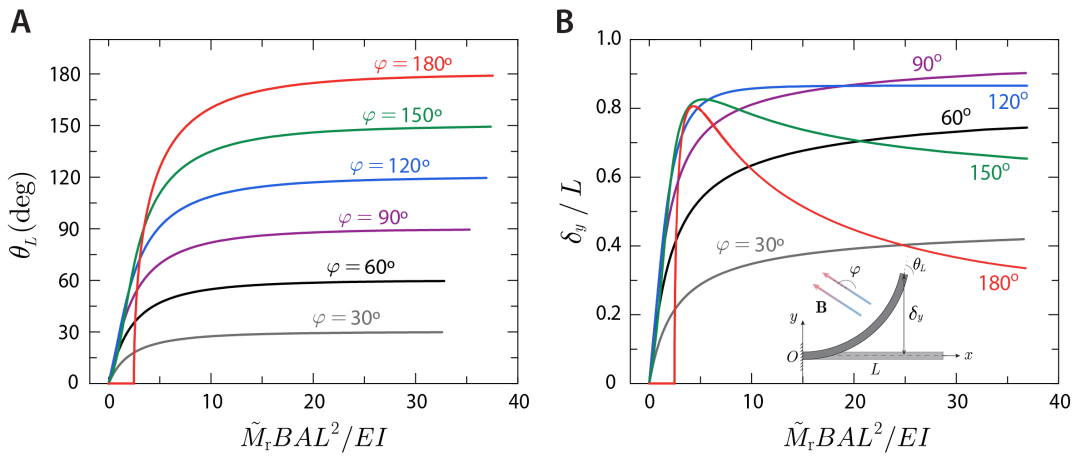

Figure 2-9: General solutions for hard-magnetic elastica under uniform magnetic fields. The free-end location of the deflected hard-magnetic elastica is plotted against the normalized actuating field strength $\tilde{M}_r B A L^2 / EI$ with varying angles φ, in terms of the (**A**) angular displacement θ_L and (**B**) normalized tip deflection δ_y / L of the beam.

2.5 Experimental Validation

2.5.1 Characterization of Material Properties

Magnetic characterization: Magnetic properties of composite samples can be measured using different magnetometry techniques. One of the most common ways to measure the magnetization properties of a sample is using a vibrating sample magnetometer (VSM) [79, 80]. In typical VSM settings, a magnetizable or already magnetized sample is placed in a spatially uniform magnetic field between a pair of electromagnets and then vibrated perpendicularly to the applied field at a prescribed frequency and amplitude (**Figure 2-10A**). The vibrating motion (usually vertical) of the magnetized sample causes the magnetic flux entering the pickup coil to change, which in turn creates an induced voltage in the coil that is proportional to the sample's magnetic moment. By measuring the induced voltage while varying the applied field strength over a range, the hysteresis curve can be obtained for ferromagnetic materials. For already magnetized samples, the measurement should be performed under weak magnetic fields to ensure that the sample's remanent magnetization remains unaffected by the applied field. It is also worth noting that the sample orientation matters because what is measured from the VSM is the component of the sample's magnetic moment vector, which is perpendicular to the pickup coil [1].
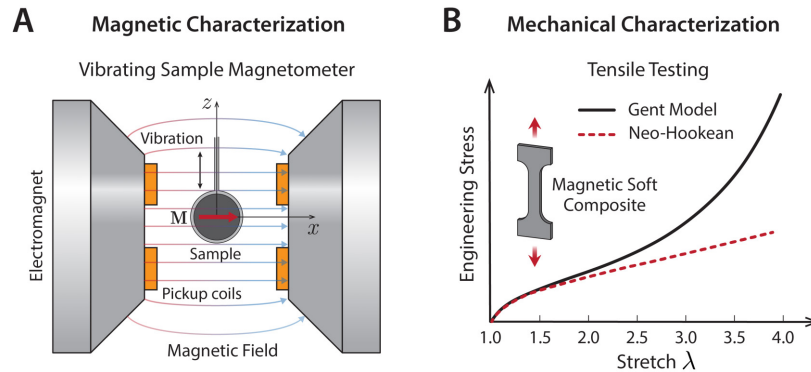
Figure 2-10: Characterization of magnetic soft materials. (**A**) Magnetic characterization of magnetic materials using a vibrating sample magnetometer (VSM) and (**B**) mechanical characterization of elastomeric composites through tensile testing, where the obtained stress-strain curve can be fitted with hyperelastic constitutive models such as Gent or neo-Hookean models.

Mechanical characterization: Mechanical properties of magnetic soft materials are as important as their magnetic properties in determining the performance and characteristics of the magnetically driven soft actuators. As mentioned earlier in **Section 2.3.4**, the mechanical response of magnetic soft composites can be described by hyperelastic constitutive models. The neo-Hookean model provides the simplest form of strain energy density (Helmholtz free energy per unit reference volume) function. For isotropic and incompressible ($J=1$) solids, the neo-Hookean model in Equation (2.37) reduces to a simpler form:

$$\psi_{\mathrm{R}}^{\mathrm{elastic}}(\mathbf{F}) = \frac{G}{2}(I_1 - 3).$$
(2.83)

It is worth noting that most rubber-like materials can be reasonably considered to be incompressible because their bulk modulus values are typically orders of magnitude greater than their shear modulus values [81]. Therefore, for incompressible magnetic elastomer composites, the constitutive equation in Equation (2.35) is modified with the additional constraint of incompressibility taken into account as

$$\boldsymbol{\sigma}^{\mathrm{elastic}} = \frac{\partial \psi_{\mathrm{R}}^{\mathrm{elastic}}}{\partial \mathbf{F}} \mathbf{F}^{\mathsf{T}} - p\mathbf{1},$$
(2.84)

where p is often termed the hydrostatic pressure, a scalar quantity that can be determined from the equilibrium equations and the boundary conditions. Substituting Equation (2.83) into Equation (2.84) gives the following form of the Cauchy stress for incompressible neo-Hookean solids:

$$\boldsymbol{\sigma}^{\mathrm{elastic}} = G\mathbf{F}\mathbf{F}^{\mathsf{T}} - p\mathbf{1}.$$
(2.85)

Under uniaxial loading, the deformation gradient $\mathbf{F}$ can be expressed in terms of the principle stretches as $[\mathbf{F}] = \mathrm{diag}\,(\lambda_1, \lambda_2, \lambda_3)$. With the incompressibility constraint ($J = \det \mathbf{F} = \lambda_1\lambda_2\lambda_3 = 1$), the deformation gradient tensor can be expressed in the matrix form as

$$[\mathbf{F}] = \begin{bmatrix} \lambda & 0 & 0 \\ 0 & \lambda^{-1/2} & 0 \\ 0 & 0 & \lambda^{-1/2} \end{bmatrix},$$
(2.86)

with $\lambda_1 = \lambda$ and $\lambda_2 = \lambda_3 = \lambda^{-1/2}$. From Equations (2.85) and (2.86), each component of

the elastic Cauchy stress is then calculated as $\sigma_{11}^{\text{elastic}} = G\lambda^2 - p$ and $\sigma_{22}^{\text{elastic}} = \sigma_{33}^{\text{elastic}} = G\lambda^{-1} - p$. With the traction-free boundary condition $\sigma_{22}^{\text{elastic}} = \sigma_{33}^{\text{elastic}} = 0$, which gives $p = G/\lambda$, the true tensile stress can then be expressed as

$$\sigma_{11}^{\text{elastic}} = G\left(\lambda^2 - \frac{1}{\lambda}\right), \tag{2.87}$$

which measures the true stress (force per unit current area) in the elongated specimen. In practice, the engineering or nominal stress, which characterizes the force per unit reference (undeformed) area, is easier to measure. From the relation between the Piola stress and the Cauchy stress in Equations (2.34) and (2.35) (i.e., $\mathbf{P} = J\boldsymbol{\sigma}\mathbf{F}^{-\mathsf{T}}$), the engineering tensile stress can be expressed as

$$P_{11}^{\text{elastic}} = G\left(\lambda - \frac{1}{\lambda^2}\right). \tag{2.88}$$

By fitting the experimentally obtained stress-stretch curve with Equation (2.88), one can find the shear modulus of the material that is assumed to be an incompressible neo-Hookean hyperelastic solid (**Figure 2-10B**). In general, the neo-Hookean model captures the experimental data reasonably well for relatively small deformation (i.e., $\lambda \leq 1.5$). At higher stretch levels, the neo-Hookean fails to predict the stiffening behavior that is observed in most rubber-like materials, and therefore other hyperelastic models (e.g., Gent, Mooney-Rivlin, Ogden, etc.) should be used along with additional fitting parameters. Given that the local maximum strain is typically around 30% (i.e., $\lambda \leq 1.3$) even for large bending, it is reasonable to use the neo-Hookean model to find the material property (i.e., shear modulus G) when characterizing the mechanical response of magnetic soft bending actuators.

2.5.2 Two Representative Cases

To validate the developed continuum model in **Section 2.3** and the theory of hard-magnetic elastica in **Section 2.4**, we compare the finite element simulation based on our continuum model and the analytical solution from the hard-magnetic elastica theory with experimental results for two representative cases under uniform actuating

fields when i) $\varphi = 90°$ ($\mathbf{B}$ perpendicular to $\tilde{\mathbf{M}}_r$) and ii) $\varphi = 180°$ ($\mathbf{B}$ antiparallel to $\tilde{\mathbf{M}}_r$). For this comparison, we will consider a set of rectangular beams made of hard-magnetic soft composites (**Figure 2-11**), for which the area moment of inertia is given by $I = WT^3/12$ with W and T denoting the width and thickness of the beam, respectively. Then, Equation (2.77) can be expressed as

$$\frac{\tilde{M}_r B}{G}\left(\frac{L}{T}\right)^2 = \frac{1}{8}\xi^2(\varphi, \theta_L), \tag{2.89}$$

where the Young's modulus E was replaced by the shear modulus G through the relation $E = 3G$, under the assumption that the material is incompressible with the bulk moudlus K being far greater than the shear modulus G (i.e., $K \gg G$), which commonly holds for typical hyperelastic solids.
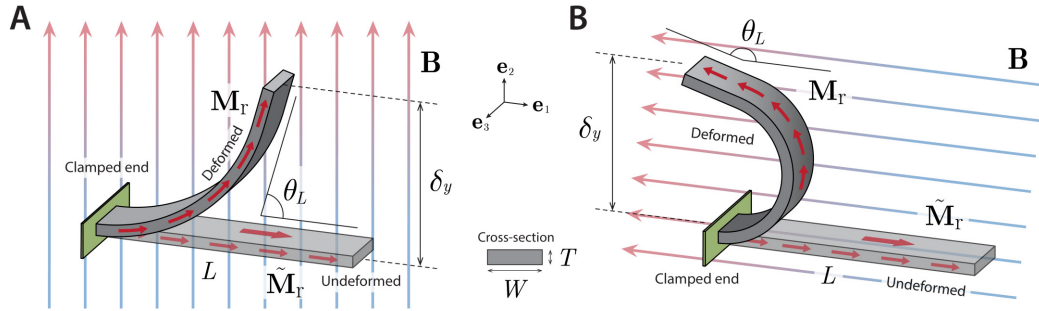
Figure 2-11: Hard-magnetic elastica with large deflection under a uniform magnetic field. A rectangular beam made of the hard-magnetic soft composite undergoes large deflection under a uniform actuating field (**A**) perpendicular ($\varphi = 90°$) and (**B**) antiparallel ($\varphi = 180°$) to its remanent magnetization $\tilde{M}_r$ in the undeformed reference configuration ($\mathbf{e}_1$-direction). One end of the beam is fixed, while the remainder is free to cause the free-end deflection δ_y/L and angular displacement θ_L during the torque-driven bending actuation.

2.5.3 Experimental Settings

For experimental measurements, test specimens were prepared by molding silicone elastomers (PDMS, Sylgard 184) containing NdFeB microparticles (particle concentration of 20% by volume) into rectangular beams with 4 different length-to-thickness ratios ($L/T = 10, 17.5, 20.5, 41$; see **Table 2.1** for detailed dimension). The cast liquid mixture in molds was cured at 120 °C for 1 hour for solidification, and then the obtained rectangular beams were magnetized to have magnetic polarities along the

length direction (**Figure 2-11**). The measured values of the composite's shear modulus G and remanent magnetization $\tilde{M}_{\mathrm{r}}$ were 303 kPa and 114 kA/m, respectively. With its one end clamped to impose the fixed boundary condition, the beam was placed in a uniform magnetic field generated by two-axes Helmholtz coils, as shown in **Figure 2-12**. The beam was placed such that the gravity was acting along the beam's width direction (i.e., $\mathbf{e}_3$-direction), and hence the gravitational effect played no role in the magnetically induced bending actuation of the beam.

Table 2.1: Dimension of beams for experiments.

L/T	$L\,(\mathrm{mm})$	$T\,(\mathrm{mm})$	$W\,(\mathrm{mm})$
10.0	11.0	1.10	5.0
17.5	19.2	1.10	5.0
20.5	17.2	0.84	5.0
41.0	17.2	0.42	5.0
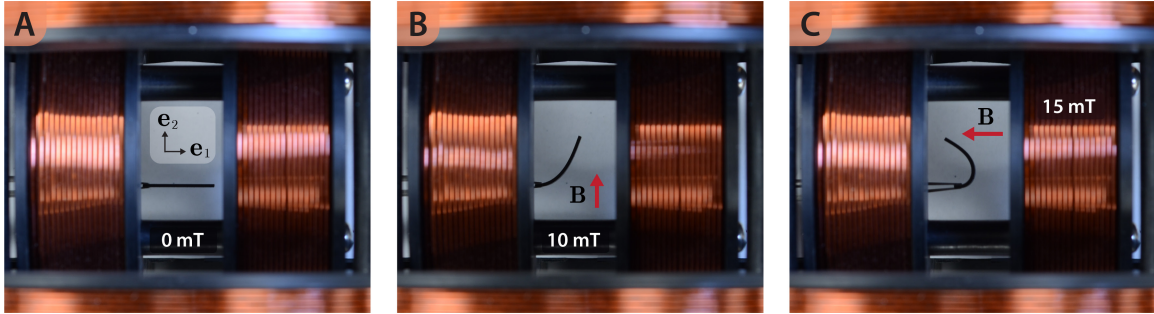
Figure 2-12: **Experimental setup for characterizing bending actuation of hard-magnetic soft beams.** A uniformly magnetized rectangular beam with $L/T = 20.5$ (**A**) in the undeformed state under zero field, (**B**) under a uniform field perpendicular to its reference configuration, and (**C**) under a uniform field antiparallel to its reference configuration.

2.5.4 Comparison and Validation Results

Bending under perpendicular fields: As can be seen in **Figure 2-13**, **A** and **B**, both the finite element simulation based on the continuum model and the theoretical model-based prediction were in good agreement with the experimental results, in terms of both the tip rotation angle θ_L (**Figure 2-13A**) and the normalized deflection δ_y/L (**Figure 2-13B**) of the beams under large deflection in the uniform magnetic fields applied perpendicularly to their remanent magnetization vectors.
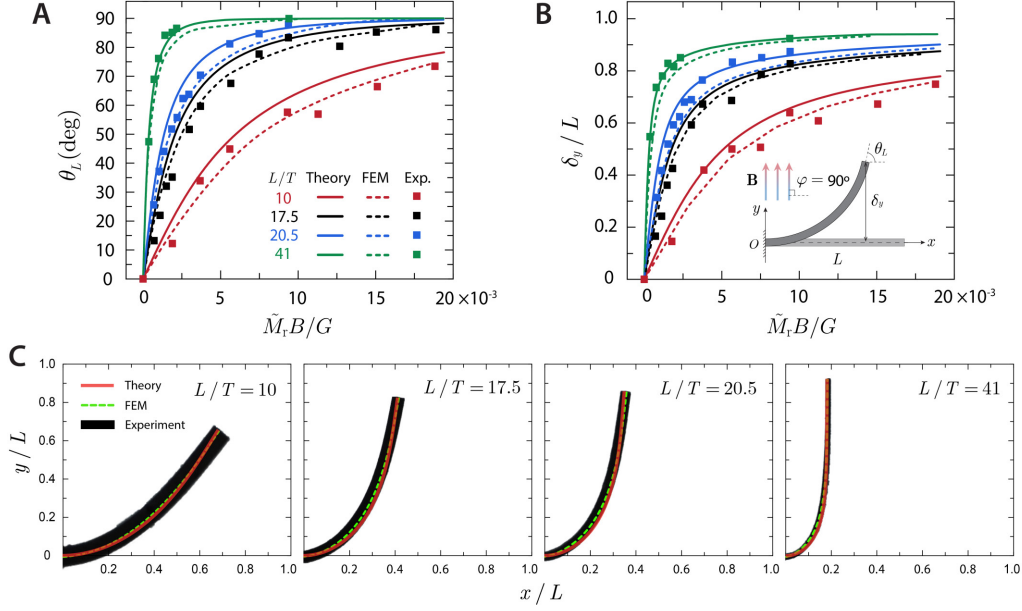
Figure 2-13: Experimental validation for bending under perpendicular fields.
Comparison of the finite element simulation based on the continuum mechanical model and the analytical solution from the hard-magnetic elastica theory with experimental results under uniform magnetic fields applied perpendicularly to the beam ($\varphi = 90°$). (**A**) Deflection angle θ_L and (**B**) normalized tip deflection δ_y/L plotted against the normalized actuating field $\tilde{M}_\mathrm{r}B/G$ for different length-to-thickness ratios L/T. (**C**) Comparison of the analytical solution, simulation, and experimental data through overlaid images of the deflected beams at each length-to-thickness ratio under an actuating field corresponding to the dimensionless parameter of $\tilde{M}_\mathrm{r}B/G = 0.0094$, with $\tilde{M}_\mathrm{r} = 114$ kA/m, $B = 25$ mT, and $G = 303$ kPa.

We observed some deviation of the analytical prediction based on the elastica theory from the finite element simulation or the experimental results, for less slender beams with relatively small length-to-thickness ratios, which is because the underlying assumption behind the elastica theory requires the beam to be slender enough to ignore transverse shearing and focus only on the centerline curve, as discussed earlier in **Section 2.4.1**. Nonetheless, there is still some deviation between the analytical solution and the finite element simulation even for slender beams. This may be attributed to the fact that in our formulation of the hard-magnetic elastica theory, for ease of calculation, we adopted the quadratic form of the bending energy in Equation (2.54), and consequently the Euler–Bernoulli relation in Equation (2.55), which assumes a linear stress profile across the cross-sectional area. However, as can be seen from the overlaid images in **Figure 2-13C**, the gap between the analytical solution and simulation or experimental results is not so significant for slender beams.

Bending under antiparallel fields: Similarly to the previous case with the beams under perpendicular actuating fields, the finite element simulation and the analytical model-based prediction were all in good agreement with the experimental data, as presented in **Figure 2-14**, **A** and **B**, for the beam deflecting under uniform actuating fields applied in the antiparallel direction ($\varphi = 180°$). **Figure 2-14C** visually confirms the good agreement by comparing the shapes of the deflected beams that were experimentally observed (left), simulated based on the continuum mechanical model (middle), and predicted based on the hard-magnetic elastica theory (right). In **Figure 2-14C**, the dashed lines on the simulation results indicate the centerlines of the deformed beams, which are overlaid on top of the experimental data for direct comparison of the profile of the deformed beams.
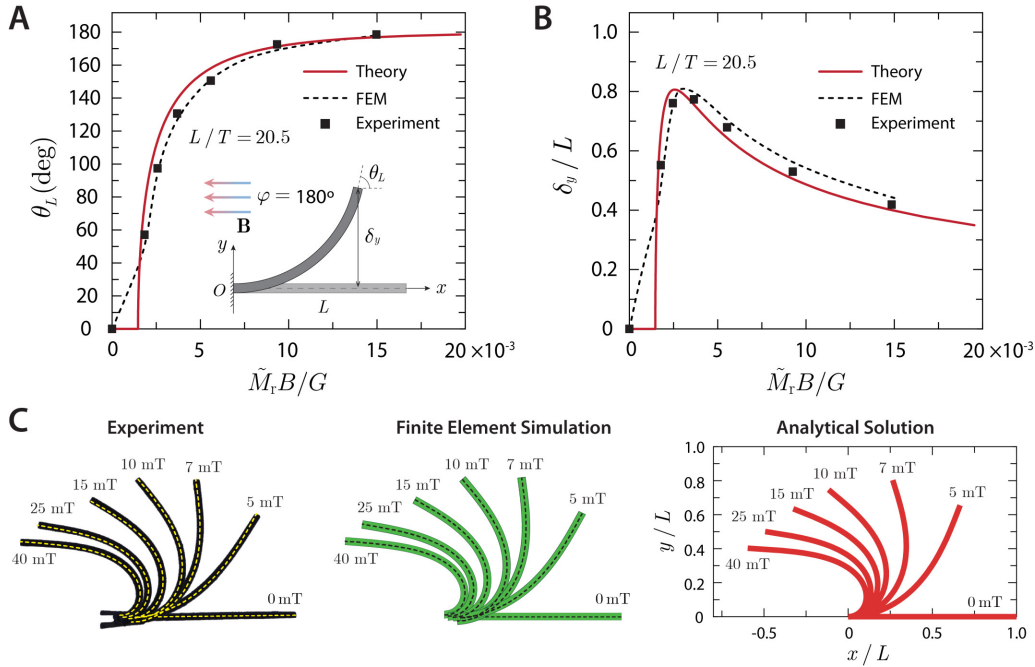
Figure 2-14: Experimental validation for bending under antiparallel fields. Comparison of the finite element simulation and the analytical solution with the experimental results for the torque-driven bending actuation of the beam under uniform antiparallel actuating fields ($\varphi = 180°$). (**A**) The tip deflection angle θ_L and (**B**) the normalized tip deflection δ_y/L are plotted against the normalized actuating field $\tilde{M}_r B/G$ for a specific case with $L/T = 20.5$. (**C**) Comparison of the experimental results, finite element simulation, and analytical solution for the beam deflecting under uniform antiparallel fields ranging from 0 to 40 mT. The dashed lines on the simulation results indicate the centerlines of the deformed beams, which are overlaid on top of the experimental data for direct comparison.

To simulate the beam deflection under an antiparallel magnetic field in finite element environments, there must be some slight misalignment between $\tilde{\mathbf{M}}_\mathrm{r}$ and $\mathbf{B}$, because homogeneous uniaxial compression of the beam, instead of bending, would happen when the field is applied in the antiparallel direction, unless the beam has geometric imperfections or perturbations. Therefore, we introduced some slight misalignment between $\tilde{\mathbf{M}}_\mathrm{r}$ and $\mathbf{B}$ to compensate for the absence of geometric imperfections in our beam model for finite element simulation. Consequently, the simulation results in **Figure 2-14** did not show the discontinuous jump in the beam's deflection that was predicted earlier in **Figure 2-9**.

2.6   Summary

In **Section 2.1**, we discussed different types of magnetic materials and their characteristics and described the promising utility of hard-magnetic soft materials as torque-driven soft bending actuators. In **Section 2.2**, we summarized some of the key concepts and fundamental equations required for mathematical modeling of magnetic soft materials and formulated the idealized constitutive laws for magnetic soft materials in terms of their magnetization behavior and characteristics during magnetic actuation. In **Section 2.3**, we developed a continuum mechanical model for hard-magnetic soft materials, using the nonlinear constitutive theory based on finite hyperelasticity, to allow for quantitative prediction of the behavior of the material with any arbitrary geometry under externally applied magnetic fields through finite element simulation based on the magnetic Cauchy stress. In **Section 2.4**, we applied geometric constraints specific to the planar motion of a slender beam made of hard-magnetic soft materials and formulated the theory of hard-magnetic elastica to provide analytical solutions for the magnetoelastic deflection of hard-magnetic soft beams under uniform actuating fields. In **Section 2.5**, we validated our developed models through a set of experiments. From their close agreement with the experimental results, we verified that both of our continuum mechanical model in **Sections 2.3** and hard-magnetic elastica theory in **2.4** are valid, offering the ability to quantitatively and accurately predict the torque-driven bending actuation of hard-magnetic soft materials even in

the presence of large nonlinear deformation. The developed theoretical models and the ensuing capabilities of quantitative and model-based prediction of the material's behavior provide a powerful tool for optimal design and control of hard-magnetic soft bending actuators, as we shall see in the following chapters.

Chapter 3

Magnetic Soft Continuum Robots

3.1 Introduction

3.1.1 Miniaturization Challenges
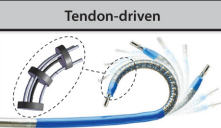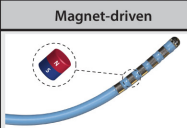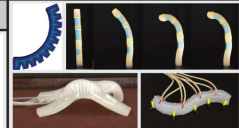
Small-scale soft continuum robots capable of navigating complex and constrained environments hold promise for medical applications [82, 83, 84] across the human body. Several continuum robot concepts have been commercialized so far, offering a range of therapeutic and diagnostic procedures that are safer for patients owing to their minimally invasive nature [85, 86, 20]. Despite these advantages, existing continuum robots are often limited to relatively large scales due to miniaturization challenges inherent in their conventional actuation mechanisms, such as pulling mechanical wires or controlling embedded rigid magnets for manipulation (**Table 3.1**). Tendon-driven continuum robots [87, 88, 89, 90] with antagonistic pairs of wires are difficult to scale down to submillimeter diameters due to increasing complexities in the fabrication process as the components become smaller [91, 92, 93]. The miniaturization challenges have rendered even the most advanced form of commercialized continuum robots, mostly for cardiac and peripheral interventions [21], unsuited for neurosurgical applications due to the considerably small and tortuous vascular structures [20].

Magnetically steerable continuum robots [94, 95, 58, 96, 97] have also remained at large scale because of the finite size of the embedded magnets required to generate deflection under applied magnetic fields. Recently, a submillimeter-scale device with

69

tiny magnets embedded in a soft polymer rod has been proposed for potential use in cardiac interventions, demonstrating magnetic steering and navigation in a coronary artery phantom [98, 99]. However, navigating the complex cerebral vasculature with fully soft-bodied continuum robots has not been realized so far. Furthermore, there are some safety concerns associated with the use of such finite-sized rigid magnets, particularly at submillimeter scale. These concerns are epitomized by the fact that several products of "magnet-tipped" guidewires seeking U.S. Food and Drug Administration (FDA) clearance for 510(k) premarket notification were later recalled because of the concern that the finite-sized magnets at the end of the device could break off [100], which may lead to undesired clinical problems.

Conventional soft robots based on pneumatic or hydraulic actuation are also difficult to miniaturize below millimeter scales, because their fabrication schemes are often unfavorable to such small size (**Table 3.1**) [82, 101]. Furthermore, these existing types of soft robots are difficult to accurately control based on quantitative models, largely because their actuation mechanisms often rely on highly nonlinear deformation or instabilities [102]. On the contrary, magnetic soft robots utilize magnetized or magnetizable microparticles as distributed actuation sources and hence can be readily miniaturized down to submillimeter scales. In addition, their actuation mechanism based on the magnetic torques and/or forces allows them to be manipulated remotely through magnetic fields while at the same time controlled accurately based on quantitative models [78, 103, 1, 2].

Table 3.1: Benefits of the magnetic soft continuum robot for miniaturization in comparison with the conventional types of continuum robots and soft robots.

Type / Features	Magnetic Soft Continuum Robot	Conventional Continuum Robots		Existing Soft Robots
		Tendon-driven	Magnet-driven	
Actuation mechanism	Magnetic fields (Untethered)	Pulling mechanical wires (Tethered)	Controlling magnets (Untethered)	Pneumatic / Hydraulic (Tethered)
Composition	Soft polymer composite with magnetic particles	Rigid links connected by mechanical wires	Elastic composite with embedded rigid magnets	Elastomer or Fiber-reinforced elastomer
Feature size (diameter)	Submillimeter (>100 μm) Easy to miniaturize	Above-millimeter (>2 mm) Difficult to miniaturize	Above-millimeter (>2 mm) Difficult to miniaturize	Centimeter scale Difficult to miniaturize

3.1.2 Benefits of Magnetic Soft Continuum Design

Composed of soft polymers containing tiny magnetic particles (**Figure 3-1A**), our magnetic soft continuum robot can be miniaturized at submillimeter scales in terms of its outer diameter. With a magnetically steerable distal tip, it can navigate through highly constrained environments such as the narrow and tortuous vasculature of the brain (**Figure 3-1B**). Unlike conventional magnet-tipped devices, in which the magnetic moment is highly localized and concentrated on the embedded magnets, our soft continuum design utilizes evenly dispersed magnetic particles as distributed actuation sources that can generate torques and forces in the presence of an external magnetic field. When the embedded particles are magnetized in the same direction, the robot's body has its own magnetic polarity and hence behaves essentially as a flexible permanent magnet, so that its direction can be controlled magnetically. The magnetic torques generated by the distributed particles collectively lead to macroscale material response in the form of torque-driven bending actuation of the continuum robot, with its distal tip aligned with the applied magnetic field (**Figure 3-1A**). With this compact and self-contained actuation mechanism, the soft continuum design offers several unique advantages in terms of flexible design for multifunctionality as well as intuitive and efficient magnetic manipulation for torque-driven bending actuation, as we shall see in the following sections.
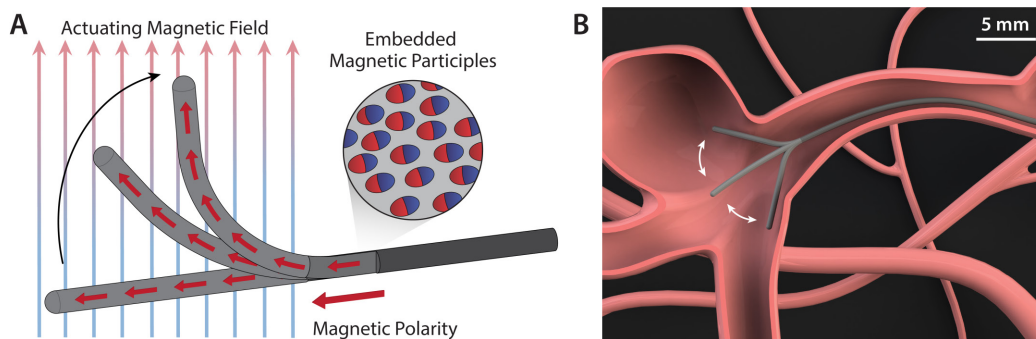
Figure 3-1: Magnetic soft continuum robots. (**A**) Illustration of a submillimeter-scale magnetic soft continuum robot navigating in the complex vasculature with an aneurysm based on its active steering under magnetic actuation. (**B**) Magnetically responsive segment of the continuum robot with programmed magnetic polarities resulting from the magnetized particles embedded in the robot's body made of soft polymer composites.

3.2 Optimal Design Strategies

3.2.1 Problem Definition

As discussed in **Sections 2.3** and **2.4**, hard-magnetic soft materials can be considered essentially soft bending actuators driven by the magnetic torque. From a materials design perspective, it is worth discussing the strategies to optimize the actuation performance of hard-magnetic soft materials. In order to achieve optimal actuation performance, a good balance between the mechanical resistance of the composite structure and the driving magnetic torque is required. For composites based on soft polymers with embedded hard-magnetic particles, both the mechanical and magnetic properties of the composite vary with the particle volume fraction denoted by ϕ. Our goal here is to find the optimal particle concentration that yields the largest bending angle or the largest actuation force under given conditions and geometry.

For the analysis, we consider a circular beam of length L and diameter D under a uniform magnetic field ($\mathbf{B} = B\,\mathbf{e}_2$) that is being applied perpendicularly (i.e., $\varphi = 90°$) to the beam with axial remanent magnetization ($\tilde{\mathbf{M}}_r = \tilde{M}_r\,\mathbf{e}_1$) in the reference configuration (**Figure 3-2A**). The area moment of inertia for its circular cross-section is given by $I = \pi D^4/64$. Then, Equation (2.77) can be expressed as

$$\frac{\tilde{M}_r B}{G}\left(\frac{L}{D}\right)^2 = \frac{3}{32}\xi^2(\theta_L) \tag{3.1}$$

in an implicit form with $\xi(\theta_L)$ given from Equation 2.76 as

$$\xi(\theta_L) = \int_0^{\theta_L} \left(\sin\theta_L - \sin\theta\right)^{-1/2} \mathrm{d}\theta. \tag{3.2}$$

3.2.2 Explicit Solutions for Small Bending

We know from **Figure 2-9A** that the bending angle of the tip (i.e., free-end slope) θ_L monotonically increases as the field strength increases. This implies that the critical concentration predicted from the small-deflection analysis will remain effective for large bending cases as well. Therefore, without loss of generality, we consider small-deflection bending, for which we can find a tractable analytical solution in an explicit

form. When the deflection angle is small, for which $\sin\theta$ can be approximated as θ (i.e., $\sin\theta \approx \theta$), and Equation 3.2 becomes $\xi(\theta_L) \approx \int_0^{\theta_L} (\theta_L - \theta)^{-1/2}\,d\theta = 2\sqrt{\theta_L}$, which leads to the deflection angle θ_L in an explicit form:

$$\theta_L = \frac{8}{3}\left(\frac{\tilde{M}_r B}{G}\right)\left(\frac{L}{D}\right)^2. \tag{3.3}$$

We also know from Equation (2.82) that the normalized deflection δ_y/L is given by

$$\frac{\delta_y}{L} = \frac{Y(\theta_L)}{\xi(\theta_L)} = \frac{16}{9}\left(\frac{\tilde{M}_r B}{G}\right)\left(\frac{L}{D}\right)^2, \tag{3.4}$$

with $Y(\theta_L) \approx \int_0^{\theta_L}\theta(\theta_L - \theta)^{-1/2}\,d\theta = \frac{4}{3}\theta_L\sqrt{\theta_L}$ for small angle θ in Equation (2.81).

The explicit expressions in Equations 3.3 and 3.4 can also be derived by considering an equivalent force acting along the applied field direction on the free end of the beam, which is given by $F_{eq} = \tilde{M}_r B A$ (see **Appendix G** for its derivation). For a cantilever beam undergoing small deflection under this point load F, the standard beam equations can be applied:

$$\theta_L = \frac{F_{eq}L^2}{2EI} \quad \text{and} \quad \frac{\delta_y}{L} = \frac{F_{eq}L^3}{3EI}, \tag{3.5}$$

with $E = 3G$ and $I = \pi D^4/64$ as discussed earlier, to derive Equations 3.3 and 3.4.
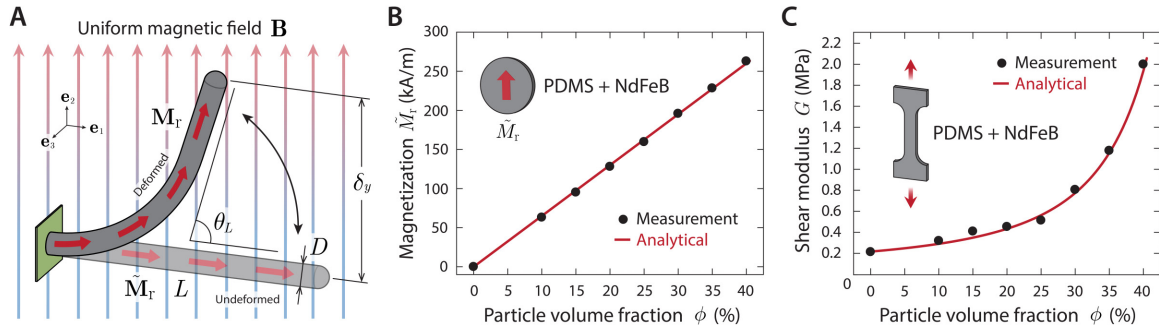
Figure 3-2: Material composition of magnetic soft continuum robot. (**A**) Circular beam of hard-magnetic soft composites (PDMS+NdFeB) with uniform magnetization $\tilde{\mathbf{M}}_r$ along the axial direction deflects toward the direction of a uniform magnetic field $\mathbf{B}$ applied perpendicularly. The unconstrained length and the outer diameter of the robot are denoted as L and D, respectively. δ_y indicates the deflection of the free end, and θ_L indicates the deflection angle. (**B**) The magnitude of the remanent magnetization ($\tilde{M}_r$) linearly increases with the volume fraction of the embedded magnetic particles ϕ. (**C**) The shear modulus of the composite (G) follows an exponential increase with the particle volume fraction.

3.2.3 Modeling of Composite Material Properties

From Equations 3.3 and 3.4, we notice that, for small bending, the deflection of the beam is linearly proportional to a dimensionless quantity, $\tilde{M}_r B/G$, while quadratically dependent on the aspect ratio, L/D. As discussed earlier, the quantity $\tilde{M}_r B/G$ can be interpreted as the actuating field strength B normalized by the material properties of the composite (magnetization $\tilde{M}_r$ and shear modulus G). Given that these material properties are dependent on the particle concentration in the composite, Equations 3.3 and 3.4 imply that there will likely be an optimal particle volume fraction at which the beam deflection is maximized.

For a uniformly magnetized homogeneous continuum, it is reasonable to assume that the remanent magnetization of the composite in the undeformed state, denoted by $\tilde{M}_r$, is linearly proportional to the particle volume fraction ϕ (**Figure 3-2B**):

$$\tilde{M}_r(\phi) = \phi\, M_p, \tag{3.6}$$

where M_p represents the remanence of the magnetized particles embedded in the composite. The shear modulus G increases nonlinearly with the particle concentration ϕ (**Figure 3-2C**). This nonlinear dependence of shear modulus can be predicted with the following equation:

$$G(\phi) = G_0 \exp\!\left(\frac{2.5\phi}{1 - 1.35\phi}\right), \tag{3.7}$$

which is also known as the Mooney model [104], under the assumption that the increase in the shear modulus of particle-filled elastomer composites is analogous to the increase in the viscosity of particle suspensions [105], with G_0 denoting the shear modulus of an unfilled elastomer. In Equation (3.7), it is also assumed that the particles are of spherical shape on average in our homogenized continuum.

3.2.4 Optimization of Actuation Performance

Maximizing the bending angle: Substituting Equations (3.6) and (3.7) into Equation (3.3) or (3.4), we can find that the deflection is maximized when the particle loading is 20.7% ($\phi = 0.207$), as shown in **Figure 3-3A**, under the same conditions

in terms of the actuating field strength B and the beam aspect ratio L/D. Even though the tractable analytical solutions in Equations (3.3) and (3.4) hold for small deflection only, the overall tendency with the optimal concentration to maximize the deflection holds true for large deformation as well, as can be seen from the finite element simulation results presented in **Figure 3-3C**. This is because the bending angle of the tip θ_L monotonically increases with $\tilde{M}_r B/G$ as discussed earlier and shown in **Figure 3-3B**. The parametric study in finite element simulation indicates that the actuation angle indeed reaches its maximum even for large deflection when the particle volume fraction is 20.7%, as predicted for the small bending case. As the applied field strength increases, the actuation angle begins to saturate while approaching 90°, making the curves around the peak flat (**Figure 3-3C**).

Maximizing the energy density: When the actuation force is of greater importance than the large deflection under the given applied field B, the material design can be optimized in terms of the energy density to maximize the mechanical work that can be produced per unit volume during actuation. Again, without loss of generality, we can consider a small bending case with the equivalent force F_{eq} acting at the free end of the beam. Then, the energy density $\mathcal{W}$, or the mechanical work done by the equivalent point force $F_{\text{eq}} = \tilde{M}_r B A$ per unit volume while deforming the beam by small deflection δ_y along the applied field direction, can be expressed as

$$\mathcal{W} = \frac{F_{\text{eq}}\delta_y}{AL} = \frac{\tilde{M}_r B \delta_y}{L} = \frac{16}{9}\left(\frac{\tilde{M}_r^2 B^2}{G}\right)\left(\frac{L}{D}\right)^2. \tag{3.8}$$

Here, it is assumed that no energy is dissipated during the deformation, based on the underlying assumption of hyperelastic solids as discussed in **Section 2.3**. Then, the optimal particle volume fraction that maximizes the energy density under the given conditions is calculated to be 29.3% ($\phi = 0.293$) as shown in **Figure 3-3D**.

This is validated by the finite element simulation for small bending (**Figure 3-3E**), which shows how the energy density varies with the particle volume fraction when $B = 5\,\text{mT}$ and $L/D = 10$. As the bending becomes larger, however, the peak at which the energy density is maximized shifts to the right, toward the higher volume

fractions (**Figure 3-3F**). The peak eventually disappears when the actuation angle saturates, after which the energy density keeps increasing with the particle volume fraction. Qualitatively, this might be attributed to the fact that the shear modulus shows a steep increase at high volume fraction ($\phi > 30\%$), as shown in **Figure 3-2C**, and starts to dominantly contribute to the energy density when the deformation level remains almost unchanged (**Figure 3-3F**).
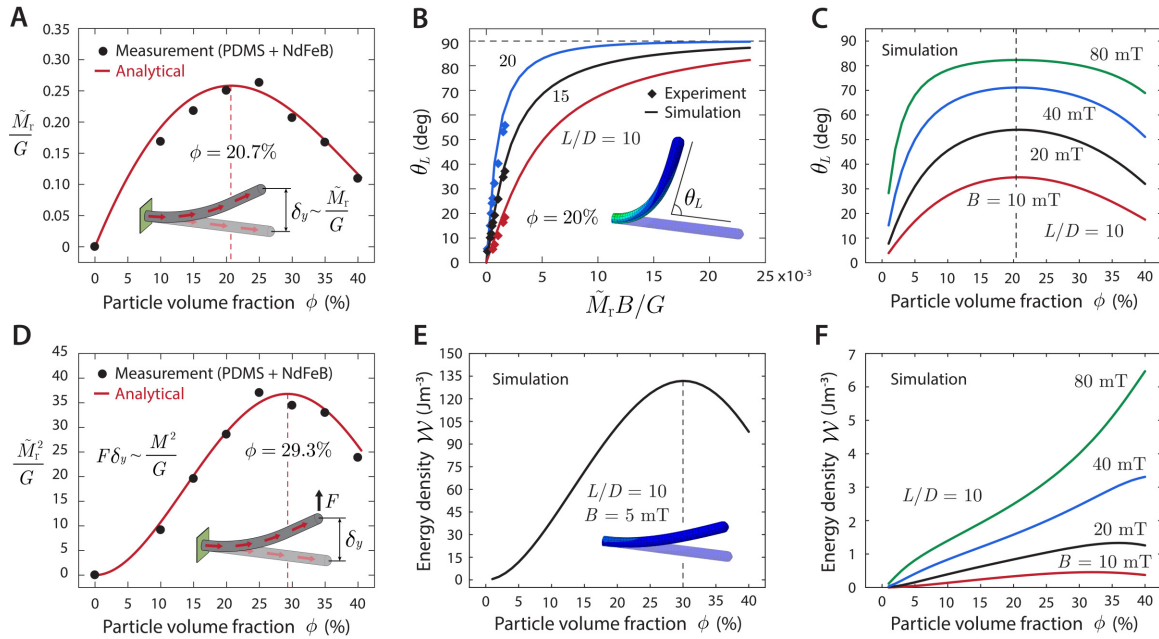
Figure 3-3: Optimal design strategies for magnetic soft continuum robots. (**A**) Analytical prediction of the variation of $\tilde{M}_r/G$, a characteristic quantity that determines the degree of deflection for small bending, with the particle volume fraction under given applied field strength for a given geometry. The unit of this quantity, T^{-1}, or equivalently Am/N, was intentionally omitted for simplicity. (**B**) Actuation angle predicted from finite element simulation and experimental measurements plotted against the applied field strength normalized by material properties ($\tilde{M}_r$ and G) for a particular material composition (20% of particle volume fraction) with different aspect ratios: $L/D = 10$, 15, 20. (**C**) The variation of actuation angle with particle concentration at different actuation field strengths: $B = 10$, 20, 40, 80 mT, predicted from simulation results when $L/D = 10$. (**D**) Analytical prediction of the variation of $\tilde{M}_r^2/G$, a quantity that characterizes the energy density in a deflected body for small bending case, with the particle volume fraction under given applied field strength for a given geometry. The unit of this quantity, A^2/N, was intentionally omitted for brevity. The average energy density was calculated in finite element simulation for (**E**) small and (**F**) large bending cases, as a function of particle concentration.

76

3.3 Materials and Fabrication Schemes

3.3.1 Magnetic Composite Ink

As discussed in **Section 2.1**, ferromagnetic materials in general develop strong induced magnetization under applied magnetic fields. Unlike soft-magnetic materials, such as pure iron, which easily lose the induced magnetization once the external field is removed (**Figure 2-2A**), hard-magnetic materials, such as neodymium-iron-boron (NdFeB), are characterized by their ability to retain high remnant magnetization against the external field once they are magnetically saturated due to their high coercivity (**Figure 2-2B**). The main body of our soft continuum robot is made of an elastomer composite that contains magnetizable microparticles (5-mm-sized on average) of a NdFeB alloy. The soft polymer matrix of the robot's body is composed of either silicone (polydimethylsiloxane; PDMS) or thermoplastic polyurethane (TPU) elastomers, depending on desired mechanical properties. As the initial step of the fabrication process, our magnetic composite ink is prepared by homogeneously mixing nonmagnetized NdFeB particles with uncured PDMS resin or TPU dissolved in solvent at a prescribed volume fraction.

To impart the desired rheological properties to the mixture for ease of fabrication later, we magnetize the whole mixture upon preparation by applying a strong impulse of magnetic fields to magnetically saturate the dispersed NdFeB particles. This turns the previously freely flowing mixture into a thixotropic paste (**Figure 3-4A**) with shear-yielding (**Figure 3-4B**) and shear-thinning (**Figure 3-4C**) properties due to the strong interaction between the permanently magnetized NdFeB microparticles. The acquired rheological properties after magnetization are not only crucial for fabrication, as detailed in the following section, but also conducive to preventing phase separation of our composite ink due to sedimentation of the dispersed particles over time (**Figure 3-4**, **D** to **F**). The suppressed phase separation guaranteed microstructural uniformity, which allows us to postulate a homogeneous continuum (**Figure 2-7A**) when modeling the macroscopic behavior of the composite to quantitatively predict the response of our soft continuum robot upon magnetic actuation.
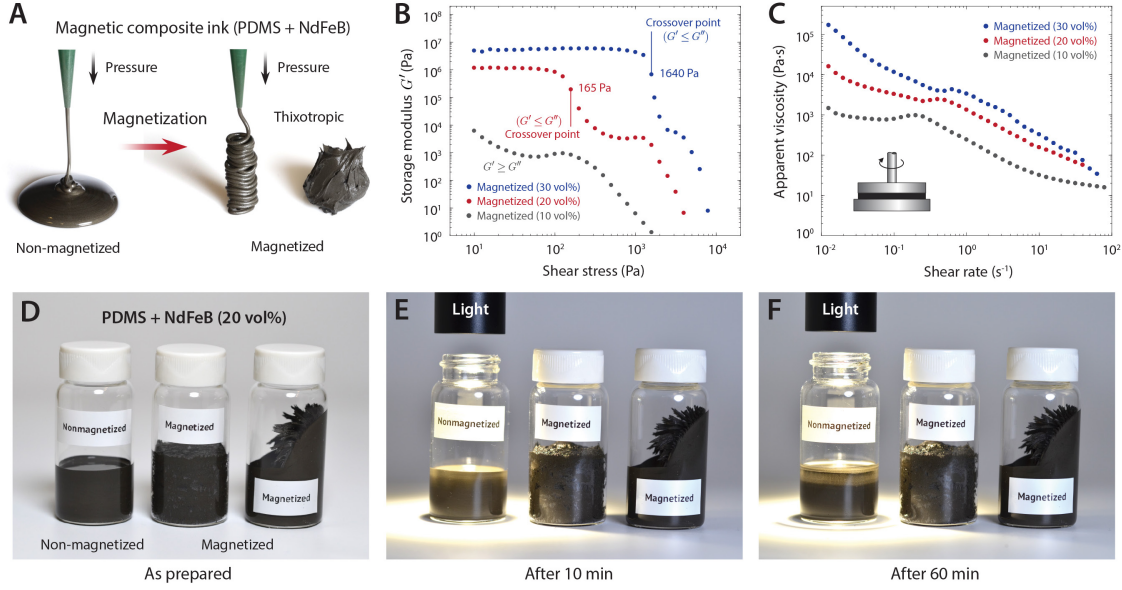
Figure 3-4: Rheological properties of hard-magnetic composite inks. (**A**) Magnetic composite ink based on PDMS + NdFeB (particle concentration of 20 vol%) before and after magnetization. After magnetization, the freely flowing ink became a thixotropic paste with shear yield stress due to the interaction between embedded magnetic particles. (**B**) Storage modulus plotted against the applied shear stress for permanently magnetized composite inks with 10 vol%, 20 vol%, and 30 vol% of NdFeB dispersed in uncured PDMS resin. The crossover point at which the storage modulus G' becomes smaller than the loss modulus G'' defines the shear yield stress beyond which the magnetized composite paste can flow. The identified shear yield stresses for 20 vol% and 30 vol% inks are 165 kPa and 1640 kPa, respectively. (**C**) Apparent viscosity plotted against the applied shear rate for 10 vol%, 20 vol%, and 30 vol% inks. The data reveals shear-thinning behavior of the thixotropic paste of magnetized ink. (**D-F**) The presence of shear yield stresses in 20 vol% magnetized inks helps to prevent the phase separation due to gravitational sedimentation of the particles over time. The vial on the left contains non-magnetized composite ink. In the middle, already magnetized composite ink is contained. On the right, non-magnetized ink is first loaded and then magnetized while being contained in the vial.

3.3.2 Fabrication Methods

The magnetic soft continuum robot can be fabricated by either printing or injection molding, both of which required extruding the thixotropic paste-like ink through a micronozzle by applying pressure (**Figure 3-5**, **A** and **B**). The shear-thinning behavior of the magnetized ink ensures that the composite ink can be easily extruded when pressurized, and the presence of yield stress helps the deposited ink maintain its shape [1] instead of spreading and becoming flat. For its application to endovascular navigation, additional mechanical support is required to ensure good "pushability"

of the device as a guidewire. For this, a stiff core wire can be incorporated into the robot's body through the injection molding. For this process, a microtube is used as a mold, into which we inject the thixotropic composite ink while locating a concentric core inside the mold. Once the printing or injection is complete, the printed or molded ink undergoes thermal curing (PDMS-based composite) or solvent evaporation (TPU-based composite) upon heating to solidify into the robot's body. During the heating process, the presence of yield stress helps the unsolidified ink maintain its shape on the printing substrate or remain stable in the mold instead of flowing and escaping due to the decrease in viscosity at the elevated temperature. For large-scale production, conventional extrusion-based methods can be used for polymer jacketing of a thermoplastic composite over a core wire (**Figure 3-5C**). After all, the magnetically active tip is uniformly magnetized along the axial direction to have the programmed magnetic polarity required to create deflection upon magnetic actuation.
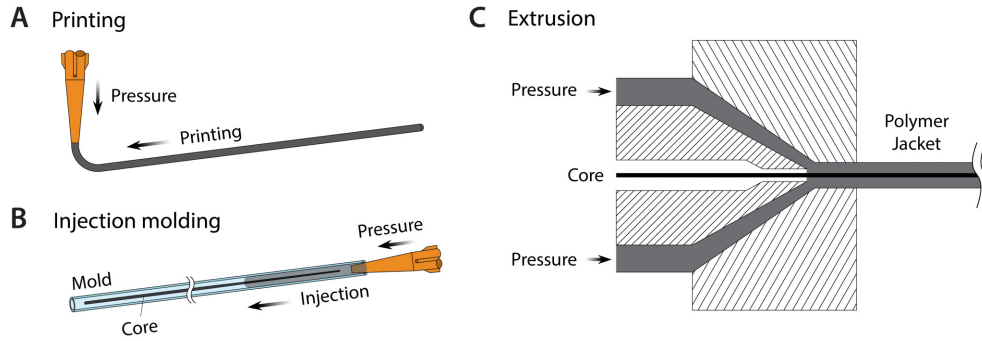
Figure 3-5: Fabrication of magnetic soft continuum robots. Fabrication methods based on (**A**) printing, (**B**) injection molding, and (**C**) extrusion. For printing, the ink is extruded through a micronozzle upon pressurization. For injection molding, the ink is injected into a micromold in which a core wire is placed. For extrusion, molten thermoplastic composite is extruded over a core wire to make it coated with a polymer jacket.

3.3.3   Hydrogel Skin for Lubricious Surface

For the endovascular application of magnetic soft continuum robots, friction acting on the device during navigation can negatively impact its advancement or retraction. To reduce the friction, the robot's surface is coated with a thin (10 to 25 μm) layer of hydrated cross-linked polymers, also referred to as *hydrogel skin* [106]. This hy-

drogel skin can effectively decrease the friction due to its high water content. The hydrogel skin is based on polydimethylacrylamide (PDMAA) that are grafted onto the elastomer chains on the robot's surface. For the hydrogel coating procedure, we followed the previously reported protocol [106]. First, the solidified robot's body is treated with an organic solution based on ethyl alcohol that contains hydrophobic photoinitiators (benzophenone). Exposure to this organic solution induces swelling-driven absorption of the photoinitiators into the robot's surface. The treated body is then immersed into a hydrogel monomer (DMAA) solution containing hydrophilic photoinitiators (Irgacure 2959). Upon exposure to ultraviolet radiation, the hydrogel monomers are polymerized by the hydrophilic initiators while covalently grafted onto the surface-bound elastomers by the activated benzophenone, leaving a thin hydrogel-polymer interpenetrated layer on the surface. The measured thickness of the hydrogel skin ranges from 10 to 25 μm from fluorescence microscope images taken from coated and uncoated samples with planar geometry (**Figure 3-6**, **A** to **D**). The microscopic images identifies the presence of the hydrogel skin on the coated samples.

The resulting hydrogel skin reduces the surface friction, which can be characterized by the friction coefficients measured from a rheometer testing while applying different levels of shear rates and normal pressure (**Figure 3-6E**). The measurements shows a 10-fold decrease in the friction coefficient (**Figure 3-6**, **H** and **I**) as a result of the lubricious hydrogel skin in all given conditions. Furthermore, the coated hydrogel skin can remain stable and undamaged even after prolonged shearing over an hour, exhibiting sufficient mechanical robustness (**Figure 3-6J**). Another measurement confirms substantial reduction (i.e., by a factor of 15) in the force required to pull the device with hydrogel skin (**Figure 3-6F**), as a consequence of the self-lubricating hydrogel skin, when compared with the pulling force required for the uncoated device without hydrogel skin (**Figure 3-6G**). The force required to pull the uncoated device at the prescribed pulling rate (200 mm/min) increases by 150% when the applied normal force increases from 2 to 5 N. For the hydrogel-coated device, however, the required pulling force increases by only 60%, which illustrates how effectively the lubricious hydrogel skin can reduce the surface friction experienced by the device.
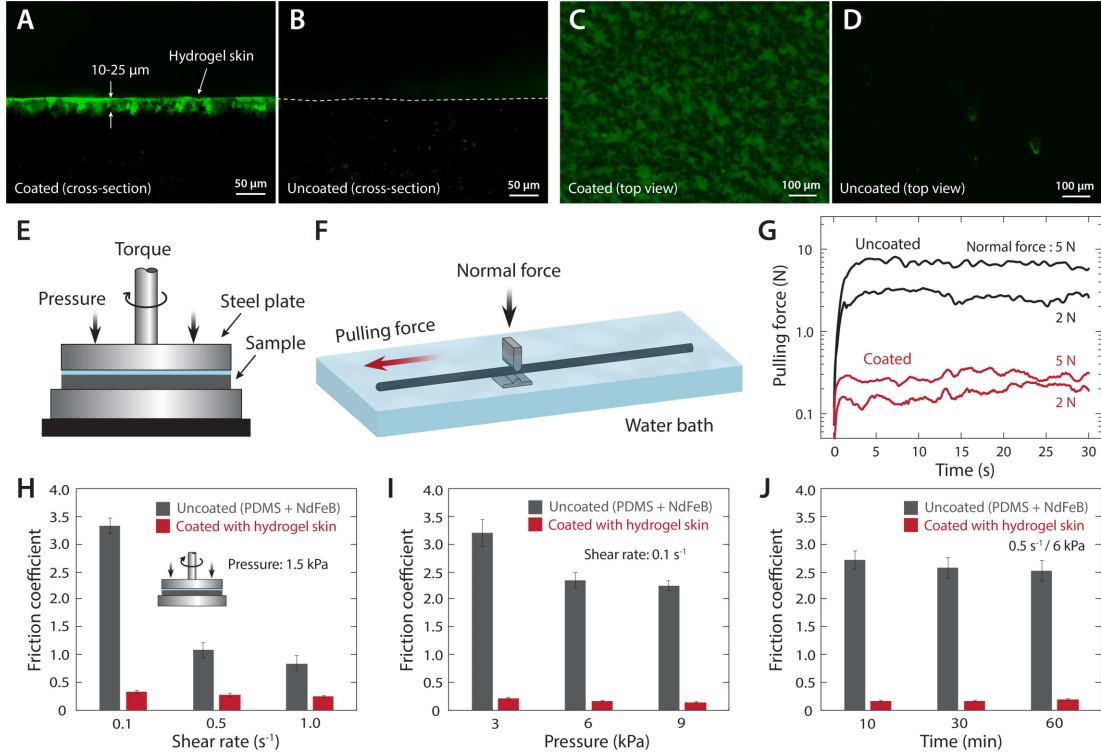
Figure 3-6: Hydrogel skin as a self-lubricating layer. Cross-sectional views of (**A**) the coated specimen of PDMS + NdFeB (20 vol%) with hydrogel skin visualized by absorbed fluorescein and (**B**) the uncoated specimen without hydrogel skin. The dashed line in (**B**) indicates the boundary of the cross-section of the uncoated specimen. (**C-D**) Top views of the coated and uncoated specimens. (**E**) Schematic of testing setup for measuring friction coefficients using a rheometer. (**F**) Schematic of testing setup for measuring force required to pull the device at a constant speed under applied normal force by the pair of grips. (**G**) Semi-log plot of the pulling force measured over time during the pullout test performed at 200 mm/min for both coated and uncoated devices under two different normal force conditions (2 and 5 N). (**H-I**) Friction coefficients measured from both coated and uncoated devices under different shear rates and normal pressure. (**J**) Friction coefficients measured from prolonged shearing of both coated and uncoated samples up to 60 min at shear rate of 0.5 s^{-1} under normal pressure of 6 kPa. The error bars indicate the standard deviations of the mean values obtained from five different measurements.

3.3.4 Silica Coating for Corrosion Prevention

Ferromagnetic alloys have a highly corrosive nature due to the high content of iron and hence can be corroded in aqueous environments (**Figure 3-7A**). To prevent corrosion of the embedded NdFeB particles at the hydrated interface with the water-containing hydrogel skin of the magnetic soft continuum robot, the NdFeB particles are coated with a thin shell of silica. The coating is based on the modified Stöber process that

81

utilizes the condensation reaction of tetraethylorthosilicate or tetramethylorthosilicate (TEOS/TMOS), which nucleated around the particles to form a cross-linked silica layer (**Figure 3-7B**). The thickness of the silica shell is measured to be 10 nm from transmission electron microscope (TEM) imaging (**Figure 3-8A**) and further verified by Fourier transform infrared spectroscopy, which indicated the presence of Si–O–Si bonds (**Figure 3-8B**). The effectiveness of the silica shell in preventing the corrosion of NdFeB particles can be verified by performing a leaching test for both coated and uncoated particles with a weak acidic solution (0.2 mM HCl, pH 3), as shown in **Figure 3-8C**. The results show highly oxidized uncoated particles but no visible change in silica-coated particles, which illustrates the anticorrosion effect of the silica shell formed around the NdFeB particles. Because of the marginal thickness of the silica shell compared with the size of microparticles, the silica coating results in a slight increase in volume, which is roughly estimated to be around 1% when assuming a uniform silica layer around a spherical particle.
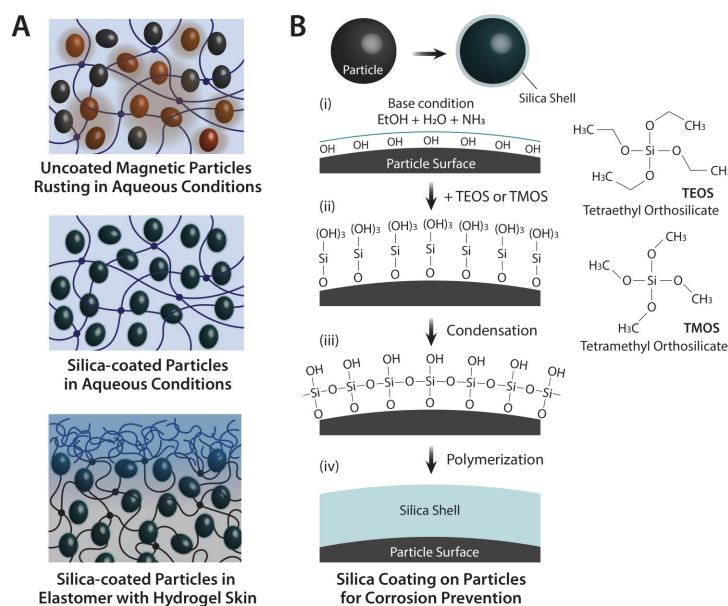
Figure 3-7: Silica coating on magnetic particles for corrosion prevention. (**A**) Corrosion of ferromagnetic particles in aqueous environments. Silica-coated particles for corrosion prevention in hydrogel-based composites or in elastomer-based composites with hydrogel skin for biocompatibility and lubrication. (**B**) Schematic of the polycondensation reaction of tetraethyl and tetramethyl orthosilicate (TEOS/TMOS) in the presence of catalysts under basic conditions, in which the nucleation and polymerization of TEOS/TMOS give rise to cross-linked layers of silica around the magnetic particles.
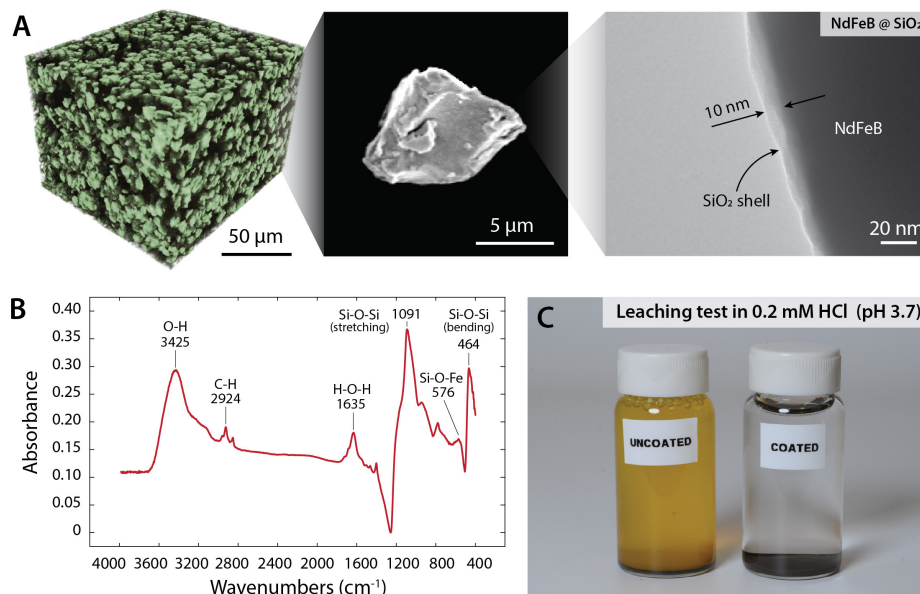
Figure 3-8: Characterizations of anti-corrosion silica coating. (**A**) Micro-computed tomography image of solidified ferromagnetic composite based on PDMS and silica-coated NdFeB particles showing uniformly dispersed particles with no obvious sign of sedimentation (left). Scanning electron microscope image of silica-coated NdFeB particles indicating the size of a single particle (middle). Transmission electron microscope image of a silicacoated NdFeB particle, from which the thickness of the silica layer is identified to be 10 nm (rigth). (**B**) Fourier transform infrared spectroscopy of silica-coated NdFeB particles clearly indicating the presence of Si–O–Si bonds. (**C**) Leaching test of both uncoated and coated NdFeB particles in 0.2 mM HCl solution (pH 3.7) for 3 days. No visible change was observed in the silica-coated particles owing to the presence of the protective silica layer, whereas the uncoated particles were highly oxidized, turning the color of the solution yellow.

3.4 Proof-of-Concept Demonstrations

3.4.1 Magnetic Steering and Navigation

In this section, we demonstrate the main capability of our magnetic soft continuum robots designed for navigating complex and constrained environments, such as vasculature, based on active steering upon the magnetic actuation and additional functionalities enabled by the functional core incorporated in the robot's body. **Figure 3-9A** illustrates the magnetic soft continuum robot passing through a set of rings using its magnetically responsive tip, which follows the direction in which the actuating field is applied. For proof-of-concept demonstration, a cylindrical permanent magnet (diameter and height of 50 mm) was used to apply the actuating magnetic

fields at a distance. The basic principle for magnetic actuation and steering was to align the central axis of the magnet along the desired direction to induce bending of the robot's tip toward the desired direction. Although the bending actuation in general is driven by the magnetic torques as discussed earlier, the spatial gradients of applied magnetic fields can also give rise to magnetic body forces, which further encourage the robot's tip to align itself along the magnet's central axis, as discussed in **Section 2.1** with **Figure 2-4**. **Figure 3-9B** shows the experimental demonstration of the fabricated prototype, which selectively navigates through a set of loosely placed rings (see **Figure 3-10A** for the detailed setup) based on steering achieved by manipulating the hand-held magnet. The demonstrated prototype was fabricated through injection molding (**Figure 3-5B**) of the PDMS + NdFeB composite ink (20 vol%) and was designed to have an outer diameter of 600 μm. To provide mechanical support and pushability required for the demonstrated task, we incorporated a nickel-titanium alloy (nitinol) core in the robot's body (**Figure 3-9A**).
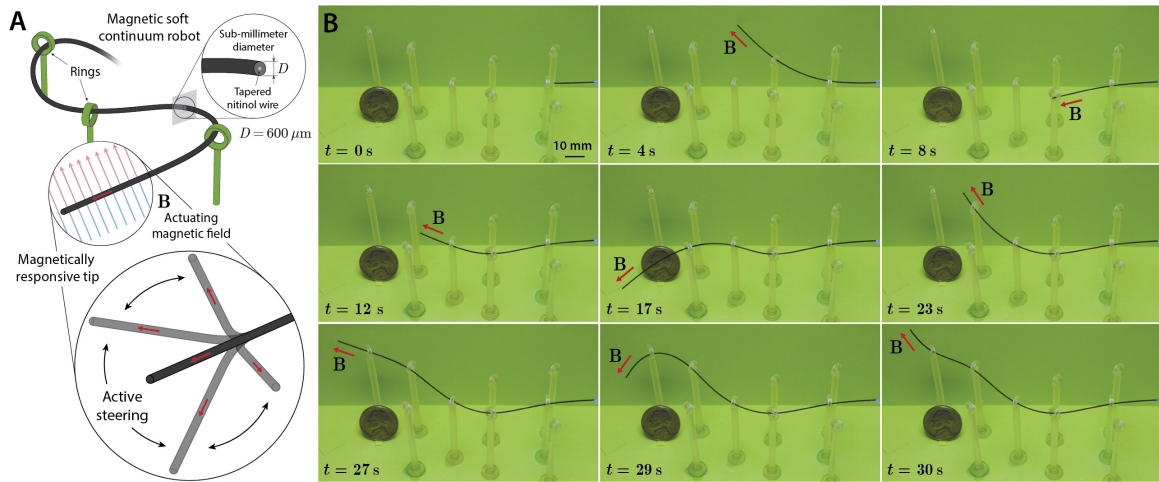
Figure 3-9: Proof-of-concept demonstration of magnetic steering and navigation. (**A**) Schematic of the demonstrated prototype with a magnetically responsive tip and a tapered nitinol core required for active steering and navigation under magnetic actuation. (**B**) Experimental demonstration of the designed prototype based on PDMS + NdFeB composite (20 vol%) selectively navigating through a set of rings based on magnetic actuation and steering. The magnetic fields for actuation (20 to 80 mT) were generated by a cylindrical permanent magnet (diameter and height of 50 mm) at a distance (40 to 80 mm). The proximal end was pushed to advance the magnetically steered distal tip of the robot during the navigation. The outer diameter of the prototype was designed to be 600 μm.

Figure 3-10: Experimental setups for the proof-of-concept demonstrations. (**A**) A set of rings loosely placed at different locations (in mm) with different heights (in mm) and tilt angles, through which the prototypes presented in **Figure 3-9** navigate selectively based on the demonstrated active steering capabilities. (**B**) A set of rings tightly placed to form a tortuous path, which is navigated by the prototype presented in **Figure 3-11**.

3.4.2 Distal Tip Design for Sharp Turns

To enable sharp turns in tortuous paths, we introduced a variation in the bending stiffness of the magnetically responsive part of the soft continuum robot. The new prototype with an outer diameter of 600 μm has a short (3-mm-long), softer segment at the distal end of the magnetically active portion. This softer segment is composed of the PDMS + NdFeB composite (20 vol%) only and thus substantially softer than the remainder that contains a stiff nitinol core (with an outher diameter of 80 μm). The effective Young's modulus of the stiffer segment is calculated to be 14 MPa from

$$E_{\text{effective}} = E_{\text{core}} \left(\frac{d}{D}\right)^4 + E_{\text{jacket}} \left(1 - \left(\frac{d}{D}\right)^4\right), \tag{3.9}$$

where E_{core} and E_{jacket} denote the Young's moduli of the nitinol core and the hard-magnetic soft polymer jacket, respectively, and d (80 μm) and D (600 μm) denote the core and jacket diameter, respectively. For the nitinol core, the Young's modulus of the martensite phase ($E_{\text{core}} = 40$ GPa) was used for calculation. For the softer segment, the measured shear modulus value ($G = 455.6$ kPa) for PDMS + NdFeB (20 vol%) in **Figure 3-2C** was used. Under the assumption of incompressible solids, this shear modulus is translated to Young's modulus of 1366.8 kPa ($E_{\text{jacket}} = 3\,G$), which is 10 times lower than that of the stiffer segment. This calculation was validated from good agreement between the simulation and experimental results in **Figure 3-3B**.

Figure 3-11: Multiple modes and degrees of distal tip deflection for sharp turns.
(**A**-**C**) Finite element simulation results identifying multiple different modes and degrees of deflection, depending on the unconstrained length of the magnetically responsive tip (consisting of stiff and soft segments) as well as the applied field strength and direction, which help to create sharp turns when navigating through tortuous paths. (**D**) The designed prototype navigating through a highly nonlinear path formed by a set of tightly spaced multiple rings. The magnetic fields for actuation (20 to 80 mT) were generated by a cylindrical permanent magnet (diameter and height of 50 mm) at a distance (from 40 to 80 mm). The proximal end was pushed to advance the magnetically steered distal end of the robot during the navigation. The outer diameter of the demonstrated prototype was 600 μm.

Both segments have uniform magnetization along the axial direction. The softer and hence more responsive tip enables multiple modes and degrees of bending depending on the direction and strength of the applied actuating field, as well as the unconstrained length of the magnetically active segment, as predicted from the finite element simulation in **Figure 3-11**. When the unconstrained length of the stiff segment equaled that of the soft segment, only the very end tip of the continuum robot reacted effectively to the applied magnetic fields, creating a J-shaped tip (**Figure 3-11A**). This is because the short unconstrained segment has a large bending stiffness due to the small aspect ratio, as predicted in **Figure 3-3B**. As the unconstrained length increased, the bending stiffness of the stiffer segment decreased, which increased the radius of curvature of overall bending upon magnetic actuation (**Figure 3-11**, **B** and **C**). **Figure 3-11D** shows the experimental demonstration of our fabricated prototype navigating through a tortuous path formed by a series of tightly spaced rings (see **Figure 3-10B** for details) based on the ability to make sharp turns.

86

3.4.3   Navigation in Realistic Anatomical Models

Using the same prototype presented earlier in **Figure 3-11**, we extend our proof-of-principle demonstration to a more realistic and clinically relevant environment based on a life-sized silicone replica of the brain's major arteries. The phantom vasculature replicates the complex and tortuous anatomy of the human neurovasculature with several acute-angled corners as well as multiple aneurysms. The silicone vessels were filled with a blood analog that simulates the friction between commercial guidewires and real blood vessels. The required task was to reach all the aneurysms present along the targeted path while demonstrating the ability to locate the robot's distal tip inside each aneurysm based on magnetic actuation and steering capabilities. In addition, direct contact of the robot with the inner wall of the aneurysms should be avoided, given the fact that aneurysms pose increased risks of rupture, which can lead to bleeding into the brain (i.e., hemorrhagic stroke).
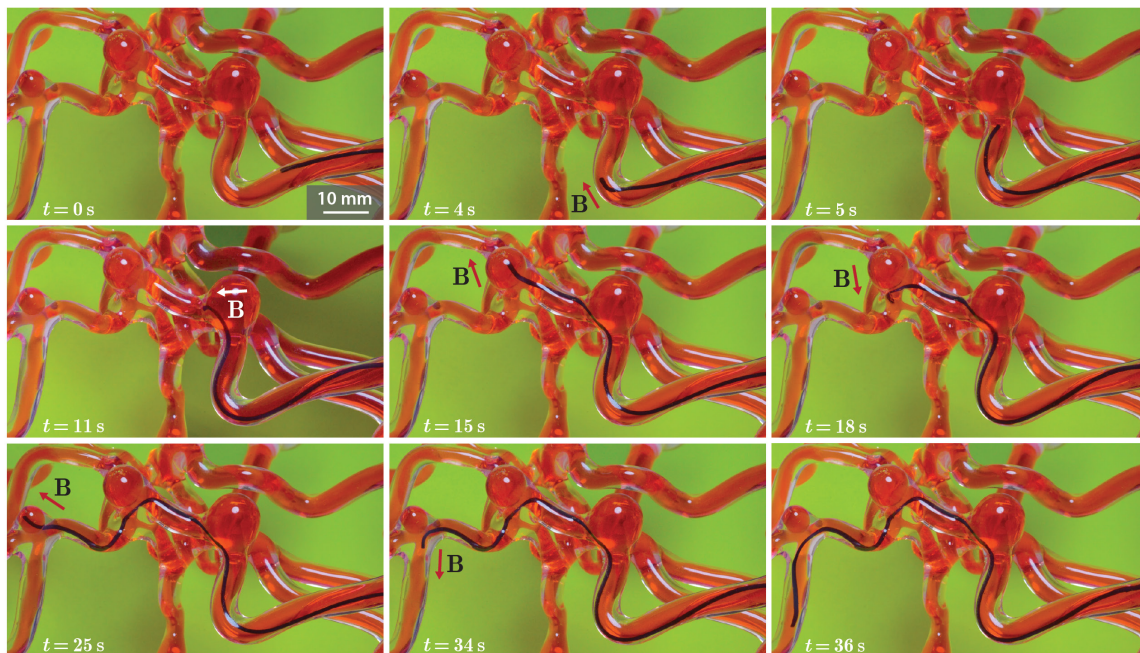
Figure 3-12: Demonstration of navigation in a neurovascular phantom. The soft continuum robot first passed through the sharp corner with acute angulation ($t = 5$ s). The robot made another sharp turn after reaching the first aneurysm ($t = 11$ s) based on the magnetic steering capability to reach the second aneurysm ($t = 15$ s). Then, it made another sharp turn at the acute-angled corner beneath the second aneurysm ($t = 18$ s) to reach the third aneurysm ($t = 25$ s) and navigated further downstream ($t = 36$ s).

As shown in **Figure 3-12**, the demonstrated prototype was able to smoothly navigate through the targeted path while completing all the required tasks without any noticeable difficulties or unintended motion. The importance and the effectiveness of the self-lubricating hydrogel skin became evident when comparing the navigating performance of the prototypes with and without hydrogel skin. The uncoated prototype suffered heavily from the substantial friction acting on the robot while going through the first acute-angled corner, exhibiting unwanted jerky movement. Despite the omnidirectional steering capability that enabled the robot to orient its distal tip toward the desired direction, the significant friction did not allow the robot's body to proceed. Upon further pushing, followed by another jerk, the uncoated prototype would collide with the inner wall of the first and second aneurysms and eventually failed to further proceed through the third acute and narrow corner.

3.4.4 Magnetically Steerable Laser Delivery

Further extending the demonstrated capabilities of the proposed concept of magnetic soft continuum robots, we demonstrate additional functionalities enabled by a functional core incorporated in the robot's body made of soft polymers. As an illustrative example with relevance to potential medical applications, we incorporated an optical fiber in the robot's body to demonstrate the concept of magnetically steerable laser delivery (**Figure 3-13A**). **Figure 3-13B** shows the experimental settings for the demonstration and the fabricated prototype, whose outer diameter (denoted D in **Figure 3-13A**) was designed to be 500 μm. The incorporated optical fiber with the outer diameter (denoted d in **Figure 3-13A**) of 245 μm consists of a silica core, cladding, and protective acrylate coating. The given task was to accurately point at the small targets (2-mm dots) with the laser beam in a desired order based on the magnetic actuation (**Figure 3-13C**), and the omnidirectional steering and flexible motion allowed the soft continuum robot to successfully carry out the desired task.

One possible example of potential medical applications of this demonstrated capability may be laser-assisted atherectomy [107] for treating vascular stenosis (or atherosclerosis; narrowing of an artery due to plaque buildup on the inner walls, as
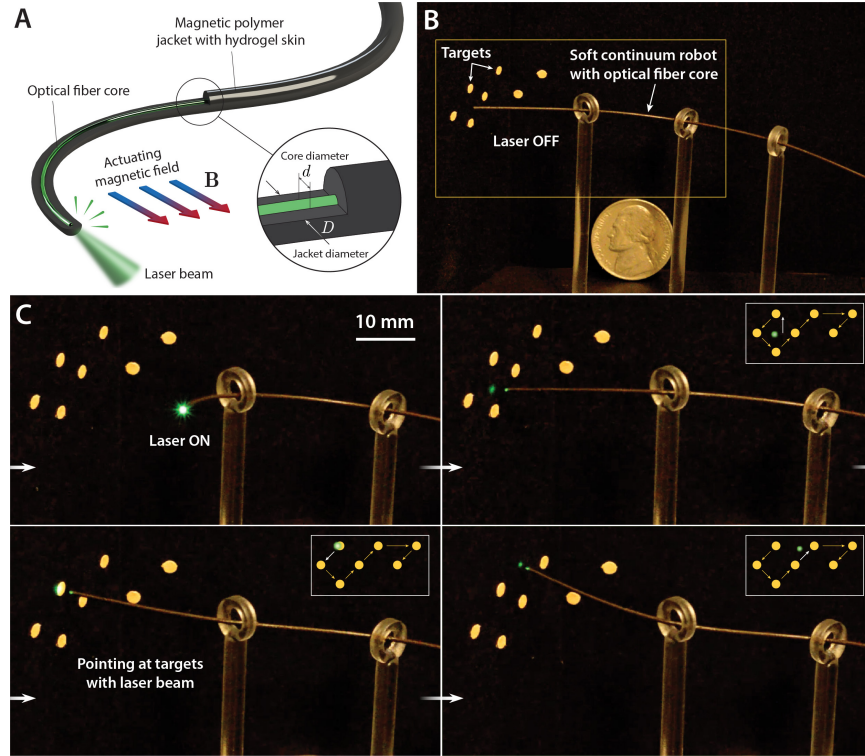
Figure 3-13: Demonstration of magnetically steerable laser delivery. (**A**) Illustration of a magnetic soft continuum robot with an optical fiber, as a functional core incorporated in the robot's body, through which the laser can be delivered. (**B**) Experimental setup for demonstrating magnetically controlled laser delivery. (**C**) Close view of the laser-emitting tip that accurately points at the small targets (2-mm dots) with the laser beam in a prescribed order based on omnidirectional magnetic steering. The magnetic fields for manipulation (20 to 80 mT) were generated by a cylindrical (diameter and height of 50 mm) permanent magnet at a distance (40 to 80 mm). The outer diameter of the demonstrated prototype was 500 μm.

illustrated in **Figure 1-1A**). This commonly occurs in the carotid artery, through which blood is supplied to the brain from the heart. As an illustrative example within this context, we demonstrated this concept using our steerable laser probe in the carotid artery section of the vascular phantom, as shown in **Figure 3-14**. In the demonstration, the continuum robot first reached the targeted site in the carotid artery and then emitted a green laser beam near the inner wall. It then changed the direction and the position of the laser-emitting tip using magnetic steering (**Figure 3-14A**). After that, it turned off the laser and navigated downstream through the carotid artery (**Figure 3-14B**). The same prototype in **Figure 3-13** with an outer diameter of 500 mm was used for this demonstration.
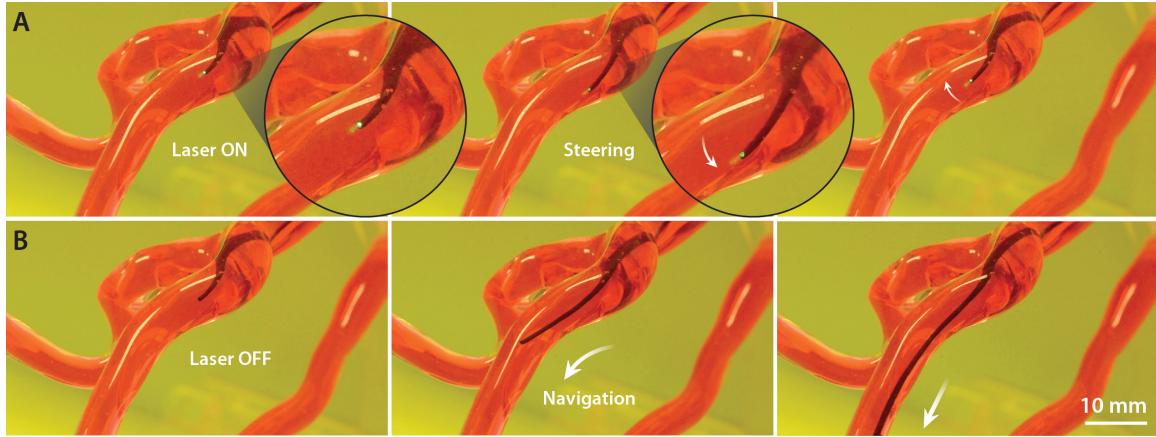
Figure 3-14: Demonstration of steerable laser delivery in the phantom carotid artery. The magnetic soft continuum robot (**A**) emitting a laser beam at different targeted sites in a phantom internal carotid artery based on magnetic steering and (**B**) navigating downstream after turning off the laser. The magnetic fields for manipulation (20 to 50 mT) were generated by a cylindrical (diameter and height of 50 mm) permanent magnet at a distance (50 to 80 mm). The proximal end was pushed to advance the robot during the navigation. The outer diameter of the demonstrated prototype was 500 μm.

However, the incorporation of an optical fiber, if not properly designed, can greatly increase the bending stiffness and may therefore limit the bending angle under given applied magnetic fields. The proof-of-concept prototype demonstrated above contained an unmodified optical fiber with a relatively thick protective acrylate coating. To reduce or eliminate the unnecessary portion of increased bending rigidity, this protective layer may be replaced with the magnetic soft polymer jacket for further development. Once such design optimization is performed, the demonstrated capability to keep the laser-emitting tip in position based on magnetic steering may help in preventing unwanted motion or displacement of the tip from the desired location during the laser ablation, thereby improving the accuracy and the safety, which are of paramount importance throughout the whole procedure. There can be more possible applications. For instance, when the magnetic soft continuum robot is equipped with a miniature complementary metal-oxide semiconductor (CMOS) sensor, while having multiple functional cores for both illumination and imaging, it may serve as a submillimeter-scale angioscope [107] that can help to better diagnose embolism (i.e., occlusion by a blood clot in **Figure 1-1A**) in the distal neurovasculature, which is far less accessible than other body parts due to the considerably smaller size.

3.5 Summary

In this chapter, we introduced a class of submillimeter-scale soft continuum robots that can be controlled magnetically. As discussed in **Section 3.1**, the soft continuum design based on hard-magnetic soft composite materials enabled facile miniaturization of the robot diameter down to submillimeter scales while providing omnidirectional steering capabilities upon magnetic actuation owing to the programmed magnetic polarities in the robot's body. In **Section 3.2**, with a simple yet effective theoretical framework, which was on the basis of the models developed in **Chapter 2**, we established a design strategy to optimize the actuation performance of the proposed magnetic soft continuum robot. In **Section 3.3**, we discussed the materials and fabrication methods to realize our submillimeter-scale magnetic soft continuum robot with practical considerations for its intravascular applications in terms of minimizing friction and corrosion prevention. The hydrogel skin grown onto the robot's surface substantially reduced the friction and hence enabled navigation through complex and constrained environments such as tortuous and narrow phantom vasculature, as clearly demonstrated in **Section 3.4**. Combined with these steering and navigating capabilities, additional functionalities such as steerable laser delivery were also demonstrated through the incorporation of an optical fiber as a functional core into the robot's body. Demonstrating these capabilities in realistic, clinically relevant environments in vitro, we illustrated the applicability of the proposed magnetic soft continuum robots for potential medical applications.

Chapter 4

Telerobotic Magnetic Neurointerventional Platform

4.1 Background on Magnetic Actuation Platforms

Manipulation of magnetic soft continuum robots can be achieved through the spatiotemporal control of the actuating magnetic field. Magnetic actuation and manipulation platforms can be categorized into different groups depending on the type of magnetic sources (permanent magnet or electromagnets) and their configuration (single, paired, or multiaxial), the characteristics of the actuating fields (spatially uniform or nonuniform, static or time-varying), and the mobility of the magnetic source (moving or stationary). In the following sections, we discuss some of the common types of magnetic actuation platforms that have been proposed for manipulation and control of magnetic objects in space for different applications.

4.1.1 Platforms based on Permanent Magnets

One of the advantages of using a permanent magnet comes from the fact that it can give rise by itself to a static and relatively strong magnetic field in outer space. Contrary to electromagnets with current-carrying coils, which are subject to heat loss, permanent magnets do not experience heat loss and hence are generally more energy-efficient than electromagnets in generating magnetic fields of the same strength. Typ-

ical electromagnets are based on stacking multiple coils around a highly permeable soft-magnetic core to concentrate the magnetic flux. Even in the presence of a core, however, the field of a permanent magnet can in general exceed that of an electromagnet of the same size by up to an order of magnitude [108].

With a single permanent magnet, magnetic manipulation can be achieved through spatial positioning of the actuating magnet while changing the position and orientation of the magnet relative to the object being manipulated. It is not uncommon to see a hand-held magnet being used to manipulate small magnetic objects in the literature, usually for validation of the proposed concepts or devices, for different applications such as capsule endoscopy [109, 110, 111, 112, 113], therapeutic delivery [51, 114, 115], endovascular navigation [3], and other general soft robotic applications [1, 116]. For more precise and reliable manipulation, a serial robot arm manipulator with multiple degrees of freedom (DOFs) can be used to carry the actuating magnet and place it around the object being manipulated (**Figure 4-1A**). While in early days heavy and bulky industrial robot manipulators were employed [117, 118, 119, 120, 121], recently more compact and lightweight robot arms have been used for magnetic manipulation in medical applications [122, 123].

A single permanent magnet, however, produces spatially nonuniform magnetic fields, and the presence of field gradients gives rise to the magnetic force as well as the magnetic torque acting on the object being manipulated (**Figure 4-1B**). The coupled interaction of magnetic force and torque, along with the complex geometry of the magnetic fields that depends on the shape of the magnet, make it nontrivial or rather difficult to precisely manipulate magnetic objects in many cases. One way to mitigate the geometrical complexity is to make the field symmetric by choosing an actuating magnet of simple symmetrical shape (e.g., cylindrical or spherical) with its remanent magnetization along the axis of symmetry. Then, the rotation of the magnet around its symmetry axis causes no change in the actuating magnetic field, which effectively reduces the DOFs involved in the manipulation of the magnet to five (three translations and two rotations). The reduction of the effective DOFs due to the symmetry of the actuating magnet is conceptually equivalent to having kinematic

redundancy when using a serial robot arm to spatially manipulate the magnet.
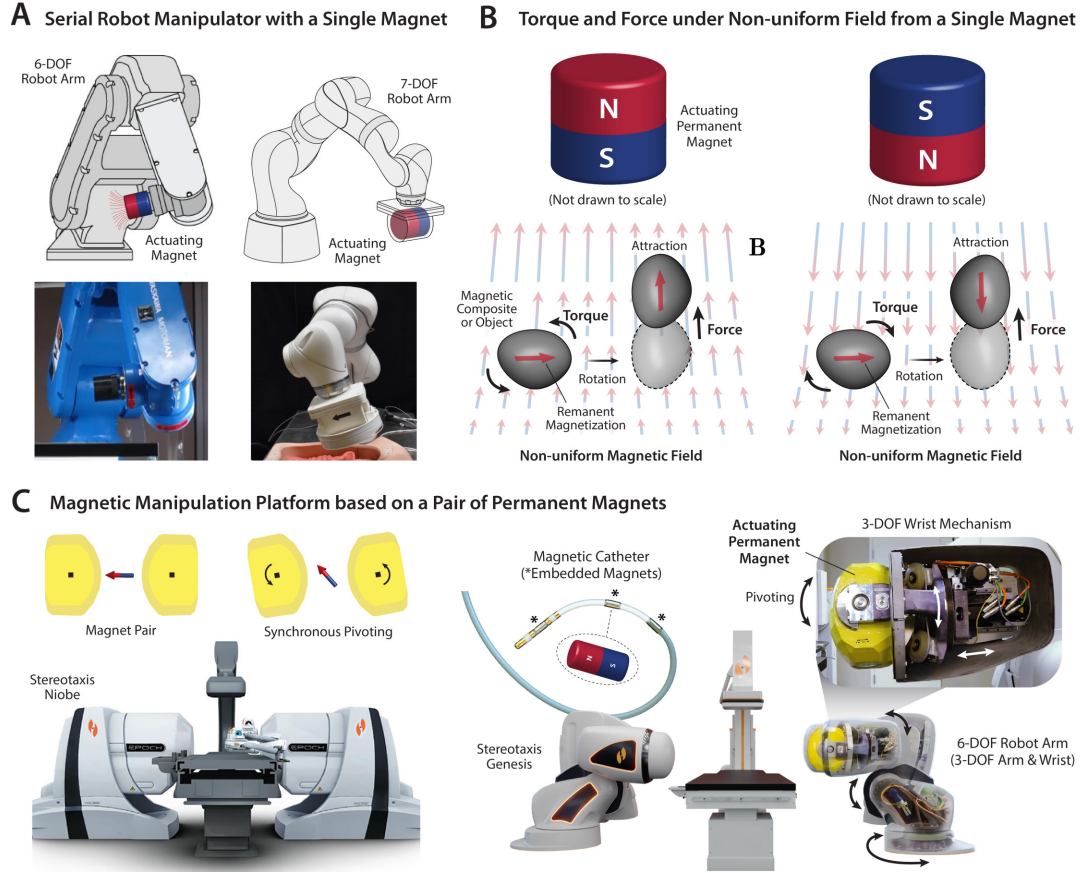
Figure 4-1: Magnetic actuation and manipulation platforms based on permanent magnets. (**A**) Multi-DOF serial robot manipulators with a single actuating magnet attached at the end for steering untethered or tethered magnetic devices. (**B**) Magnetic torque and force on a hard-magnetic object in spatially nonuniform fields from a single actuating magnet. (**C**) Stereotaxis Niobe® and Genesis® platforms based on a pair of large permanent magnets for steering magnetic catheters by changing the applied field direction through synchronous pivoting of the actuating magnets.

For purely torque-based actuation and manipulation, spatially uniform magnetic fields can be created when two permanent magnets are configured in such a way that their opposite poles face each other. Commercially available magnetic actuation platforms based on spatially uniform fields include the Niobe® and Genesis® systems of Stereotaxis Inc., which use a pair of large permanent magnets (**Figure 4-1C**). These systems have been used mostly for cardiac electrophysiology to treat heart arrhythmia using magnetic ablation catheters with a few rigid magnets incorporated in the distal portion for steering purposes [124, 125]. By synchronously rotating

the two actuating magnets, each around its pivot inside the casing, these magnetic actuation platforms can create relatively uniform magnetic fields of 80-100 mT in any direction in the workspace between the magnets and hence enable force-free, intuitive steering control of the magnetic catheters [17, 125, 126, 127, 128].

4.1.2 Platforms based on Electromagnets

While current-carrying coils are generally less energy-efficient in producing magnetic fields than permanent magnets, magnetic actuation platforms based on electromagnets offer several benefits that make them preferable to permanent magnets in many practical applications. Electromagnets provide a larger design space, with a variety of possible configurations of multiaxial coils, and a larger control space as well due to the ability to quickly turn on and off each coil or reverse the magnetic polarities of the individual coils to create complex (rotating or oscillating) fields without the need to move the set of coils physically. Furthermore, magnetic actuation platforms based on electromagnets can be designed to provide the capability to control both the magnetic force and torque either independently or simultaneously [58, 129, 130], to enable more flexible and sophisticated manipulation of magnetic objects within the workspace. To date, numerous types of magnetic actuation and manipulation systems based on electromagnets have been developed, which vary in the shape, number, and configuration of the current-carrying coils. According to the classification used by Abbott *et al.* [129], magnetic actuation and manipulation platforms based on electromagnets can be categorized into magnetically orthogonal or nonorthogonal systems.

Magnetically orthogonal systems: Magnetically orthogonal systems utilize special types of electromagnets, based on either circular or saddle coils arranged in pairs, which are designed to produce spatially uniform fields or constant field gradients in the workspace. When two identical circular coils are separated coaxially by a distance equal to their radius r and carry equal currents in the same direction, the field produced between the two coils in the axial direction (z-axis) is nearly uniform (**Figure 4-2A**). This is known as the Helmholtz coil configuration, and a pair of coils in such

an arrangement is commonly called a Helmholtz coil-pair [131]. The magnitude of the uniform field is proportional to the current strength i and inversely proportional to the radius (i.e., $B_z \sim i/r$), and a Helmholtz coil-pair can be used to apply a uniform torque on a magnetic object in the workspace. When the two circular coils are separated further by a distance $\sqrt{3}r$ and carry equal currents in the opposite direction (**Figure 4-2B**), the pair of coils can generate a nearly constant field gradient in the axial direction ($\partial B_z/\partial z$), the magnitude of which is proportional to the current i and inversely proportional to the square of the radius (i.e., $\partial B_z/\partial z \sim i/r^2$). Such an arrangement is called the Maxwell coil configuration [132], which can be used to apply a uniform force on a magnetic object in the workspace. These circular coil-pairs are easy to construct and offer good accessibility to the workspace of cylindrical shape.
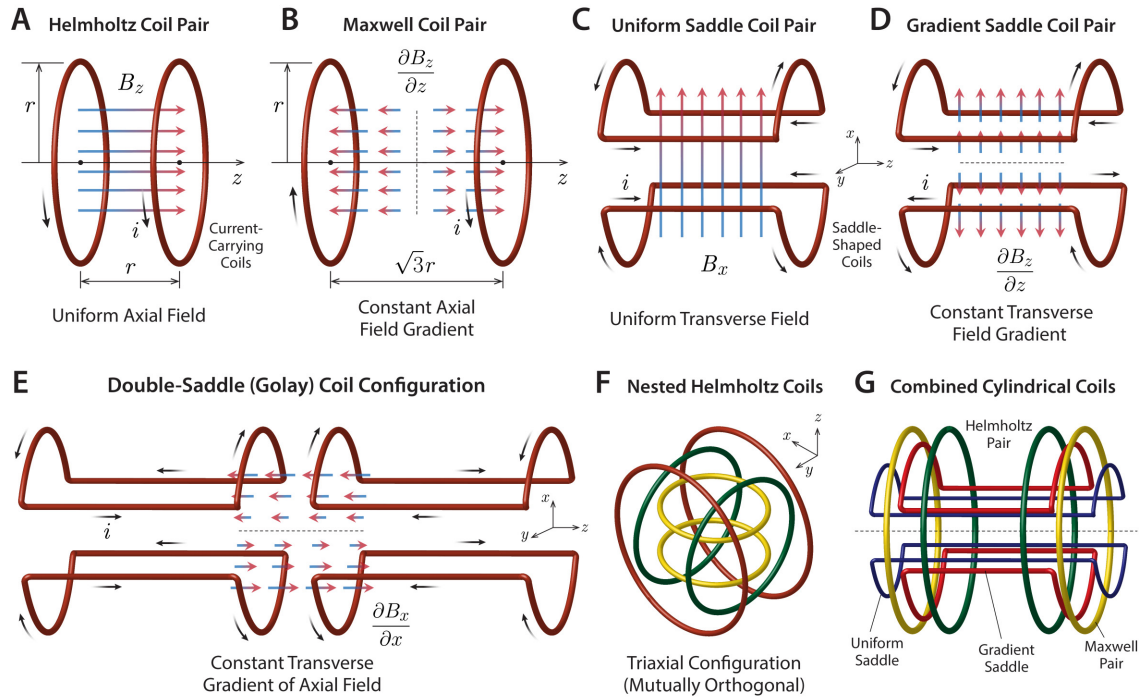
Figure 4-2: Magnetically orthogonal actuation platforms. (**A**) Helmholtz and (**B**) Maxwell coil pairs for creating a uniform axial field (Helmholtz) or field gradient (Maxwell). Saddle-shaped coil pair for creating (**C**) a uniform transverse field or (**D**) a constant transverse field gradient depending on the direction of currents. (**E**) Golay coil configuration based on two saddle coil pairs for creating a constant transverse gradient of the axial magnetic field. (**F**) Nested Helmholtz coils in mutually orthogonal triaxial configuration for creating uniform actuating fields in three different directions. (**G**) Combination of different coil-pair types for multi-DOF magnetic manipulation based on magnetic torques and forces in a cylindrical workspace.

Magnetically nonorthogonal systems: Another class of magnetic actuation and manipulation platforms, termed the magnetically nonorthogonal system [129], utilizes multiple columnar coils with soft-magnetic cores that are arranged around the workspace such that they all point to the center of the workspace. The fields generated by individual electromagnets are superimposed to create desired fields and field gradients for manipulation, and hence all electromagnets are active in general. Various designs of actuation platforms based on eight electromagnets (**Figure 4-3A**) have been developed [95, 133, 134, 135, 136, 137, 138], which have different characteristics and performances in terms of torque- and force-generation capabilities and the accessibility of the workspace surrounded by the electromagnets [129, 139].
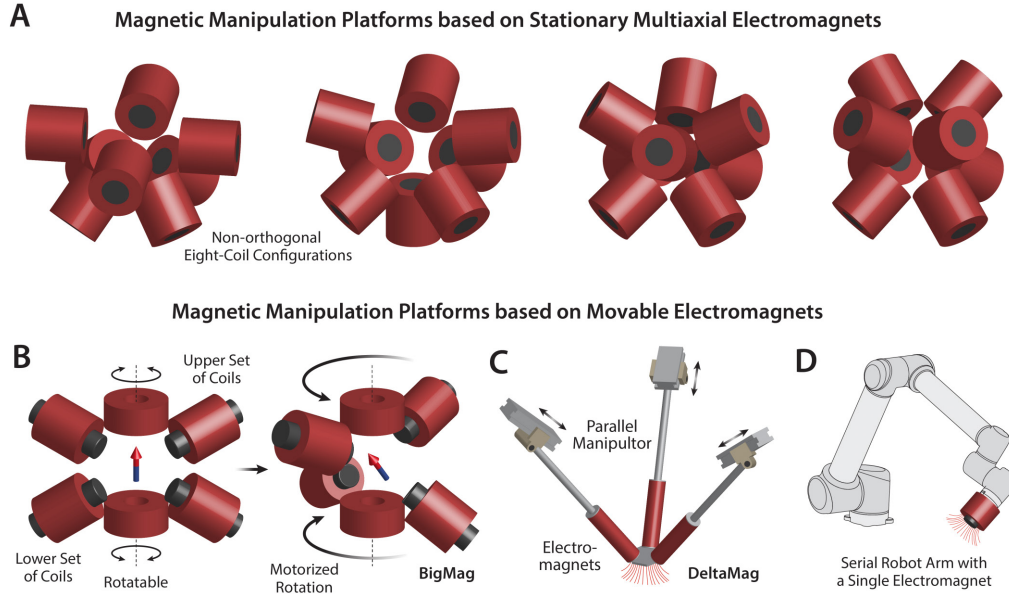
Figure 4-3: Magnetically nonorthogonal actuation platforms. (**A**) Representative examples of magnetic actuation and manipulation platforms based on stationary multiaxial electromagnets in nonorthogonal eight-coil configurations [129, 139]. Magnetic manipulation platforms based on movable electromagnets: (**B**) motorized actuation of rotatable electromagnets [140, 141] and (**C**) a parallel [142, 143] or (**D**) a serial [144, 145, 146, 147] robot manipulator for controlling the position and orientation of the actuating electromagnet.

The number of coils can be increased for systems based on stationary electromagnets to have manipulation redundancy [129, 148] or to enable spatially selective magnetic actuation [149, 150]. The number of coils can be reduced as well by adding motorized actuators [140, 141] (**Figure 4-3D**) or a parallel robot manipulator

[142, 143] (**Figure 4-3E**) to rotate or move the electromagnets, which helps to increase the available workspace by reducing the number of electromagnets. A 6-DOF serial robot arm with a single electromagnet at its end-effector (**Figure 4-3F**) has also been proposed and demonstrated as a magnetic manipulation platform for steering tethered magnetic devices such as a magnet-tipped catheter [144, 145, 146, 147]. Instead of employing a multi-DOF serial robot arm to change the position and orientation of a single electromagnet, a simple passive arm has been used to carry and hold a cube-shaped electromagnet consisting of three nested mutually orthogonal coils, also known as Omnimagnet [151, 152], to control a magnetically steerable cochlear implant [153]. When compared with the platforms based on multiple stationary electromagnets (**Figure 4-3**, **A** to **C**), these mobile electromagnetic actuation platforms can provide a larger workspace for more flexible operation with increased compatibility with external imaging or sensing devices.

4.1.3 Limitations of Existing Platforms

There are some magnetic actuation platforms that have been commercialized for clinical use at human-body scale. Commercially available platforms based on a pair of permanent magnets include the Stereotaxis Niobe® (**Figure 4-1A**) and Genesis®, and platforms based on electromagnets include the Magnetecs CGCI (Catheter Guidance Control and Imaging; **Figure 4-4B**) [124, 135, 154] and the Aeon Phocus [133, 137] systems (**Figure 4-4C**), which are based on eight stationary electromagnets. The electromagnetic actuation platforms are capable of independently controlling both the field and field gradient at any location in the workspace [58, 110]. These commercially available systems have been used mostly exclusively for cardiac electrophysiology to treat arrhythmia using magnetically controlled ablation catheters.

While these commercialized systems could be used to control our magnetic soft continuum robots or guidewires as shown in **Figure 4-4**, **D** and **E**, and given the previously reported results based on magnet-tipped guidewires [17, 127, 128, 126], such heavy and bulky, hence immobile, platforms may not be ideal for endovascular neurosurgery, especially in the context of telerobotic stroke intervention. Furthermore, the

99

available angulation for the monoplane C-arm is limited for those existing systems due to the confined space between the permanent or elecgtromagnets (**Figure 4-4, A** to **C**). For example, the Niobe$^{\circledR}$ system allows the C-arm rotation of only 28° in left or right anterior oblique projection [17], as can be seen in **Figure 4-4F**.

For complex neuroendovascular procedures, biplane fluoroscopy based on a pair of C-arms for simultaneous projections from two different angles is preferred as it helps to better identify complex angulations of the intracranial vessels. While monoplane fluoroscopy can be used for stroke interventions [155, 156, 157], biplane imaging in general could provide better state observation of the guidewire in more complex vascular anatomies and hence potentially improve the operator's confidence, thereby leading to reduced intraoperative risk [155, 156]. However, those commercial platforms in **Figure 4-4, A** to **C**, are by no means compatible with the standard biplane angiography suite (**Figure 1-2B**) due to the large mechanical footprint of their bulky magnet/coil setups. These limitations necessitate a more compact, light-weight, and mobile platform for image-guided neurovascular intervention.
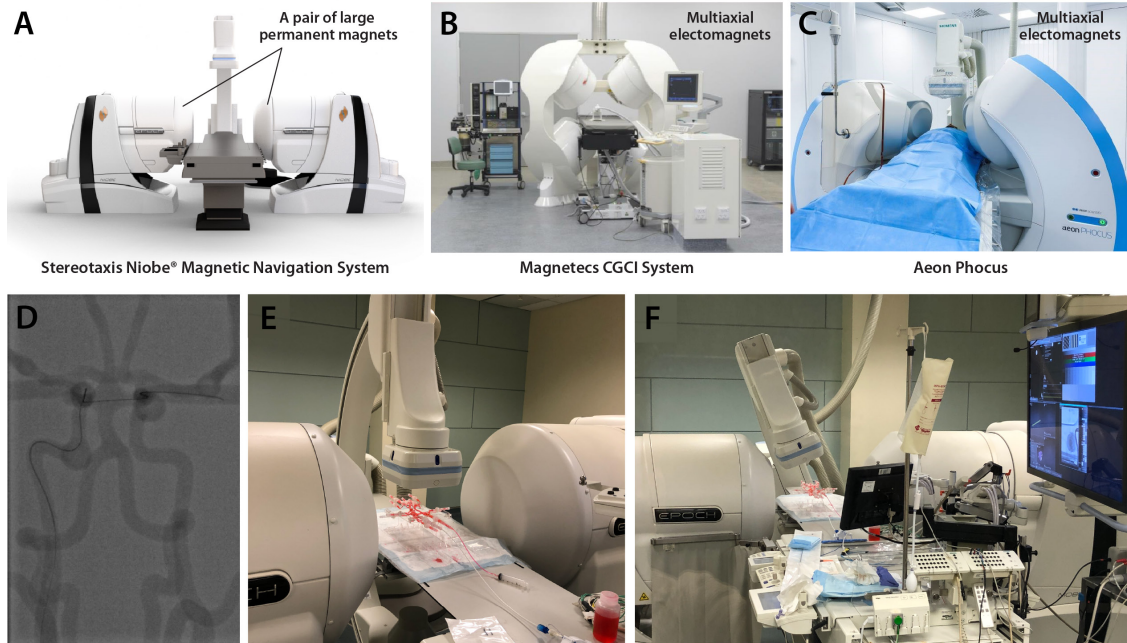

Figure 4-4: Stereotaxis Niobe$^{\circledR}$ system tested for manipulating the magnetic soft continuum guidewire. (**A-B**) X-ray fluoroscopic images of the magnetic soft continuum guidewire in the silicone phantom under anteroposterior projection of the C-arm. (**C**) Limited angulation of the C-arm due to the confined space between the actuating magnets.

4.2 Telerobotic Neurointerventional Platform

4.2.1 System Design Overview

Figure 4-5 provides an overview of our telerobotic neurointerventional system deployed in clinical settings for image-guided endovascular procedures, with a C-arm fluoroscope providing real-time imaging of the magnetic soft continuum robot (or simply 'magnetic guidewire') navigating in the patient's blood vessels under magnetic manipulation. Mounted on a mobile platform beside the operating table, the robot arm is teleoperated by an operator (i.e., the neurointerventionalist) from a remote-control console to steer the magnetic guidewire by varying the position and orientation of the magnet at the robot arm's end-effector around the patient's head. The guidewire/microcatheter advancing unit is placed near the patient to advance or retract the guidewire and the microcatheter from their proximal ends through the femoral or radial artery access point.
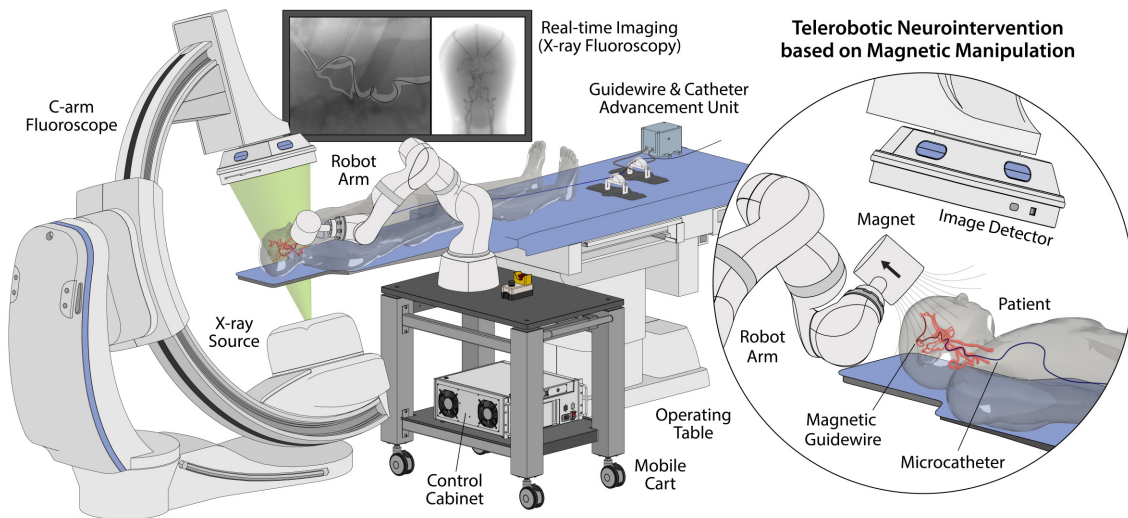
Figure 4-5: Overview of the telerobotic neurointerventional platform based on magnetic manipulation. The system features a light-weight, compact robot arm with an actuating magnet attached to its end-effector to remotely control a magnetically steerable soft continuum robot (or simply magnetic guidewire) through spatial positioning of the magnet around the patient's head. Mounted on a mobile platform beside the operating table, the robot arm is teleoperated from a remote-control console to steer the magnetic guidewire under real-time fluoroscopic imaging. The system further integrates a guidewire/microcatheter advancing unit based on a pair of motorized linear drives that can advance or retract the guidewire and a microcatheter upon remote control.

The magnetic guidewire has a steerable distal portion, which can be manipulated through spatial positioning of the actuating magnet at the robot arm's end-effector relative to the steerable tip (**Figure 4-6A**). While spatial positioning of the magnet requires at most six degrees of freedom (DOFs), our system uses a 7-DOF serial robot arm manipulator with seven revolute joints (**Figure 4-6A**) to take advantage of its kinematic redundancy for safer operation in cluttered environments with a confined workspace. The extra DOF provides an increased level of dexterity that helps the robot arm avoid singularities and joint limits [158] as well as workspace obstacles (i.e., the patient, C-arm, operating table, radiation shields). The guidewire and the microcatheter can be advanced or retracted individually by a pair of advancing units, each of which uses a worm drive to convert the rotary motion transmitted from the DC motor at the base through a flexible shaft to a linear motion (**Figure 4-6A**).

The whole system is teleoperated from the remote-control console under visual feedback from real-time fluoroscopic imaging of the magnetic guidewire in the blood vessels (**Figure 4-6B**). Containing the magnetic particles that are radiopaque, the magnetic guidewire is naturally visible under x-ray as shown earlier in **Figure 4-4D**. The configuration of the robot arm is visualized in real time on the control workstation based on the joint position data (**Figure 4-6B**). This real-time visualization helps the operator observe the current state of the robot arm while controlling it remotely. It can also be used for preprocedural planning and/or training of the robot manipulation in a virtual environment replicating the real world, including the surrounding objects that are known a priori (i.e., 3D CAD models), to help prevent collisions during operation while performing magnetic steering and navigation. Spatial positioning of the actuating magnet can be achieved via 6-DOF position control of the robot arm's end-effector with a joystick controller, and advancement or retraction of the guidewire and the microcatheter can be controlled either independently or simultaneously with the joystick buttons (**Figure 4-6C**). The operator could observe and confirm the current states of the guidewire and the microcatheter from the fluoroscopic images while operating the robot arm and the guidewire/catheter advancing units with the joystick controller from the remote-control console (**Figure 4-6B**).
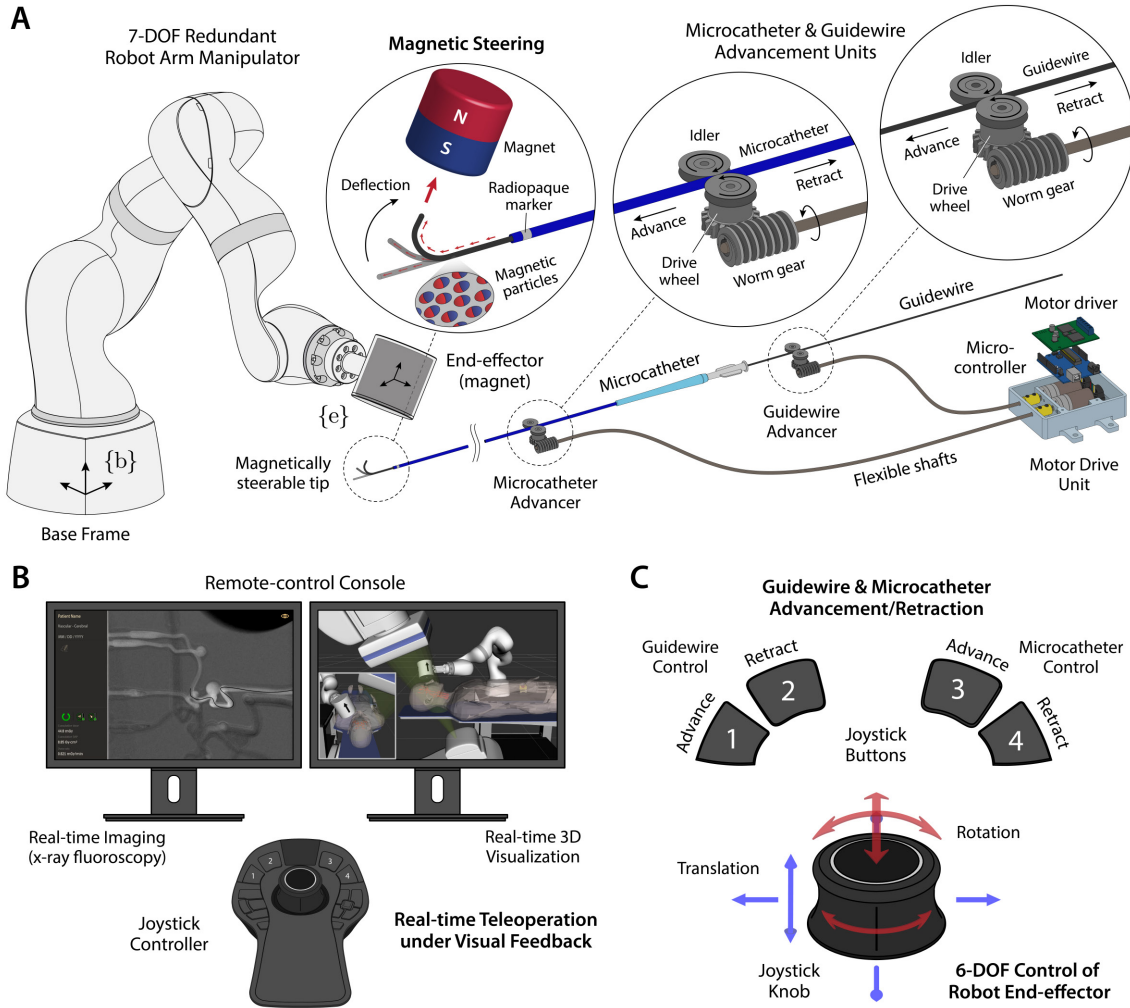
Figure 4-6: Description of the telerobotic neurointerventional system. (**A**) The robot arm has 7 degrees of freedom (DOF) with kinematic redundancy for flexible manipulation and safer operation in cluttered environments. The magnetic soft continuum guidewire has a magnetically responsive tip that contains magnetic particles, and hence can be steered by the actuating magnet at the robot arm's end-effector. The guidewire is compatible with a standard microcatheter which travels over the guidewire along the navigated path. The guidewire and the microcatheter can be advanced or retracted by a pair of advancing units, each of which uses a worm drive to convert the rotary motion of the DC motor at the base to a linear motion. (**B**) The system is teleoperated from the remote-control console under feed-back from real-time imaging of the guidewire/microcatheter in the blood vessels and virtual visualization of the robot arm. The magnetic guidewire is naturally visible under x-ray due to the embedded magnetic particles, and the position of the microcatheter can be identified by the radiopaque marker at the distal end. The robot arm is visualized in a virtual environment that replicates the real world on the control workstation to allow the operator to avoid collisions with surrounding objects while teleoperating the robot arm. (**C**) Spatial positioning of the magnet is achieved via 6-DOF position control of the robot arm's end-effector with a joystick controller, and advancement or retraction of the guidewire and the microcatheter can be controlled either independently or simultaneously with the joystick buttons.

4.2.2　Ream-time Teleoperation Interface

Our teleoperation interface enables spatial positioning of the actuating magnet at the end of the robot arm through real-time position control of the robot arm's end-effector using a joystick controller with a 6-DOF knob. With this 6-DOF joystick knob, the operator can intuitively move and tilt the actuating magnet to change its position and orientation relative to the magnetic guidewire for steering purposes, as illustrated in **Figure 4-7A**.

We describe the configuration of the robot arm using a joint-space vector $\mathbf{q} \in \mathbb{R}^7$ which represents the joint angles of the 7 revolute axes. The position and orientation of the end-effector frame ({e} in **Figure 4-6A**) relative to the robot arm's base frame ({b} in **Figure 4-6A**) are defined by a task-space vector $\mathbf{x} \in \mathbb{R}^6$ with its first three components representing the position and the last three components representing the orientation. The differential kinematics, or the relation between the small change in the joint positions $\delta\mathbf{q}$ and the corresponding change in the end-effector pose $\delta\mathbf{x}$, can then be written as

$$\delta\mathbf{x} = \frac{\partial \mathbf{f}(\mathbf{q})}{\partial \mathbf{q}} = \mathbf{J}(\mathbf{q})\delta\mathbf{q}, \tag{4.1}$$

where $\mathbf{J}(\mathbf{q}) \in \mathbb{R}^{6\times7}$ is the Jacobian, or the partial derivatives of the forward kinematics defined by a mapping $\mathbf{x} = \mathbf{f}(\mathbf{q})$ with $\mathbf{f}$ denoting a nonlinear vector function. Upon the operator's joystick manipulation, 6-DOF motion commands are produced as a combined set of incremental motions (translations and rotations) in each DOF, which are scaled and converted into the end-effector's linear and angular motions in the task-space coordinates. The motion commands for the end-effector $\delta\mathbf{x}$ are then transformed into the joint commands $\delta\mathbf{q}$ by multiplying the pseudo-inverse of the Jacobian $\mathbf{J}^\dagger(\mathbf{q})$:

$$\delta\mathbf{q} = \mathbf{J}^\dagger(\mathbf{q})\delta\mathbf{x} = \mathbf{J}^\mathsf{T}(\mathbf{q})\big(\mathbf{J}(\mathbf{q})\mathbf{J}^\mathsf{T}(\mathbf{q})\big)^{-1}\delta\mathbf{x}, \tag{4.2}$$

which returns the minimum-norm solution for redundant manipulators like the one used in the present work by minimizing the two-norm $\|\delta\mathbf{q}\| = \sqrt{\delta\mathbf{q}^\mathsf{T}\delta\mathbf{q}}$ [159]. The joint commands are added to the current joint positions to get new joint position values, which are sent to the robot arm controller (i.e., control cabinet in **Figure 4-5**) to execute the motion that achieves the desired configuration of the robot arm.
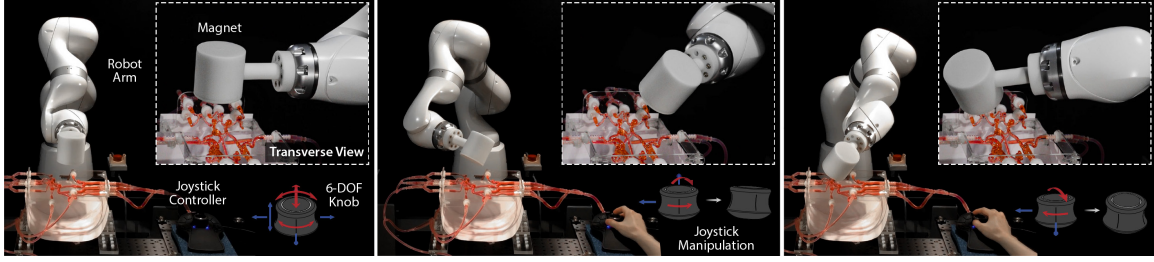
Figure 4-7: Spatial positioning of the actuating magnet through real-time joystick teleoperation. 6-DOF control of the robot end-effector's position and orientation through joystick manipulation for spatial positioning of the actuating magnet around a life-sized neurovascular phantom.

4.2.3   Additional Operational Modes

Impedance control for compliance: For typical teleoperation tasks, the robot arm is position-controlled with high stiffness, exhibiting little change in the end-effector pose or the joint positions against external force disturbance. The robot arm can also be impedance-controlled to have compliance for potentially safer operation in cluttered environments by modulating the stiffness values. The impedance control mode can be turned on/off by pressing designated joystick button to allow the operator to quickly switch from/to the default position control mode. By setting the stiffness values to zeros while maintaining some level of damping coefficients in the impedance control mode, the robot arm can be manually controlled and reconfigured to change the magnet's position and orientation more quickly and intuitively (i.e., hand-guiding mode) or the robot arm's con-figuration while maintaining the magnet's position and orientation through the internal motions (i.e., null-space motion).

Manual reconfiguration of the robot arm: Although the real-time joystick teleoperation interface enables intuitive control and manipulation of the magnet for steering and navigation (**Figure 4-7**), there may exist some occasions in which the operator or onsite staff wants to change the robot arm's configuration as well as the end-effector pose at the same time more swiftly and intuitively. For example, this may be desired when the staff is deploying the robot arm in preparation of interventional procedures and needs to bring the actuating magnet close to the anatomically relevant side of the patient's head. For such applications, we implemented a hand-guiding

functionality in our control interface to allow the operator to manually reconfigure the robot arm effortlessly upon demand, as demonstrated in **Figure 4-8A**.

Null-space motion using kinematic redundancy: There may be some other cases in which the robot arm needs to be reconfigured while maintaining the magnet position and orientation—for example, to ensure clearance for the C-arm's motion during repositioning, angulation, or rotation to perform angiography or adjust the angle of view for better state observation. We implemented another control mode for such applications to allow the operator to change the robot arm's configuration easily through the null-space motion, which is the arm's internal motion that results from the kinematic redundancy, as shown in **Figure 4-8B**. These additional modes can be turned on/off by pressing the designated joystick buttons to allow the operator to quickly switch from/to the default position control mode.
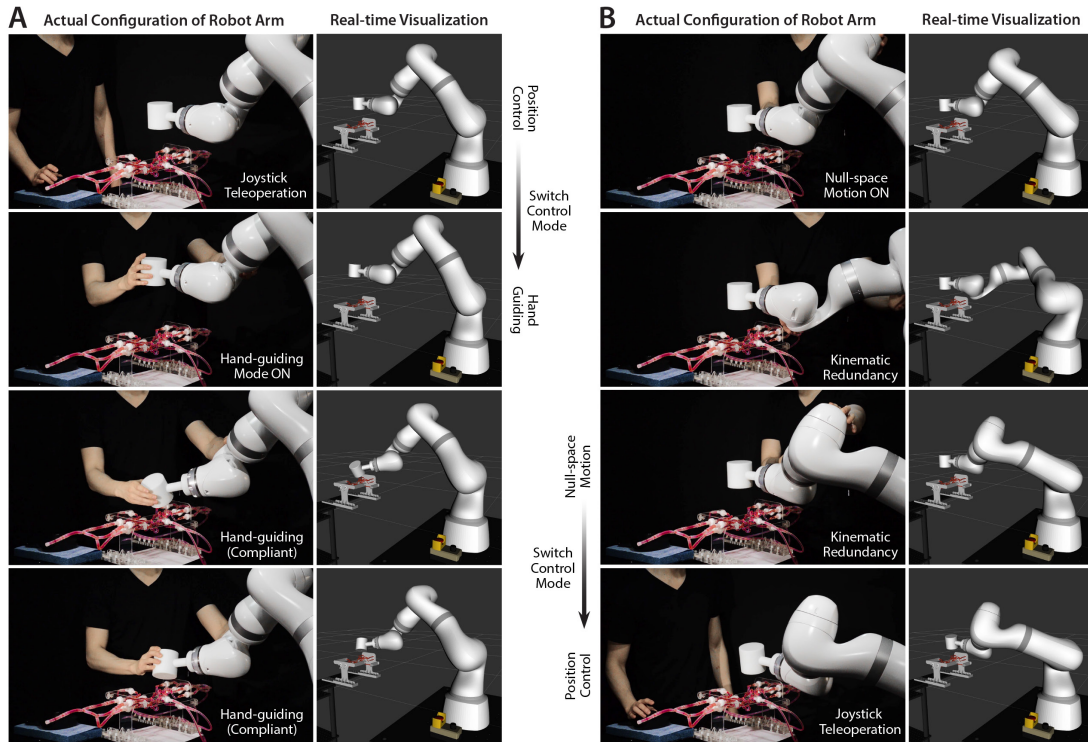
Figure 4-8: Additional operational modes for manual manipulation of the robot arm. (**A**) Hand-guiding mode to enable manual reconfiguration of the robot arm to change the end-effector pose more quickly and intuitively. (**B**) Null-space motion exploiting the kinematic redundancy and internal motions of the robot arm to enable intermittent manual reconfiguration of the robot arm while maintaining the magnet's position and orientation.

4.3 Magnetic Steering Control Principles

4.3.1 Magnetic Soft Continuum Guidewire

We designed our magnetic guidewire to have an outer diameter of 400 μm with greatly improved mechanical robustness, when compared with the proof-of-concept prototype demonstrated in **Figure 3-12**, in terms of both strength and toughness while maintaining good steerability. With these improvements, the newly designed magnetic guidewire is as thin and flexible as standard neurovascular guidewires (typically with outer diameters of 0.014 inches) and compatible with commercially available microcatheters for neurovascular interventions.

The magnetic guidewire consists of a tapered core of nickel-titanium alloy (nitinol), which is coated with a soft, yet durable polymer jacket composed of thermoplastic polyurethane (TPU) with embedded neodymium-iron-boron (NdFeB) particles. With the NdFeB particles in the polymer jacket magnetized along the guidewire's axial direction, the distal portion (50 mm from the end) of the guidewire is magnetically responsive and can be steered with an actuating magnet (**Figure 4-6A**), utilizing the magnetic torques and forces generated from the embedded magnetic dipoles under the applied fields and field gradients. The NdFeB particle loading concentration was determined to be 20% by volume according to the optimal design strategies described in **Section 3.2**. The resultant magnetic polymer jacket has the magnetization of 128 kA/m and the shear modulus of 1210 kPa (**Figure 4-9A**).

To enable sharp turns at acute-angled corners in blood vessels with clinically challenging tortuosity, a short segment (4-mm-long; denoted L_2 in **Figure 4-10A**) at the distal end of the guidewire's magnetically responsive portion is composed of the TPU + NdFeB composite only, without the stiff nitinol core, and is therefore much softer and more responsive than the remainder that contains the nitinol core. When magnetic fields are applied by the actuating magnet, the unconstrained portion (free from contact with blood vessels) of the guidewire's steerable tip of length L, which consists of a stiffer segment of length L_1 that contains the nitinol core and the softer segment of length L_2 that does not contain the stiff core, deflects either toward or away
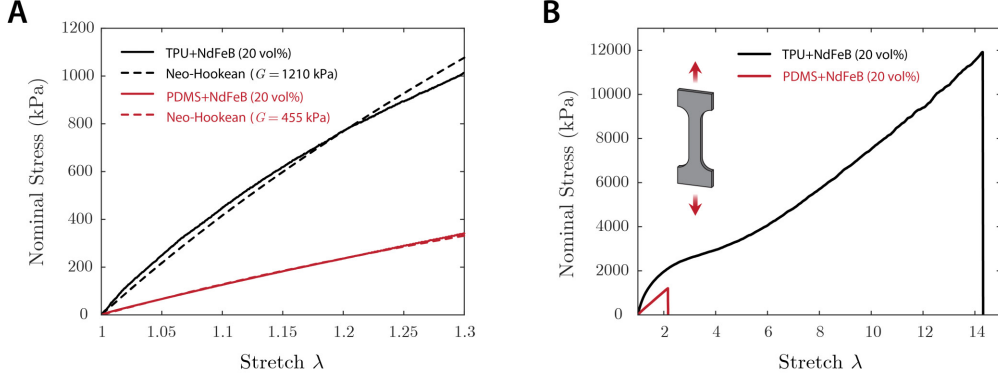
Figure 4-9: Mechanical characterization of magnetic polymer composites. Nominal tensile stress-stretch curve for the magnetic polymer composite based on TPU + NdFeB (20 vol%) plotted (**A**) over a range of small stretch ($\lambda < 1.3$) for measuring shear modulus and (**B**) up to the fracture point ($\lambda = 14.3$) for measuring tensile strength and stretchability. With the TPU-based composite, both the tensile strength and the stretchability have been greatly improved (by 10 and 7 times, respectively) when compared with the PDMS-based composite used for the prototype demonstrated in **Figure 3-12**. TPU: thermoplastic polyurethane; NdFeB: neodymium-iron-boron; PDMS: polydimethylsiloxane.

from the magnet depending on the magnetic polarity of the actuating magnet (**Figure 4-10A**). Tensile strength testing demonstrated that the TPU + NdFeB composite can withstand tensile stresses up to 12 MPa, which translates into 1.5 N of tensile forces on the distal tip of the guidewire, while being stretched beyond 14 times its original length (**Figure 4-9B**). The measured tensile strength of the distal tip is comparable to that of commercially available neurovascular guidewires of similar dimension such as ASAHI CHIKAI® 0.014-inch guidewires with a tensile strength of 2.45 N [160]. However, the high stretchability of the TPU + NdFeB composite could provide greater resistance in terms of the energy required to cause fracture or joint failure at the distal tip when compared with conventional guidewires which typically have flexible spring or coil tips that are subject to brittle fracture.

4.3.2   Magnetic Fields from the Actuating Magnet

For the actuating magnet, we consider an axially magnetized, NdFeB (N52-grade) magnet of cylindrical shape (diameter and thickness of $2R$; **Figure 4-10A**) with an axisymmetric field distribution (**Figure 4-11**). For cylindrical magnets with the same diameter-to-thickness ratio, the shape of the magnetic field remains the same when

normalized by the magnet's characteristic dimension (e.g., radius R). Therefore, the magnetic field at a certain point around the magnet can be expressed as a vector function of the spatial location of the point (denoted by a position vector $\mathbf{p}$ with respect to the magnet center in cylindrical coordinates) in a normalized form (by the magnet radius R) as

$$\mathbf{B}(\mathbf{p}) = B_{\text{re}}\,\boldsymbol{\mathcal{F}}(\mathbf{p}/R),\tag{4.3}$$

where B_{re} is the remanence of the magnet and $\boldsymbol{\mathcal{F}}$ denotes the vector function whose implicit form can be found in [161, 162, 163]. Along the magnet's central axis, the magnitude of the magnetic field can be expressed explicitly in a normalized form as

$$B = \frac{B_{\text{re}}}{2}\left(\frac{d/R+1}{\sqrt{(d/R+1)^2+1}} - \frac{d/R-1}{\sqrt{(d/R-1)^2+1}}\right),\tag{4.4}$$

where d is the distance from the center of the magnet to the point of interest or measurement along the centerline (i.e., $\pm z$-direction in **Figure 4-11**).
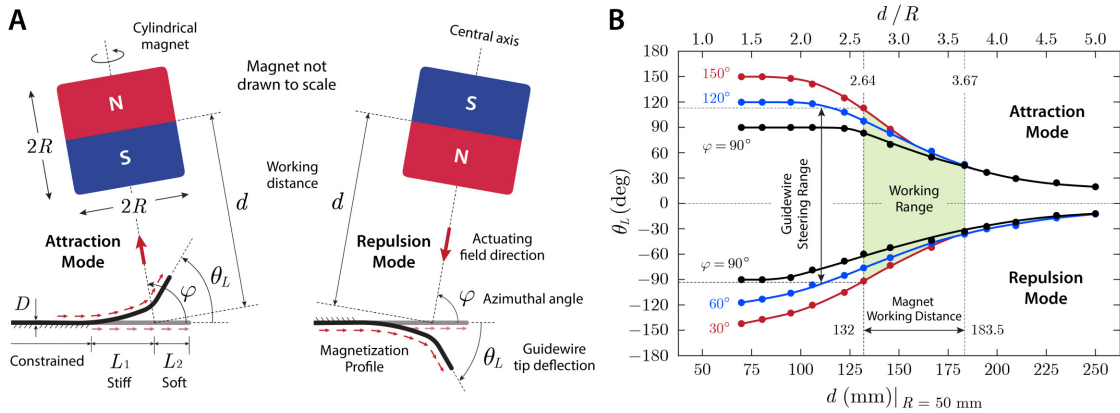
Figure 4-10: Principal modes of steering control with a single actuating magnet. (**A**) Attraction and repulsion modes for steering control of the magnetic guidewire with a single magnet of cylindrical shape (diameter and thickness of $2R$). The magnet working distance, denoted by d, is defined as the distance from the center of the magnet to the base of the guidewire's softer tip. The angular position of the magnet relative to the guidewire's reference state is defined by the azimuthal angle φ, and the tip deflection angle is denoted by θ_L. D indicates the outer diameter of the guidewire, and L_1 and L_2 denote the stiff and soft segments in the unconstrained (i.e., free to bend) portion of the guidewire's steerable tip, respectively. (**B**) Characterization of the magnetic guidewire's behavior under magnetic manipulation with a single magnet. The tip deflection angle θ_L was measured while varying the working distance and the angular position of the actuating magnet in the attraction and repulsion modes (guidewire dimension: $D = 400$ μm, $L_1 = 6$ mm, $L_2 = 4$ mm).
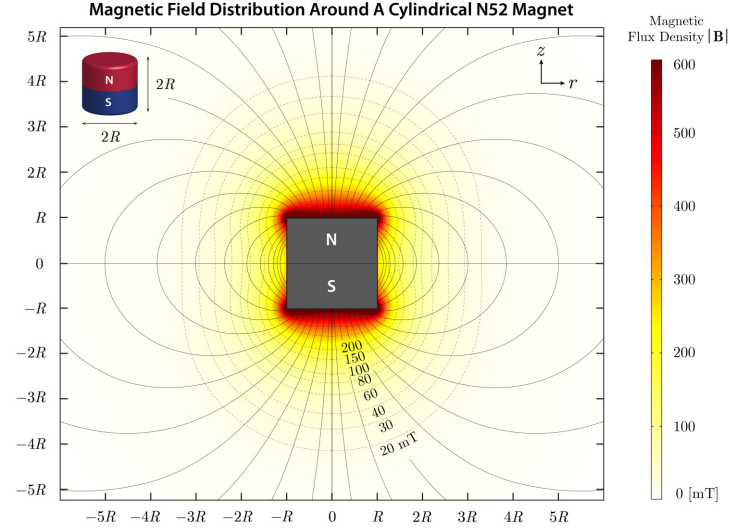
Figure 4-11: Magnetic fields around a cylindrical magnet. Axisymmetric magnetic field distribution around a N52-grade cylindrical magnet with diameter and thickness of $2R$ and remanence $B_{\mathrm{re}} = 1.45$ T. The solid lines indicate the field directions, and the dotted lines form the contours around which the magnetic flux densities are indicated.
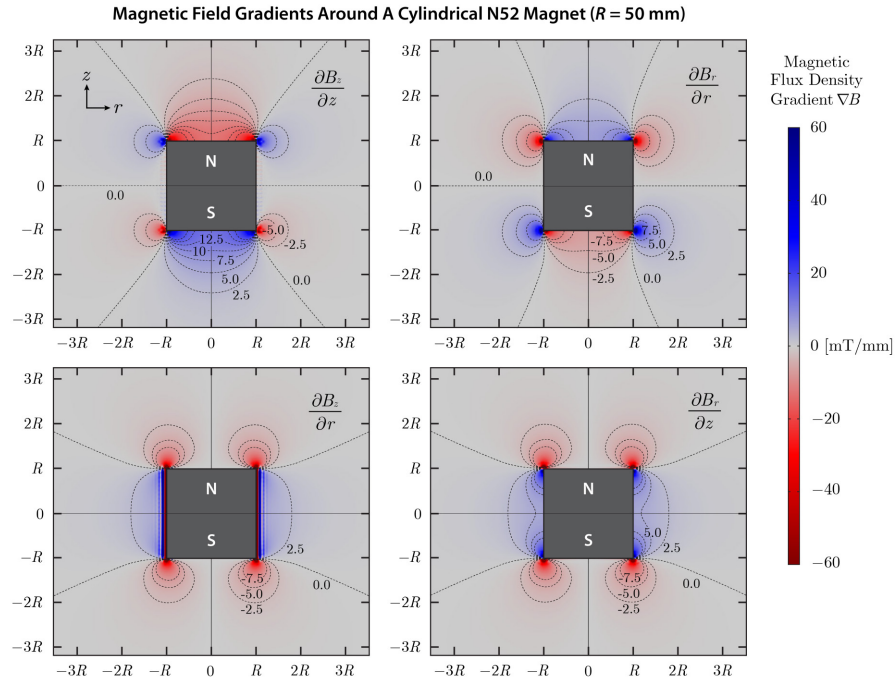
Figure 4-12: Spatial gradients of the magnetic fields around a cylindrical magnet. Non-zero components of the field gradients are presented for a N52-grade cylindrical magnet with remanence $B_{\mathrm{re}} = 1.45$ T and diameter and thickness of 100 mm. Along the center axis of the magnet, the diagonal terms of the field gradient tensor in Equation (2.46) (i.e., $\partial B_z/\partial z$ and $\partial B_r/\partial r$) give rise to magnetic body forces acting on the steerable tip of the guidewire, whereas the off-diagonal terms (i.e., $\partial B_z/\partial r$ and $\partial B_r/\partial z$) are effectively zero.
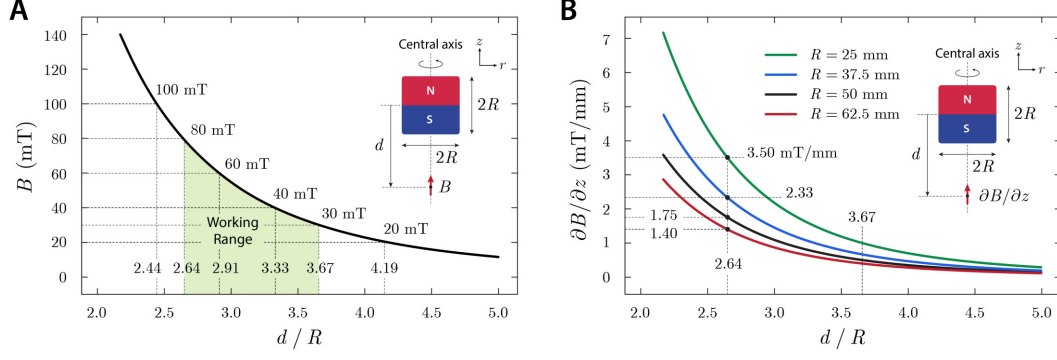
Figure 4-13: Magnetic field and field gradient along the central axis of a cylindrical magnet. (**A**) Magnetic flux density B along the central axis of the magnet plotted against the normalized working distance d/R. For typical steering tasks, the required magnetic field strength ranges from 30 to 80 mT, which correspond to the upper ($d/R = 3.67$) and lower ($d/R = 2.64$) boundaries of the working range for the magnet in the attraction and repulsion modes. (**B**) Magnetic field gradients $\partial B/\partial z$ along the axial direction plotted against the normalized working distance d/R for different sized magnets of the same shape ($R = 25, 37.5, 50, 62.5$ mm). The field gradient values at the lower boundary of the working range ($d/R = 2.64$) are presented on the plot.

Because the magnetic field strength decreases with the normalized distance d/R, as shown in **Figure 4-13A**, the actuating magnet should be large enough to steer the guidewire at a reasonable working distance discussed above. Typical steering and navigational tasks require the actuating field strength of at most 80 mT, which corresponds to the flux density at $d/R = 2.64$ from the center of the magnet as predicted from Equation (4.4) and shown in **Figure 4-13A**. For a cylindrical magnet with diameter and thickness of 100 mm (i.e., $R = 50$ mm) and $B_{\mathrm{re}} = 1.45$ T, for example, this normalized distance translates into 132 mm from the magnet's center (or 82 mm from the magnet's surface). At this point, the field gradient along the centerline is calculated to be 1.75 mT/mm from the derivative of Equation (4.3) as shown in **Figures 4-12** and **4-13B**. Then, the magnetic torque density is evaluated to be 10.24 kN/m², and the moment acting on the guidewire's steerable tip of length L ($4 \leq L \leq 10$ mm) by the magnetic body force (per unit volume) is estimated to be 0.90 to 2.24 kN/m², which is around 10% to 20% of the magnetic torque density. The contribution of the magnetic body force to the steering of the distal tip further diminishes as the magnet size increases (i.e., inversely proportional to

111

R; **Figures 4-13B**), when compared to that of the magnetic torque. This implies that, for the magnetic guidewire, the magnetic torques are still the primary source of actuation even when it is steered by a single permanent magnet, provided that the actuating magnet is much larger than the steerable tip of the guidewire (i.e., $R \gg L$) and sufficiently far from the guidewire tip ($d > 2R$). Under these conditions, the tip deflection behavior of the guidewire can be characterized as a function of the normalized working distance from the magnet.

4.3.3   Working Distance for the Actuating Magnet

To define the range of working distance for the actuating magnet, we should consider the workspace constraints due to the patient geometry and surrounding objects as well as the spatial distribution of magnetic fields around the magnet. We first estimated a possible working range for the actuating magnet to steer the guidewire while it is spatially positioned near the patient's head, with considerations of the average head size [164] and the anatomical location and orientation of intracranial arteries (**Figure 4-14**). For guidewire navigation in cerebral arteries, it is reasonable to consider the distance from the surface of the magnet to the Circle of Willis—an arterial network in the middle of the head (between the right and left hemispheres; see **Figure 4-15A**)— which can be regarded as the farthest area within the cranium from the magnet.

Assuming that the magnet is positioned in one of the nearest possible locations around the head with some safety margins considered, the estimated distance from the magnet surface to the Circle of Willis is around 100 mm, as illustrated on the sagittal plane in **Figure 4-14**. Then, for navigation from the proximal to the distal areas of cerebral arteries, the effective working distance between the magnet surface and the guidewire's steerable tip would be below 100 mm and further decrease as the guidewire is advanced to the periphery. For example, if the guidewire is currently in the distal end (C4 in **Figure 4-15B**) of the left internal carotid artery (ICA; **Figure 4-15B**) and about to navigate through the left middle cerebral artery (MCA; **Figure 4-15B**), the estimated working distance from the magnet surface to the guidewire at the ICA bifurcation is around 80 to 90 mm, as illustrated on the frontal and transverse

planes in **Figure 4-14**. Then, the magnetic field applied from this distance by the magnet should be strong enough to induce the deflection of the guidewire tip along the desired direction toward the left M1 segment.
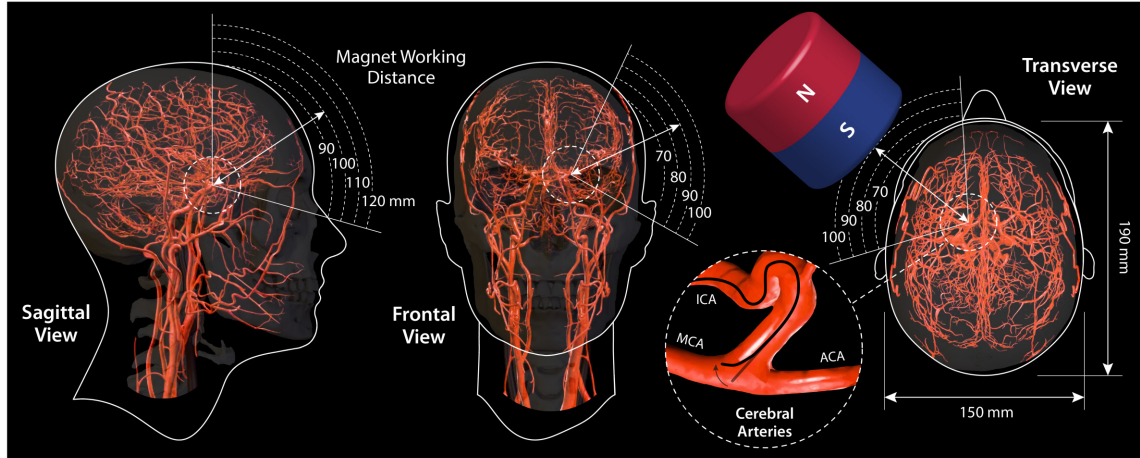
Figure 4-14: Magnet working distance considering the patient geometry and neurovascular anatomy. Working distance and area for a cylindrical magnet (diameter and thickness of 100 mm) around the head considering the average head size [164] and anatomical location and orientation of intracranial arteries illustrated on the sagittal, frontal, and transverse planes. When viewed from the sagittal plane, the distance from the surface of the magnet to the Circle of Willis in the middle of the head is estimated to be around 100 mm. When viewed from the frontal and transverse planes, the distance from the surface of the magnet to left ICA bifurcation is estimated to be 80 to 90 mm. ICA: internal carotid artery; MCA/ACA: middle/anterior cerebral artery.
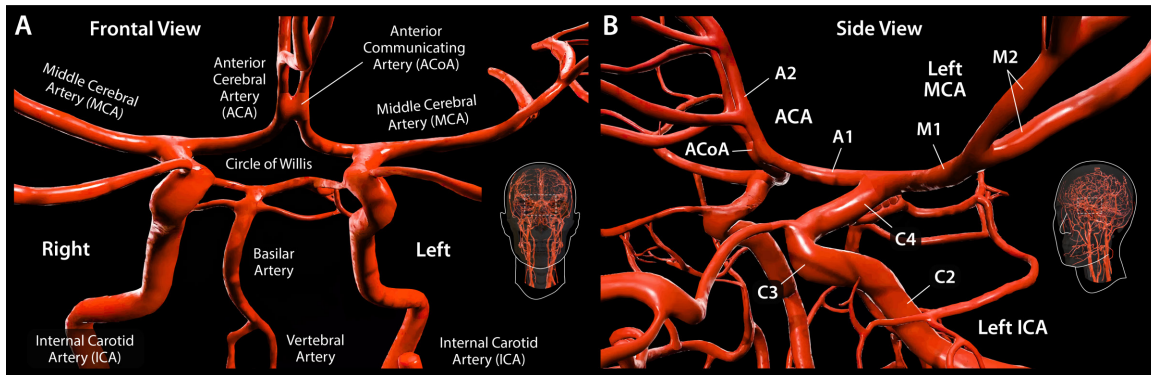
Figure 4-15: Anatomy and nomenclature of intracranial arteries. (**A**) Intracranial arteries viewed from the frontal plane. (**B**) Branches and segments of the internal carotid artery (ICA; C2, C3, and C4), anterior cerebral artery (ACA; A1 and A2), and middle cerebral artery (MCA; M1 and M2) in the left hemisphere are indicated. For the segments of the ICA, several classification schemes and various numbering systems exist. Here, we follow the simple system corresponding to the description by Gibo and colleagues [165]: C4: Supraclinoid, C3: Cavernous, C2: Petrous, C1: Cervical (C1 is not shown in the figure).

4.3.4   Principal Modes of Steering Control

The most straightforward way to steer the magnetic guidewire with a single magnet is to position the magnet in such a way that the guidewire's distal tip bends toward the magnet. Such wire tip motion can be achieved by aligning the magnet's magnetic moment, which points from the south to the north pole of the magnet along its central axis, with the desired steering direction to which the tip deflection is to occur. We define this mode of steering control, which seemingly attracts the distal end of the guidewire, as the *attraction mode* (**Figure 4-10A**). If the magnet is flipped, with its magnetic moment reversed, the guidewire tip would be repelled away from the magnet surface. By the same token, we define this mode of steering control as the *repulsion mode* (**Figure 4-10A**). We define the angular position of the magnet relative to the guidewire by the azimuthal angle (denoted by φ in **Figure 4-10A**), which is the angle formed by the line connecting the base of the guidewire's softer tip in the undeformed reference state and the center of the magnet with respect to the straight tip of the guidewire. The working distance of the magnet is defined as the distance from the base of the guidewire's softer tip in the reference state to the center of the magnet (denoted by d in **Figure 4-10A**).

The tip deflection angle (denoted θ_L in **Figure 4-10A**) varies with the working distance (**Figure 4-14**), which is normalized by the magnet's radius R for nondimensional representation as discussed above. The deflection angle also varies with the magnet's angular position φ, helping to achieve larger deflection when φ is greater than 90° in the attraction mode or smaller than 90° in the repulsion mode, respectively (**Figure 4-10B**). It is worth noting that the asymmetry between the attraction and repulsion modes is attributed to the influence of magnetic forces resulting from the spatial gradients of the actuating fields discussed above. In both the attraction and repulsion modes, the bending actuation is initiated and driven by the magnetic body torques, because the magnetic body forces are almost negligible in the initial undeformed configuration. As the guidewire tip deforms and becomes more aligned with the applied fields, the magnetic body forces increase and attract the guidewire tip toward the magnet in both steering modes, as can be anticipated from Equation

(2.46). Consequently, the magnetic body forces help to increase the tip deflection angle in the attraction mode while decreasing the deflection angle in the repulsion mode, which leads to the slightly asymmetric profiles of the tip deflection angle as presented in **Figure 4-10B**.
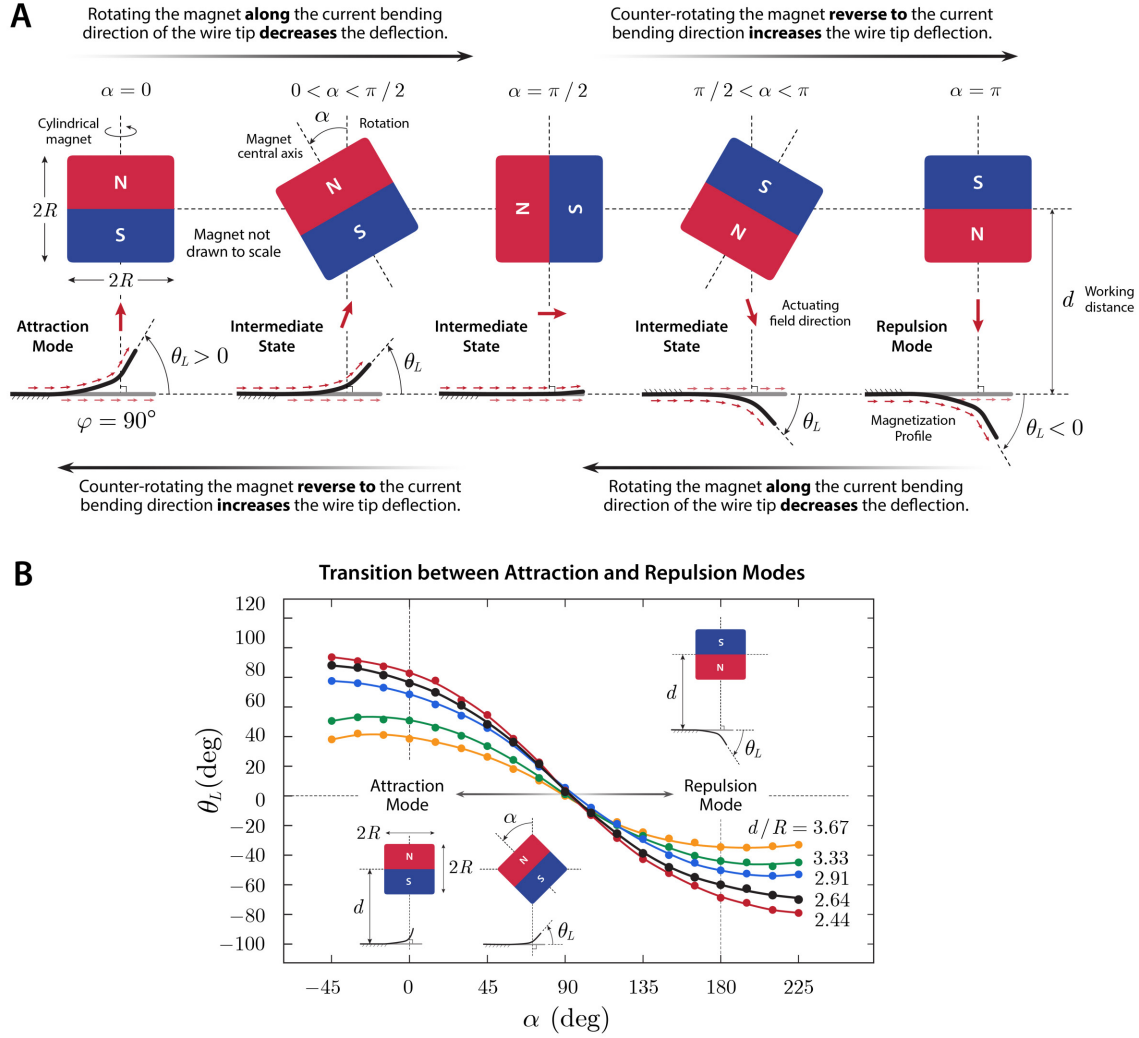
Figure 4-16: Transition between the attraction and repulsion steering modes. (**A**) Schematic representation and (**B**) characterization of the magnetic guidewire's behavior during the transition between the attraction and repulsion modes. Rotating the magnet along the current bending direction of the guidewire tip (i.e., either clockwise or counterclockwise) causes the tip to unwind itself, decreasing the deflection angle θ_L, when transitioning from either the attraction or the repulsion mode to an intermediate state. Counter-rotating the magnet reverse to the current bending direction, on the other hand, causes the tip to bend further toward or away from the magnet, increasing the deflection angle, when transitioning from an intermediate state to the attraction or the repulsion mode.

Transition between the attraction and repulsion modes can be achieved through flipping the magnet by rotating the axis 7 of the robot arm by 180°, during which the steerable tip of the guidewire also changes its configuration in response to the rotation of the magnet, as illustrated in **Figure 4-16A**. The rotation angle (denoted by α in **Figure 4-16A**) is defined as the deviation of the central axis of the magnet from its unrotated state (in the attraction mode with $\varphi = 90°$ in **Figure 4-16A**). Rotating the magnet along the current bending direction of the guidewire tip (i.e., either clockwise or counterclockwise) causes the tip to unwind itself, decreasing the deflection angle θ_L, when transitioning from either the attraction or the repulsion mode to an intermediate state (**Figure 4-16A**). Counter-rotating the magnet reverse to the current bending direction, on the other hand, causes the guidewire tip to bend further toward or away from the magnet, increasing the deflection angle, when transitioning from an intermediate state to the attraction or the repulsion mode, as illustrated in **Figure 4-16A**. The behavior of the guidewire tip in response to the rotation of the magnet, which is initially positioned at $\varphi = 90°$ with $\alpha = 0°$ (i.e., attraction mode), is characterized while varying a from $-45°$ to $225°$ as presented in **Figure 4-16B**.

4.3.5   Auxiliary Modes of Steering Control

Although the attraction and repulsion modes serve as the primary steering modes because of the intuitive control principles, they may not suffice for every possible case, especially when navigating in areas with unfavorable vascular anatomy for spatial positioning of the magnet due to workspace constraints. For such occasions, in which minimal motion of the robot arm is desirable, steering control of the magnetic guidewire can also be achieved through rotation of the magnet around its center, which corresponds to rotation of the end-effector around the axis 7 of the robot arm. We define the rotation angle (denoted by α in **Figure 4-17A**) as the deviation of the central axis of the magnet from its unrotated state, in which the magnet is positioned at the zero angular position ($\varphi = 0$) with its axis aligned with the undeformed (straight) tip of the guidewire from some working distance d (**Figure 4-17A**). The

tip deflection angle θ_L varies with the magnet's rotation angle α ranging from $-180°$ to $180°$, as well as the normalized working distance d/R, as characterized in **Figure 4-17B**. When the magnet rotates clockwise ($\alpha < 0$) from the unrotated state, the guidewire tip bends counter-clockwise ($\theta_L > 0$); when the magnet rotates counter-clockwise ($\alpha > 0$), the guidewire tip bends clockwise ($\theta_L < 0$), just as two meshed gears turn in opposite directions. For the magnet positioned at either $-135° < \alpha < -90°$ or $90° < \alpha < 135°$, we define another useful steering mode, so-called the *oblique repulsion mode* (**Figure 4-17A**), which helps to deflect the guidewire tip up to around $90°$ at the normalized working distance of 2.64 (**Figure 4-17B**).
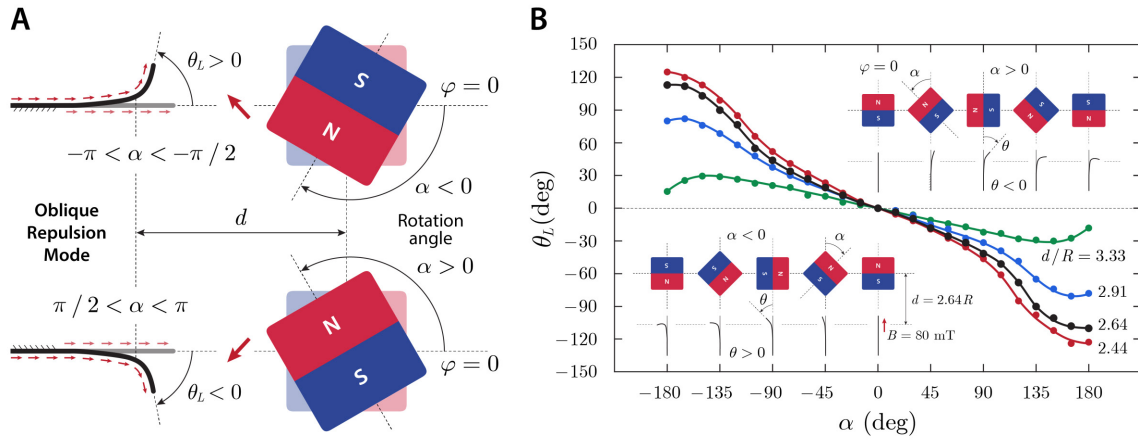
Figure 4-17: Definition and characterization of the oblique repulsion mode. (**A**) Schematic representation of the oblique repulsion mode in which the guidewire tip deflects in response to the magnet's peripheral fields outside of the core fields along the axial direction. The rotation angle α is defined as the deviation of the central axis of the magnet from its unrotated state, in which the magnet is positioned at the zero angular position ($\varphi = 0$) with its axis aligned with the undeformed tip of the guidewire from some working distance d. (**B**) Characterization of the tip deflection angle θ_L while varying the rotation angle α from $-180°$ to $180°$ at different normalized working distance d/R. When the magnet rotates clockwise ($\alpha < 0$) from the unrotated state, the guidewire tip bends counterclockwise ($\theta_L > 0$); when the magnet rotates counterclockwise ($\alpha > 0$), the guidewire tip bends clockwise ($\theta_L < 0$).

4.3.6 Size of the Actuating Magnet

The mappings between the position and orientation of the magnet and the behavior of the guidewire's distal tip presented in **Figure 4-10B** and **Figure 4-17B** provide guidance on how to manipulate the magnet to achieve desired states of the guidewire.

We define the range of working distances for the magnet in the attraction or repulsion mode as $2.64 < d/R < 3.67$ in terms of the normalized distance (**Figure 4-10B**). The lower and upper boundaries correspond to the points along the central axis of the magnet at which the magnetic flux density is 80 mT and 30 mT, respectively, according to Equation (4.4) (**Figure 4-13A**). Within this range, the tip deflection angle can reach up to around 120° in the attraction mode and around 90° in the repulsion mode as shown in **Figure 4-10B**. If we allow the magnet to approach the patient's head as close as 70 mm (in terms of the distance from the magnet surface to the target vasculature) in the scenario discussed above (**Figure 4-14**), the size of the smallest possible magnet is calculated to be around 85 mm in terms of both diameter and thickness ($R = 42.5$ mm). If we increase the minimum allowable distance (between the magnet surface and the target vasculature) to 85 mm, including some safety margins (around 20 mm from the head surface), the required diameter/thickness of the magnet becomes around 100 mm ($R = 50$ mm), which is considered the ideal size of the magnet to be used in realistic clinical settings. Hence, a cylindrical magnet with size of 100 mm was employed and mounted on the most distal joint/link of the robot arm with its magnetic moment aligned perpendicularly to the joint axis.

4.4   Summary

In **Section 4.1**, we reviewed different types of existing magnetic manipulation platforms and discussed their merits and demerits in terms of both magnetic actuation capacity and compatibility with standard imaging modalities for neurovascular intervention in comparison with our proposed system based on a robot arm with a single actuating magnet. In **Section 4.2**, we provided system-level description of our telerobotic neurointerventional platform including the real-time teleoperation interface and general workflow for our system in realistic clinical settings for image-guided neurovascular intervention. In **Section 4.3**, we defined principal and auxiliary modes of steering control for our magnetic soft continuum guidewire with a single actuating magnet on the basis of quantitative analyses and characterization of the guidewire's

behavior under the influence of the applied actuating field as well as the working distance of the magnet with considerations of the geometrical constraints pertaining to the patient geometry in realistic clinical settings. Based on the quantitative analyses, we also provide our rationale behind the determined size of the actuating magnet for clinical use. In **Chapter 5**, we extensively validate our system design through a set of in vitro benchtop experiments as well as in vivo animal studies.

Chapter 5

Telerobotically Assisted Neurovascular Interventions

5.1 Telerobotically Controlled Magnetic Navigation

5.1.1 In Vitro Verification with Anatomical Models

Demonstration under real-time optical imaging: For validation of the developed telerobotic neurointerventional platform, we first evaluated its steering and navigational performance in vitro with an anatomical model that replicate the human intracranial arteries (**Figure 5-1A**). This anatomical model includes both carotid and vertebral arteries and a complete circle of Willis in realistic dimensions. Multiple aneurysms with different neck morphologies, sizes and angulations from the carrier vessel are present on the model, as identified in **Figure 5-1B**. The silicone vessels were filled with a blood-mimicking fluid, along with a peristaltic pump employed to generate pulsatile flow, to simulate the friction between commercial hydrophilic guidewire/catheter surfaces and the real blood vessels.

As part of benchtop verification, we first demonstrated our system's capability to guide selective navigation in different branches of cerebral arteries in a 3D neurovascular phantom under real-time optical imaging (**Figure 5-2A**) through telerobotically controlled magnetic manipulation (**Figure 5-2B**). The task was performed in the
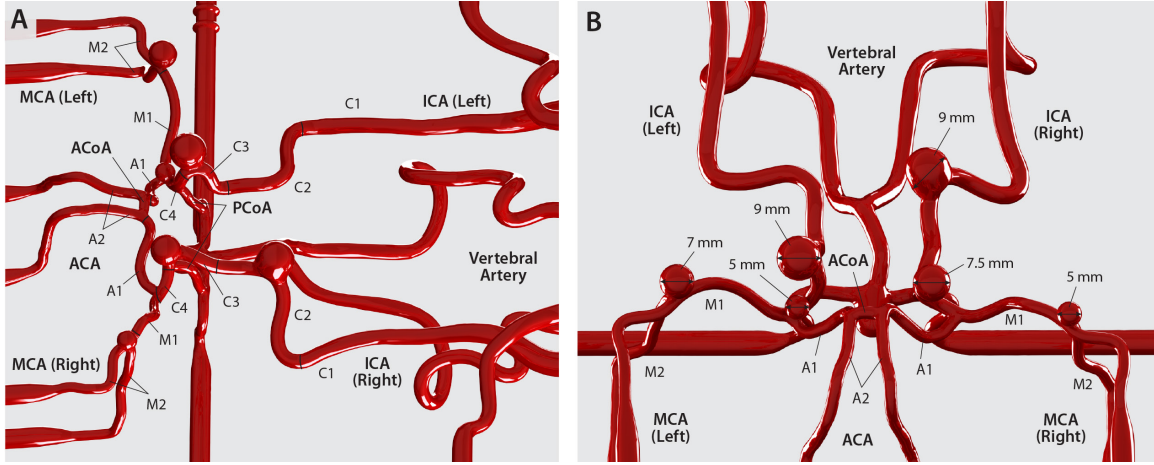
Figure 5-1: Neurovascular phantom model used in the benchtop verification. (**A**) Anatomy and nomenclature of the phantom neurovasculature (ICA: internal carotid artery; MCA: middle cerebral artery; ACA: anterior cerebral artery; ACoA: anterior communicating artery; PCoA: posterior communicating artery). The ICA is divided into supraclinoid (C4), cavernous (C3), petrous (C2), and cervical (C1) segments, following [165]. The acute-angled corner between the cavernous and supraclinoid portions of the ICA is defined as the carotid siphon. (**B**) Detailed location and dimensions of the aneurysms present in the anatomical model. The given dimensions indicate the inner diameter of the aneurysms.

presence of virtual C-arm models implemented in the robot arm's task space to simulate the workspace constraints in clinical settings for complex neurovascular interventions under biplane fluoroscopy (**Figure 5-2C**). In addition to the C-arm models, a virtual human patient on the operating table was also modeled in the robot's task space to ensure that the robot arm manipulation could be performed safely without collisions with the surrounding objects.

The 3D neurovascular phantom was accessed from the left internal carotid artery (ICA; **Figure 5-1**) with the magnetic guidewire and the microcatheter, which were advanced up to the left ICA bifurcation (A1-M1 junction) using the remotely controlled advancing unit. After positioning the actuating magnet to direct the guidewire tip toward the A1 segment of the left anterior cerebral artery (ACA; **Figure 5-1**) through repulsive steering, as shown in **Figure 5-2B** (00:01), the guidewire was advanced up to the anterior communicating artery (ACoA; **Figure 5-1**) and then to the M1 segment of the right middle cerebral artery (MCA), as shown in **Figure 5-2A** (00:03). Then, the guidewire was magnetically steered and manipulated within the confined space of ACoA complex to selectively reach the right and left A2 segments,

as shown in **Figure 5-2A** (00:14∼00:39), which demonstrates our system's capability to control the magnetic guidewire remotely and precisely to navigate distal branches in the complex cerebral vasculature.
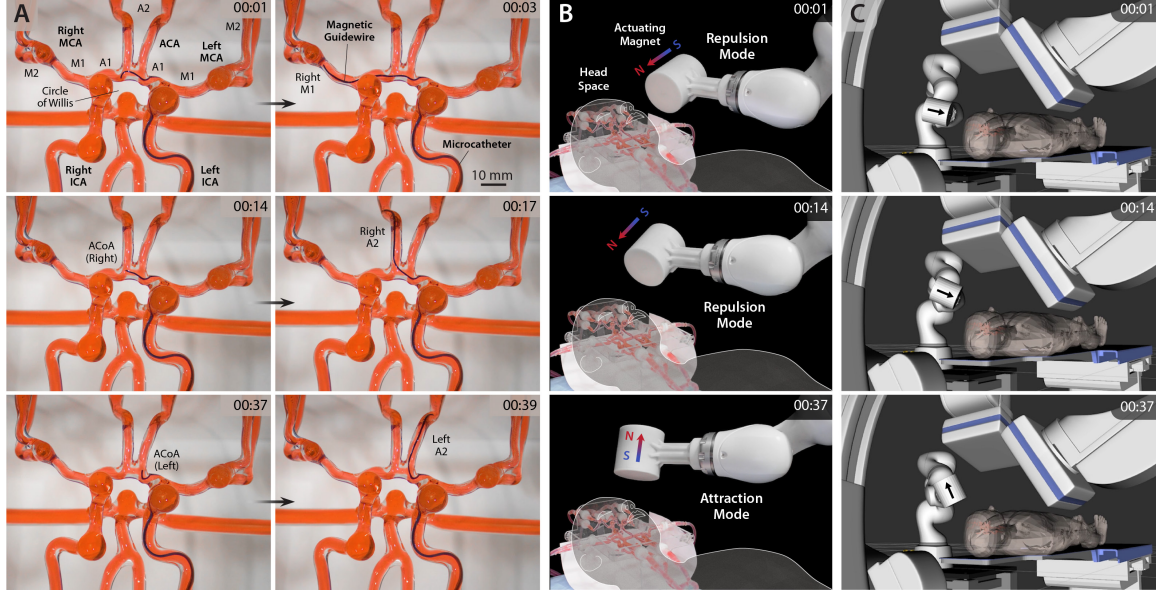
Figure 5-2: **Benchtop demonstration of telerobotically controlled magnetic steering and navigation in cerebral arteries.** (**A**) Magnetic steering and navigation in different branches of cerebral arteries. The magnetic guidewire is advanced from the internal carotid artery (ICA) bifurcation (A1-M1 junction) under repulsive steering to reach the left A1 segment and then the right A1 and M1 segments sequentially (00:01∼00:03). After repositioning the magnet to reduce the steering torque, the guidewire is advanced to reach the right A2 segment of the anterior cerebral artery (ACA) under the repulsive steering mode (00:14∼00:17). After flipping the magnet to utilize attractive steering, the guidewire tip is directed toward the left A2 segment and advanced (00:37 00:39). (**B**) The robot arm's motion and configuration are visualized during the demonstrated steering and navigational task. (**C**) The C-arm and human patient models implemented in the robot arm's virtual task space simulate the realistic workspace constraints in clinical settings for neurovascular interventions under biplane fluoroscopy.

Demonstration under real-time x-ray fluoroscopy: Next, to demonstrate the compatibility of our developed system with standard image-guided procedures based on x-ray, we use the same anatomical model in **Figure 5-1** to perform magnetic steering and navigation under real-time x-ray fluoroscopy (**Figure 5-3**). As shown in **Figure 5-3A**, our magnetic soft continuum guidewire was clearly visible under x-ray fluoroscopy as standard neurovascular guidewires, and the movement of the steerable tip in response to the actuating magnet was also clearly observed under the low dose

(0.35 mGy/min) of x-ray fluoroscopy with a pulse rate of 15 p/s. The C-arm configuration shown in **Figure 5-3B** was determined to provide a semi-anteroposterior projection for the target vasculature by angulating in the cranial direction by 28° and then rotating by 12.5° to be in the right anterior oblique position (see **Figure 5-4** for the C-arm nomenclature). With respect to the fixed frame of reference defined in **Figure 5-3C**, the same configuration can be achieved by rotating the C-arm around the y-axis by 28° and then around the x-axis by –12.5° from the upright position.
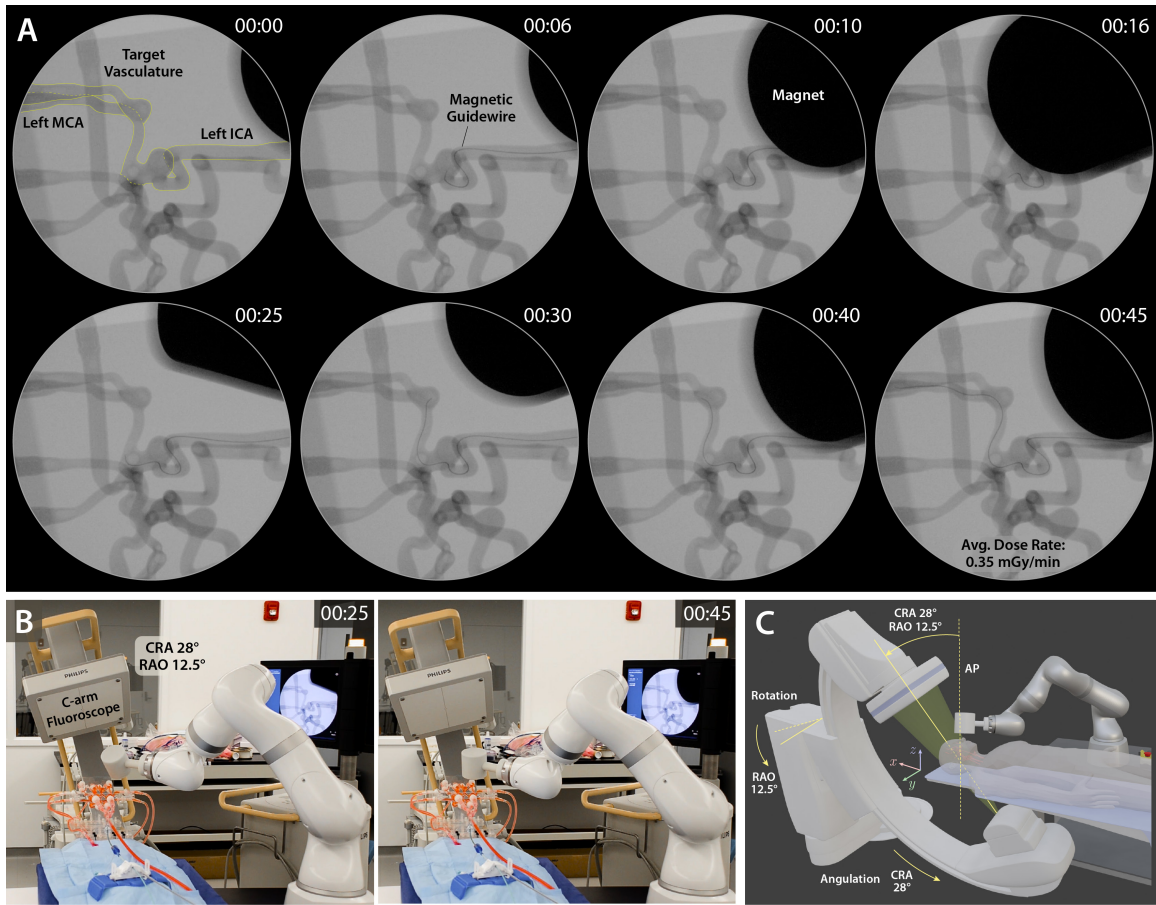
Figure 5-3: Navigation in the left middle cerebral artery (MCA) under real-time x-ray fluoroscopy. (A) The magnetic guidewire is steered from the left internal carotid artery (ICA) to the inferior M2 segment of the left MCA of the neurovascular phantom under low-dose, pulsed fluoroscopy with the average dose rate of 0.35 mGy/min and the pulse rate of 15 p/s, with no x-ray contrast agent used. **(B-C)** With cranial angulation of 28° (CRA 28°) and right anterior oblique rotation of 12.5° (RAO 12.5°), the C-arm provides a semi-anteroposterior (AP) projection for the target vasculature. Under this semi-AP projection, the guidewire tip was visible at all times during the navigation without its view being blocked by the actuating magnet even when the magnet appears partially on the fluoroscopic images.

124
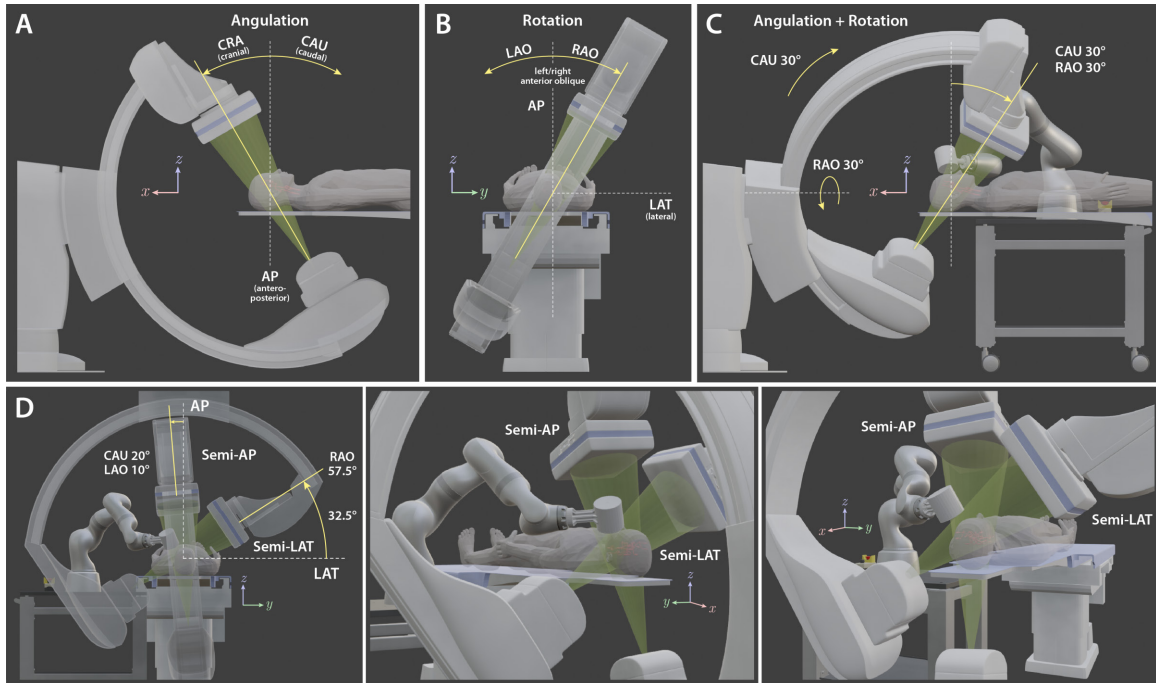
Figure 5-4: Nomenclature for the angulation and rotation of C-arm fluoroscope.
(**A**) The term *angulation* refers to orbital rotation of the C-arm around the y-axis from the upright position for anteroposterior (AP) projection. Depending on the angulation direction and the resulting change in the position of the image detector relative to the patient, the angulated C-arm configuration is defined as either cranial (CRA) or caudal (CAU) position. (**B**) The term *rotation* refers to tilting of the C-arm sideways around the x-axis from the upright position for AP projection. Depending on the direction of rotation and the resulting change in the position of the image detector relative to the patient, the rotated C-arm configuration is defined as either left/right anterior oblique (LAO/RAO) position. (**C**) If the C-arm is angulated in the CAU direction by 30° and rotated toward the RAO position by 30°, the resulting configuration is referred to as CAU 30° and RAO 30°. (**D**) Illustration of the robot arm deployed in biplanar imaging settings for complex neurovascular interventions based on a pair of C-arms for simultaneous projections from two different angles.

In this chosen semi-anteroposterior projection, the guidewire tip was clearly visible in the fluoroscopic images at all times during the navigation even without the use of x-ray contrast agent. The actuating magnet did not block the view of the guidewire tip during the steering tasks even though it partially appeared on the fluoroscopic images. To safely pass the first aneurysm at the acute-angled corner in the left ICA, the guidewire tip was directed posteriorly under repulsive steering to avoid contact with the aneurysm and then advanced up to the junction between the left MCA and the ACA, as shown in **Figure 5-3A** (00:06∼00:25). Then, the distal tip was oriented laterally to make a 90° turn toward the left MCA under attractive steering,

to prevent it from latching onto the small aneurysm at the MCA-ACA junction, and then advanced up to the third aneurysm at the MCA bifurcation, as shown in **Figure 5-3A** (00:25∼00:30). The steerable tip was then directed posteriorly toward the inferior branch of the left MCA through repulsive steering and further advanced to reach the distal end of the branch without making contact with the aneurysm at the corner (MCA bifurcation), as shown in **Figure 5-3A** (00:40∼00:45).
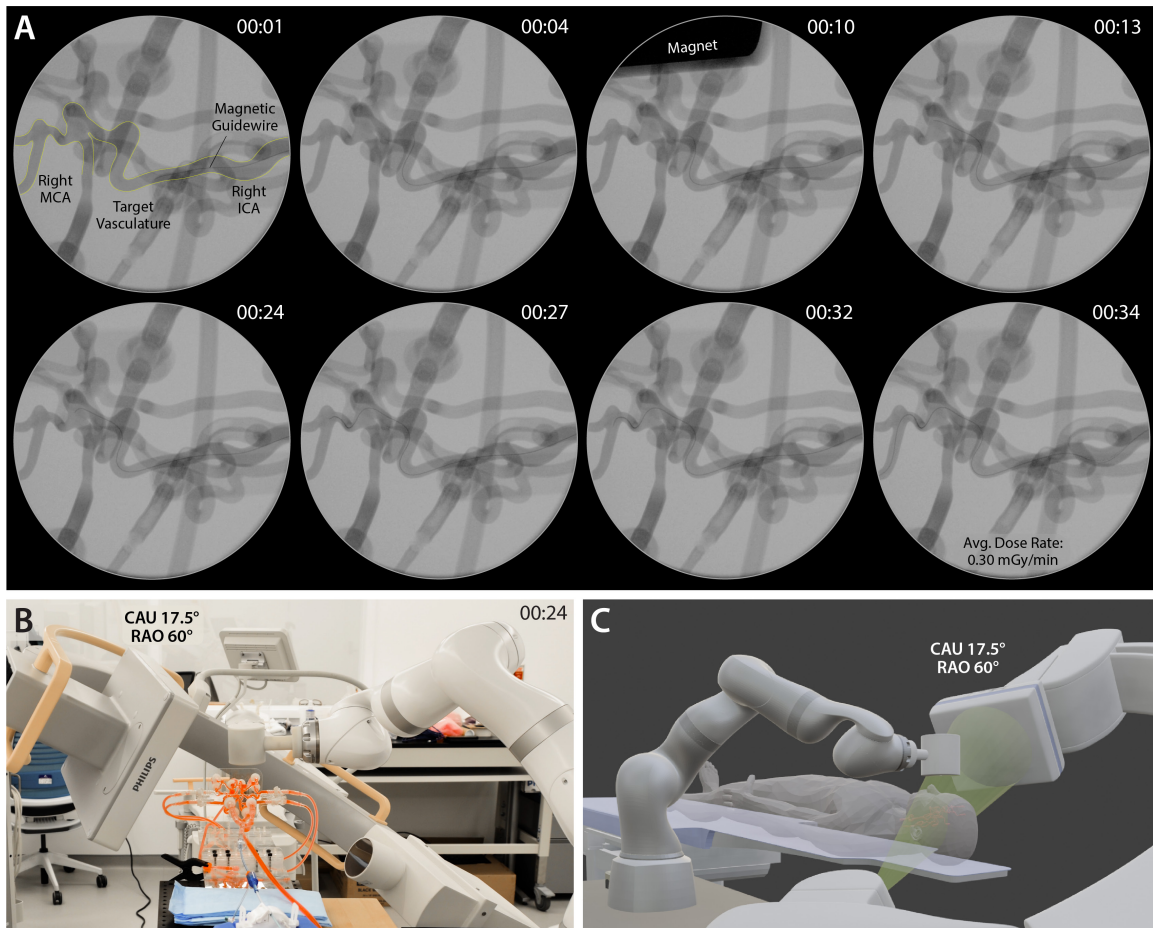
Figure 5-5: Navigation in the right middle cerebral artery (MCA) under real-time x-ray fluoroscopy. (**A**) The magnetic guidewire is steered from the right internal carotid artery (ICA) to the inferior M2 segment of the right MCA of the neurovascular phantom under low-dose, pulsed fluoroscopy with the average dose rate of 0.30 mGy/min and the pulse rate of 15 p/s, with no x-ray contrast agent used. (**B-C**) With caudal angulation of 17.5° (CAU 17.5°) and right anterior oblique rotation of 60° (RAO 60°), the C-arm machine provides a semi-lateral projection for the target vasculature in the demonstrated navigation. Under this semi-lateral projection, the guidewire tip is visible at all times during the navigation, and the actuating magnet appears partially on the fluoroscopic image only when steering the guidewire under the oblique repulsion mode at the first aneurysm.

We demonstrated another navigational task from the right ICA to the inferior M2 segment of the right MCA. As shown in **Figure 5-5A**, the guidewire tip's movement in response to the magnet motion was clearly visible under the low-dose fluoroscopy with an average dose rate of 0.30 mGy/min. The C-arm configuration was determined to provide a semi-lateral projection with caudal angulation of 17.5° (see **Figure 5-4** for C-arm nomenclature) and right anterior oblique rotation of 60° as shown in **Figure 5-5**, **B** and **C**. The guidewire tip was clearly visible at all times during the navigation as shown in **Figure 5-5A**. The neurovascular phantom we used had a large aneurysm at the 90° corner in the right proximal ICA (C2 in **Figure 5-1A**). Starting from the right ICA, the guidewire was magnetically steered using the oblique repulsion mode to cross the aneurysm without touching its inner wall and advanced up to the next aneurysm located in the right carotid siphon (the acute-angled corner of the cavernous (C3) ICA; see **Figure 5-1A**), as shown in **Figure 5-5A** (00:01∼00:13). Then, the guidewire tip was directed toward the distal ICA (C4 in **Figure 5-1A**) using repulsive steering to avoid contact with the second aneurysm wall, after which the guidewire was advanced until the distal tip reached the MCA bifurcation (M1-M2 junction), as shown in **Figure 5-5**A (00:24∼00:27). The magnetic guidewire was then advanced up to the inferior M2 segment under repulsive steering as shown in **Figure 5-5**A (00:32∼00:34). The magnet appeared on the image when steering the guidewire through the oblique repulsion mode while crossing the first aneurysm, but it did not block the view of the guidewire tip.

5.1.2   Guidewire Tip Visibility during Magnetic Steering

It is worth noting that the actuating magnet did not block the view of the distal tip of the magnetic guidewire in the demonstrated navigational tasks above, even though it partially appeared on the optical or x-ray images. To better illustrate this point regarding the steering principle for our magnetic guidewire, we employed a 2D neurovascular model with planar geometry (**Figure 5-6A**). While in a simplified planar form, the model appropriately represented all native pathway attributes as well as the various anticipated curvatures and disease states such as cerebral aneurysms.
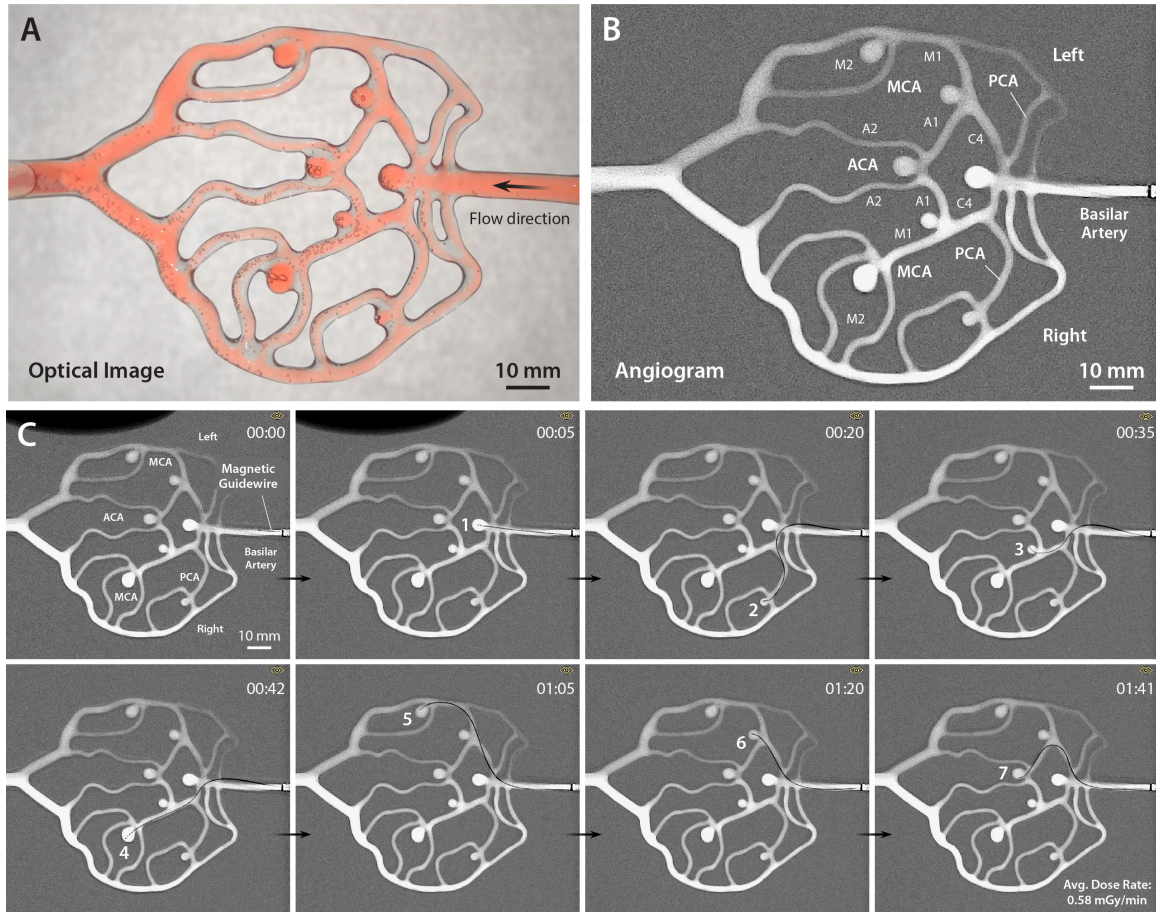
Figure 5-6: 2D neurovascular model used to illustrate of the guaranteed visibility of the guidewire tip during magnetic steering. The magnetic guidewire selectively reaches all of the aneurysms present in the 2D neurovascular model using either attractive or repulsive steering under real-time x-ray fluoroscopy. The actuating magnet does not block the view of the distal tip while it is being magnetically steered because the magnet moves sideways (laterally to the target vasculature).

Using this 2D neurovascular model, we demonstrated our system's capability to guide access to each of the aneurysms present in the model selectively through real-time teleoperation of the system under x-ray fluoroscopy (**Figure 5-6B**). Starting from the basilar artery, the magnetic guidewire was first advanced to reach the first aneurysm at the basilar terminus with its straight distal tip under no effective magnetic steering as shown in **Figure 5-6C** (00:00∼00:05). Positioned on the left side of the 2D phantom, the actuating magnet was angled and rotated relative to the distal tip of the magnetic guidewire to utilize either attractive or repulsive steering to guide its selective access to all other aneurysms in sequence, as shown in **Figure**

128

5-6C (00:20∼01:41). The degree of tip bending was controlled by bringing the actuating magnet either closer to or further away from the steerable tip through joystick teleoperation of the robot arm's end-effector.

As can be seen in **Figure 5-6C**, the actuating magnet did not block the view of the distal tip while it was being magnetically steered to selectively reach all the aneurysms in the model cerebral vasculature. This is because, for the 2D vascular model that was chosen on purpose to illustrate this point, the plane of view (anteroposterior projection) for state observation of the magnetic guidewire corresponds to the plane on which the distal tip is being steered by the actuating magnet in the target vasculature. Hence, the magnet moving sideways (i.e., laterally to the target vasculature) should not block the view of the steerable tip of the guidewire, even if it can partially appear on the fluoroscopic images. This argument that the actuating magnet would not block the view of the distal tip of the magnetic guidewire during steering and navigation should generally hold for 3D vascular structure as well, as verified in the previous demonstrations presented in **Figures 5-2**, **5-3**, and **Figure 5-5**, provided that a suitable projection (i.e., the plane of view) was chosen for optimal state observation of the distal tip angle in the target vasculature.

5.1.3   In Vitro Verification in Realistic Clinical Settings

To evaluate our system's performance in a more realistic setting, we used a human head phantom with cranial housing and intracranial arteries (**Figure 5-7**). The cranial housing of the head phantom imposed realistic workspace constraints of the patient geometry, which was discussed earlier with **Figure 4-14**) in **Section 4.3.3**, and it helped us to verify whether the actuating magnet with diameter and thickness of 100 mm (which was determined from quantitative analyses in **Section 4.3.6**) could steer the magnetic guidewire in the center of the intracranial space.

Given that the vasculature between the proximal intracranial ICA to the MCA bifurcation (see **Figure 4-15** for neurovascular anatomy) is the most common site for stroke or aneurysm intervention [166, 167], we chose to demonstrate magnetic steering and navigation in the left MCA of the phantom. First, to identify the 3D

structure of the targeted vasculature, a series of images was obtained from 3D rotational angiography with the use of iodinated x-ray contrast mdeia, following the standard procedure for image-guided neurovascular intervention. The obtained image data were reconstructed into a 3D vessel model (**Figure 5-8A**), which allowed us to see the entire vascular structure from different perspectives.
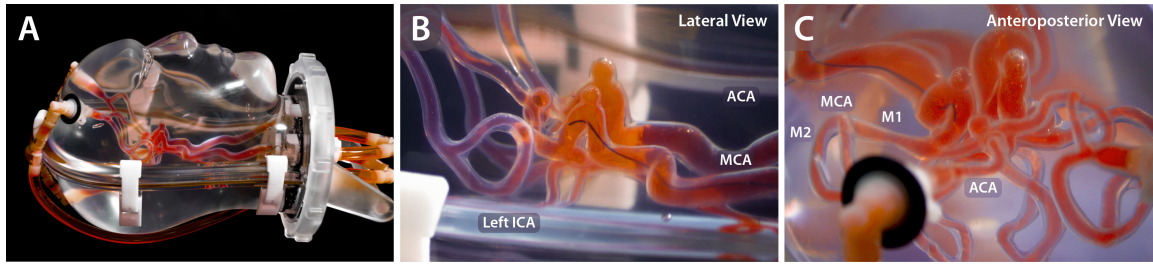
Figure 5-7: 3D neurovascular model with cranial housing to simulate realistic patient geometry. (**A**) Realistic human head phantom with replicated intracranial arteries based on silicone vessels and with cranial housing to simulate the geometrical constraints due to patient's head discussed in **Figure 4-14**. (**B**) Lateral and (**C**) anteroposterior views of the magnetic guidewire navigating in the left ICA with its distal tip being directed toward the descending portion of the carotid siphon under repulsive steering to avoid contact with the aneurysm at the apex of the carotid siphon.
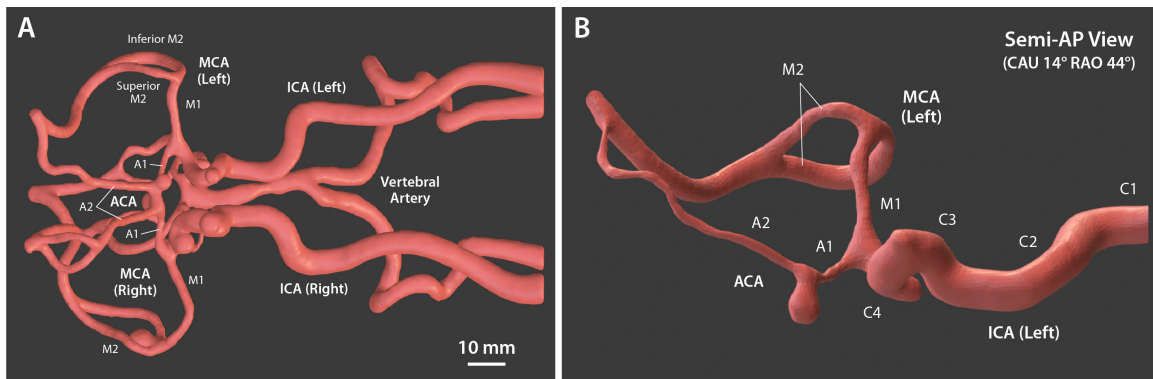
Figure 5-8: 3D vascular model of the intracranial arteries of the head phantom. Reconstructed 3D models of (**A**) the entire phantom vasculature and (**B**) the targeted path from left ICA to MCA from the chosen semi-anteroposterior projection for demonstration.

Based on the vessel model, a semi-anteroposterior projection with caudal angulation of 14° and right anterior oblique rotation of 44° (CAU 14° and RAO 44°) was chosen to provide clear view of all the important anatomical landmarks along the chosen path from the left ICA to MCA, as annotated in **Figures 5-8B** and **5-9A**. These

130

critical anatomical landmarks includes the carotid siphon—the U-shaped part of the ICA between the cavernous (C3) and supraclinoid (C4) segments—with an aneurysm, the ICA bifurcation (A1-M1 junction), and the MCA bifurcation (M1-M2 junction). The 3D model of the targeted path was also used for preprocedural planning and simulation of the robot arm's motion, path, and configuration for spatial positioning of the actuating magnet to steer the magnetic guidewire at those acute-angled corners or bifurcation points identified from the 3D vessel model.
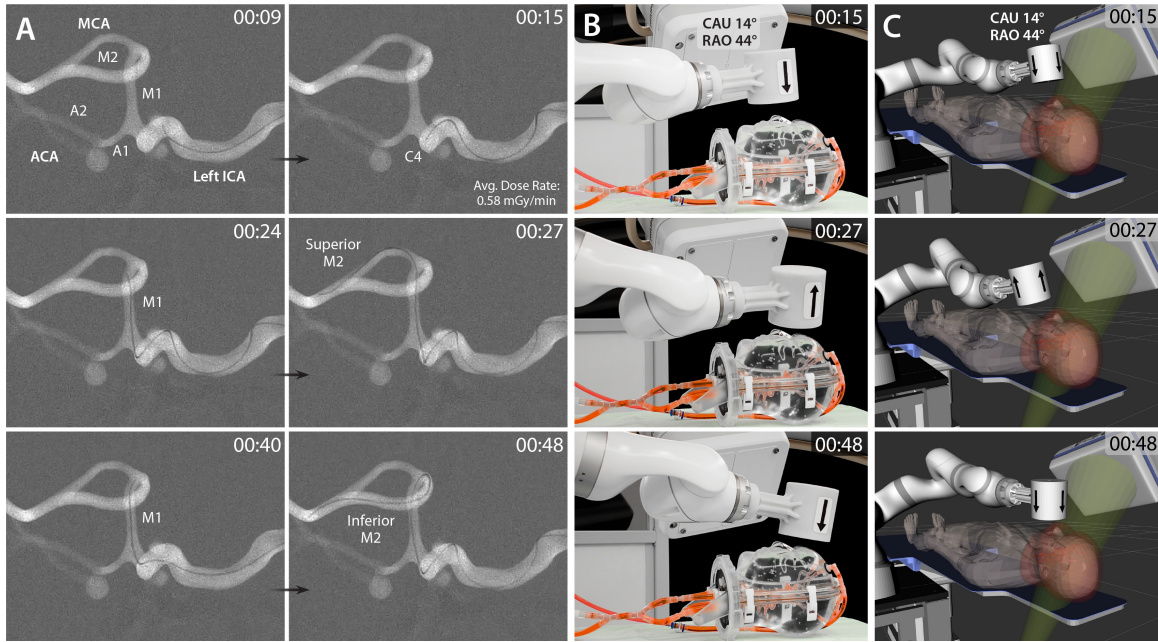
Figure 5-9: In vitro demonstration of magnetic steering and navigation in intracranial arteries under real-time x-ray fluoroscopy. (**A**) Fluoroscopic images of the magnetic guidewire navigating from the left ICA to MCA under telerobotically controlled magnetic steering to reach the superior and inferior M2 segments selectively in sequence. As part of the preprocedural step, digital subtraction angiography (DSA) was performed to visualize the target vasculature as a roadmap for guidewire steering and navigation. ICA: internal carotid artery; MCA/ACA: middle/anterior cerebral artery. (**B**) Actual view and (**C**) virtual visualization of the robot arm with an actuating magnet, the C-arm providing the semi-AP projection for the target vasculature in caudal angulation of 14° (CAU 14°) and right anterior oblique rotation of 44° (RAO 44°), the human head phantom (or equivalently the virtual human patient) on the operating table. The arrow on the actuating magnet indicating the magnet's polarity identifies which steering mode is being used.

Starting from the left proximal ICA, the guidewire was first advanced to reach the carotid siphon at which a saccular aneurysm (with an inner diameter of 4 mm)

was present. As the guidewire entered the ascending part of the carotid siphon in the absence of magnetic steering, the straight tip of the guidewire was naturally directed toward the aneurysm (at the apex of the carotid siphon) as can be seen in **Figures 5-9A** (00:04). To prevent the guidewire tip from contacting the inner wall of the aneurysm upon further advancement, the actuating magnet was placed above the carotid siphon for repulsive steering (**Figures 5-8**, **B** and **C**; 00:15), under which the guidewire tip was directed toward the descending segment of the carotid siphon so that it could pass the acute-angled corner without touching the aneurysm, as shown in **Figures 5-9A** (00:15). The guidewire was then further advanced up to the superior M2 segment under attractive steering at the ICA bifurcation (A1-M1 junction) to direct the distal tip to-ward the M1 branch, as shown in **Figures 5-9A** (00:24∼00:27). The guidewire was then retracted back to the MCA bifurcation while flipping and repositioning the magnet for repulsive steering to reorient the guidewire tip toward the inferior M2 segment, after which the guidewire was advanced until it reached the end of the inferior M2 segment, as shown in **Figures 5-9A** (00:40∼00:48). Again, the C-arm and the human patient models in the robot's virtual task space (**Figures 5-9C**) helped to ensure that the robot could be operated without collisions.

This set of demonstrations with realistic in vitro phantoms verifies that magnetic steering and navigation in intracranial arteries can be achieved with minimal motion of the actuating magnet through teleoperation of the system under visual feedback from real-time imaging and visualization in the presence of realistic workspace constraints. The experimental results presented from **Sections 5.1.1** to **5.1.3** demonstrate the capability of our telerobotically controlled magnetic guidewire to selectively reach the distal branches of cerebral arteries under magnetic steering, despite the presence of complex angulation and large aneurysms at the acute-angled corners in the models.

5.1.4   Compatibility with Standard Biplane Fluoroscopy

The demonstrations presented above were based on single-plane fluoroscopy. While it was possible to perform each task under single-plane imaging, we found that having two different projections under biplanar imaging could be beneficial for better state

observation of the guidewire in complex angulations of intracranial vessels. **Figure 5-10** illustrates this point by showing the same path demonstrated in **Figure 5-3A** under two different C-arm configurations—one with CRA 23° and RAO 19° for semi-anteroposterior view and the other with CRA 6° and RAO 80° for semi-lateral view, where the two projections are complementary to each other. For example, the semi-anteroposterior projection provided a better view of the guidewire tip around the small aneurysm at the ICA bifurcation, whereas the semi-lateral projection allowed better observation of the wire tip orientation at the MCA bifurcation (**Figure 5-10**).

To experimentally verify our system's compatibility with the standard biplane fluoroscopy in terms of the available workspace for the robot arm, we also performed the navigational task demonstrated in **Figure 5-9** (from the left ICA to the M2 segments with the human head phantom) in a neurointerventional biplane angiography suite, as shown in **Figure 5-11**. Based on the reconstructed 3D vessel model from rotational angiography (**Figure 5-8A**), two different projections were determined to provide clear view of all the important anatomical landmarks in the targeted path in the model vasculature, as shown in **Figure 5-11**, **A** and **B**.

The semi-anteroposterior projection (with CRA 19° and RAO 40°) showed the left ICA bifurcation (A1-M1 junction) more clearly, while the semi-lateral projection (with CRA 6° and RAO 118°) showed the aneurysm at the carotid siphon and the MCA bifurcation more clearly, as shown in **Figure 5-11**, **C** and **D**, respectively. During the navigation, the semi-lateral projection helped to better identify the guidewire tip orientation at locations where the semi-anteroposterior projection alone might not suffice, allowing for safer manipulation of the guidewire with reduced potential risks of the aneurysm present on the path being touched or struck by the guidewire. Throughout the entire navigation under biplane fluoroscopy, the actuating magnet approached the head space most closely when steering the magnetic guidewire at the carotid siphon with an aneurysm in the left ICA. The corresponding magnet position and robot configuration are visualized and shown from different perspectives in **Figure 5-11**, **E** and **F**, respectively. This reveals that there was a sufficient gap between the magnet and the head surface even when the magnet was closest.
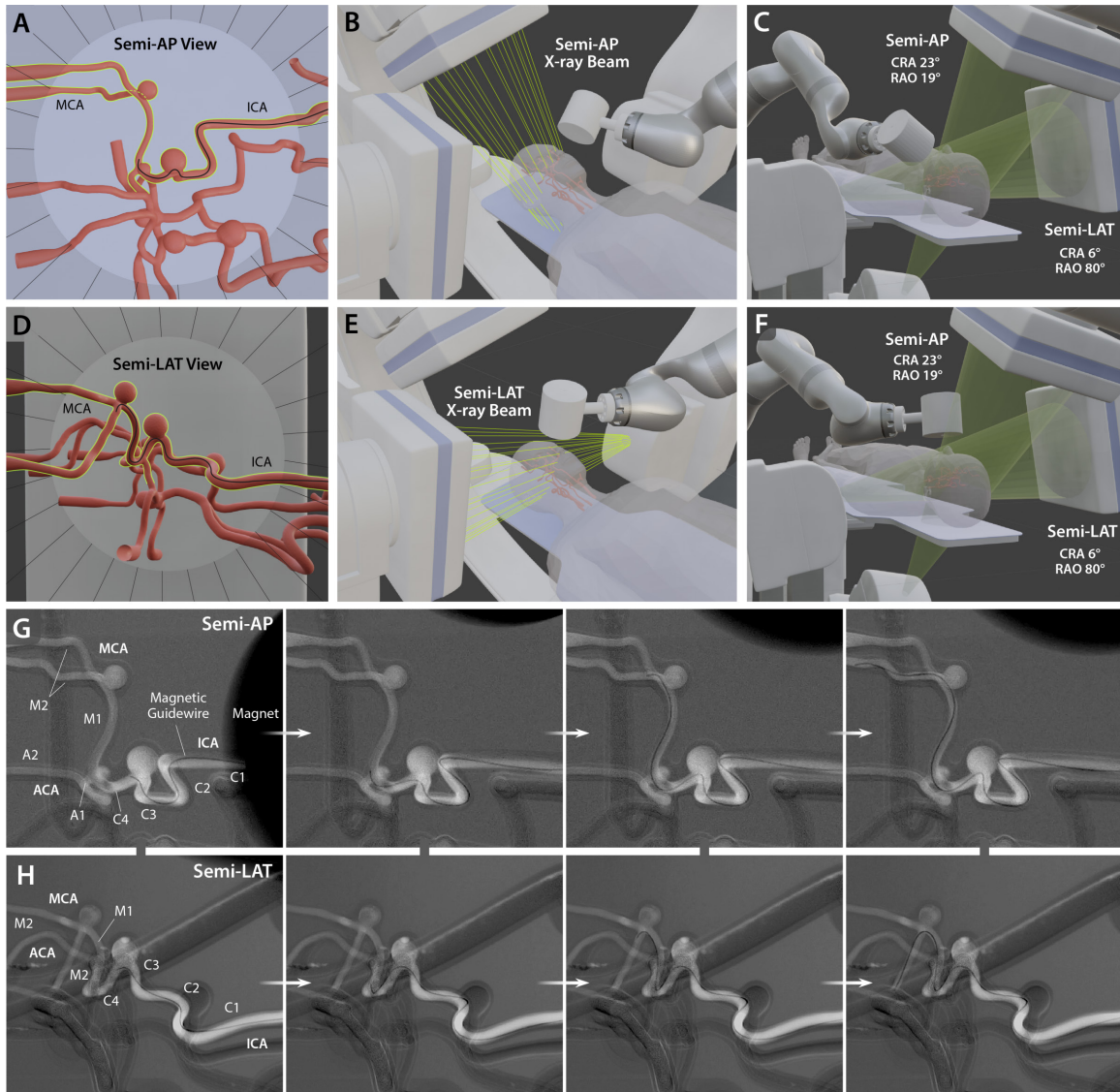
Figure 5-10: Simulated biplane fluoroscopy based on combination of two monoplane results and C-arm configurations. (**A**-**C**) When the guidewire tip is at the internal carotid artery (ICA) bifurcation (A1-M1 junction), the semi-anteroposterior (AP) projection can best visualize the tip movement. For effective steering of the guidewire tip at the ICA bifurcation, the actuating magnet is positioned mostly sideways with its movement in the lateral direction, and the magnet would not block the view of the guidewire tip on the semi-AP projection. (**D**-**F**) When the guidewire tip reaches the middle cerebral artery (MCA) bifurcation (M1-M2 junction), the semi-lateral (LAT) projection provides a clearer view of the guidewire tip deflection, which is now driven by the magnet moving mostly in the vertical direction. Therefore, the magnet would not block the view of the guidewire tip on the semi-LAT projection. (**G**) Semi-AP and (**H**) semi-LAT monoplane fluoroscopic images of magnetic navigation in the same vascular path are combined and synchronized to simulate biplane settings with simultaneous projections. As illustrated in (**C**) and (**F**), the available workspace is sufficient for the robot arm to manipulate the magnet.
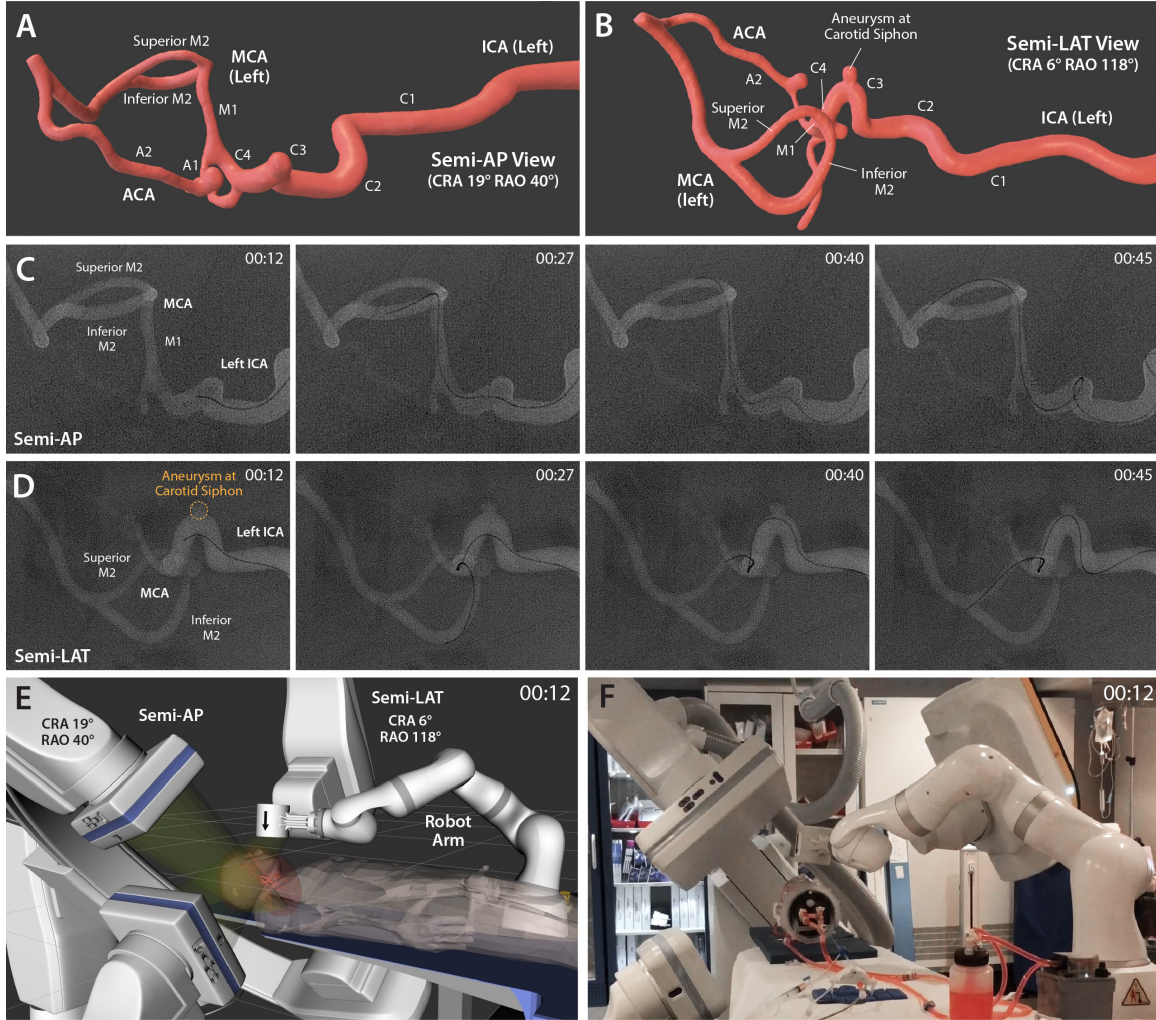
Figure 5-11: Experimental demonstration of magnetic steering and navigation under biplane x-ray fluoroscopy. (**A**) Semi-anteroposterior (AP) view of the targeted path from the left ICA to MCA providing clear view of the ICA bifurcation (A1-M1 junction). (**B**) Semi-lateral (LAT) view providing clear view of the aneurysm at the carotid siphon and the superior and inferior M2 segments at the MCA bifurcation. (**C-D**) Fluoroscopic images of the magnetic guidewire navigating in the target vasculature from the two different projections (semi-AP with CRA 19° and RAO 40° and semi-LAT with CRA 6° and RAO 118°). (**E-F**) Real-time visualization and actual view of the teleoperated robot arm under the biplane fluoroscopy setting. The available workspace between the two C-arms was sufficient for the robot arm to manipulate the magnet around the head phantom.

Overall, the available workspace between the two C-arms was sufficient for the robot arm to manipulate the magnet around the head phantom (or equivalently the virtual patient's head shown in **Figure 5-11E**) without collisions while steering the guidewire in the intracranial vessels. This validates that our telerobotic neurointerventional system is also compatible with standard biplane fluoroscopy based on a

pair of C-arms for simultaneous projections from two different angles. This result also suggests that our platform based on a compact, lightweight robot arm could be a cost-efficient alternative to the existing magnetic navigation systems in realizing robotic telesurgery for stroke intervention.

While single-plane imaging sufficed for most of the navigational tasks demonstrated, biplanar imaging offered benefits when identifying complex angulations of intracranial vessels. In this light, standard biplane fluoroscopy may be used when our system is operated in comprehensive stroke centers or tertiary hospitals that are equipped with biplane angiography suites. It is worth noting, however, that primary care centers in rural areas are not necessarily equipped with biplane systems due mainly to higher acquisition and maintenance costs. Recent studies [155, 156, 157] have shown that experienced neurointerventionalists can perform complex endovascular procedures such as mechanical thrombectomy equally safely and effectively on monoplane systems by utilizing angulation or rotation of the C-arm as they do the same procedures on biplane systems. For these reasons, in the context of telerobotic stroke intervention, we envision that our system could allow the experienced interventionalists at large institutions to perform surgical tasks remotely on patients at their local hospitals equipped with monoplane fluoroscopy systems.

5.2 Steering and Navigation Performance Evaluation

5.2.1 In Vivo Verification with Porcine Artery Model

The series of in vitro phantom studies allowed us to assess the physical and mechanical properties of the magnetic guidewire, such as radiopacity, stiffness, lubricity, and durability, in addition to the steering performance in the simulated human neurovascular anatomy with clinically challenging tortuosity and disease states. While indispensable, performance evaluation in vitro based on anatomical models in general does not fully characterize all clinical experiences, outcomes, and risks [16]. To verify our system's performance under realistic in vivo conditions while assessing the viscoelastic and physiological responses of blood vessels during the endovascular

manipulation, we conducted animal testing using a porcine model.

Although pigs have been considered as excellent experimental animals for medical research because of the similarities between human and porcine biology [168], their head and neck geometry and intracranial arterial anatomy are quite different from those of humans (**Figure 5-12A**). For example, in the pig exists a small and dense network (i.e., plexus) of interconnected vessels called *rete mirabile*, from which the internal carotid artery originates intracranially. In addition, the porcine intracranial arteries are much smaller in diameter (1 mm or less) than the human intracranial arteries (2 to 5 mm), and two middle cerebral arteries (MCAs) emerge from the internal carotid artery (ICA) in each hemisphere of the pig unlike human anatomy.

In a pivotal paper, Carniato et al. reported an animal model for in vivo evaluation of neuroendovascular devices based on the porcine brachial artery in the flexed forelimb position (**Figure 5-12B**), which is to replicate the clinically challenging tortuosity of the human ICA at the carotid siphon [169]. Following the reported protocol for the porcine brachial artery tortuosity model, we evaluated our system's steering and navigation performances in the porcine brachial artery with accentuated tortuosity in the maximally flexed position, as presented in **Figure 5-13**.
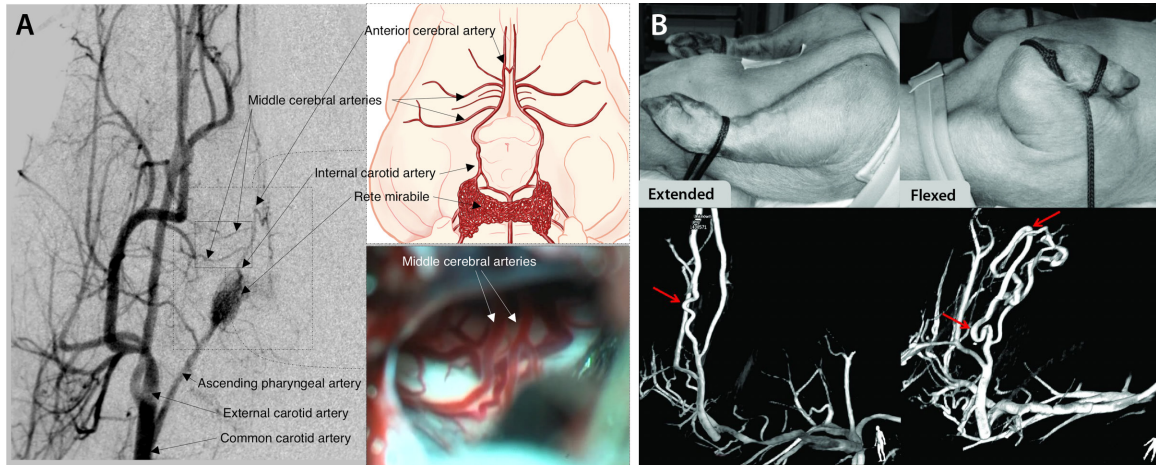
Figure 5-12: Porcine brachial artery tortuosity model for testing neuroendovascular devices. (**A**) Porcine neurovascular anatomy with a network of small, interconnected vessels called *rete mirabile* and two branches of middle cerebral artery emerging from the internal carotid artery in each hemisphere [168]. (**B**) Porcine brachial artery in the extended and fully flexed forelimb positions and the change in tortuosity of the brachial artery [169].

In vivo animal testing setup: A female Yorkshire swine of 56 kg was used for our animal testing. All procedures were conducted in accordance with the protocol approved by the Institutional Animal Care and Use Committee (IACUC) of University of Massachusetts Medical School and the Committee on Animal Care (CAC) of Massachusetts Institute of Technology. Following the previously reported protocol [169], the swine was anesthetized and maintained with mechanical ventilation under continuous monitoring of its physiologic status. A 10-Fr hemostatic introducer (Check-Flo Performer® Introducer, Cook Medical) was placed in the right femoral artery by using a modified Seldinger technique. A 0.035-inch diagnostic guidewire (Glidewire, Terumo) was manually manipulated under x-ray fluoroscopy to reach the brachial branch of the right subclavian artery, and a 7-Fr guide catheter (Destination® Guiding Sheath, Terumo) was advanced manually over the diagnostic guidewire to be placed in the proximal brachial artery for contrast injection and angiography. After removing the diagnostic guidewire, the magnetic guidewire was then advanced up to the proximal brachial artery to initiate the preclinical evaluation of magnetic steering and navigation through real-time teleoperation of the system.

First, a series of images of the target vasculature in the right forelimb was obtained from 3D rotational angiography while injecting the contrast agent through a 7-Fr guide catheter positioned in the brachial branch of the subclavian artery in the flexed forelimb position (**Figure 5-13A**). The acquired images were then reconstructed into a 3D vessel model (**Figure 5-13B**), which allowed for a detailed view of the vascular structure from different perspectives for preprocedural planning. Based on the reconstructed 3D vessel model, a semi-anteroposterior projection was chosen to provide clear view of all the side branches (numbered in **Figure 5-13**, **B** and **D**) present along the target path in the brachial artery, through the C-arm configuration with CRA 4° and LAO 34° (**Figure 5-13C**). Then, digital subtraction angiography was performed to visualize the target vasculature on the live fluoroscopy images from the chosen projection. The vessel roadmap taken from the angiography was graphically overlaid on top of the fluoroscopic images for clear representation, and the guidewire was highlighted to make it clearly visible in **Figure 5-13D**.
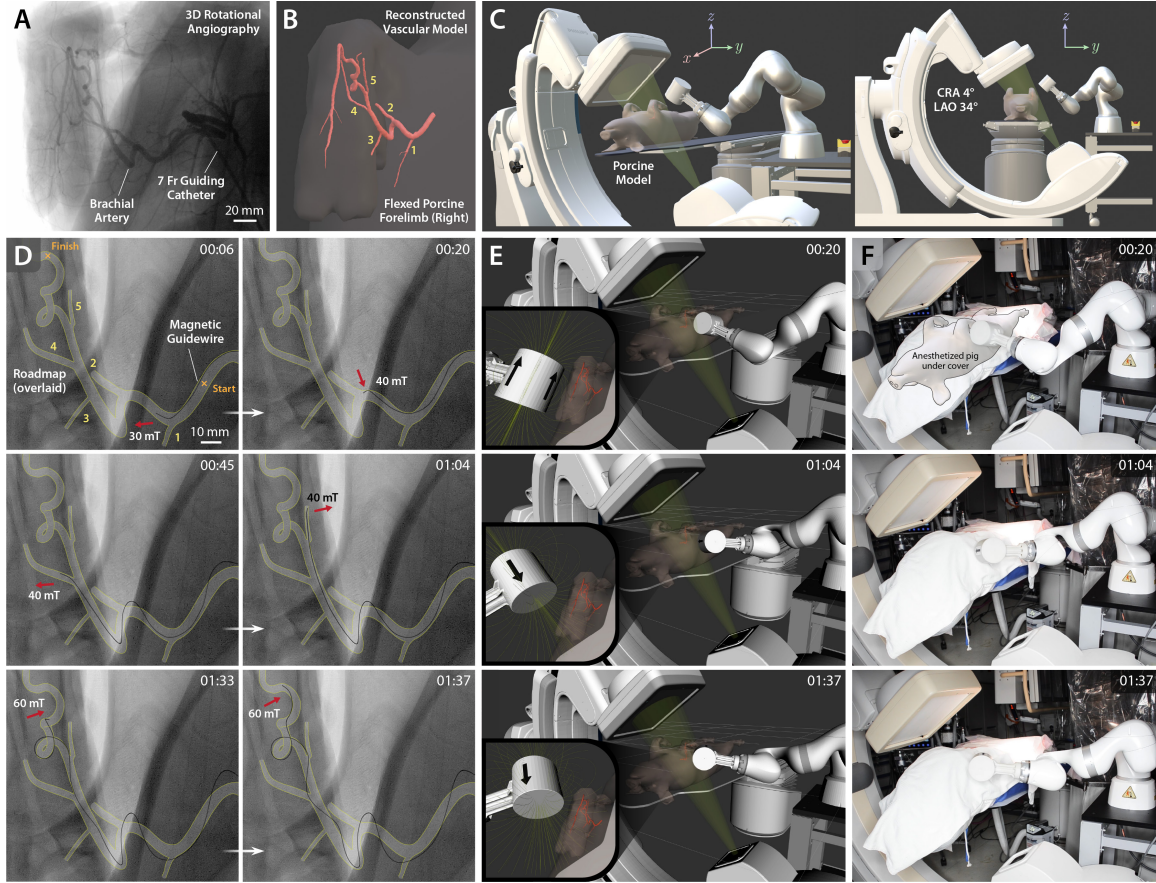
Figure 5-13: In vivo demonstration of telerobotically controlled magnetic navigation in porcine brachial artery. (**A**) 3D rotational angiography of the porcine brachial artery with accentuated tortuosity in the maximally flexed forelimb position to replicate the tortuosity of the human carotid siphon. (**B**) Reconstructed 3D model of the target vasculature viewed from a semi-anteroposterior (AP) projection with all the side branches along the path clearly shown and numbered. (**C**) Graphical representation of the experimental setup with the C-arm configuration for the chosen semi-AP projection with CRA 4° and LAO 34°). (**D**) Fluoroscopic images of the magnetic guidewire navigating in the target vasculature under telerobotically controlled magnetic steering avoiding entering undesired branches (1 and 2) at the acute-angled corners (00:06∼00:20). The guidewire was steered to selectively reach the side branches (4 and 5) present on the path (00:45∼01:04) and then reach the goal after negotiating the tortuous region with 360-degree and 90-degree turns (01:33∼01:37). (**E**) Real-time visualization of the robot arm in a virtual environment simulating the physical testing setup including the C-arm and the anesthetized pig on the operating table. The target vasculature and the magnetic field lines around the actuating magnet are also visualized in real time to enable preprocedural planning of the robot arm's motion for spatial positioning of the magnet relative to the target vasculature. (**F**) Actual view of the robot arm positioning the magnet based on the prescribed magnet position and orientation for the steering and navigational task upon the operator's command from the remote-control console. Out of respect for the animal and to comply with the Institutional Animal Care and Use Committee (IACUC) policy on photography of research animals, the pig was covered during the video recording.

The first two side branches (1 and 2 in **Figure 5-13**, **B** and **D**) in the proximal brachial artery were located at the acute-angled corners, into which the straight tip of the guidewire would have naturally been directed if it were not steered by the externally applied magnetic fields. To prevent the guidewire tip from entering the undesired branch at each corner, the position and orientation of the actuating magnet were identified such that the guidewire tip could be steered toward the desired path, using the 3D vessel model implemented in the virtual task space of the robot arm for real-time visualization and motion planning (**Figure 5-13E**).

The corresponding end-effector pose and the configuration of the robot arm were prescribed so that the actuating magnet could readily be positioned upon the operator's command from the remote-control console to steer the magnetic guidewire, as shown in **Figure 5-13**, **D** to **F** (00:06∼00:20). To demonstrate selective navigation in different branches in the distal area, the magnet pose was prescribed such that the guidewire tip could be steered to selectively reach branches 4 and 5 consecutively, as shown in **Figure 5-13**, **D** to **F** (00:45∼01:04). Lastly, the guidewire tip was advanced into the tortuous area with a 360-degree turn followed by another sharp turn before the goal location. The guidewire tip was initially directed toward the entering curve of the 360-degree turn, repelled sideways at the 90-degree corner to make its shape favorable for the sharp turn, and then advanced until it reached the goal, as shown in **Figure 5-13**, **D** to **F** (01:33∼01:37). It is worth noting that the x-ray fluoroscopy was intermittently stopped while repositioning the robot arm to minimize the radiation exposure to the animal as well as the staff present in the catheterization laboratory.

One noticeable difference observed from the in vivo testing above was that the guidewire in the proximal area tended to deviate more greatly from the vessel roadmap as it proceeded more distally along the path, as shown in **Figure 5-13D**, which was rarely observed in the silicone vessels during our in vitro phantom studies presented earlier. This can be attributed to the deformation of the soft blood vessels due to the stiff guidewire, which normally occurs during endovascular navigation with standard guidewires. Nonetheless, the deformation of the proximal vessels had no effect on the steering of the distal tip of the magnetic guidewire. Except for this apparent deviation

of the guidewire from the roadmap, the behavior of the magnetic guidewire in the tortuous porcine brachial artery during the steering and navigational task in vivo was close to that observed in the silicone phantoms, in terms of the device performance and characteristics such as steerability, lubricity, and durability. Notably, no adverse biological or physiological responses such as thrombosis or hemorrhagic complications due to endothelial injury such as vessel dissection or perforation were observed during the demonstrated steering and navigational task in vivo. In addition, no adverse events were observed due to the presence of the magnetic field during the setup, use, and completion of the experiment. These results validate the safety and effectiveness of the telerobotically controlled magnetic steering and navigation in complex and tortuous vasculature in realistic in vivo conditions.

5.2.2   Usability Testing and Learning Curve Assessment

Our system allows the operator to remotely control the magnetic guidewire by manipulating the actuating magnet through the robot arm while advancing or retracting the guidewire along with the microcatheter for endovascular navigation and intervention. Although the primary role of the magnetic guidewire is the same as that of conventional ones, in terms of enabling access to the target lesion to initiate interventional procedures, the way in which the magnetic guidewire is manipulated for steering purposes is quite different from the manually controlled passive guidewires based on the twisting maneuver. Hence, new users must be trained to learn how to drive the robot arm and the advancing units with the given teleoperation interface to be able to manipulate the magnetic guidewire and microcatheter under feedback from real-time imaging and visualization.

To assess the learning curve and evaluate the user experience, we conducted a pilot study with 6 participants who had no prior experiences with the developed telerobotic manipulation platform. The novice group consisted of 2 engineers with expertise in robotically assisted image-guided therapy and 4 experienced neurointerventionalists. For this learning curve assessment, we use the same 3D neurovascular phantom demonstrated in **Figure 5-3** and conducted the experiment in the catheter-

ization laboratory equipped with a standard neurointerventional angiography suite (**Figure 5-14**, **A** and **B**). The given task for learning curve assessment was endovascular navigation from the left proximal internal carotid artery (ICA) to the inferior M2 segment of the left middle cerebral artery (MCA), as shown in **Figure 5-14C**.
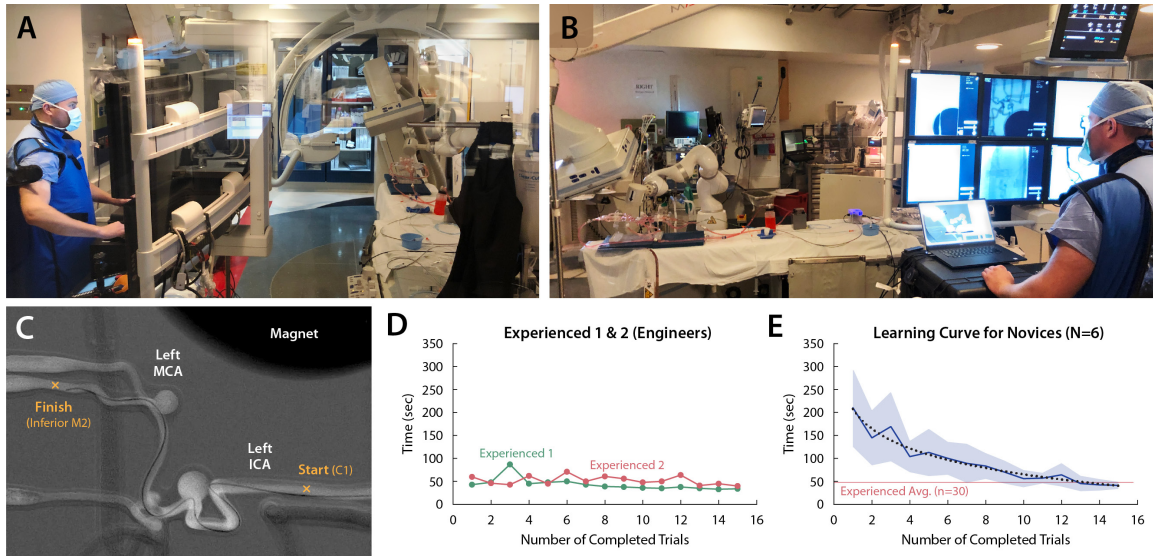
Figure 5-14: **Learning curve assessment for magnetic steering and navigation through real-time teleoperation of the system under fluoroscopic imaging.** (**A-B**) Experimental setup for the usability testing and learning curve assessment using a 3D neurovascular phantom under single-plane x-ray fluoroscopy. (**C**) Defined navigational task for the learning curve assessment from the left internal carotid artery (ICA) to the inferior M2 segment of the middle cerebral artery (MCA). (**D**) Time it took for experienced users to complete the defined task versus the number of completed trials (15 trials each from 2 experienced users). (**E**) Average learning curve for the novice group (2 engineers and 4 neurointerventionalists with no prior experience with the developed system) based on the average procedural time (mean ± standard deviation) for each trial. The mean values are fitted with a logarithmic curve, and the standard deviation is given as the shaded area below/above the curve. The individual learning curves are presented in **Figure 5-15**. Comparison of the navigational performance of an experienced neurointerventionalist with the manually controlled passive guidewire and the telerobotically controlled magnetic guidewire (after training) for the same navigational task is available in **Figure 5-16**.

Learning curves were obtained by tracking procedural time taken for the defined task as a metric for performance over 15 consecutive trials for each participant. Prior to data collection from the novice group, procedural time was measured from 2 experienced users (over 15 consecutive trials for each) for comparison. As shown in **Figure 5-14D**, the experienced group displayed relatively consistent performance with small

deviations over the repeated trials. On average, it took 47.8 ± 12.2 s (mean $\pm$ standard deviation) for the experienced group to complete the given task. The novice group was trained by the experienced users to learn the magnetic steering principles. As part of the training curriculum, each novice performed 3 practice runs to familiarize themselves with real-time teleoperation of the system under the guidance of the experienced users before starting to track the procedural time.

The average learning curve of the novice group is presented in **Figure 5-14E**, with the individual learning curves presented as well in **Figure 5-15**, where each dataset was fitted with a logarithmic curve. The average learning curve was short, exhibiting fast decay of the measured time over the number of completed trials. On average, the novice group was able to reduce the procedural time by half after around 5 trials and reach the similar proficiency level of the experienced group after around 12 trials (**Figure 5-14E**). The average of the entire trials ($n = 90$; 15 trials from each of the 6 novices) was 92.8 ± 61.7 s, which was almost double that of the experienced group with much greater deviations.
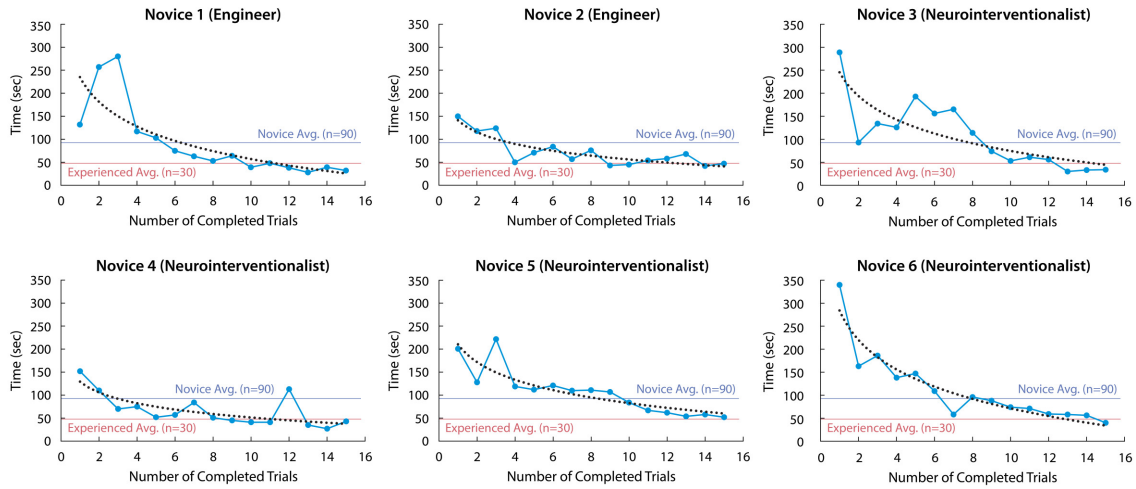

Figure 5-15: Individual learning curves for novices performing magnetic steering and navigation through real-time teleoperation of the system under fluoroscopic imaging. The average time it took for each participant in the novice group (2 engineers and 4 neurointerventionalists with no prior experience with the developed system) to complete the defined task in **Figure 5-14C** versus the number of completed trials (fitted with a logarithmic curve), which is compared with the average procedural time for the experienced group ($n = 30$; 15 trials from each of the 2 experienced users) as well as the total average of the novice group ($n = 90$; 15 trials from each of the 6 novices).

143

One of the main difficulties faced by the novices while performing the given task was the presence of the large aneurysm at the acute-angled corner in the carotid siphon, which imposed a navigational challenge that turned out to be the main rate-limiting factor. Even though the guidewire tip was seemingly directed correctly toward the desired branch (C4; see **Figure 5-1A**), it tended to exit the desired branch and inadvertently fall into the aneurysm upon further advancement of the guidewire when the actuating magnet was wrongly positioned or oriented, producing insufficient repulsive steering torque. This navigational challenge, however, became certainly manageable after a few trials and could eventually be overcome by every participant, leading to the time reduction. The average of the last 5 trials of the novice group ($n = 30$; last 5 trials from each of the 6 novices) was 50.1 ± 17.4 s, which was close to the average procedural time (47.8 ± 12.2 s) of the experienced group ($n = 30$; 15 trials from each of the 2 experienced users). We found no statistically significant difference between the two datasets from Welch's t-test (two-sample t-test assuming unequal variances). These results verify that our designed system requires a relatively short period of time for new users to learn how to navigate clinically challenging anatomy with the magnetic guidewire through real-time teleoperation of the system.

5.2.3   Comparison with Conventional Passive Guidewires

We further evaluated the steering and navigational performance of our telerobotically controlled magnetic guidewire in comparison with that of a manually manipulated conventional guidewire by an experienced neurointerventionalist as shown in **Figure 5-16A**. For this comparison of the steering and navigational performance, the interventionalist performed the same navigational task demonstrated earlier in **Figure 5-13C** using a standard 0.014-inch neurovascular guidewire (Synchro 2, Stryker) with a shapeable distal tip for steering purposes (**Figure 5-16**, **B** and **C**). The procedural time it took for the interventionalist to complete the task was measured over 10 consecutive trials (**Figure 5-15D**). Before measuring time, the interventionalist was given several practice trials to familiarize himself with the given vascular anatomy and to produce steady-state performances for fair comparison.
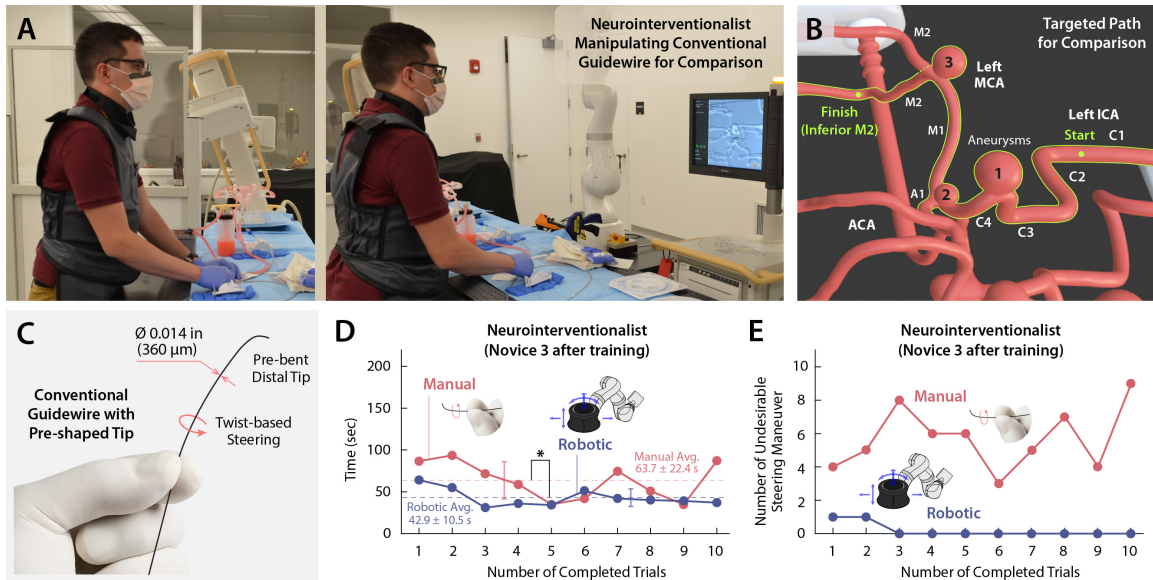
Figure 5-16: Clinician's performance with a telerobotically controlled magnetic guidewire in comparison with that with a manually controlled passive guidewire. (**A**) An experienced neurointerventionalist manually manipulating a conventional neurovascular guidewire with pre-bent distal tip for twist-based steering under real-time x-ray fluoroscopy. (**B**) Defined navigational task for the performance comparison from the left internal carotid artery (ICA) to the inferior M2 segment of the middle cerebral artery (MCA). (**C**) Conventional neurovascular guidewire (Synchro 2, Stryker) with an outer di-ameter of 0.014 inches (360 m) and pre-bent (shapeable) distal tip. (**D**) Comparison of the procedural time (average ± standard deviation) for the trained neurointerventionalist to complete the defined navigational task using the manually controlled passive guidewire and the telerobotically controlled magnetic guidewire over 10 consecutive trials ($n = 10$) for each experiment. Error bars with whiskers indicate the standard deviation of the measured time, and statistically significant differences are indicated with asterisks (*$P < 0.05$). The interventionalist has +4 years of training and experiences in endovascular neurointervention based on conventional guidewire manipulation and was trained with the telerobotic manipulation system for less than 1 hour (see Novice 3 in **Figure 5-15**). (**E**) The number of incidents with undesirable guidewire behavior such as the distal tip colliding with or looping inside aneurysms or falling into undesired branches during the given navigational task.

One of the navigational challenges encountered was the acutely angled left carotid siphon with a large aneurysm (Aneurysm 1 in **Figure 5-16B**), where the 90°-angled tip of the guidewire frequently failed to pass the sharp corner due to the presence of large open space inside the aneurysm. Crossing this corner with the pre-shaped guidewire was successful only in 5 trials (Trials 3, 4, 5, 6 and 10) out of the 10 consecutive trials. In those 5 successful trials, however, the guidewire's pre-bent tip was prone to fall into the posterior communicating artery (PCoA; see **Figure 5-1A**)

upon further advancement after passing the aneurysm, which was unintended. When the guidewire continuously failed to cross the corner (Trials 1, 2, 7, 8, and 9), the interventionalist chose to loop the guidewire in the aneurysm to access the desired branch. However, this guidewire looping maneuver can be potentially dangerous, especially in ruptured or in partially thrombosed aneurysms due to the risk of bleeding or displacement of thrombus [170], which can lead to undesirable situations due to hemorrhagic or thromboembolic complications.

We also noticed that the pre-bent tip of the guidewire occasionally latched onto a small aneurysm (Aneurysm 2 in **Figure 5-16B**) located at the distal end of the supraclinoid (C4) ICA, as can be seen in **Figure 5-17A** (00:42). At the MCA bifurcation with another aneurysm (Aneurysm 3 in **Figure 5-16B**), the pre-shaped guidewire also frequently failed to access the desired inferior M2 branch, encountering a similar navigational challenge due to the presence of an aneurysm at the acutely angled corner in 6 trials (Trials 3, 4, 5, 7, 8, and 10). In these 6 trials, accessing the desired branch required another potentially risky looping maneuver to pass the corner with the aneurysm, as shown in **Figure 5-16F** (00:58∼01:14). Overall, the manually controlled passive guidewire showed unpredictable behavior in those clinically challenging areas, causing several unintended or undesirable incidents such as the guidewire tip colliding with aneurysms, looping inside aneurysms, or falling into undesired branches. The number of such undesirable events encountered while manually manipulating the guidewire was counted for each trial as presented in **Figure 5-16E**.

Unlike the manually controlled passive guidewire, the telerobotically controlled magnetic guidewire enabled access to the clinically challenging branches without requiring a dangerous looping maneuver in the aneurysm sac and obviated unexpected or unintended guidewire tip movements, as can be seen in **Figures 5-16E** and **5-17B**. Overall, the average time to complete the given task was shorter with the telerobotically controlled magnetic guidewire (42.9 ± 10.5 s) when compared with the manually controlled passive guidewire (63.7 ± 22.4 s), and we found statistically significant difference in the procedural time between the two approaches ($P < 0.05$) during the 10 consecutive trials.

A   Manually Controlled Passive Guidewire with Pre-bent Tip by Neurointerventionalist

00:08 — Insufficient tip angle for acute-angled corner — Manual–Trial 7

00:11 — Insufficient tip angle for acute-angled corner

00:25 — Pre-bent tip stuck in acute-angled corner

00:26 — Collision with aneurysm upon sudden release — 10 mm

00:42 — Pre-bent tip latching onto the 2nd aneurysm

00:49 — Insufficient tip angle for acute-angled corner

00:58 — Guidewire looping inside the aneurysms

01:14 — Overall riskier maneuver despite the longer time required for navigation

B   Telerobotically Controlled Magnetic Guidewire with Steerable Tip by Neurointerventionalist

00:14 — Magnetically Steerable Tip — Magnet — Robotic–Trial 7

00:30 — On-demand tip bending at acute-angled corners

00:38 — On-demand tip bending at acute-angled corners

00:42 — Safer and quicker access to hard-to-reach target — 10 mm

Figure 5-17: Comparison of the steering and navigational performances of the manually controlled passive guidewire and the telerobotically controlled magnetic guidewire. (**A**) The pre-bent tip of the conventional guidewire tended to undergo unpredictable and undesirable motion while making frequent contact with the aneurysms present along the path due to the limited steering capability based on twisting maneuver. (**B**) The magnetic guidewire demonstrated smooth navigation in the narrow and tortuous pathways without any unintended distal tip movement or contact with the aneurysms along the navigated path due to its active steering.

Figure 5-18 illustrates one of the inherent limitations with the conventional passive guidewires with pre-shaped tips. In this demonstration, the same path demonstrated in **Figure 5-5** from the right ICA to the aneurysm at the right M1-M2 junction was navigated using the standard neurovascular guidewire with its 90° tip initially. This single-angled tip, however, was not ideal for the given path and failed to cross the wide-neck aneurysm at the corner, as can be seen in **Figure 5-18A**. In the second trial after reshaping into a double-angled tip, the modified tip was still unable to cross the large gap within the aneurysm, as shown in **Figure 5-18B**. Successful crossing was made possible only after another reshaping maneuver to make the distal tip triple angled, as can be seen in **Figure 5-18C** (00:00∼00:10). The increased radius of curvature, however, resulted in greater resistance due to the dragging of the bent tip on the vessel wall, causing the guidewire to buckle to form a loop inside the wide-neck aneurysm at the corner, as observed in **Figure 5-18C** (00:14∼00:34). To

circumvent these seemingly contradicting situations, in practice, multiple reshaping of the distal tip as well as repetitive retraction and advancement of the guidewire and microcatheter are necessary, which inevitably increases the overall procedural time and hence the radiation exposure to the patient and interventionalists.
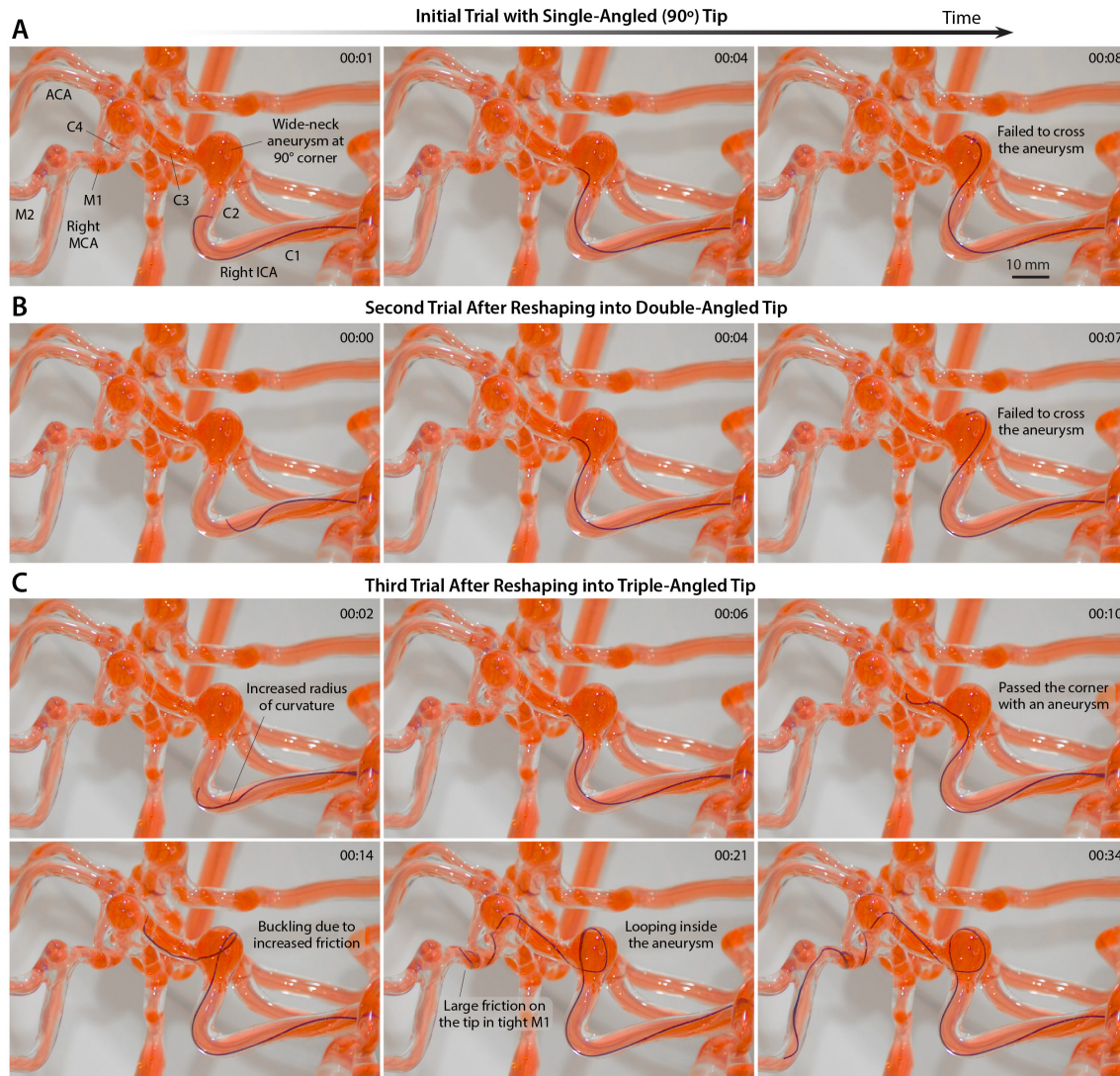
Figure 5-18: Illustration of the functional limitations inherent in manually controlled passive guidewires with shapeable distal tips. (**A**) Initial trial of navigation in the right ICA with a wide-neck aneurysm at the 90° corner of the petrous (C2) segment with a conventional neurovascular guidewire with a single-angled (90°) distal tip which was not ideal to cross the wide-neck aneurysm. (**B**) Second trial after reshaping into a double-angled tip, which also failed to cross the large gap within the aneurysm. (**C**) Third trial after another reshaping maneuver to make the distal tip triple angled, which resulted in greater resistance due to the dragging of the bent tip on the vessel, causing the guidewire to buckle to form a loop inside the wide-neck aneurysm at the corner (00:14~00:34).

While conducting the experiments to compare the steering and navigational performance of our telerobotically controlled magnetic guidewire and that of the manually controlled passive guidewire in **Figures 5-16** and **5-17**, we also assessed the operator's workload in each trial using the NASA Task Load Index [171] as presented in **Figure 5-19**. We found statistically significant ($P < 0.05$) reduction in the operator's workload in terms of the mental demand, temporal demand, performance, effort, and frustration with the telerobotically controlled magnetic guidewire when compared with the manually controlled passive guidewire.
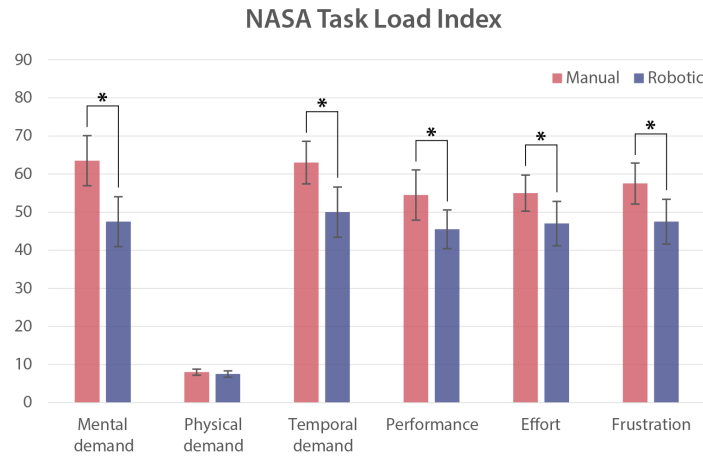
Figure 5-19: Workload assessment during the comparison of performances with the manually controlled passive guidewire and with the telerobotically controlled magnetic guidewire. Mental demand indicates how much mental and perceptual activity was required. Physical demand indicates how much physical activity was required. Temporal demand indicates how much time pressure the operator felt due to the rate or pace at which the tasks occurred. Performance indicates how successful the operator thinks he/she was in accomplishing the goals of the task. It should be noted that a lower score indicates that the operator was more satisfied with his/her performance during the task. Effort indicates how hard the operator had to work both mentally and physically to accomplish his/her level of performance. Frustration level indicates how discouraged and stressed the operator felt during the task. Error bars indicate standard errors of the mean scores from the 10 trials ($n = 10$). Statistically significant differences are indicated with asterisks ($^*P < 0.05$).

These experimental results with quantitative comparison data demonstrate that the telerobotically controlled magnetic guidewire can help to reduce the procedural time as well as the potential risk of vascular perforation or aneurysm rupture while allowing for the operator to work remotely to minimize the radiation exposure. The results also indicate that the telerobotically controlled magnetic navigation could be

149

more predictable and less dependent on the experience and skill of the operator when compared with the manually controlled passive guidewire. This performance comparison was conducted by only one interventionalist and hence further studies based on a multiuser trial will be required to confirm the comparison results. Nonetheless, given the technical challenges and functional limitations inherent in conventional guidewires with shapeable or pre-shaped distal tips, we believe that the demonstrated steering and navigational capabilities of our telerobotic neurointerventional system suggest its potential for improving the quality of endovascular neurosurgery by enabling safer and quicker access to hard-to-reach lesions in the complex neurovasculature.

5.2.4   Comparison with Magnet-tipped Guidewires

Lastly, we compared the steering and navigational performance of our magnetic soft continuum guidewire with that of the conventional magnet-tipped design based on a rigid, finite-sized magnet attached to the distal end of a flexible guidewire. The magnet-tipped guidewire for comparison was fabricated by attaching a cylindrical NdFeB magnet (axially magnetized) with diameter of 400 μm and length of 4 mm at the distal end of a 0.016-inch neurovascular guidewire (Headliner, Terumo). The potted magnet was coated with a thin layer of soft composite based on TPU mixed with tungsten powder, where the tungsten particles were used as nonmagnetic radiopaque fillers. For fair comparison, other mechanical properties and the dimension of the magnet-tipped guidewire were designed to be close to those of our magnetic guidewire except for the distal portion with the embedded rigid magnet. The outer diameter of the distal tip of the magnet-tipped guidewire was approximately 600 μm, due to the presence of the finite-sized magnet within the polymer jacket, and further miniaturization was practically infeasible as the potted NdFeB magnet was prone to brittle fracture during the fabrication process when even thinner magnets were used to reduce the diameter.

We hypothesized that the rigid and stiff distal tip of the magnet-tipped guidewire could make it difficult to navigate narrow and winding pathways in the distal cerebral vasculature as it lacks the ability to conform to the given environment. To validate

this, we chose to navigate the distal branches of cerebral arteries in the 2D neurovascular model, which was shown earlier in **Figure 5-6**, using our magnetic guidewire and the magnet-tipped guidewire. For fair comparison of their navigational performances, both were manipulated using our telerobotic neurointerventional platform.
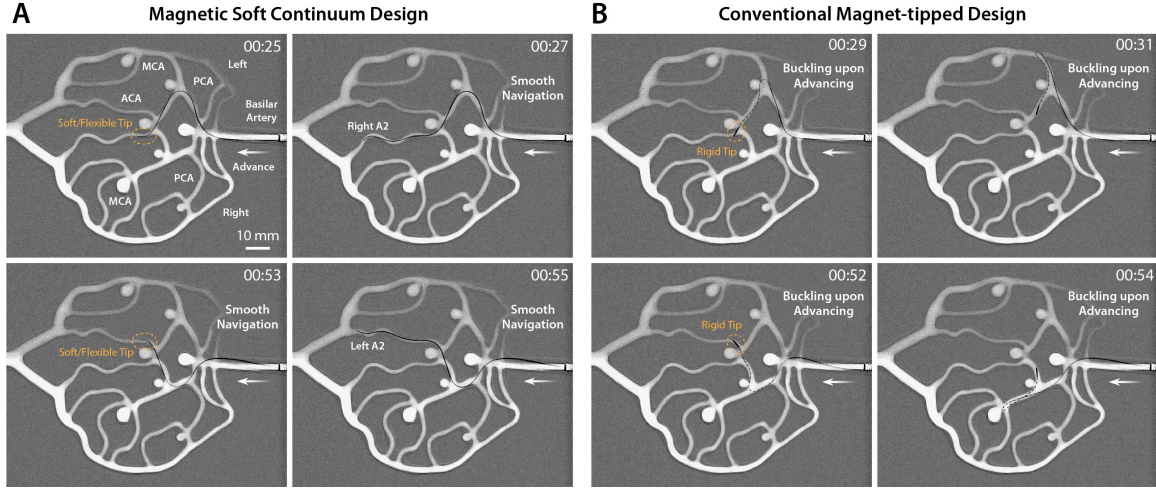
Figure 5-20: Comparison of steering and navigational performance with the conventional magnet-tipped design. (**A**) The magnetic soft continuum design with a soft and flexible distal tip and (**B**) the conventional magnet-tipped design with a rigid and stiff distal tip. The flexible distal tip of the magnetic soft continuum robot enables smooth navigation in the tight and tortuous areas in the ACA, whereas the rigid and stiff tip of the magnet-tipped guidewire prevents it from working through the target vasculature due to the lack of ability to conform to the given environment, which leads to the buckling and herniation of the guidewire in the middle of the navigated path upon further advancement. ACA: anterior cerebral artery, MCA: middle cerebral artery, PCA: posterior cerebral artery.

As demonstrated in **Figure 5-20B**, the magnet-tipped guidewire tended to buckle in the middle of the navigated path upon further advancement and herniate into the open space of an undesired branch, as the rigid distal tip did not allow the guidewire to pass the sharp corners in the tight areas of the ACA. This undesirable event was repeatedly observed in other similarly narrow and winding pathways in the model neurovasculature, validating the above-mentioned hypothesis. On the contrary, our magnetic soft continuum guidewire demonstrated the ability to conform to the environment using its soft and flexible distal tip and smoothly navigated the narrow and winding pathways of the model cerebral vasculature, as can be seen in **Figure 5-20A**. This result illustrates the unique advantage of our magnetic soft continuum

design over the conventional magnet-tipped guidewires in realizing structurally simple yet effective means of magnetic steering at submillimeter scales for neurovascular applications.
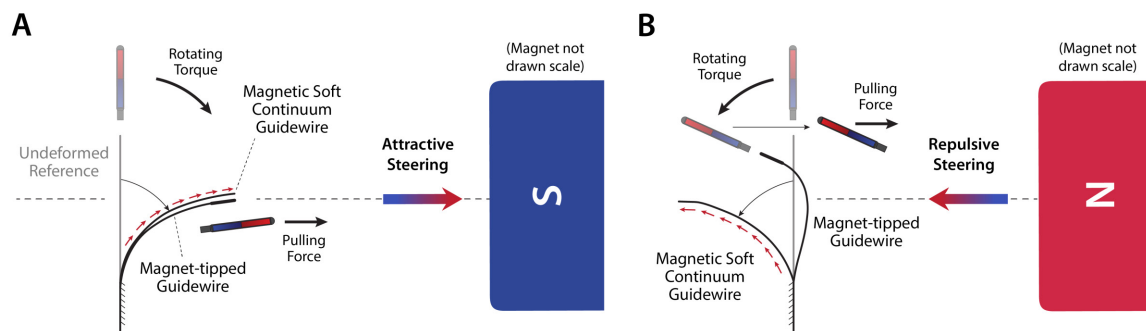
Figure 5-21: Comparison of the behavior of a magnetic continuum guidewire and a magnet-tipped guidewire in attractive and repulsive steering modes with a single actuating magnet. The magnetic continuum guidewire exhibits relatively symmetric behavior in the attractive (**A**) and repulsive (**B**) steering modes, whereas the magnet-tipped guidewire shows largely asymmetric behavior due mainly to the strong attractive force acting on the embedded magnet at the end towards the actuating magnet in both steering modes.

Another key difference between our magnetic soft continuum design and the conventional magnet-tipped design lies in their steering principles. We know from Equation (2.46) that the magnetic force can be suppressed by minimizing the effect of field gradients while reducing the strength of the object's magnetic moment. By reducing the strength of the overall magnetic moment through dispersing small magnetic particles instead of embedding finite-sized permanent magnets, magnetic forces acting on our magnetic soft continuum guidewire can be effectively suppressed. In other words, our magnetic guidewire with uniformly distributed magnetic particles have much diluted magnetization across the device, whereas the conventional magnet-tipped design with a finite-sized magnet attached to its end has highly concentrated and localized magnetic moment at the distal tip. Because the magnetic force always tends to attract the embedded magnets toward the actuating magnet, steering control of the magnet-tipped devices using a single magnet can be easily complicated by the coupled interaction from the magnetic torques and forces, exhibiting largely asymmetric behavior between the attractive and repulsive steering modes, as illustrated in **Figure 5-21**. On the contrary, our magnetic soft continuum guidewire can utilize

the magnetic torque as the primary source of actuation in steering control while experiencing negligible influence from the magnetic force to maintain almost symmetric behavior in both attractive or repulsive steering modes.

5.3 Telerobotically Assisted Therapeutic Procedures

As demonstrated in **Section 5.1**, the primary role of our magnetic guidewire is to provide safe and fast access to target lesions in the complex neurovasculature. Once the guidewire reaches the target lesion, a microcatheter is advanced over the guidewire along the navigated path, after which the guidewire is withdrawn. Then, the microcatheter serves as a physical channel through which the therapeutics can be delivered to the target lesion. For endovascular treatments of aneurysms or stroke, therapeutic devices such as embolization coils or a stent retriever need to be delivered to the target lesion through a microcatheter. In this section, we further demonstrate our system's capability to telerobotically assist therapeutic procedures that are commonly performed in endovascular neurosurgery such as coil embolization for treating intracranial aneurysms and clot retrieval thrombectomy for treating ischemic stroke.

5.3.1 Endovascular Treatment of Cerebral Aneurysms

Aneurysms are localized points of vessel-wall weakening that create saccular or fusiform dilatations of the vessel wall leading to risk of rupture [172]. Intracranial aneurysms are typically treated endovascularly by deploying coils through a microcatheter to promote thrombosis within the aneurysm to eliminate blood flow into the dilated area, thereby reducing the risk of rupture [173]. To demonstrate robotically assisted aneurysm coiling with our developed telerobotic neurointerventional platform, we used the same 3D neurovascular phantom with multiple aneurysms (**Figure 5-1**) that was used for benchtop verification in **Section 5.1** and **5.2**. The most distal (and hence most difficult-to-reach) aneurysms at the left and right MCA bifurcations (M1-M2 junctions) were chosen for demonstration of coil embolization through our telerobotic neurointerventional platform.
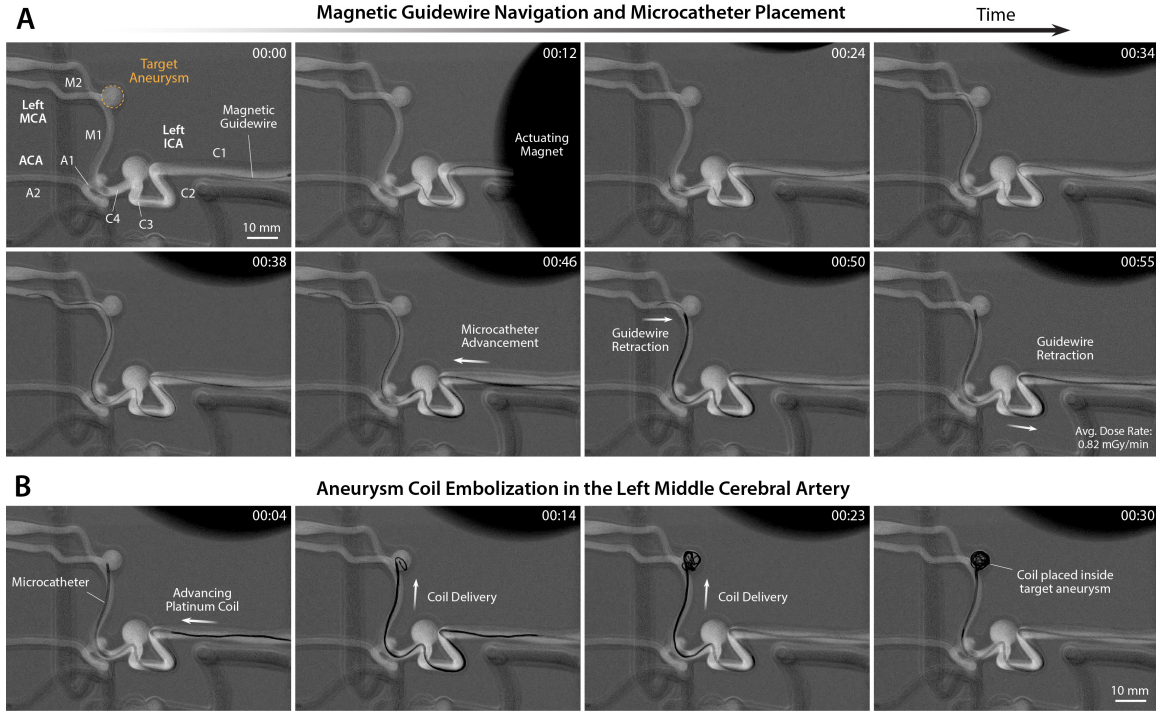
Figure 5-22: Demonstration of telerobotically assisted aneurysm coil embolization in the middle cerebral artery. (**A**) Magnetic steering and guidewire navigation up to the target aneurysm in the left middle cerebral artery (MCA) (00:00~00:38) and microcatheter placement in the target aneurysm sac while retracting the guidewire (00:46~00:55) through real-time teleoperation of the system under x-ray fluoroscopy. (**B**) Coiling of the target aneurysm by delivering embolization coils into the aneurysm sac through the placed microcatheter under joystick teleoperation of the advancing unit.

To reach the target aneurysm at the left MCA bifurcation, the magnetic guidewire was first steered in the left internal carotid artery (ICA), where a large saccular aneurysm (with an inner diameter of 9 mm) was present in the carotid siphon (**Figure 5-1**). To cross the large gap within the aneurysm while avoiding contact with the inner wall of the aneurysm, the guidewire was manipulated under repulsive steering and advanced to the ICA bifurcation (A1-M1 junction) as shown in **Figure 5-22A** (00:00~00:12). Then, the guidewire was directed toward the left M1 segment to make a 90° turn under attractive steering, without touching the small aneurysm (with an inner diameter of 5 mm) located at the distal ICA (C4 in **Figure 5-1A**), and then advanced up to the target aneurysm (with an inner diameter of 7 mm) at the left MCA bifurcation (M1-M2 junction) as shown in **Figure 5-22A** (00:24). The guidewire was then directed toward the inferior M2 segment through repulsive

steering to avoid touching the target aneurysm upon further advancement, as shown in **Figure 5-22A** (00:34∼00:38).

Then, the microcatheter was advanced up to the M1-M2 junction, after which the magnetic guidewire was retracted so that the microcatheter's distal tip could be placed inside the target aneurysm, as shown in **Figure 5-22A** (00:46∼00:55). After full retraction and withdrawal from the microcatheter, the magnetic guidewire was replaced by an embolization coil device with its push wire engaged with the guidewire advancing unit. After the device exchange, the coil was advanced and delivered through the microcatheter into the target aneurysm under the joystick control of the advancing unit, as shown in **Figure 5-22B** (00:04∼00:30). The real-time x-ray fluoroscopy confirmed successful coil placement in the target aneurysm.

We performed another aneurysm coiling with our telerobotic neurointerventional system in the most distal aneurysm at the right MCA bifurcation, as presented in **Figure 5-23A**. Two large aneurysms were present in the neurovascular phantom (**Figure 5-1**), one with an inner diameter of 9 mm at the corner in the right ICA (C2) and the other with an inner diameter of 7.5 mm at the carotid siphon (C3-C4). Both of them were imposing navigational challenges due to their presence at the acute-angled corners. The C-arm configuration was determined to provide a semi-lateral projection with caudal angulation of 18° (CAU 18°) and right anterior oblique rotation of 60° (RAO 60°).

Starting from the proximal ICA, the guidewire was magnetically steered using the oblique repulsion mode to cross the first aneurysm without touching its inner wall and then advanced up to the second aneurysm as shown in **Figure 5-23A** (00:00∼00:10). Then, the guidewire tip was directed toward the distal ICA (C4) using repulsive steering to avoid contact with the second aneurysm, after which the guidewire was advanced until its distal tip reached the right MCA bifurcation (M1-M2 junction), as shown in **Figure 5-23A** (00:30). The guidewire was then further advanced to reach the inferior M2 segment under repulsive steering, as shown in **Figure 5-23A** (00:37∼00:39), which was to ensure that sufficient distance from the target aneurysm to the guidewire tip was reserved for smooth microcatheter advancement over the

guidewire. The microcatheter was then advanced up to the target aneurysm while retracting the guidewire so that the microcatheter tip could be placed in the aneurysm sac, after which the guidewire was completely withdrawn, as shown in **Figure 5-23A** (00:39∼00:56). An embolization coil was delivered through the microcatheter under the joystick control of the advancing unit until the aneurysm became densely packed with the coil, as shown in **Figure 5-23B**.
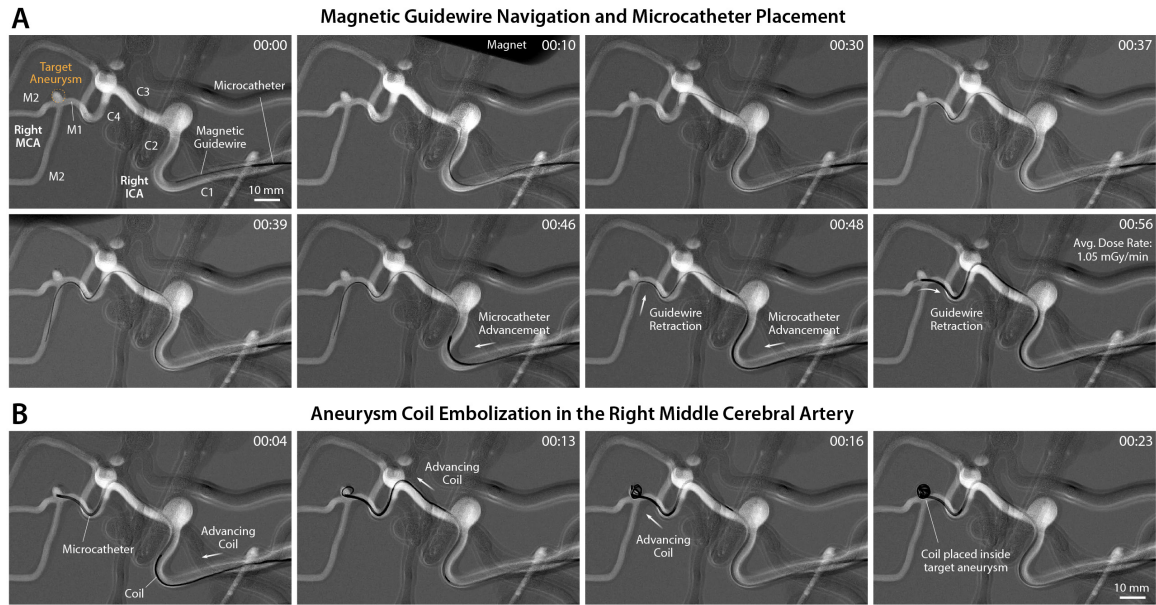
Figure 5-23: Telerobotically assisted aneurysm coiling in the right middle cerebral artery. (**A**) Guidewire navigation under magnetic manipulation up to the target lesion in the right middle cerebral artery (MCA) through real-time teleoperation of the robot arm (00:00∼00:39) and microcatheter placement in the targeted aneurysm upon the retraction of the guidewire (00:46∼00:56). (**B**) Endovascular coiling of the target aneurysm by delivering embolization coils into the aneurysm sac through the microcatheter.

These experimental results presented in **Figures 5-22** and **5-23** clearly suggest the potential of our system for robotically assisted endovascular coiling of cerebral aneurysms to treat or prevent hemorrhagic stroke with potentially reduced operative time, perioperative risk, and x-ray exposure. These results also illustrate the versatile applicability of our system to endovascular coiling for treating intracranial aneurysms in more distal and hence more difficult-to-reach areas of the cerebral vasculature, when compared with the existing vascular robotic systems that have been limitedly applicable to intracranial aneurysms in relatively easy-to-reach areas (**Figure 1-4**).

5.3.2 Endovascular Treatment of Ischemic Stroke

Next, we investigated the feasibility of our system for endovascular treatment of ischemic stroke due to cerebral infarction. For the feasibility test, we used a simulated, nonbiological blood clot to create occlusion in the M1 segment—one of the most common sites for a thrombus to lodge to cause cerebral ischemia [166]—in the right middle cerebral artery (MCA) of the same neurovascular phantom we used for demonstrating the aneurysm coiling procedures. The artificial clot used in our experiment had similar mechanical and viscoelastic properties to a real blood clot [174]. Given that the clot by itself was not visible under x-ray, the magnetic navigation and clot retrieval procedures were initially performed under real-time optical imaging (x-ray results will follow) to better visualize the process, as shown in **Figure 5-24**.

Steering control and manipulation of the magnetic guidewire to the occluded site were similar to what was described for the previous demonstration of guidewire navigation in the same path presented in **Figure 5-23**, until the distal tip of the guidewire reached the clot, as shown in**Figure 5-24A** (00:00∼00:34). The guidewire was further advanced so that the distal tip thrust itself into the tiny gap between the clot and the vessel wall, under careful control of the guidewire advancing unit to avoid touching the inner wall of the first aneurysm at the corner. The guidewire tended to buckle inside the aneurysm upon further push, due to the high resistance from the clot. To avoid buckling by adding more mechanical support to the guidewire, the microcatheter was carefully advanced up to the clot while at the same time controlling the guidewire, after which the guidewire was advanced to pass through the artificial clot, as can be seen in **Figure 5-24A** (01:35). With the aid of magnetic steering at the MCA bifurcation, the microcatheter was placed across the occlusion such that its distal end was positioned distal to the thrombus, as shown in **Figure 5-24A** (01:42).

After withdrawing the guidewire, mechanical thrombectomy was performed to retrieve the clot using a commercially available revascularization device (i.e., a stent retriever; Solitaire™ X Revascularization Device, Medtronic). Delivery of the stent retriever was performed manually following the standard procedure after inserting the stent introducer sheath into the hub of the microcatheter. The stent push wire
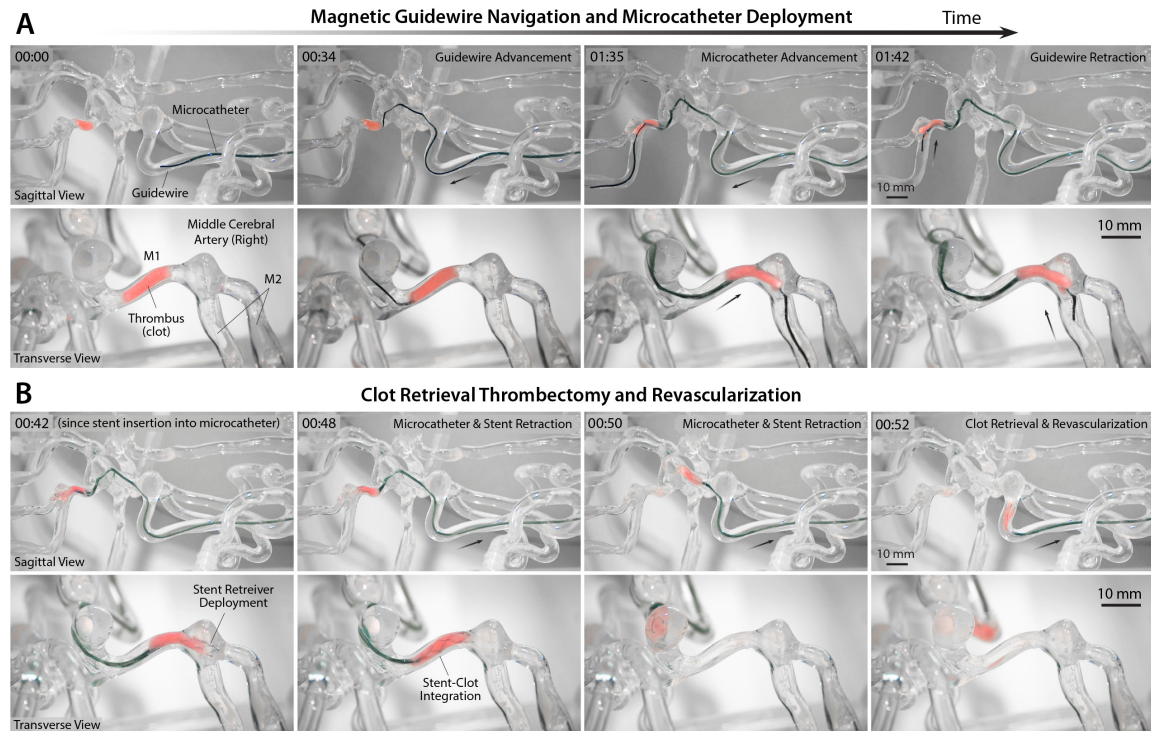
Figure 5-24: Demonstration of telerobotically assisted clot retrieval thrombectomy and revascularization in the cerebral vasculature. (**A**) Navigation up to the simulated clot in the M1 segment of the right middle cerebral artery (MCA) with the telerobotically con-trolled magnetic guidewire (00:00~00:34) and microcatheter placement across the thrombus with the aid of magnetic steering at the MCA bifurcation (01:35~01:42) under real-time optical imaging to show the clot during the interventional process. (**B**) Deployment of a stent retriever across the thrombus (00:42~00:48) and retrieval of the clot upon withdrawal of the stent retriever and the microcatheter for revascularization of the occluded site (00:50~00:52). The same clot retrieval procedure performed under real-time x-ray fluoroscopy is also presented in **Figure 5-25**.

was advanced within the microcatheter until the distal markers of the stent retriever lined up with the distal end of the microcatheter. Then, the microcatheter was carefully withdrawn under the joystick control of the catheter advancing unit while fixing the stent push wire to maintain the position of the stent until the distal end of the microcatheter was just proximal to the thrombus, thereby fully deploying the stent across the thrombus, as shown in **Figure 5-24B** (00:42). After confirming the stent deployment from the real-time imaging, the microcatheter and the stent as a unit were withdrawn to retrieve the clot and revascularize the occluded site (M1), as shown in **Figure 5-24B** (00:48~00:52).
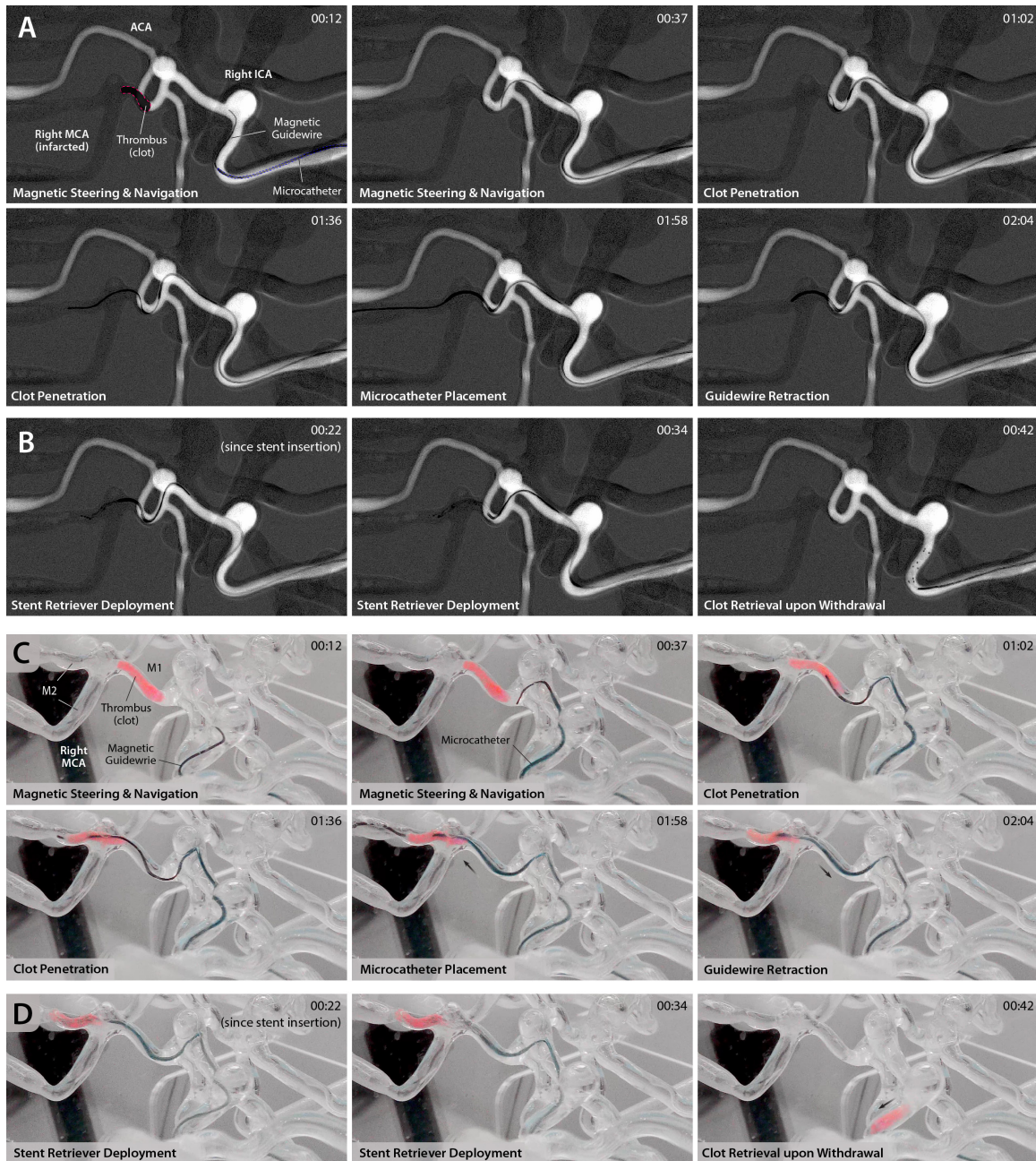
Figure 5-25: Telerobotically assisted clot retrieval procedure in the cerebral vasculature performed under x-ray fluoroscopy. (**A**) Navigation up to the simulated clot in the M1 segment of the right middle cerebral artery (MCA) with the telerobotically controlled magnetic guidewire (00:00∼00:37) and microcatheter placement across the thrombus with the aid of magnetic steering at the MCA bifurcation (01:02∼02:04) under real-time x-ray fluoroscopy. (**B**) Deployment of a stent retriever device across the thrombus (00:22∼00:34) and retrieval of the clot from the occluded site (00:42) through joystick teleoperation of the guidewire/microcatheter advancing unit. The guidewire advancing unit was used to advance or retract the stent retriever after device exchange upon the withdrawal of the magnetic guidewire from the microcatheter. (**C-D**) Corresponding optical images of the demonstrated clot retrieval process in (**A-B**) juxtaposed for showing the clot which is not visible under x-ray by itself.

We repeated the clot retrieval procedure under real-time x-ray fluoroscopy as shown in **Figure 5-25**, **A** and **B**. It is worth noting that the infarcted right MCA was missing on the digital subtraction angiography (i.e., roadmap) images due to the occlusion in M1 blocking contrast flow (see corresponding optimal images in **Figure 5-25**, **C** and **D**), which is the same phenomenon observed in real stroke cases. The overall procedure and the workflow were similar to the previous demonstration in **Figure 5-24**. However, greater distal migration of the clot was observed while advancing the guidewire and placing the microcatheter, as shown in **Figure 5-24C** (01:02∼01:58), possibly due to the presence of pulsatile flow generated by the peristaltic pump. In contrast to the previous demonstration in which the stent retriever device was manually manipulated, this time we used the advancing unit and the joystick controller to manipulate both the stent retriever and the microcatheter when deploying the stent and retrieving the clot (**Figure 5-25**, **B** and **D**) to avoid radiation exposure during the procedures. Only the device exchange was done manually, after removing the guidewire from the microcatheter, by engaging the stent push with the guidewire advancing unit. The results presented in **Figures 5-24** and **5-25** demonstrate the potential of our system for telerobotically assisted clot retrieval thrombectomy for treating ischemic stroke.

5.4   Summary

In **Section 5.1**, we presented a series of in vitro phantom studies using realistic anatomical models, which clearly illustrated our system's steering and navigational performance in the complex and tortuous vasculature of the brain. We verified that the single actuating magnet could effectively steer our magnetic soft continuum guidewire with minimal motion of the robot arm by exploiting flipping of the magnet to change the direction of the steerable tip of the guidewire. We also demonstrated that the unique steering control principle of our magnetic guidewire guarantees the visibility of its steerable tip on the real-time x-ray images during the steering and navigational task. As an extension of our discussion in **Section 4.1** on the compatibility of existing magnetic actuation platforms with biplane imaging for complex

neuroendovascular procedures, we experimentally demonstrated that our proposed system based on a single light-weight robot arm is fully compatible with standard biplane fluoroscopy.

In **Section 5.2**, we evaluated the steering and navigational performance of our system under realistic in vivo conditions using the porcine brachial artery tortuosity model and verified the safety and effectiveness of our magnetic soft continuum guidewire. We assessed the learning curves for a group of neurointerventionalists with no prior experience of using our system and verified that our developed system requires a relatively short learning curve. We also experimentally verified that, When compared with manually controlled passive guidewires, the greater controllability and maneuverability of our magnetic soft continuum guidewire with active steering capabilities helps to achieve safer and quicker access to hard-to-reach areas in the complex neurovasculature with greatly reduced procedural time and number of undesirable steering maneuvers. We also demonstrated that our unique soft continuum design allows for smoother navigation in narrow and tight spaces when compared with the conventional magnet-tipped guidewire with a rigid and stiff tip.

In **Section 5.3**, we demonstrated our system's ability to guide telerobotically assisted therapeutic procedures for endovascular treatments of cerebral aneurysms and ischemic stroke using the realistic anatomical models with simulated disease states. The experimental results also verified that our magnetic soft continuum guidewire is compatible with standard devices in terms of its dimension and functions for neurovascular intervention. The series of demonstrations have validated the determined size of the actuating magnet is suitable for its use in realistic clinical settings. Further increasing the size of the actuating magnet may allow greater safety margins in terms of its working distance, but the use of a larger magnet would likely affect the flexibility and dexterity of the robot arm due mainly to the greater constraints in terms of the available workspace in cluttered environments. Because it is known that the magnetic susceptibility of biological tissues in the human head causes negligible effect (i.e., below 1%) on the actuating field strength [175], the magnet size verified from the series of benchtop verification would likely be applicable to clinical scenarios.

Chapter 6

Conclusions and Future Work

6.1 Summary of Contributions

Aimed at enabling robotic applications to endovascular neurosurgery for treating stroke and aneurysms, we have introduced our telerobotic neurointerventional platform that allows for precise robotic control of the magnetic soft continuum robot for navigating the complex and tortuous vasculature of the brain. The active steering of our magnetic guidewire can be controlled remotely with a teleoperated robot arm with an actuating magnet, and its advancement or retraction can be controlled with a set of motorized linear drives under visual feedback from real-time x-ray fluoroscopy. Through the series of benchtop testing, we have shown that our system performs as intended in simulated clinical environments representing the human neurovascular anatomy with clinically challenging tortuosity and disease states such as multiple aneurysms and vascular occlusions. Through the preclinical testing, we have also demonstrated the safety and effectiveness of our developed system for its use in realistic in vivo conditions as well. We have further demonstrated our system's ability to assist therapeutic procedures for endovascular treatments of aneurysms and ischemic stroke in cerebral arteries while negotiating complex anatomical structures. To the best of our knowledge, this work is the first to demonstrate the feasibility of telerobotically assisted aneurysm coil embolization and clot retrieval thrombectomy in cerebral arteries with clinically challenging anatomies, although in a realistic

anatomical model, among the previously reported vascular robotic systems in the literature [17, 20, 21, 22, 23, 24, 25, 27].

It is worth noting that the concept of magnetically guided intravascular devices has existed for decades [176, 177, 178, 179, 180, 181]. Despite the long and checkered history of using magnetism to direct intravascular devices [17], there are currently no viable magnetic guidewire/catheter products or commercially available robotic systems to magnetically manipulate such devices for neurovascular applications, where the active steering capability is most needed. Several magnetic guidewire products were introduced for coronary and peripheral interventions in the past by Stereotaxis Inc., in the form of "magnet-tipped" guidewires with a small magnet attached to the distal end tip [17, 126, 127, 128]. There have been some similar variants proposed in the research domain, with a few magnets embedded in the distal portion of the guidewire [99]. Such magnet-tipped guidewires, however, entail potential risks of embolization because the magnet at the end could break off, as discussed in **Section 3.1.1**. Furthermore, lacking the ability to conform to the given environment, the rigid and stiff tip of magnet-tipped guidewires could make it particularly challenging to work through narrow and winding pathways in the distal cerebral vasculature, as illustrated in **Section 5.2.4**. More importantly, the use of finite-sized, rigid magnets in a thin, flexible device often leads to discontinuous dimensions or mechanical properties along the magnet-tipped guidewire [182], which could significantly compromise its compatibility with other interventional devices (balloon catheters or microcatheters) that are indispensable for the endovascular treatment of aneurysms or stroke.

It is also worth noting that magnetic actuation based on a multi-DOF robot arm with a single magnet has been explored in previous studies for different applications such as magnetic capsule endoscopes [73, 121, 122, 123, 183, 184, 155]. While the underlying mechanism of using magnetic torques and forces for device control is similar, the hardware design and control strategies of the previously reported systems are specific to their devices based on rigid, finite-sized magnets and hence not directly applicable to steering control of our magnetic continuum guidewire, as discussed in **Section 5.2.4**. When it comes to magnetic actuation systems of other types, there

are commercialized platforms based on either a pair of large permanent magnets or a set of multiaxial electromagnets, as discussed in **Section 4.1**, mostly exclusively for cardiac electrophysiology to treat arrhythmia using magnetically controlled ablation catheters. While these commercialized systems could be used to control our magnetic soft continuum guidewire, the critical disadvantage of these systems is in their limited compatibility with the standard imaging modality based on x-ray fluoroscopy due to their bulky magnet/coil setups. Our compact single-arm-based platform allows much wider C-arm rotation angles for better state observation and is fully compatible with biplane angiography suites, as demonstrated in the series of benchtop and preclinical evaluations in **Chapter 5**. We therefore believe that our proposed platform based on a compact, lightweight robot arm could therefore suggest a cost-efficient alternative to those existing systems in the context of telerobotic stroke intervention.

6.2   Biocompatibility for Clinical Translation

To ensure the safety and effectiveness of our magnetic soft continuum robot for its preclinical applications and clinical translation, further studies will be required to evaluate the biocompatibility of the device for its intended use. In the context of the regulatory process for medical devices, different levels of biocompatibility are required for the device materials depending on the level of interaction with the human body, considering the type and duration of contact with biological materials (e.g., tissues, cells, blood), following relevant standards such as the ISO 10993 series [185, 186, 187, 188] and the related Food and Drug Administration (FDA) guidance [189] for 510(k) premarket notification or premarket approval (PMA) processes depending on the device classification for FDA regulatory pathways.

For intravascular guidewires, FDA's 510(k) premarket clearance requires biocompatibility testing of all patient-contacting materials present in the device [16]. According to ISO 10993-1 [185], guidewires are classified as externally communicating devices with limited (<24 hour) duration direct contact with the circulating blood, for which the following end-points should be addressed in the biocompatibility evalu-

ation: cytotoxicity and hemocompatibility (thrombosis, coagulation, hemolysis, and complement activation). Although these tests have not been conducted in the current thesis, there is ample evidence that the materials used for the proposed devices would likely be biocompatible.

Cytotoxicity: First, both PDMS and TPU are known to be biocompatible with no acute cytotoxicity, as reported in a large volume of literature [190, 191, 192, 193]. The hydrogel skin, which encapsulates the robot's body, is also considered to be biocompatible, given that both PDMAA polymers and hydrogels have been reported to have no cytotoxicity [194, 195]. As discussed in **Section 3.3.4**, ferromagnetic materials including iron and iron-based alloys can be cytotoxic due to their corrosive nature [196, 197]. Although bare NdFeB materials are in general considered to be moderately cytotoxic due mainly to their highly corrosive nature, NdFeB magnets coated with noncorrosive metals or metallic alloys (e.g., tin, titanium, and nickel-copper) are known to be biocompatible and hence are widely used in orthodontic and orthopedic appliances [196, 198, 199]. It has also been shown from cell viability testing that, for relatively short-term (i.e., 24 hours) exposure to aqueous environments, magnetic soft composites based on silicone elastomers containing bare (uncoated) NdFeB microparticles are biocompatible [200], which can be attributed to the fact that the particles are contained within the polymer matrix. For our magnetic soft continuum robots, the particles are encapsulated in the silica shell, PDMS or TPU matrices, and hydrogel skin, and therefore we believe that the device would likely be biocompatible with no acute cytotoxicity. We also expect that the anti-corrosion coatings would be helpful to ensure sufficient shelf-life of the magnetic soft continuum robots when they are commercialized as medical devices.

Hemocompatibility: For clinical applications that involve contact of the device with circulating blood, hemocompatibility should also be evaluated to ensure that the device materials cause no adverse responses such as thrombosis, coagulation, hemolysis, and complement activation during their intended uses. For example, thrombosis on the robot may not only impede the functionality of the magnetic soft continuum

robot (e.g., increasing the mechanical rigidity) but also lead to thromboembolic complications such as distal occlusions. Material-mediated complement activation is a complex process that depends on multiple factors such as the physical and chemical properties of the material and the surface area and surface architecture of the device [189, 201]. Further studies will be required to evaluate such material-mediated biological and physiological responses to evaluate both short-term and long-term systemic responses and thereby to ensure the safety of magnetic soft materials and robots for their applications to blood-contacting medical devices.

Particulate generation: Particulates generated during clinical use of intravascular guidewires, if any, may also lead to undesirable outcomes such pulmonary embolism/infarction, myocardial embolism/infarction, or embolic stroke. Therefore, to use our magnetic soft continuum robot as a neurovascular guidewire, it will need to be evaluated for particle generation, in addition to the coating integrity assessment presented in **Figure 3-6J**, to address potential safety concerns by verifying that the embedded magnetic particles do not fall off even under continuous shearing. We have not observed any particulate generated during or after the prolonged shearing test in **Figure 3-6J** or the benchtop demonstrations with in vitro phantoms using our prototyes. For more rigorous validation, however, we will need to use optical techniques for particle detection (e.g., light obscuration, light refraction) under continuous flow conditions to simulate blood flow.

6.3 Considerations for Future Developments

There are some potential technical and logistical issues to consider for further translation of our proposed telerobotic neurointerventional system into the clinic. Below, we summarize some technical considerations for future developments of our system.

Low-latency telecommunications: First, communication delays are inevitable in teleoperation systems due to signal propagation time and bandwidth constraints. Because our telerobotic system does not involve any dynamic motion of the robot arm, communication delays are nearly imperceptible to a human operator teleoperating the

system from the remote-control console, which is a few meters away from the robot arm. For long-distance intervention in a robotic telesurgery scenario, however, the increased latency may negatively affect the steering control and navigational performance of our system. A recent study reported telerobotically assisted percutaneous coronary intervention (PCI) in human patients that was performed remotely (32 km away) using the CorPath® GRX system under reliable network connection [202]. The measured network delay was around 50 ms, and the authors reported that the delay did not result in any noticeable procedural or technical difficulties. We expect that advances in low-latency telecommunications (e.g., 5G wireless network) and improvements in network connectivity [203, 204] would help to realize long-distance telerobotic stroke intervention [13, 26] when combined with our system.

Contingency plans with teleproctoring: Contingency plans must also exist for periprocedural complications to ensure the feasibility of remotely performed interventions through our proposed system. Even though the critical components of endovascular procedures can be performed remotely by a skilled interventionalist (i.e., off-site expert) from another hospital, other personnel (i.e., on-site local interventionalist and/or staff) will need to be present in the operating room for perioperative assistance from establishing vascular access and handling the C-arm machine to addressing any potential problems or complications that may arise before/during/after the intervention [13, 14]. In this light, the emerging telepresence or teleproctoring systems based on low-latency, high-resolution streaming technology, such as the Tegus system [205, 206], will greatly benefit both the off-site and on-site interventionalists by enabling bi-directional communication as well as high-resolution image transmission for real-time fluoroscopic images and visualization of robot configuration.

Tactile and haptic feedback: Next, like other commercial vascular robotic systems with linear drives for guidewire and catheter advancement, the advancing unit of our system does not provide any tactile or haptic feedback. While the lack of tactile or haptic feedback is often considered one of the major drawbacks of existing vascular robotic systems [20], it should be noted that interventionalists rely mostly on visual

feedback when manually manipulating a conventional guidewire. Some recent studies support this standpoint reporting that the lack of tactile feedback in the CorPath® GRX system did not result in any procedural challenges or adverse clinical outcomes [24, 25], mainly because of the ability to detect obstacles and friction visually by observing subtle changes in the shape and motion of the guidewire. Likewise, we believe that the tactile feedback may not be a critical factor for telerobotically performed endovascular navigation as the system provides the ability to stop advancing or retracting the guidewire and microcatheter immediately when the operator observes any undesirable behavior of the device from real-time fluoroscopic imaging. Nonetheless, we believe the implementation of force-sensing and haptic feedback technologies would help to improve the control interface and operator performance [14], which is therefore an area for future exploration.

Pre-procedural planning and automation: From the presented in vitro and in vivo studies in this thesis, we found that pre-operative imaging (i.e., 3D rotational angiography and reconstructed 3D vessel models) can play a pivotal role in pre-procedural planning of the robot arm's motion, path, and configuration for spatial positioning of the actuating magnet to steer the magnetic guidewire at critical locations such as branching points or sharp corners in the target vasculature. We envision that pre-planned robot motion for spatial positioning of the actuating magnet based on the pre-operative imaging data can help to make the system far easier for interventionalists to use by reducing the operator's workload in real-time teleoperation of the robot arm with a joystick controller. This pre-procedural planning will also be crucial for future developments of the proposed robotic neurointerventional platform towards semi-autonomous or fully autonomous endovascular navigation in the complex neurovasculature based on magnetic manipulation. In doing so, model-based estimation and control of the magnetic soft continuum guidewire under the action of a single actuating magnet will also be an important area for future development, given the practical constraints on real-time 3D shape sensing and tracking capabilities due to the projected challenges in miniaturizing sensors or reconstructing the 3D guidewire shapes from the standard mono- or bi-plane x-ray fluoroscopic images.

Appendix A

Magnetic Force and Torque from Potential Energy

Here, we provide derivation of Equation (2.3) from Equation (2.2) using some relevant vector and tensor identities. The first term on the right-hand side of Equation (2.2), $\mathbf{m} \cdot \delta \mathbf{B}$, can be calculated as follows:

$$
\begin{aligned}
\mathbf{m} \cdot \delta \mathbf{B} = \mathbf{m} \cdot \left(\frac{\partial \mathbf{B}}{\partial \mathbf{x}} \, \delta \mathbf{x} \right) &= m_i \, \frac{\partial B_i}{\partial x_j} \, \delta x_j = \delta x_j \, \frac{\partial B_i}{\partial x_j} \, m_i \\
&= \delta x_j \left(\left(\operatorname{grad} \mathbf{B} \right)^{\mathsf{T}} \right)_{ji} m_i = \delta x_j \left(\left(\operatorname{grad} \mathbf{B} \right)^{\mathsf{T}} \mathbf{m} \right)_j \\
&= \delta \mathbf{x} \cdot \left(\operatorname{grad} \mathbf{B} \right)^{\mathsf{T}} \mathbf{m}.
\end{aligned}
\tag{A.1}
$$

On the right-hand side of Equation (2.2), $\delta \mathbf{m}$ denotes the infinitesimal rotation of the magnetic moment vector $\mathbf{m}$ around an axial vector $\delta \boldsymbol{\theta}$ (the magnitude of which indicates the angle of rotation) and is related to $\delta \boldsymbol{\theta}$ by $\delta \mathbf{m} = \delta \boldsymbol{\theta} \times \mathbf{m}$. Then, the second term on the right-hand side of Equation (2.2) becomes $(\delta \boldsymbol{\theta} \times \mathbf{m}) \cdot \mathbf{B}$, which can be expressed interchangeably as

$$
\mathbf{B} \cdot (\delta \boldsymbol{\theta} \times \mathbf{m}) = \delta \boldsymbol{\theta} \cdot (\mathbf{m} \times \mathbf{B}) = \mathbf{m} \cdot (\mathbf{B} \times \delta \boldsymbol{\theta}),
\tag{A.2}
$$

from the following relation involving the inner and cross products of three vectors: $\mathbf{u} \cdot (\mathbf{v} \times \mathbf{w}) = \mathbf{v} \cdot (\mathbf{w} \times \mathbf{u}) = \mathbf{w} \cdot (\mathbf{u} \times \mathbf{v})$. This relation, also known as the *scalar triple product* [207], can be shown to hold for all vectors $\mathbf{u}$, $\mathbf{v}$, and $\mathbf{w}$ using indicial notation:

$$\mathbf{u} \cdot (\mathbf{v} \times \mathbf{w}) = u_i(\varepsilon_{ijk}v_jw_k) = v_j(\varepsilon_{jki}w_ku_i) = \mathbf{v} \cdot (\mathbf{w} \times \mathbf{u})$$
$$= w_k(\varepsilon_{kij}u_iv_j) = \mathbf{w} \cdot (\mathbf{u} \times \mathbf{v}). \tag{A.3}$$

Then, Equation (2.2) can be written as

$$-\delta u_m = \mathbf{m} \cdot \delta\mathbf{B} + \delta\mathbf{m} \cdot \mathbf{B} = \delta\mathbf{x} \cdot \left(\text{grad}\,\mathbf{B}\right)^{\mathsf{T}}\mathbf{m} + \delta\boldsymbol{\theta} \cdot (\mathbf{m} \times \mathbf{B}), \tag{A.4}$$

where $\left(\text{grad}\,\mathbf{B}\right)^{\mathsf{T}} = \text{grad}\,\mathbf{B}$ for irrotational (curl-free) magnetic fields, as discussed in **Section 2.3.6**, to yield Equation (2.3), which leads to the expressions for the magnetic force and torque presented in Equations (2.4) and (2.5), respectively.

Appendix B

Conservation of Magnetic Charge

Here, we derive the transformation rule for the remanent magnetization vector of a deformable magnetized body between its undeformed reference and deformed current configurations in Equation (2.39) presented in **Section 2.3.4**. First, from Equation (2.13), we can express the magnetic charge density of an ideal hard-magnetic soft material in the current configuration as

$$\rho_{\mathrm{m}} = -\mu_0 \operatorname{div} \mathbf{M}_{\mathrm{r}} = -\mu_0 \frac{\partial M_{\mathrm{r}\,i}}{\partial x_i}, \tag{B.1}$$

with $\operatorname{div} \mathbf{M}_{\mathrm{r}}$ denoting the spatial divergence of the remanent magnetization $\mathbf{M}_{\mathrm{r}}$ with respect to $\mathbf{x}$ in the current (deformed) configuration. Correspondingly, the magnetic charge density in the undeformed reference configuration can be expressed as

$$\tilde{\rho}_{\mathrm{m}} = -\mu_0 \operatorname{Div} \tilde{\mathbf{M}}_{\mathrm{r}} = -\mu_0 \frac{\partial \tilde{M}_{\mathrm{r}\,i}}{\partial X_i}, \tag{B.2}$$

with $\operatorname{Div} \tilde{\mathbf{M}}_{\mathrm{r}}$ denoting the material divergence of $\tilde{\mathbf{M}}_{\mathrm{r}}$ with respect to $\mathbf{X}$ in the reference configuration (**Figure B-1**).
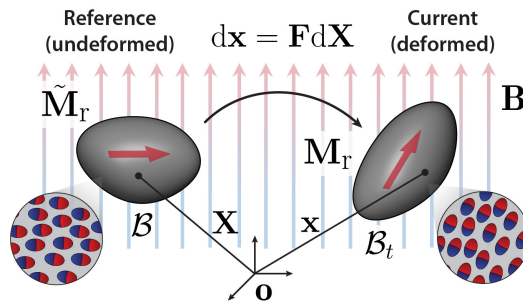

Figure B-1: Kinematic relation for ideal hard-magnetic soft materials.

Conservation of the magnetic charge during the deformation requires

$$\int_{\mathcal{B}} \operatorname{Div} \tilde{\mathbf{M}}_r \, dV = \int_{\mathcal{B}_t} \operatorname{div} \mathbf{M}_r \, dv, \tag{B.3}$$

where dV and dv denote the infinitesimal volume elements in the reference and current configurations, respectively, which are related by $dv = J \, dV$ as discussed in **Section 2.3.2**. Applying the divergence theorem, Equation (B.3) can be expressed as

$$\oint_{\partial\mathcal{B}} \tilde{\mathbf{M}}_r \cdot \mathbf{N} \, dA = \oint_{\partial\mathcal{B}_t} \mathbf{M}_r \cdot \mathbf{n} \, da, \tag{B.4}$$

where dA and da denote the infinitesimal area elements in the reference and current configurations, respectively, while $\mathbf{N}$ and $\mathbf{n}$ denote the unit normal vector of the infinitesimal area elements in the reference and current configurations, respectively. Applying the Nanson's formula: $\mathbf{n} \, da = J \, \mathbf{F}^{-\mathsf{T}} \mathbf{N} \, dA$, Equation (B.4) is re-written as

$$\oint_{\partial\mathcal{B}} \tilde{\mathbf{M}}_r \cdot \mathbf{N} \, dA = \oint_{\partial\mathcal{B}} \mathbf{M}_r \cdot J\left(\mathbf{F}^{-\mathsf{T}} \mathbf{N}\right) dA. \tag{B.5}$$

Then, applying the tensor identity, $\mathbf{u} \cdot \mathbf{S}^{\mathsf{T}} \mathbf{v} = (\mathbf{S}\mathbf{u}) \cdot \mathbf{v}$, from the definition of the transpose of a tensor $\mathbf{S}$ for all vectors $\mathbf{u}$ and $\mathbf{v}$ [208, 207], Equation (B.5) can be re-written as

$$\oint_{\partial\mathcal{B}} \tilde{\mathbf{M}}_r \cdot \mathbf{N} \, dA = \oint_{\partial\mathcal{B}} J\left(\mathbf{F}^{-1} \mathbf{M}_r\right) \cdot \mathbf{N} \, dA, \tag{B.6}$$

from which we find the relation between $\tilde{\mathbf{M}}_r$ and $\mathbf{M}_r$ as presented in Equation (2.39): $\mathbf{M}_r = J^{-1} \mathbf{F} \tilde{\mathbf{M}}_r$.

It is worth noting that Equation (B.3), along with Equations (2.29) and (2.39), leads to the following kinematic relation for divergence of a vector field:

$$\operatorname{Div} \mathbf{A} = J \operatorname{div}\left(J^{-1} \mathbf{F} \mathbf{A}\right), \tag{B.7}$$

which generally holds for any vector field $\mathbf{A}$ [67].

Appendix C

Derivation of Elastic and Magnetic Cauchy Stresses

Here we provide detailed derivation of the specific forms of the elastic and magnetic parts of the Cauchy stress presented in Equations (2.41) to (2.44).

Elastic part of the Cauchy stress: First, we start from the elastic part of the Helmholtz free energy based on the neo-Hookean model in Equation (2.37). From the hyperelastic constitutive relation in Equation (2.34), the elastic part of the Piola stress can be calculated as follows:

$$
\begin{aligned}
\mathbf{P}^{\text{elastic}} &= \frac{\partial \psi_{\text{R}}^{\text{elastic}}}{\partial \mathbf{F}} = \frac{G}{2} \frac{\partial}{\partial \mathbf{F}} \left(J^{-2/3} I_1 \right) + \frac{K}{2} \frac{\partial}{\partial \mathbf{F}} \left(J - 1 \right)^2 \\
&= \frac{G}{2} \left(-\frac{2}{3} J^{-5/3} \frac{\partial J}{\partial \mathbf{F}} I_1 + J^{-2/3} \frac{\partial I_1}{\partial \mathbf{F}} \right) + K \left(J - 1 \right) \frac{\partial J}{\partial \mathbf{F}},
\end{aligned}
\tag{C.1}
$$

with $J = \det \mathbf{F}$ and $I_1 = \text{tr}\left(\mathbf{F}^\mathsf{T} \mathbf{F} \right)$ as defined in **Sections 2.3.2** and **2.3.3**. Then, the partial derivatives can be calculated as

$$
\frac{\partial J}{\partial \mathbf{F}} = \frac{\partial}{\partial \mathbf{F}} \left(\det \mathbf{F} \right) = \left(\det \mathbf{F} \right) \mathbf{F}^{-\mathsf{T}} = J \mathbf{F}^{-\mathsf{T}},
\tag{C.2}
$$

$$
\frac{\partial I_1}{\partial \mathbf{F}} = \frac{\partial}{\partial \mathbf{F}} \left(\text{tr}\left(\mathbf{F}^\mathsf{T} \mathbf{F} \right) \right) = 2 \mathbf{F}.
\tag{C.3}
$$

Equation (C.2) is obtained from the standard formula for the derivative of the de-

terminant a second-order tensor [63, 209, 210], while Equation (C.3) can be derived using indicial notation, along with $\left(\mathbf{F}^\mathsf{T}\mathbf{F}\right)_{ij} = \left(\mathbf{F}^\mathsf{T}\right)_{ik}\left(\mathbf{F}\right)_{kj} = F_{ki}F_{kj}$ and $\mathrm{tr}\left(\mathbf{F}^\mathsf{T}\mathbf{F}\right) = \left(\mathbf{F}^\mathsf{T}\mathbf{F}\right)_{mm} = F_{km}F_{km}$, as:

$$\frac{\partial}{\partial F_{ij}}\left(\mathrm{tr}\left(\mathbf{F}^\mathsf{T}\mathbf{F}\right)\right) = \frac{\partial}{\partial F_{ij}}\left(F_{km}F_{km}\right) = 2\frac{\partial F_{km}}{\partial F_{ij}}F_{km} = 2\,\delta_{ki}\,\delta_{mj}F_{km} = 2F_{ij}, \qquad \text{(C.4)}$$

where δ_{ij} is the Kronecker delta that is defined as

$$\delta_{ij} = \begin{cases} 1 & \text{if} \quad i = j \\ 0 & \text{if} \quad i \neq j \end{cases}. \qquad \text{(C.5)}$$

Substituting Equations (C.2) and (C.3) to Equation (C.1), we obtain

$$\mathbf{P}^{\text{elastic}} = GJ^{-2/3}\left(-\frac{1}{3}\mathbf{F}^{-\mathsf{T}}I_1 + \mathbf{F}\right) + KJ(J-1)\mathbf{F}^{-\mathsf{T}}, \qquad \text{(C.6)}$$

as presented in Equation (2.41). Then, from Equation (2.35), we obtain the elastic part of the Cauchy stress as given in Equation (2.42):

$$\boldsymbol{\sigma}^{\text{elastic}} = GJ^{-5/3}\left(\mathbf{F}\mathbf{F}^\mathsf{T} - \frac{I_1}{3}\mathbf{1}\right) + K(J-1)\mathbf{1}. \qquad \text{(C.7)}$$

Magnetic part of the Cauchy stress: From the magnetic part of the Helmholtz free energy in Equation (2.40), the magnetic Piola stress can be calculated as follows:

$$\mathbf{P}^{\text{magnetic}} = \frac{\partial \psi_{\text{R}}^{\text{magnetic}}}{\partial \mathbf{F}} = \frac{\partial}{\partial \mathbf{F}}\left(-\mathbf{F}\tilde{\mathbf{M}}_{\text{r}} \cdot \mathbf{B}\right), \qquad \text{(C.8)}$$

which can be expressed using indicial notation as

$$P_{ij}^{\text{magnetic}} = \frac{\partial}{\partial F_{ij}}\left(-F_{mk}(\tilde{\mathbf{M}}_{\text{r}})_k\,B_m\right) = -(\tilde{\mathbf{M}}_{\text{r}})_k\,B_m\frac{\partial F_{mk}}{\partial F_{ij}}$$
$$= -(\tilde{\mathbf{M}}_{\text{r}})_k\,B_m\,\delta_{mi}\,\delta_{kj} = -B_i(\tilde{\mathbf{M}}_{\text{r}})_j, \qquad \text{(C.9)}$$

which is equivalent to $\mathbf{P}^{\text{magnetic}} = -\mathbf{B} \otimes \tilde{\mathbf{M}}_{\text{r}}$, as presented in Equation (2.43). Then, from Equation (2.35), we obtain the magnetic Cauchy stress in indicial form as

$$\sigma_{ij}^{\text{magnetic}} = J^{-1}P_{ik}^{\text{magnetic}}\left(\mathbf{F}^\mathsf{T}\right)_{kj} = -J^{-1}B_i(\tilde{\mathbf{M}}_{\text{r}})_k\,F_{jk} = -J^{-1}B_iF_{jk}(\tilde{\mathbf{M}}_{\text{r}})_k, \qquad \text{(C.10)}$$

which is equivalent to

$$\boldsymbol{\sigma}^{\text{magnetic}} = -J^{-1}\big(\mathbf{B} \otimes \tilde{\mathbf{M}}_{\text{r}}\big)\mathbf{F}^{\mathsf{T}} = -J^{-1}\mathbf{B} \otimes \mathbf{F}\tilde{\mathbf{M}}_{\text{r}} = -\mathbf{B} \otimes \mathbf{M}_{\text{r}}, \qquad \text{(C.11)}$$

as presented in Equation (2.44).

Appendix D

Justification of the Use of Neo-Hookean Hyperelastic Model

Justification of hyperelasticity: Our continuum mechanical model for ideal hard-magnetic soft materials in **Section 2.3** was based on the hyperelastic constitutive equations in Equations (2.34) and (2.35). In obtaining Equation (2.34) from Equation (2.33), the underlying assumption was that the material is perfectly elastic so that there is no internal energy dissipation during the magnetoelastic deformation of the material. Particulate-filled polymer composites, however, typically undergo softening of the matrices following the mechanical dissipation or hysteresis, which is also known as the Mullins effect [211, 212]. The energy dissipated during the deformation of filled elastomers can be attributed to the disruption of the interfacial binding between the embedded particles and the surrounding polymer matrices.
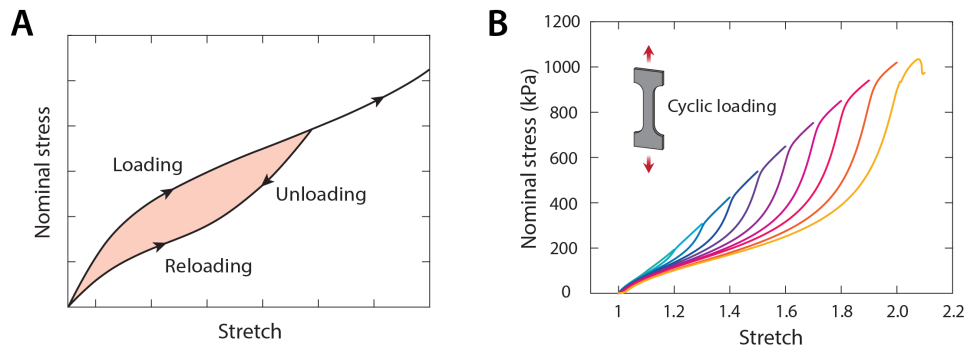
Figure D-1: Energy dissipated during the deformation of particulate-filled elastomers.

The energy dissipation in filled elastomers and the consequent hysteretic macroscopic behavior can be explained with **Figure D-1A**, where the area between the loading and unloading curves indicates the amount of energy dissipated during the cyclic loading and unloading process. Our hard-magnetic soft composite (particle volume fraction $\phi = 20\%$) also exhibits such hysteretic behavior upon cyclic loading, as shown in **Figure D-1B**, and the amount of dissipate energy increases as the stretch level increases. To quantitatively capture such dissipative macroscopic behavior, other phenomenological constitutive models, such as the Ogden-Roxburgh model [213], will need to be adopted. As shown in **Figure D-1B**, however, the dissipated energy is not very substantial when the stretch level is small (i.e., $\lambda \leq 1.3$). For our hard-magnetic soft bending actuators, the maximum local strain even during their large deflection is typically below 30%, for which the material can be safely assumed to be nearly perfectly elastic to justify the use of hyperelastic constitutive equations.
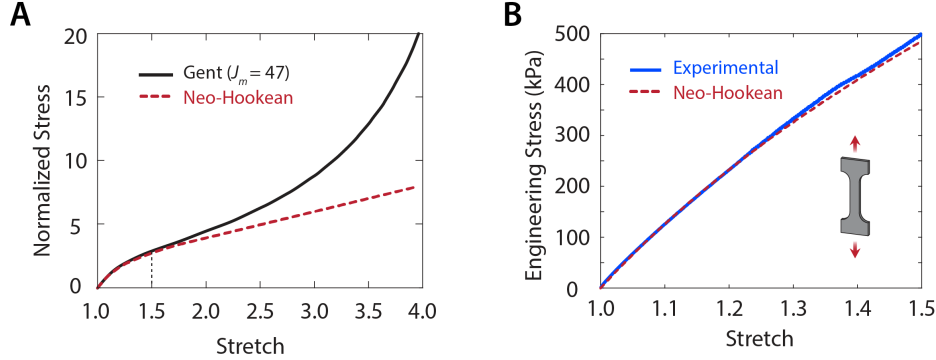
Figure D-2: Justification of the use of the neo-Hookean model for hard-magnetic soft bending actuators.

Justification of neo-Hookean solids: In **Section 2.3.4**, we adopted the simplest neo-Hookean hyperelastic model in a generalized form given in Equation 2.37. Typical elastomers exhibit stiffening behavior when deformed beyond a certain level of stretch as the polymer chained are stretched to resist further elongation, as illustrated in **Figure D-2A**. Such stiffening behavior at large stretch values can be modeled by adopting the Gent or Arruda–Boyce hyperelastic constitutive model, but it cannot be captured by the simple neo-Hookean model, as shown in **Figure D-2A**. However, as discussed above, the maximum strain level during the torque-driven bending actuation

of the hard-magnetic soft materials is limited below 30% (i.e., $\lambda \leq 1.3$), under which the neo-Hookean model can capture the material's behavior (i.e., the stress-stretch curve) quite accurately, as experimentally verified in **Figure D-2B**. Therefore, it is reasonable to use the simplest neo-Hookean hyperelastic model for modeling the hard-magnetic soft materials as torque-driven soft bending actuators.

Appendix E

Derivation of Force and Torque from Magnetic Cauchy Stress

As discussed in **Section 2.3.5**, the magnetic Cauchy stress in Equation (2.44) allows us to treat the magnetic body force and torque as stresses in a homogeneous continuum. Here we derive the magnetic body force and torque in Equations (2.50) and (2.51) from the magnetic Cauchy stress. Substituting Equation (2.44) in its indicial form, i.e., $\sigma_{ij}^{\mathrm{magnetic}} = -B_i\,(\mathbf{M}_\mathrm{r})_j$, we can express the magnetic body force density using indicial notation as

$$
\begin{aligned}
\left(\bar{\mathbf{f}}_\mathrm{m}\right)_i = -\left(\mathrm{div}\,\boldsymbol{\sigma}^{\mathrm{magnetic}}\right)_i &= -\frac{\partial \sigma_{ij}^{\mathrm{magnetic}}}{\partial x_j} = \frac{\partial}{\partial x_j}\left(B_i\,(\mathbf{M}_\mathrm{r})_j\right) \\
&= \frac{\partial B_i}{\partial x_j}(\mathbf{M}_\mathrm{r})_j + B_i\frac{\partial (\mathbf{M}_\mathrm{r})_j}{\partial x_j} \qquad\qquad \text{(E.1)} \\
&= \left(\mathrm{grad}\,\mathbf{B}\right)_{ij}(\mathbf{M}_\mathrm{r})_j + \cancel{\left(\mathrm{div}\,\mathbf{M}_\mathrm{r}\right)}B_i,
\end{aligned}
$$

where the second term vanishes with $\mathrm{div}\,\mathbf{M}_\mathrm{r} = 0$ for uniformly magnetized ideal hard-magnetic soft materials with zero net magnetic charge (i.e., $\rho_\mathrm{m} = 0$). Then, Equation (E.1) can be written equivalently as

$$
\bar{\mathbf{f}}_\mathrm{m} = -\mathrm{div}\,\boldsymbol{\sigma}^{\mathrm{magnetic}} = (\mathrm{grad}\,\mathbf{B})\mathbf{M}_\mathrm{r}, \qquad\qquad \text{(E.2)}
$$

as presented in Equation (2.50).

Similarly, substituting Equation (2.44) in its indicial form into Equation (2.51),

we can express the magnetic body torque density using indicial notation as

$$\left(\bar{\boldsymbol{\tau}}_\mathrm{m}\right)_i = -\varepsilon_{ijk}\,\sigma_{kj}^{\mathrm{magnetic}} = \varepsilon_{ijk}\left(\mathbf{M}_\mathrm{r}\right)_j B_k = \left(\mathbf{M}_\mathrm{r}\times\mathbf{B}\right)_i, \tag{E.3}$$

which is equivalent to

$$\bar{\boldsymbol{\tau}}_\mathrm{m} = -\boldsymbol{\mathcal{E}} : \left(\boldsymbol{\sigma}^{\mathrm{magnetic}}\right)^\mathsf{T} = \mathbf{M}_\mathrm{r}\times\mathbf{B}, \tag{E.4}$$

as presented in Equation (2.51).

It is worth noting that, as discussed in Equation (2.52), the magnetic body force in Equation (E.2) can also be expressed as the negative gradient of the magnetic potential energy per unit volume in its indicial form as

$$\begin{aligned}
\left(\bar{\mathbf{f}}_\mathrm{m}\right)_i &= -\left(\operatorname{grad}\psi^{\mathrm{magnetic}}\right)_i = \left(\operatorname{grad}\left(\mathbf{M}_\mathrm{r}\cdot\mathbf{B}\right)\right)_i \\
&= \frac{\partial}{\partial x_i}\left(\left(\mathbf{M}_\mathrm{r}\right)_j B_j\right) = \frac{\partial(\mathbf{M}_\mathrm{r})_j}{\partial x_i}B_j + \left(\mathbf{M}_\mathrm{r}\right)_j\frac{\partial B_j}{\partial x_i} \\
&= \left(\left(\operatorname{grad}\mathbf{M}_\mathrm{r}\right)^\mathsf{T}\right)_{ij}B_j + \left(\left(\operatorname{grad}\mathbf{B}\right)^\mathsf{T}\right)_{ij}(\mathbf{M}_\mathrm{r})_j,
\end{aligned} \tag{E.5}$$

which is equivalent to

$$\bar{\mathbf{f}}_\mathrm{m} = \left(\operatorname{grad}\mathbf{M}_\mathrm{r}\right)^\mathsf{T}\mathbf{B} + \left(\operatorname{grad}\mathbf{B}\right)^\mathsf{T}\mathbf{M}_\mathrm{r}, \tag{E.6}$$

where the first term vanishes with $\operatorname{grad}\mathbf{M}_\mathrm{r} = \mathbf{0}$ for uniformly magnetized ideal hard-magnetic soft materials. For irrotational (curl-free) magnetic fields with no free current, the spatial gradient of $\mathbf{B}$ field is symmetric (i.e., $\operatorname{grad}\mathbf{B} = \left(\operatorname{grad}\mathbf{B}\right)^\mathsf{T}$), which leads to

$$\bar{\mathbf{f}}_\mathrm{m} = (\operatorname{grad}\mathbf{B})\mathbf{M}_\mathrm{r}, \tag{E.7}$$

which is the same as Equation (E.2) above.

Appendix F

Differentiation of A Rotation Tensor

For the rotation around the z-axis ($\mathbf{e}_3$-direction), the rotation tensor $\mathbf{R}$ is given by

$$\mathbf{R} = \cos\theta\,\mathbf{e}_1 \otimes \mathbf{e}_1 - \sin\theta\,\mathbf{e}_1 \otimes \mathbf{e}_2 + \sin\theta\,\mathbf{e}_2 \otimes \mathbf{e}_1 + \cos\theta\,\mathbf{e}_2 \otimes \mathbf{e}_2 + \mathbf{e}_3 \otimes \mathbf{e}_3, \qquad \text{(F.1)}$$

whose matrix form is given in Equation (2.56). The derivative of the rotation tensor $\mathbf{R}(\theta)$ with respect to θ can be expressed as the skew-symmetric matrix of the unit axis vector (which is $\mathbf{e}_3$ in this case) multiplied by the rotation itself:

$$\frac{\partial\mathbf{R}(\theta)}{\partial\theta} = \mathbf{S}(\mathbf{e}_3)\mathbf{R}(\theta), \qquad \text{(F.2)}$$

where the skew-symmetric matrix of a vector $\mathbf{u}$, denoted by $\mathbf{S}(\mathbf{u})$, is defined as

$$\mathbf{S}(\mathbf{u}) = u_3(\mathbf{e}_2 \otimes \mathbf{e}_1 - \mathbf{e}_1 \otimes \mathbf{e}_2) + u_2(\mathbf{e}_1 \otimes \mathbf{e}_3 - \mathbf{e}_3 \otimes \mathbf{e}_1) + u_1(\mathbf{e}_3 \otimes \mathbf{e}_2 - \mathbf{e}_2 \otimes \mathbf{e}_3). \quad \text{(F.3)}$$

When operating on a vector $\mathbf{v}$, the skew-symmetric tensor $\mathbf{S}(\mathbf{u})$ produces the cross product of the two tensors: $\mathbf{S}(\mathbf{u})\,\mathbf{v} = \mathbf{u} \times \mathbf{v}$, which transforms the first term on the right-hand side of Equation (2.62) into

$$\frac{\partial\mathbf{R}}{\partial\theta}\,\tilde{\mathbf{M}}_\mathrm{r} \cdot \mathbf{B} = \left(\mathbf{e}_3 \times \mathbf{R}\tilde{\mathbf{M}}_\mathrm{r}\right) \cdot \mathbf{B} = \mathbf{e}_3 \cdot \left(\mathbf{R}\tilde{\mathbf{M}}_\mathrm{r} \times \mathbf{B}\right) = \left[\mathbf{R}\tilde{\mathbf{M}}_\mathrm{r} \times \mathbf{B}\right]_3, \qquad \text{(F.4)}$$

as given in Equation (2.63).

Appendix G

Equivalent Point Force in Torque-driven Bending Actuation

Here, we consider a case in which a force, denoted by a vector $\mathbf{F}_{\text{eq}}$, is acting on the free end of a beam in equilibrium in its deformed configuration, in the absence of the influence of external magnetic fields (i.e., no magnetic body torque and force), as illustrated on the right-hand side in **Figure G-1**. The force $\mathbf{F}_{\text{eq}}$ is being applied to the free end at an angle φ relative to the beam's undeformed reference configuration (i.e., $\mathbf{F}_{\text{eq}} = F_{\text{eq}} \cos \varphi \, \mathbf{e}_1 + F_{\text{eq}} \sin \varphi \, \mathbf{e}_2$). Referring to **Figure G-1**, we can set the following bending moment balance at the point on the beam $P(x, y)$:

$$\left[\boldsymbol{\mathcal{M}} + \mathbf{r} \times \mathbf{F}_{\text{eq}} \right]_3 = -\mathcal{M}(x, y) - F_{\text{eq}} \cos \varphi \, (\delta_y - y) + F_{\text{eq}} \sin \varphi \, (\delta_x - x) = 0. \quad \text{(G.1)}$$

Note that the horizontal component, $F_{\text{eq}} \cos \varphi$, should be negative when $\varphi > 90°$. Then, from the moment-curvature relation in Equation (2.55), we can obtain

$$\mathcal{M}(x, y) = EI \frac{\mathrm{d}\theta}{\mathrm{d}s} = -F_{\text{eq}} \cos \varphi \, (\delta_y - y) + F_{\text{eq}} \sin \varphi \, (\delta_x - x). \quad \text{(G.2)}$$

By differentiating Equation (G.2) with respect to the arc length s and applying the differential kinematic relations in Equation (2.78), we obtain

$$EI \frac{\mathrm{d}^2\theta}{\mathrm{d}s^2} = F_{\text{eq}} \cos \varphi \frac{\mathrm{d}y}{\mathrm{d}s} - F_{\text{eq}} \sin \varphi \frac{\mathrm{d}x}{\mathrm{d}s}$$

$$= F_{\text{eq}} \cos \varphi \sin \theta - F_{\text{eq}} \sin \varphi \cos \theta = -F_{\text{eq}} \sin (\varphi - \theta). \quad \text{(G.3)}$$
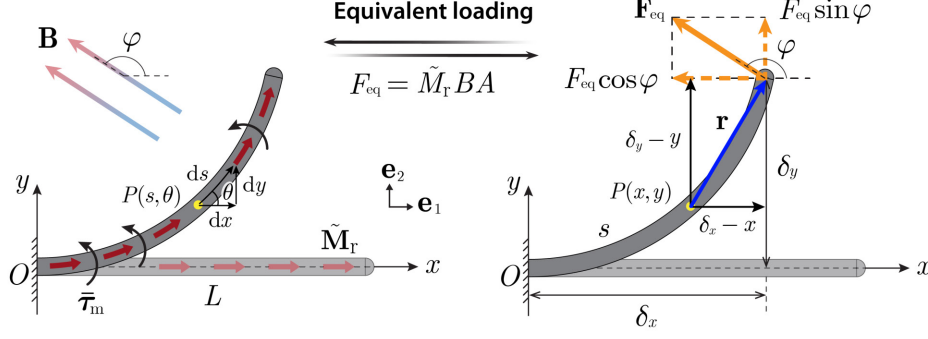
Figure G-1: Equivalent point force in torque-driven bending actuation.

Comparing Equation (G.3) with the governing equation presented in Equation (2.40) in **Section 2.4.3**, we notice that the force acting on the free end of the beam is equivalent to

$$F_{\mathrm{eq}} = \tilde{M}_{\mathrm{r}} B A. \tag{G.4}$$

It is worth noting that the uniform actuating field $\mathbf{B}$ and the equivalent point force $\mathbf{F}_{\mathrm{eq}}$ at the free end of the beam are applied at an angle φ relative to the beam's undeformed reference configuration. It is also worth noting that the two scenarios in **Figure G-1** share the same boundary conditions: $\theta(0) = 0$ and $\theta'(L) = 0$.

Bibliography

[1] Y. Kim, H. Yuk, R. Zhao, S. A. Chester, and X. Zhao, "Printing ferromagnetic domains for untethered fast-transforming soft materials," *Nature*, vol. 558, no. 7709, pp. 274–279, 2018.

[2] R. Zhao, Y. Kim, S. A. Chester, P. Sharma, and X. Zhao, "Mechanics of hard-magnetic soft materials," *Journal of the Mechanics and Physics of Solids*, vol. 124, pp. 244–263, 2019.

[3] Y. Kim, G. A. Parada, S. Liu, and X. Zhao, "Ferromagnetic soft continuum robots," *Science Robotics*, vol. 4, no. 33, p. eaax7329, 2019.

[4] L. Wang, Y. Kim, C. F. Guo, and X. Zhao, "Hard-magnetic elastica," *Journal of the Mechanics and Physics of Solids*, vol. 142, p. 104045, 2020.

[5] Y. Kim and X. Zhao, "Magnetic soft materials and robots," *Chemical Reviews*, vol. 122, no. 5, pp. 5317–5364, 2022.

[6] Y. Kim, E. Genevriere, P. Harker, J. Choe, M. Balicki, R. W. Regenhardt, J. E. Vranic, A. A. Dmytriw, A. B. Patel, and X. Zhao, "Telerobotic neurovascular interventions with magnetic manipulation," *Science Robotics*, vol. 7, p. eabg9907, 2022.

[7] Y. Kim, E. Genevriere, P. Harker, J. Choe, M. Balicki, A. B. Patel, and X. Zhao, "Telerobotically controlled magnetic soft continuum robots for neurovascular interventions," in *2022 IEEE International Conference on Robotics and Automation (ICRA)*, 2022.

[8] Y. Kim, X. Zhao, and H. Yuk, "Programmable soft materials containing ferromagnetic domains and methods of making," US Patent Application, Publication number: US 2020/0223099 A1 (pending).

[9] Y. Kim and X. Zhao, "Magnetically steerable continuum robotic guidewires for neurovascular applications," 2021, US Patent 11,103,324 (granted).

[10] Centers for Disease Control and Prevention (CDC), Division for Heart Disease and Stroke Prevention, "Stroke Facts," https://www.cdc.gov/stroke/facts.htm, 2021, accessed: 2021-05-25.

[11] S. S. Virani, A. Alonso, E. J. Benjamin, M. S. Bittencourt, C. W. Callaway, A. P. Carson, A. M. Chamberlain, A. R. Chang, S. Cheng, F. N. Delling, L. Djousse, M. S. Elkind, J. F. Ferguson, M. Fornage, S. S. Khan, B. M. Kissela, K. L. Knutson, T. W. Kwan, D. T. Lackland, T. T. Lewis, J. H. Lichtman, C. T. Longenecker, M. S. Loop, P. L. Lutsey, S. S. Martin, K. Matsushita, A. E. Moran, M. E. Mussolino, A. M. Perak, W. D. Rosamond, G. A. Roth, U. K. Sampson, G. M. Satou, E. B. Schroeder, S. H. Shah, C. M. Shay, N. L. Spartano, A. Stokes, D. L. Tirschwell, L. B. VanWagner, and C. W. Tsao, "Heart disease and stroke statistics—2020 update: A report from the american heart association," *Circulation*, vol. 141, no. 9, pp. e139–e596, 2020.

[12] World Health Organization (WHO), WHO Global Health Estimates, "The Top 10 Causes of Death," https://www.who.int/news-room/fact-sheets/detail/the-top-10-causes-of-death, 2020, accessed: 2020-12-09.

[13] S. S. Panesar, J. J. Volpi, A. Lumsden, V. Desai, N. S. Kleiman, T. L. Sample, E. Elkins, and G. W. Britz, "Telerobotic stroke intervention: A novel solution to the care dissemination dilemma," *Journal of Neurosurgery*, vol. 132, no. 3, pp. 971–978, 2020.

[14] M. Goyal, G. R. Sutherland, S. Lama, P. Cimflova, N. Kashani, A. Mayank, M.-N. Psychogios, L. Spelle, V. Costalat, N. Sakai, and J. M. Ospel, "Neurointerventional robotics: Challenges and opportunities," *Clinical Neuroradiology*, vol. 30, no. 2, pp. 203–208, 2020.

[15] C. R. Gomez, "Editorial: Time is brain!" *Journal of Stroke and Cerebrovascular Diseases*, vol. 3, no. 1, pp. 1–2, 1993.

[16] U.S. Food and Drug Administration (FDA), Center for Devices and Radiological Health, "Coronary, Peripheral, and Neurovascular Guidewires—Performance Tests and Recommended Labeling," FDA-2018-D-1775, 2019. https://www.fda.gov/media/113959/download.

[17] T. Krings, J. Finney, P. Niggemann, P. Reinacher, N. Lück, A. Drexler, J. Lovell, A. Meyer, R. Sehra, P. Schauerte, M. Reinges, F. J. Hans, and A. Thron, "Magnetic versus manual guidewire manipulation in neuroradiology: In vitro results," *Neuroradiology*, vol. 48, no. 6, pp. 394–401, 2006.

[18] M. R. Harrigan and J. P. Deveikis, *Handbook of Cerebrovascular Disease and Neurointerventional Technique*. Totowa, NJ: Humana Press, 2013, ch. General Considerations for Neurointerventional Procedures, pp. 153–185.

[19] C. E. Hoffler and A. M. Ilyas, "Fluoroscopic radiation exposure: Are we protecting ourselves adequately?" *Journal of Bone and Joint Surgery*, vol. 97, no. 9, 2015.

[20] S. A. Menaker, S. S. Shah, B. M. Snelling, S. Sur, R. M. Starke, and E. C. Peterson, "Current applications and future perspectives of robotics in cerebrovascular and endovascular neurosurgery," *Journal of NeuroInterventional Surgery*, vol. 10, no. 1, pp. 78–82, 2018.

[21] J. Bonatti, G. Vetrovec, C. Riga, O. Wazni, and P. Stadler, "Robotic technology in cardiovascular medicine," *Nature Reviews Cardiology*, vol. 11, no. 5, pp. 266–275, 2014.

[22] J. Troccaz, G. Dagnino, and G.-Z. Yang, "Frontiers of medical robotics: From concept to systems to clinical translation," *Annual Review of Biomedical Engineering*, vol. 21, no. 1, pp. 193–218, 2019.

[23] J. Chakravartti and S. V. Rao, "Robotic assisted percutaneous coronary intervention: Hype or hope?" *Journal of the American Heart Association*, vol. 8, no. 13, p. e012743, 2019.

[24] V. M. Pereira, N. M. Cancelliere, P. Nicholson, I. Radovanovic, K. E. Drake, J.-M. Sungur, T. Krings, and A. Turk, "First-in-human, robotic-assisted neuroendovascular intervention," *Journal of NeuroInterventional Surgery*, vol. 12, no. 4, pp. 338–340, 2020.

[25] G. W. Britz, J. Tomas, and A. Lumsden, "Feasibility of robotic-assisted neurovascular interventions: Initial experience in flow model and porcine model," *Neurosurgery*, vol. 86, no. 2, pp. 309–314, 2020.

[26] K. C. Sajja, A. Sweid, F. Al Saiegh, N. Chalouhi, M. B. Avery, R. F. Schmidt, S. I. Tjoumakaris, M. R. Gooch, N. Herial, R. Abbas, H. Zarzour, V. Romo, R. Rosenwasser, and P. Jabbour, "Endovascular robotic: feasibility and proof of principle for diagnostic cerebral angiography and carotid artery stenting," *Journal of NeuroInterventional Surgery*, vol. 12, no. 4, pp. 345–349, 2020.

[27] V. M. Pereira, P. Nicholson, N. M. Cancelliere, X. Y. E. Liu, R. Agid, I. Radovanovic, and T. Krings, "Feasibility of robot-assisted neuroendovascular procedures," *Journal of Neurosurgery*, pp. 1–13, 2021.

[28] M. R. Jolly, J. D. Carlson, and B. C. Muñoz, "A model of the behaviour of magnetorheological materials," *Smart Materials and Structures*, vol. 5, no. 5, pp. 607–614, 1996.

[29] L. C. Davis, "Model of magnetorheological elastomers," *Journal of Applied Physics*, vol. 85, no. 6, pp. 3348–3351, 1999.

[30] P. von Lockette, S. E. Lofland, J. Biggs, J. Roche, J. Mineroff, and M. Babcock, "Investigating new symmetry classes in magnetorheological elastomers: Cantilever bending behavior," *Smart Materials and Structures*, vol. 20, no. 10, p. 105022, 2011.

[31] E. Galipeau and P. Ponte Castañeda, "A finite-strain constitutive model for magnetorheological elastomers: Magnetic torques and fiber rotations," *Journal of the Mechanics and Physics of Solids*, vol. 61, no. 4, pp. 1065–1090, 2013.

[32] Y. Han, W. Hong, and L. E. Faidley, "Field-stiffening effect of magneto-rheological elastomers," *International Journal of Solids and Structures*, vol. 50, no. 14, pp. 2281–2288, 2013.

[33] R. Bustamante, "Transversely isotropic nonlinear magneto-active elastomers," *Acta Mechanica*, vol. 210, no. 3, pp. 183–214, 2010.

[34] Y. Han, A. Mohla, X. Huang, W. Hong, and L. E. Faidley, "Magnetostriction and field stiffening of magneto-active elastomers," *International Journal of Applied Mechanics*, vol. 07, no. 01, p. 1550001, 2015.

[35] I. Brigadnov and A. Dorfmann, "Mathematical modeling of magneto-sensitive elastomers," *International Journal of Solids and Structures*, vol. 40, no. 18, pp. 4659–4674, 2003.

[36] A. Dorfmann and R. W. Ogden, "Nonlinear magnetoelastic deformations of elastomers," *Acta Mechanica*, vol. 167, no. 1, pp. 13–28, 2004.

[37] R. Bustamante, A. Dorfmann, and R. W. Ogden, "Universal relations in isotropic nonlinear magnetoelasticity," *The Quarterly Journal of Mechanics and Applied Mathematics*, vol. 59, no. 3, pp. 435–450, 2006.

[38] M. Zrínyi, L. Barsi, and A. Büki, "Deformation of ferrogels induced by nonuniform magnetic fields," *The Journal of Chemical Physics*, vol. 104, no. 21, pp. 8750–8756, 1996.

[39] M. Zrínyi, L. Barsi, and A. Büki, "Ferrogel: A new magneto-controlled elastic medium," *Polymer Gels and Networks*, vol. 5, no. 5, pp. 415–427, 1997.

[40] Y. Han, W. Hong, and L. Faidley, "Coupled magnetic field and viscoelasticity of ferrogel," *International Journal of Applied Mechanics*, vol. 03, no. 02, pp. 259–278, 2011.

[41] P. Gebhart and T. Wallmersperger, "A general framework for the modeling of porous ferrogels at finite strains," *Journal of the Mechanics and Physics of Solids*, vol. 122, pp. 69–83, 2019.

[42] Y. Kim and X. Zhao, "Soft microbots programmed by nanomagnets," *Nature*, vol. 575, pp. 58–59, 2019.

[43] A. du Plessis d'Argentré, S. Perry, Y. Iwata, H. Iwasaki, E. Iwase, A. Fabozzo, I. Will, D. Rus, D. D. Damian, and S. Miyashita, "Programmable medicine: Autonomous, ingestible, deployable hydrogel patch and plug for stomach ulcer therapy," in *2018 IEEE International Conference on Robotics and Automation (ICRA)*, 2018, pp. 1511–1518.

[44] S. Miyashita, S. Guitron, K. Yoshida, S. Li, D. D. Damian, and D. Rus, "Ingestible, controllable, and degradable origami robot for patching stomach wounds," in *2016 IEEE International Conference on Robotics and Automation (ICRA)*, 2016, pp. 909–916.

[45] S. Yim, E. Gultepe, D. H. Gracias, and M. Sitti, "Biopsy using a magnetic capsule endoscope carrying, releasing, and retrieving untethered microgrippers," *IEEE Transactions on Biomedical Engineering*, vol. 61, no. 2, pp. 513–521, 2014.

[46] D. Son, H. Gilbert, and M. Sitti, "Magnetically actuated soft capsule endoscope for fine-needle biopsy," *Soft Robotics*, vol. 7, no. 1, pp. 10–21, 2020.

[47] L. Bowen, K. Springsteen, H. Feldstein, M. Frecker, T. W. Simpson, and P. von Lockette, "Development and validation of a dynamic model of magneto-active elastomer actuation of the origami waterbomb base," *Journal of Mechanisms and Robotics*, vol. 7, no. 1, 2015.

[48] J. M. Ginder, S. M. Clark, W. F. Schlotter, and M. E. Nichols, "Magnetostrictive phenomena in magnetorheological elastomers," *International Journal of Modern Physics B*, vol. 16, no. 17n18, pp. 2412–2418, 2002.

[49] M. Schümann and S. Odenbach, "In-situ observation of the particle microstructure of magnetorheological elastomers in presence of mechanical strain and magnetic fields," *Journal of Magnetism and Magnetic Materials*, vol. 441, pp. 88–92, 2017.

[50] J. E. Martin, R. A. Anderson, D. Read, and G. Gulley, "Magnetostriction of field-structured magnetoelastomers," *Physical Review E*, vol. 74, p. 051507, 2006.

[51] X. Zhao, J. Kim, C. A. Cezar, N. Huebsch, K. Lee, K. Bouhadir, and D. J. Mooney, "Active scaffolds for on-demand drug and cell delivery," *Proceedings of the National Academy of Sciences*, vol. 108, no. 1, pp. 67–72, 2011.

[52] H. Haider, C. H. Yang, W. J. Zheng, J. H. Yang, M. X. Wang, S. Yang, M. Zrínyi, Y. Osada, Z. Suo, Q. Zhang, J. Zhou, and Y. M. Chen, "Exceptionally tough and notch-insensitive magnetic hydrogels," *Soft Matter*, vol. 11, pp. 8253–8261, 2015.

[53] M. Zrinyi, "Magnetically responsive polymer gels and elastomers: Properties, synthesis and applications," in *Smart Polymers and their Applications*, M. R. Aguilar and J. San Román, Eds. Woodhead Publishing, 2014, pp. 134–165.

[54] V. Q. Nguyen and R. V. Ramanujan, "Novel coiling behavior in magnet-polymer composites," *Macromolecular Chemistry and Physics*, vol. 211, no. 6, pp. 618–626, 2010.

[55] V. Q. Nguyen, A. S. Ahmed, and R. V. Ramanujan, "Morphing soft magnetic composites," *Advanced Materials*, vol. 24, no. 30, pp. 4041–4054, 2012.

[56] A. Crivaro, R. Sheridan, M. Frecker, T. W. Simpson, and P. von Lockette, "Bistable compliant mechanism using magneto active elastomer actuation," *Journal of Intelligent Material Systems and Structures*, vol. 27, no. 15, pp. 2049–2061, 2016.

[57] G. Bertotti, *Hysteresis in Magnetism: For Physicists, Materials Scientists, and Engineers*. San Diego, CA: Academic Press, 1998, ch. Maxwell's Equations in Magnetic Media, pp. 81–102.

[58] J. Edelmann, A. J. Petruska, and B. J. Nelson, "Magnetic control of continuum devices," *The International Journal of Robotics Research*, vol. 36, no. 1, pp. 68–85, 2017.

[59] L. Anand and S. Govindjee, *Continuum Mechanics of Solids*. New York, NY: Oxford University Press, 2020, ch. Kinematics, pp. 35–67.

[60] G. A. Holzapfel, *Nonlinear Solid Mechanics: A Continuum Approach for Engineering Science*. Chichester: John Wiley & Sons, 2001, ch. Kinematics, pp. 55–106.

[61] G. A. Holzapfel, *Nonlinear Solid Mechanics: A Continuum Approach for Engineering Science*. Chichester: John Wiley & Sons, 2001, ch. Balance Principles, pp. 131–174.

[62] M. E. Gurtin, E. Fried, and L. Anand, *The Mechanics and Thermodynamics of Continua*. New York, NY: Cambridge University Press, 2010, ch. Basic Thermodynamical Principles, pp. 181–205.

[63] L. Anand and S. Govindjee, *Continuum Mechanics of Solids*. New York, NY: Oxford University Press, 2020, ch. Finite Elasticity, pp. 611–635.

[64] L. Anand and S. Govindjee, *Continuum Mechanics of Solids*. New York, NY: Oxford University Press, 2020, ch. Finite Elasticity of Elastomeric Materials, pp. 637–654.

[65] G. A. Holzapfel, *Nonlinear Solid Mechanics: A Continuum Approach for Engineering Science*. Chichester: John Wiley & Sons, 2001, ch. Hyperelastic Materials, pp. 205–295.

[66] A. Dorfmann and R. Ogden, "Magnetoelastic modelling of elastomers," *European Journal of Mechanics – A/Solids*, vol. 22, no. 4, pp. 497–507, 2003.

[67] L. Dorfmann and R. W. Ogden, *Nonlinear theory of electroelastic and magnetoelastic interactions*. New York, NY: Springer, 2014, ch. Nonlinear Elasticity Background, pp. 47–90.

[68] G. A. Holzapfel, *Nonlinear Solid Mechanics: A Continuum Approach for Engineering Science*. Chichester: John Wiley & Sons, 2001, ch. The Concept of Stress, pp. 109–129.

[69] R. Abeyaratne, "Continuum Mechanics, Volume II of Lecture Notes on the Mechanics of Solids," http://web.mit.edu/abeyaratne/lecture_notes.html, 2014.

[70] M. E. Gurtin, E. Fried, and L. Anand, *The Mechanics and Thermodynamics of Continua*. New York, NY: Cambridge University Press, 2010, ch. Basic Mechanical Principles, pp. 125–179.

[71] T. Bretl and Z. McCarthy, "Quasi-static manipulation of a kirchhoff elastic rod based on a geometric analysis of equilibrium configurations," *The International Journal of Robotics Research*, vol. 33, no. 1, pp. 48–68, 2014.

[72] F. Jiang, S. Tian, and W. Yu, "Nonlinear modelling of axially deformable elastica based on hyperelasticity," in *57th AIAA/ASCE/AHS/ASC Structures, Structural Dynamics, and Materials Conference*, 2016.

[73] L. B. Kratchman, T. L. Bruns, J. J. Abbott, and R. J. Webster, "Guiding elastic rods with a robot-manipulated magnet for medical applications," *IEEE Transactions on Robotics*, vol. 33, no. 1, pp. 227–233, 2017.

[74] I. Tunay, "Spatial continuum models of rods undergoing large deformation and inflation," *IEEE Transactions on Robotics*, vol. 29, no. 2, pp. 297–307, 2013.

[75] O. M. O'Reilly, "Modeling nonlinear problems in the mechanics of strings and rods," in *Interaction of Mechanics and Mathematics*, L. Truskinovsky, Ed. Springer, 2017.

[76] K. M. de Payrebrune and O. M. O'Reilly, "On constitutive relations for a rod-based model of a pneu-net bending actuator," *Extreme Mechanics Letters*, vol. 8, pp. 38–46, 2016.

[77] I. Tunay, "Modeling magnetic catheters in external fields," in *The 26th Annual International Conference of the IEEE Engineering in Medicine and Biology Society*, vol. 1, 2004, pp. 2006–2009.

[78] G. Z. Lum, Z. Ye, X. Dong, H. Marvi, O. Erin, W. Hu, and M. Sitti, "Shape-programmable magnetic soft matter," *Proceedings of the National Academy of Sciences*, vol. 113, no. 41, pp. E6007–E6015, 2016.

[79] S. E. Sandler, B. Fellows, and O. T. Mefford, "Best practices for characterization of magnetic nanoparticles for biomedical applications," *Analytical Chemistry*, vol. 91, no. 22, pp. 14 159–14 169, 2019.

[80] R. W. Chantrell and K. O'Grady, "Magnetic characterization of recording media," *Journal of Physics D: Applied Physics*, vol. 25, no. 1, pp. 1–23, 1992.

[81] D. Tabor, "The bulk modulus of rubber," *Polymer*, vol. 35, no. 13, pp. 2759–2763, 1994.

[82] M. Cianchetti, C. Laschi, A. Menciassi, and P. Dario, "Biomedical applications of soft robotics," *Nature Reviews Materials*, vol. 3, no. 6, pp. 143–153, 2018.

[83] G.-Z. Yang, J. Bellingham, P. E. Dupont, P. Fischer, L. Floridi, R. Full, N. Jacobstein, V. Kumar, M. McNutt, R. Merrifield *et al.*, "The grand challenges of science robotics," *Science Robotics*, vol. 3, no. 14, p. eaar7650, 2018.

[84] M. Runciman, A. Darzi, and G. P. Mylonas, "Soft robotics in minimally invasive surgery," *Soft Robotics*, vol. 6, no. 4, pp. 423–443, 2019.

[85] H. Rafii-Tari, C. Payne, and G.-Z. Yang, "Current and emerging robot-assisted endovascular catheterization technologies: A review," *Annals of Biomedical Engineering*, vol. 42, no. 4, pp. 697–715, 2014.

[86] J. Burgner-Kahrs, D. C. Rucker, and H. Choset, "Continuum robots for medical applications: A survey," *IEEE Transactions on Robotics*, vol. 31, no. 6, pp. 1261–1280, 2015.

[87] D. B. Camarillo, C. R. Carlson, and J. K. Salisbury, "Configuration tracking for continuum manipulators with coupled tendon drive," *IEEE Transactions on Robotics*, vol. 25, no. 4, pp. 798–808, 2009.

[88] M. Mahvash and P. E. Dupont, "Stiffness control of surgical continuum manipulators," *IEEE Transactions on Robotics*, vol. 27, no. 2, pp. 334–345, 2011.

[89] T. Kato, I. Okumura, S.-E. Song, A. J. Golby, and N. Hata, "Tendon-driven continuum robot for endoscopic surgery: Preclinical development and validation of a tension propagation model," *IEEE/ASME Transactions on Mechatronics*, vol. 20, no. 5, pp. 2252–2263, 2015.

[90] M. M. Dalvand, S. Nahavandi, and R. D. Howe, "An analytical loading model for n-tendon continuum robots," *IEEE Transactions on Robotics*, vol. 34, no. 5, pp. 1215–1225, 2018.

[91] Y.-H. Kim, Y.-J. Park, H. In, C. W. Jeong, and K.-J. Cho, "Design concept of hybrid instrument for laparoscopic surgery and its verification using scale model test," *IEEE/ASME Transactions on Mechatronics*, vol. 21, no. 1, pp. 142–153, 2016.

[92] Z. Li, L. Wu, H. Ren, and H. Yu, "Kinematic comparison of surgical tendon-driven manipulators and concentric tube manipulators," *Mechanism and Machine Theory*, vol. 107, pp. 148–165, 2017.

[93] Y. Hu, W. Li, L. Zhang, and G.-Z. Yang, "Designing, prototyping, and testing a flexible suturing robot for transanal endoscopic microsurgery," *IEEE Robotics and Automation Letters*, vol. 4, no. 2, pp. 1669–1675, 2019.

[94] M. P. Armacost, J. Adair, T. Munger, R. R. Viswanathan, F. M. Creighton, D. T. Curd, and R. Sehra, "Accurate and reproducible target navigation with the Stereotaxis Niobe® magnetic navigation system," *Journal of Cardiovascular Electrophysiology*, vol. 18, pp. S26–S31, 2007.

[95] V. N. Le, N. H. Nguyen, K. Alameh, R. Weerasooriya, and P. Pratten, "Accurate modeling and positioning of a magnetically controlled catheter tip," *Medical Physics*, vol. 43, no. 2, pp. 650–663, 2016.

[96] C. Chautems, S. Lyttle, Q. Boehler, and B. J. Nelson, "Design and evaluation of a steerable magnetic sheath for cardiac ablations," *IEEE Robotics and Automation Letters*, vol. 3, no. 3, pp. 2123–2128, 2018.

[97] J. Edelmann, A. J. Petruska, and B. J. Nelson, "Estimation-based control of a magnetic endoscope without device localization," *Journal of Medical Robotics Research*, vol. 3, no. 01, p. 1850002, 2018.

[98] A. K. Hoshiar, S. Jeon, K. Kim, S. Lee, J.-y. Kim, and H. Choi, "Steering algorithm for a flexible microrobot to enhance guidewire control in a coronary angioplasty application," *Micromachines*, vol. 9, no. 12, p. 617, 2018.

[99] S. Jeon, A. K. Hoshiar, K. Kim, S. Lee, E. Kim, S. Lee, J.-y. Kim, B. J. Nelson, H.-J. Cha, B.-J. Yi, , and H. Choi, "A magnetically controlled soft microrobot steering a guidewire in a three-dimensional phantom vascular network," *Soft Robotics*, vol. 6, no. 1, pp. 54–68, 2019.

[100] U.S. Food and Drug Administration (FDA), "Class 2 Medical Device Recalls: Cronus Endovascular Guidewires," 510(k) Number: K021363, FDA, 2004. https://www.accessdata.fda.gov/scripts/cdrh/cfdocs/cfRES/res.cfm?start_search=1&knumber=K021363.

[101] T. Ranzani, S. Russo, N. W. Bartlett, M. Wehner, and R. J. Wood, "Increasing the dimensionality of soft microstructures through injection-induced self-folding," *Advanced Materials*, vol. 30, no. 38, p. 1802739, 2018.

[102] J. T. Overvelde, T. Kloek, J. J. D'haen, and K. Bertoldi, "Amplifying the response of soft actuators by harnessing snap-through instabilities," *Proceedings of the National Academy of Sciences*, vol. 112, no. 35, pp. 10 863–10 868, 2015.

[103] W. Hu, G. Z. Lum, M. Mastrangeli, and M. Sitti, "Small-scale soft-bodied robot with multimodal locomotion," *Nature*, vol. 554, no. 7690, pp. 81–85, 2018.

[104] M. Mooney, "The viscosity of a concentrated suspension of spherical particles," *Journal of Colloid Science*, vol. 6, no. 2, pp. 162–170, 1951.

[105] S. Ahmed and F. Jones, "A review of particulate reinforcement theories for polymer composites," *Journal of Materials Science*, vol. 25, no. 12, pp. 4933–4942, 1990.

[106] Y. Yu, H. Yuk, G. A. Parada, Y. Wu, X. Liu, C. S. Nabzdyk, K. Youcef-Toumi, J. Zang, and X. Zhao, "Multifunctional "hydrogel skins" on diverse polymers with arbitrary shapes," *Advanced Materials*, vol. 31, no. 7, p. 1807101, 2019.

[107] C. R. Pasarikovski, J. Cardinell, and V. X. D. Yang, "Perspective review on applications of optics in cerebral endovascular neurosurgery," *Journal of Biomedical Optics*, vol. 24, no. 3, p. 030601, 2019.

[108] S. Erni, S. Schürle, A. Fakhraee, B. E. Kratochvil, and B. J. Nelson, "Comparison, optimization, and limitations of magnetic manipulation systems," *Journal of Micro-Bio Robotics*, vol. 8, no. 3, pp. 107–120, 2013.

[109] I. Rahman, M. Pioche, C. S. Shim, S. P. Lee, I.-K. Sung, J.-C. Saurin, and P. Patel, "Magnetic-assisted capsule endoscopy in the upper gi tract by using a novel navigation system (with video)," *Gastrointestinal Endoscopy*, vol. 83, no. 5, pp. 889–895, 2016.

[110] N. Shamsudhin, V. I. Zverev, H. Keller, S. Pane, P. W. Egolf, B. J. Nelson, and A. M. Tishin, "Magnetically guided capsule endoscopy," *Medical Physics*, vol. 44, no. 8, pp. e91–e111, 2017.

[111] J. Keller, C. Fibbe, F. Volke, J. Gerber, A. C. Mosse, M. Reimann-Zawadzki, E. Rabinovitz, P. Layer, and P. Swain, "Remote magnetic control of a wireless capsule endoscope in the esophagus is safe and feasible: Results of a randomized, clinical trial in healthy volunteers," *Gastrointestinal Endoscopy*, vol. 72, no. 5, pp. 941–946, 2010.

[112] J. Keller, C. Fibbe, F. Volke, J. Gerber, A. C. Mosse, M. Reimann-Zawadzki, E. Rabinovitz, P. Layer, D. Schmitt, V. Andresen *et al.*, "Inspection of the human stomach using remote-controlled capsule endoscopy: A feasibility study in healthy volunteers (with videos)," *Gastrointestinal Endoscopy*, vol. 73, no. 1, pp. 22–28, 2011.

[113] M. F. Hale, I. Rahman, K. Drew, R. Sidhu, S. A. Riley, P. Patel, and M. E. McAlindon, "Magnetically steerable gastric capsule endoscopy is equivalent to flexible endoscopy in the detection of markers in an excised porcine stomach model: results of a randomized trial," *Endoscopy*, vol. 47, no. 07, pp. 650–653, 2015.

[114] X. Liu, Y. Yang, M. E. Inda, S. Lin, J. Wu, Y. Kim, X. Chen, D. Ma, T. K. Lu, and X. Zhao, "Magnetic living hydrogels for intestinal localization, retention, and diagnosis," *Advanced Functional Materials*, vol. 31, no. 27, p. 2010918, 2021.

[115] X. Yang, W. Shang, H. Lu, Y. Liu, L. Yang, R. Tan, X. Wu, and Y. Shen, "An agglutinate magnetic spray transforms inanimate objects into millirobots for biomedical applications," *Science Robotics*, vol. 5, no. 48, p. eabc8191, 2020.

[116] J. Zhang, Z. Ren, W. Hu, R. H. Soon, I. C. Yasa, Z. Liu, and M. Sitti, "Voxelated three-dimensional miniature magnetic soft machines via multimaterial heterogeneous assembly," *Science Robotics*, vol. 6, no. 53, p. eabf0112, 2021.

[117] G. Ciuti, R. Donlin, P. Valdastri, A. Arezzo, A. Menciassi, M. Morino, and P. Dario, "Robotic versus manual control in magnetic steering of an endoscopic capsule," *Endoscopy*, vol. 42, no. 02, pp. 148–152, 2010.

[118] G. Ciuti, P. Valdastri, A. Menciassi, and P. Dario, "Robotic magnetic steering and locomotion of capsule endoscope for diagnostic and surgical endoluminal procedures," *Robotica*, vol. 28, no. 2, pp. 199–207, 2010.

[119] S. Tognarelli, V. Castelli, G. Ciuti, C. Di Natali, E. Sinibaldi, P. Dario, and A. Menciassi, "Magnetic propulsion and ultrasound tracking of endovascular devices," *Journal of Robotic Surgery*, vol. 6, no. 1, pp. 5–12, 2012.

[120] A. W. Mahoney and J. J. Abbott, "Generating rotating magnetic fields with a single permanent magnet for propulsion of untethered magnetic devices in a lumen," *IEEE Transactions on Robotics*, vol. 30, no. 2, pp. 411–420, 2014.

[121] A.W. Mahoney and J. J. Abbott, "Five-degree-of-freedom manipulation of an untethered magnetic device in fluid using a single permanent magnet with application in stomach capsule endoscopy," *The International Journal of Robotics Research*, vol. 35, no. 1-3, pp. 129–147, 2016.

[122] G. Pittiglio, L. Barducci, J. W. Martin, J. C. Norton, C. A. Avizzano, K. L. Obstein, and P. Valdastri, "Magnetic levitation for soft-tethered capsule colonoscopy actuated with a single permanent magnet: A dynamic control approach," *IEEE Robotics and Automation Letters*, vol. 4, no. 2, pp. 1224–1231, 2019.

[123] J. C. Norton, P. R. Slawinski, H. S. Lay, J. W. Martin, B. F. Cox, G. Cummins, M. P. Desmulliez, R. E. Clutton, K. L. Obstein, S. Cochran *et al.*, "Intelligent magnetic manipulation for gastrointestinal ultrasound," *Science Robotics*, vol. 4, no. 31, p. eaav7725, 2019.

[124] B. L. Nguyen, J. L. Merino, and E. S. Gang, "Remote navigation for ablation procedures–a new step forward in the treatment of cardiac arrhythmias," *European Cardiology*, vol. 6, no. 3, pp. 50–56, 2010.

[125] G. Bassil, S. M. Markowitz, C. F. Liu, G. Thomas, J. E. Ip, B. B. Lerman, and J. W. Cheung, "Robotics for catheter ablation of cardiac arrhythmias: Current technologies and practical approaches," *Journal of Cardiovascular Electrophysiology*, vol. 31, no. 3, pp. 739–752, 2020.

[126] S. Ramcharitar, M. S. Patterson, R. J. Van Geuns, C. Van Meighem, and P. W. Serruys, "Technology insight: Magnetic navigation in coronary interventions," *Nature Clinical Practice Cardiovascular Medicine*, vol. 5, no. 3, pp. 148–156, 2008.

[127] M. Schiemann, R. Killmann, M. Kleen, N. Abolmaali, J. Finney, and T. J. Vogl, "Vascular guide wire navigation with a magnetic guidance system: Experimental results in a phantom," *Radiology*, vol. 232, no. 2, pp. 475–481, 2004.

[128] K. Tsuchida, H. M. García-García, W. J. van der Giessen, E. P. McFadden, M. van der Ent, G. Sianos, H. Meulenbrug, A. T. Ong, and P. W. Serruys, "Guidewire navigation in coronary artery stenoses using a novel magnetic navigation system: First clinical experience," *Catheterization and Cardiovascular Interventions*, vol. 67, no. 3, pp. 356–363, 2006.

[129] J. J. Abbott, E. Diller, and A. J. Petruska, "Magnetic methods in robotics," *Annual Review of Control, Robotics, and Autonomous Systems*, vol. 3, pp. 57–90, 2020.

[130] Z. Yang and L. Zhang, "Magnetic actuation systems for miniature robots: A review," *Advanced Intelligent Systems*, vol. 2, no. 9, p. 2000082, 2020.

[131] E. M. Purcell, "Helmholtz coils revisited," *American Journal of Physics*, vol. 57, no. 1, pp. 18–22, 1989.

[132] R. Turner, "Gradient coil design: a review of methods," *Magnetic Resonance Imaging*, vol. 11, no. 7, pp. 903–920, 1993.

[133] C. Chautems, A. Tonazzini, Q. Boehler, S. H. Jeong, D. Floreano, and B. J. Nelson, "Magnetic continuum device with variable stiffness for minimally invasive surgery," *Advanced Intelligent Systems*, vol. 2, no. 6, p. 1900086, 2020.

[134] E. Diller and M. Sitti, "Three-dimensional programmable assembly by untethered magnetic robotic micro-grippers," *Advanced Functional Materials*, vol. 24, no. 28, pp. 4397–4404, 2014.

[135] E. S. Gang, B. L. Nguyen, Y. Shachar, L. Farkas, L. Farkas, B. Marx, D. Johnson, M. C. Fishbein, C. Gaudio, and S. J. Kim, "Dynamically shaped magnetic fields: Initial animal validation of a new remote electrophysiology catheter guidance and control system," *Circulation: Arrhythmia and Electrophysiology*, vol. 4, no. 5, pp. 770–777, 2011.

[136] I. S. M. Khalil, V. Magdanz, S. Sanchez, O. G. Schmidt, and S. Misra, "Three-dimensional closed-loop control of self-propelled microjets," *Applied Physics Letters*, vol. 103, no. 17, p. 172404, 2013.

[137] S. L. Charreyron, Q. Boehler, B. Kim, C. Weibel, C. Chautems, and B. J. Nelson, "Modeling electromagnetic navigation systems," *IEEE Transactions on Robotics*, vol. 37, no. 4, pp. 1009–1021, 2021.

[138] J. Li, H. Wang, J. Cui, Q. Shi, Z. Zheng, T. Sun, Q. Huang, and T. Fukuda, "Magnetic micromachine using nickel nanoparticles for propelling and releasing in indirect assembly of cell-laden micromodules," *Micromachines*, vol. 10, no. 6, p. 370, 2019.

[139] A. Pourkand and J. J. Abbott, "A critical analysis of eight-electromagnet manipulation systems: The role of electromagnet configuration on strength, isotropy, and access," *IEEE Robotics and Automation Letters*, vol. 3, no. 4, pp. 2957–2962, 2018.

[140] J. Sikorski, A. Denasi, G. Bucchi, S. Scheggi, and S. Misra, "Vision-based 3D control of magnetically actuated catheter using BigMag—An array of mobile electromagnetic coils," *IEEE/ASME Transactions on Mechatronics*, vol. 24, no. 2, pp. 505–516, 2019.

[141] V. K. Venkiteswaran, D. K. Tan, and S. Misra, "Tandem actuation of legged locomotion and grasping manipulation in soft robots using magnetic fields," *Extreme Mechanics Letters*, vol. 41, p. 101023, 2020.

[142] L. Yang, X. Du, E. Yu, D. Jin, and L. Zhang, "DeltaMag: An electromagnetic manipulation system with parallel mobile coils," in *2019 International Conference on Robotics and Automation (ICRA)*, 2019, pp. 9814–9820.

[143] B. Wang, K. F. Chan, K. Yuan, Q. Wang, X. Xia, L. Yang, H. Ko, Y.-X. J. Wang, J. J. Y. Sung, P. W. Y. Chiu, and L. Zhang, "Endoscopy-assisted magnetic navigation of biohybrid soft microrobots with rapid endoluminal delivery and imaging," *Science Robotics*, vol. 6, no. 52, p. eabd2813, 2021.

[144] C. Heunis, J. Sikorski, and S. Misra, "Flexible instruments for endovascular interventions: Improved magnetic steering, actuation, and image-guided surgical instruments," *IEEE Robotics & Automation Magazine*, vol. 25, no. 3, pp. 71–82, 2018.

[145] J. Sikorski, C. M. Heunis, F. Franco, and S. Misra, "The ARMM system: An optimized mobile electromagnetic coil for non-linear actuation of flexible surgical instruments," *IEEE Transactions on Magnetics*, vol. 55, no. 9, pp. 1–9, 2019.

[146] C. M. Heunis, Y. P. Wotte, J. Sikorski, G. P. Furtado, and S. Misra, "The ARMM system—Autonomous steering of magnetically-actuated catheters: Towards endovascular applications," *IEEE Robotics and Automation Letters*, vol. 5, no. 2, pp. 705–712, 2020.

[147] C. M. Heunis, B. F. Barata, G. P. Furtado, and S. Misra, "Collaborative surgical robots: Optical tracking during endovascular operations," *IEEE Robotics & Automation Magazine*, vol. 27, no. 3, pp. 29–44, 2020.

[148] D. Son, X. Dong, and M. Sitti, "A simultaneous calibration method for magnetic robot localization and actuation systems," *IEEE Transactions on Robotics*, vol. 35, no. 2, pp. 343–352, 2018.

[149] J. Rahmer, C. Stehning, and B. Gleich, "Spatially selective remote magnetic actuation of identical helical micromachines," *Science Robotics*, vol. 2, no. 3, p. eaal2845, 2017.

[150] J. Rahmer, C. Stehning, and B. Gleich, "Remote magnetic actuation using a clinical scale system," *PLOS ONE*, vol. 13, no. 3, p. e0193546, 2018.

[151] A. J. Petruska and J. J. Abbott, "Omnimagnet: An omnidirectional electromagnet for controlled dipole-field generation," *IEEE Transactions on Magnetics*, vol. 50, no. 7, pp. 1–10, 2014.

[152] A. J. Petruska, A. W. Mahoney, and J. J. Abbott, "Remote manipulation with a stationary computer-controlled magnetic dipole source," *IEEE Transactions on Robotics*, vol. 30, no. 5, pp. 1222–1227, 2014.

[153] T. L. Bruns, K. E. Riojas, D. S. Ropella, M. S. Cavilla, A. J. Petruska, M. H. Freeman, R. F. Labadie, J. J. Abbott, and R. J. Webster, "Magnetically steered robotic insertion of cochlear-implant electrode arrays: System integration and first-in-cadaver results," *IEEE Robotics and Automation Letters*, vol. 5, no. 2, pp. 2240–2247, 2020.

[154] D. Filgueiras-Rama, A. Estrada, J. Shachar, S. Castrejón, D. Doiny, M. Ortega, E. Gang, and J. L. Merino, "Remote magnetic navigation for accurate, real-time catheter positioning and ablation in cardiac electrophysiology procedures," *Journal of Visualized Experiments*, no. 74, p. e3658, 2013.

[155] C. Bellemare and T. Poder, "Effectiveness of biplane angiography compared to monoplane angiography for vascular neuro-interventions: A systematic review of the literature," *Clinical Radiology*, vol. 72, no. 7, pp. 612.e1–612.e5, 2017.

[156] B. Friedrich, C. Maegerlein, D. Lobsien, S. Mönch, M. Berndt, D. Hedderich, S. Wunderlich, D. Michalski, M. Lehm, T. Boeckh-Behrens *et al.*, "Endovascular stroke treatment on single-plane vs. bi-plane angiography suites," *Clinical Neuroradiology*, vol. 29, no. 2, pp. 303–309, 2019.

[157] A. Guenego, P. J. Mosimann, M. Wintermark, J. J. Heit, K. Zuber, T. Dobrocky, J. A. Lotterie, P. Nicholson, D. G. Marcellus, J. M. Olivot *et al.*, "Safety and effectiveness of neuro-thrombectomy on single compared to biplane angiography systems," *Scientific Reports*, vol. 10, no. 1, pp. 1–8, 2020.

[158] S. Chiaverini, G. Oriolo, and I. D. Walker, "Kinematically redundant manipulators," in *Springer Handbook of Robotics*, B. Siciliano and O. Khatib, Eds. Springer, 2008, pp. 245–268.

[159] K. Lynch and F. C. Park, *Modern Robotics: Mechanics, Planning, and Control.* Cambridge: Cambridge University Press, 2017, ch. Inverse Kinematics, pp. 187–202.

[160] "ASAHI Neurovascular Guidewire Instruction for Use," Asahi Intecc, 2012. https://asahi-inteccusa-medical.com/wp-content/uploads/2019/07/ASAHI-IFU-Neurovascular-Guidewire.pdf.

[161] D. J. Craik, *Magnetism: Principles and Applications.* Wiley, 1995.

[162] J. S. Agashe and D. P. Arnold, "A study of scaling and geometry effects on the forces between cuboidal and cylindrical magnets using analytical force solutions," *Journal of Physics D: Applied Physics*, vol. 41, no. 10, p. 105001, 2008.

[163] C. Di Natali, M. Beccani, and P. Valdastri, "Real-time pose detection for magnetic medical devices," *IEEE Transactions on Magnetics*, vol. 49, no. 7, pp. 3524–3527, 2013.

[164] Z. Zhuang and B. Bradtmiller, "Head-and-face anthropometric survey of U.S. respirator users," *Journal of Occupational and Environmental Hygiene*, vol. 2, no. 11, pp. 567–576, 2005.

[165] H. Gibo, C. Lenkey, and A. L. Rhoton, "Microsurgical anatomy of the supraclinoid portion of the internal carotid artery," *Journal of Neurosurgery*, vol. 55, no. 4, pp. 560–574, 1981.

[166] M. R. Harrigan and J. P. Deveikis, *Handbook of Cerebrovascular Disease and Neurointerventional Technique.* Totowa, NJ: Humana Press, 2013, ch. Treatment of Acute Ischaemic Stroke, pp. 343–398.

[167] S. Torikoshi and Y. Akiyama, "A concealed intracranial aneurysm detected after recanalization of an occluded vessel: A case report and literature review," *Interventional Neurology*, vol. 4, no. 3-4, pp. 90–95, 2016.

[168] F. Arikan, T. Martinez-Valverde, A. Sanchez-Guerrero, M. Campos, M. Esteves, D. Gandara, R. Torne, L. Castro, A. Dalmau, J. Tibau, and J. Sahuquillo, "Malignant infarction of the middle cerebral artery in a porcine model. a pilot study," *PLOS ONE*, vol. 12, no. 2, p. e0172637, 2017.

[169] S. Carniato, M. Mehra, R. King, A. K. Wakhloo, and M. J. Gounis, "Porcine brachial artery tortuosity for in vivo evaluation of neuroendovascular devices," *American Journal of Neuroradiology*, vol. 34, no. 4, pp. E36–E38, 2013.

[170] A. von Hessling, T. R. Del Castillo, G. Karwacki, and J. E. Roos, "The columbus steerable guidewire in neurointerventions: Early clinical experience and applications," *Journal of Neurointerventional Surgery*, vol. 14, no. 3, pp. 291–296, 2022.

[171] A. P. Mamunes, F. Campisano, J. Martin, B. Scaglioni, E. Mazomenos, P. Valdastri, and K. L. Obstein, "Magnetic flexible endoscope for colonoscopy: An initial learning curve analysis," *Endoscopy International Open*, vol. 9, no. 02, pp. E171–E180, 2021.

[172] T. Krings, D. M. Mandell, T.-R. Kiehl, S. Geibprasert, M. Tymianski, H. Alvarez, K. G. Terbrugge, and F.-J. Hans, "Intracranial aneurysms: From vessel wall pathology to therapeutic approach," *Nature Reviews Neurology*, vol. 7, no. 10, pp. 547–559, 2011.

[173] R. M. Starke, A. Turk, D. Ding, R. W. Crowley, K. C. Liu, N. Chalouhi, D. M. Hasan, A. S. Dumont, P. Jabbour, C. R. Durst, and R. D. Turner, "Technology developments in endovascular treatment of intracranial aneurysms," *Journal of NeuroInterventional Surgery*, vol. 8, no. 2, pp. 135–144, 2016.

[174] "ASIST™ Proprietary Thrombus Simulant," Vascular Simulations (Mentice), 2020. https://www.mentice.com/asist.

[175] J. J. Tharayil, S. M. Goetz, J. M. Bernabei, and A. V. Peterchev, "Field distribution of transcranial static magnetic stimulation in realistic human head model," *Neuromodulation: Technology at the Neural Interface*, vol. 21, no. 4, pp. 340–347, 2018.

[176] H. Tillander, "Magnetic guidance of a catheter with articulated steel tip," *Acta Radiologica*, vol. 35, no. 1, pp. 62–64, 1951.

[177] J. F. Alksne, "Magnetically controlled intravascular catheter," *Surgery*, vol. 64, no. 1, pp. 339–345, 1968.

[178] J. Molcho, H. Karny, E. H. Frei, and H. M. Askenasy, "Selective cerebral catheterization," *IEEE Transactions on Biomedical Engineering*, no. 2, pp. 134–140, 1970.

[179] H. L. Cares, J. R. Hale, D. B. Montgomery, H. A. Richter, and W. H. Sweet, "Laboratory experience with a magnetically guided intravascular catheter system," *Journal of Neurosurgery*, vol. 38, no. 2, pp. 145–154, 1973.

[180] S. K. Hilal, W. Jost Michelsen, J. Driller, and E. Leonard, "Magnetically guided devices for vascular exploration and treatment: Laboratory and clinical investigations," *Radiology*, vol. 113, no. 3, pp. 529–540, 1974.

[181] M. S. Grady, M. A. Howard, R. G. Dacey, W. Blume, M. Lawson, P. Werp, and R. C. Ritter, "Experimental study of the magnetic stereotaxis system for catheter manipulation within the brain," *Journal of Neurosurgery*, vol. 93, no. 2, pp. 282–288, 2000.

[182] A. Azizi, C. C. Tremblay, K. Gagné, and S. Martel, "Using the fringe field of a clinical mri scanner enables robotic navigation of tethered instruments in deeper vascular regions," *Science Robotics*, vol. 4, no. 36, p. eaax7342, 2019.

[183] A. Z. Taddese, P. R. Slawinski, M. Pirotta, E. De Momi, K. L. Obstein, and P. Valdastri, "Enhanced real-time pose estimation for closed-loop robotic manipulation of magnetically actuated capsule endoscopes," *The International Journal of Robotics Research*, vol. 37, no. 8, pp. 890–911, 2018.

[184] J. W. Martin, B. Scaglioni, J. C. Norton, V. Subramanian, A. Arezzo, K. L. Obstein, and P. Valdastri, "Enabling the future of colonoscopy with intelligent and autonomous magnetic manipulation," *Nature Machine Intelligence*, vol. 2, no. 10, pp. 595–606, 2020.

[185] International Organization for Standardization (ISO), "ISO 10993-1 Biological Evaluation of Medical Devices—Part 1: Evaluation and Testing within a Risk Management Process," 2018.

[186] International Organization for Standardization (ISO), "ISO 10993-4 Biological Evaluation of Medical Devices—Part 4: Selection of Tests for Interactions with Blood," 2017.

[187] International Organization for Standardization (ISO), "ISO 10993-5 Biological Evaluation of Medical Devices—Part 5: Tests for In Vitro Cytotoxicity," 2009.

[188] International Organization for Standardization (ISO), "ISO 10993-12 Biological Evaluation of Medical Devices—Part 12: Sample Preparation and Reference Materials," 2012.

[189] U.S. Food and Drug Administration (FDA) Center for Devices and Radiological Health, "Use of International Standard ISO 10993-1 Biological Evaluation of Medical Devices—Part 1: Evaluation and Testing within a Risk Management Process," 2020.

[190] R. Yoda, "Elastomers for biomedical applications," *Journal of Biomaterials Science, Polymer Edition*, vol. 9, no. 6, pp. 561–626, 1998.

[191] D. Fallahi, H. Mirzadeh, and M. T. Khorasani, "Physical, mechanical, and biocompatibility evaluation of three different types of silicone rubber," *Journal of Applied Polymer Science*, vol. 88, no. 10, pp. 2522–2529, 2003.

[192] A. Rahimi and A. Mashak, "Review on rubbers in medicine: Natural, silicone and polyurethane rubbers," *Plastics, Rubber and Composites*, vol. 42, no. 6, pp. 223–230, 2013.

[193] K. P. Rajan, A. Al-Ghamdi, R. Parameswar, and G. B. Nando, "Blends of thermoplastic polyurethane and polydimethylsiloxane rubber: Assessment of biocompatibility and suture holding strength of membranes," p. 240631, 2013.

[194] F. Wang, X. Yong, J. Deng, and Y. Wu, "Poly(N,N-dimethylacrylamide-octadecyl acrylate)-clay hydrogels with high mechanical properties and shape memory ability," *RSC Advances*, vol. 8, pp. 16 773–16 780, 2018.

[195] L. Weng, A. Gouldstone, Y. Wu, and W. Chen, "Mechanically strong double network photocrosslinked hydrogels from N,N-dimethylacrylamide and glycidyl methacrylated hyaluronan," *Biomaterials*, vol. 29, no. 14, pp. 2153–2163, 2008.

[196] V. E. Donohue, F. McDonald, and R. Evans, "In vitro cytotoxicity testing of neodymium-iron-boron magnets," *Journal of Applied Biomaterials*, vol. 6, no. 1, pp. 69–74, 1995.

[197] A. Francis, Y. Yang, S. Virtanen, and A. R. Boccaccini, "Iron and iron-based alloys for temporary cardiovascular applications," *Journal of Materials Science: Materials in Medicine*, 2015.

[198] M. Hopp, S. Rogaschewski, and T. Groth, "Testing the cytotoxicity of metal alloys used as magnetic prosthetic devices," *Journal of Materials Science: Materials in Medicine*, vol. 14, no. 4, pp. 335–345, 2003.

[199] L. Calabrese, A. Caprì, F. Fabiano, L. Bonaccorsi, C. Borsellino, and E. Proverbio, "Corrosion behaviour of a silane protective coating for NdFeB magnets in dentistry," *International Journal of Corrosion*, vol. 2015, p. 345038, 2015.

[200] Y. Li, Z. Qi, J. Yang, M. Zhou, X. Zhang, W. Ling, Y. Zhang, Z. Wu, H. Wang, B. Ning, H. Xu, W. Huo, and X. Huang, "Origami NdFeB flexible magnetic membranes with enhanced magnetism and programmable sequences of polarities," *Advanced Functional Materials*, vol. 29, no. 44, p. 1904977, 2019.

[201] S. M. Moghimi, A. J. Andersen, D. Ahmadvand, P. P. Wibroe, T. L. Andresen, and A. C. Hunter, "Material properties in complement activation," *Advanced Drug Delivery Reviews*, vol. 63, no. 12, pp. 1000–1007, 2011.

[202] T. M. Patel, S. C. Shah, and S. B. Pancholy, "Long distance tele-robotic-assisted percutaneous coronary intervention: A report of first-in-human experience," *EClinicalMedicine*, vol. 14, pp. 53–58, 2019.

[203] X. Jiang, H. Shokri-Ghadikolaei, G. Fodor, E. Modiano, Z. Pang, M. Zorzi, and C. Fischione, "Low-latency networking: Where latency lurks and how to tame it," *Proceedings of the IEEE*, vol. 107, no. 2, pp. 280–306, 2018.

[204] J. Zheng, Y. Wang, J. Zhang, W. Guo, X. Yang, L. Luo, W. Jiao, X. Hu, Z. Yu, C. Wang *et al.*, "5G ultra-remote robot-assisted laparoscopic surgery in China," *Surgical Endoscopy*, vol. 34, no. 11, pp. 5172–5180, 2020.

[205] M. Bechstein, J.-H. Buhk, A. M. Frölich, G. Broocks, U. Hanning, M. Erler, M. Anđelković, D. Debeljak, J. Fiehler, and E. Goebell, "Training and supervision of thrombectomy by remote live streaming support (RESS)," *Clinical Neuroradiology*, vol. 31, no. 1, pp. 181–187, 2021.

[206] M. Bechstein, S. Elsheikh, F. Wodarg, C. A. Taschner, U. Hanning, J.-H. Buhk, R. McDonough, E. Goebell, J. Fiehler, and M. Bester, "Republished: Interhospital teleproctoring of endovascular intracranial aneurysm treatment using a dedicated live-streaming technology: first experiences during the COVID-19 pandemic," *Journal of Neurointerventional Surgery*, vol. 13, no. 2, p. e1, 2021.

[207] L. Anand and S. Govindjee, *Continuum Mechanics of Solids.* New York, NY: Oxford University Press, 2020, ch. Vectors and Tensors: Algebra, pp. 3–22.

[208] M. E. Gurtin, E. Fried, and L. Anand, *The Mechanics and Thermodynamics of Continua.* New York, NY: Cambridge University Press, 2010, ch. Vector and Tensor Algebra, pp. 1–37.

[209] P. M. Mariano and L. Galano, *Fundamentals of the Mechanics of Solids.* New York, NY: Springer, 2015, ch. Tensor Algebra and Tensor Calculus, pp. 385–403.

[210] M. E. Gurtin, E. Fried, and L. Anand, *The Mechanics and Thermodynamics of Continua.* New York, NY: Cambridge University Press, 2010, ch. Vector and Tensor Analysis, pp. 39–57.

[211] L. Mullins, "Softening of Rubber by Deformation," *Rubber Chemistry and Technology*, vol. 42, no. 1, pp. 339–362, 1969.

[212] A. Dorfmann and R. W. Ogden, "A constitutive model for the mullins effect with permanent set in particle-reinforced rubber," *International Journal of Solids and Structures*, vol. 41, no. 7, pp. 1855–1878, 2004.

[213] R. W. Ogden and D. G. Roxburgh, "A pseudo–elastic model for the mullins effect in filled rubber," *Proceedings of the Royal Society of London. Series A: Mathematical, Physical and Engineering Sciences*, vol. 455, no. 1988, pp. 2861–2877, 1999.